Norwegian University of Life Sciences
Faculty of Biosciences
Department of Plant Sciences

Philosophiae Doctor (PhD)
Thesis 2023:14

Cell fate and blade patterning during the early growth of *Saccharina latissima* sporophytes

Celleutvikling og blad-mønsterdanning i tidlige stadier av *Saccharina latissima* sporofytter

Ioannis Theodorou

Cell fate and blade patterning during the early growth of *Saccharina latissima* sporophytes

Celleskjebne og bladmønster under i tidlige stadier av *Saccharina latissima* sporofytter

Philosophiae Doctor (PhD) Thesis

Ioannis Theodorou

Norwegian University of Life Sciences
Faculty of Biosciences
Department of Plant Sciences

Ås 2022
Großfahner, Germany (2022)

Thesis number 2023:14
ISSN 1894-6402
ISBN 978-82-575-2043-4

Norwegian University
of Life Sciences

Cartographie des destins cellulaires dans les jeunes sporophytes en croissance de l'algue brune *Saccharina latissima*

Cell fate and blade patterning during the early growth of *Saccharina latissima* sporophytes

Co-tutelle

Philosophiae Doctor (PhD) Thesis

Ioannis Theodorou

Collaborating groups:

Morphogenesis of Macroalgae (MMA), Roscoff Biological Station, Laboratory of integrative biology in marine models, CNRS, Sorbonne University (SU), Roscoff, France

Plant Sciences Department, Faculty of Biosciences, Norwegian University of Life Sciences (NMBU), Ås, Norway

Großfahner, Germany (2022)

Ås, Norway (2022)

Supervisors:

Dr. Bénédicte Charrier (Main supervisor, SU)
Research Director, LBI2M, MMA, SBR, Sorbonne Université, CNRS, Roscoff, France

Dr. Hilde-Gunn Opsahl Sorteberg (Main supervisor, NMBU)
Professor, IPV, Genetics and Plant Breeding, NMBU, Ås, Norway

Dr. Mallikarjuna Rao Kovi (Co-supervisor, NMBU)
Researcher, IPV, Genetics and Plant Breeding, NMBU, Ås, Norway

Evaluation committee:

Dr. John H. Bothwell
Associate Professor, Department of Biosciences, University of Durham, Durham, UK

Dr. Jean-Christophe Palaqui
Research Scientist, IJPB, INRAE, AgroParisTech, Université Paris-Saclay, Versailles, France

Dr. Christiaan van der Schoot, (Coordinator, NMBU)
Professor, IPV, Plant Biology and Plant Biotechnology, NMBU, Ås, Norway

Dr. Alex McDougall, (Coordinator, SU)
Research director, LBDV, Sorbonne Université, CNRS, Villefranche sur Mer, France

Author's note

This thesis follows the standards required by the Norwegian University of Life Sciences. It consists of an introductory section ("kappe") that presents the main principles on which this study is based and its purpose. This is followed by a brief presentation of the research results (Papers) and how they relate to the objectives of the PhD project. The main research work is presented after the kappe in the form of articles (Papers). Due to the complex nature of the doctoral project, there are no publications yet, other than a protocol. The articles presented are all at the manuscript stage. One of them is almost ready for submission, while the others are still in the process of preparation and further work.

Dedicated to my brother, my parents

and my family

Αφιερωμένη στον Αλέξανδρο

στην Γιώτα

στον Γιώργο

στην Νία

στην Σαπφώ

και την Άννα

Table of Contents

Acknowledgements

I would like to thank Bénédicte Charrier and Hilde-Gunn Opsahl Sorteberg for trusting me with this complex and demanding project. I feel especially grateful for the patience that they showed and being always openminded when discussing and arguing with me. I feel honored that I have worked with them, and their teachings and advice will remain.

I would like to thank my thesis committee, Phillippe Andrey, Floris Bosveld and Agnès Boutet for their advices and scientific interest. I think they helped a lot out and more meetings with them would have been good. Many gratitudes to the ED and its presidents (and generally administration in SU and NMBU) for always having to deal with my cottutelle agreement or my long and annoying emails.

I am grateful to Mallikarjuna Rao Kovi, taking the role of co-supervisor for Norway. I owe to him and Akyel a lot for teaching me bioinformatics, especially how to use R and interact with different tools on a non-graphical UI. Many thanks to Sylvia for her lessons in handling samples for RNA extraction. She was a tough teacher but good. I would like to thank the Genetics and breeding group for the opportunity to have a glimpse at the more applied direction of Science. Different approaches, different mindsets but nevertheless exciting to interact with. There are some brilliant people that unfortunately due to the restriction of time I couldn't appreciate more or get to know them better.

I would like to thank the MMA group in Roscoff. I am grateful to Bernard our bioinformatician for all the sleepless times and straining his eyes, his efforts on the models simulation and his overall stance as a scientist and colleague. I would like also to express my gratitude to Samuel Boscq, Sabine Chenivesse and Natalie Desban for all the fruiful discussions and efforts. Brainstorming, putting theories into discussion, arguing often with each other maybe sometimes too strongly but this is the way of the Morphogenesis of Macroalgae group, these have shaped me as young ambitious scientist and I hope I can honor the principles and the spirit that I got transferred.

Next, I would like to thank in my native language the people who supported me to this journey, whom due to my immigration outside of Greece I don't have often the opportunity to express my gratitude and many of them I miss dearly but they have supported me all these years during my bachelor and master studies and raising me up:

Στο μακρύ μου ταξίδι μέχρι εδώ είχα πρωτίστως την στήριξη του αδερφού μου Αλέξανδρου Παπακώστα, της μητέρας μου Παναγιώτας Καλαντζή και του πατέρα μου Γεώργιου Θεοδώρου. Χωρίς εκείνους θα ήμουν πιθανότατα ένα πολύ διαφορετικό άτομο, τους ευχαριστώ για την υπομονή τους και το κουράγιο τους όλα αυτά τα χρόνια. Σημαντική πυξίδα υπήρξε ο πρώτος μου υπεύθυνος, ο επίκουρος καθηγητής Χρίστος Κατσαρός, στις αρχές και αξίες που πρέπει να διέπουν ένα επιστήμονα καθώς και το μεράκι στην έρευνα. Ευχαριστώ γενικότερα όλους τους καθηγητές μου από το τμήμα Βιολογίας του ΕΚΠΑ για τις γνώσεις και βάσεις που μου δοθήκαν. Ευχαριστώ τους φίλους μου από την Ελλάδα Νάντια Δανιά, Δημήτρη Μακρέα, Γιώργο Νικολόπουλο, Κατερίνα Δούκα, Θοδωρή Ταμιωλάκη, Μαρία Κορίνη που με άντεχαν

όταν νερντούλιαζα και παραπονιόμουν, υπερεκτιμώ όλη την υποστήριξη ηθική και ψυχολογική όλα αυτά τα χρόνια.

Δυστυχώς όλα αυτά τα χρόνια μακριά από την Ελλάδα είχα ελάχιστες επαφές με Έλληνες. Κυρίως λοιπόν κράτησα επαφή με την χώρα μου εκτός από τα τηλέφωνα με την οικογένεια μου, αλλά και μέσω της Ελληνοφρένειας, την αγαπημένης μου εκπομπής από τα 17 αν θυμάμαι καλα. Πολλά ευχαριστώ λοιπόν και στον Θύμιο Καλαμούκη και Αποστόλη Μπαρμπαγιάννη.

To the English speakers:

I would like to thank most of all my Rostbratel, Nichen and Sapphuchen, my family in Germany for putting up with me and my peculiarities as well as with the distance. I had been cutoff for too long from them and my Greek family to pursue my studies and goals. Their psychological support was essential, especially when I had to deal with shitty people or a shitty situation. I cannot forget to thank Sandra, Jonas and Jens Beck for their great hospitality and warm embrace, and a place that I can call my second home. I think more often than enough a silly comment from Anna, a shenanigan (that I had to be strict about it) of Nea and a sweet smile from Sappho were my fuel to push forward. Family is often treated by most scientists as a heavy stone that you have to carry around but is not right. Family is the base of the stair; they push us and support us to progress we cannot reach anywhere without them.

I have made several friends in Roscoff and some acquintances in Norway. I would like to thank them too. Specifically, Orestis, Joost, Marieke, David, Cedric, Cedric Jacob and his sweet mother Marilou, Eugenie, Qi Qun, Yacine, Marina, Sam, P.G., Guillaume, Kevin. I forget many of them. They made my time in Roscoff very pleasant. Cheers to everyone and hope to share a wine, a beer and a rum again at Albatros or Ty Pierre. And from Norway, many thanks to Camilla, Domniki, Martin, Marian, Akyel and Alye

English Summary

Saccharina latissima is a multicellular parenchymatic photosynthetic organism in the group of brown algae (Phaeophyceae). It belongs specifically to the group of kelps (Laminariales), a group that has recently acquired great economic and ecological importance. Notably, our knowledge for *Saccharina* and the other kelps is restricted to their physiological and ecological traits while our understanding on their development is mostly outdated or incomplete. Their life cycle is diplobiotic with heteromorphous generations. Specifically, the large and conspicuous plant is the sporophyte, and the microscopic stage is represented by two dioecious gametophytes. The early development of the sporophyte is a largely unknown process.

The aim of this project was to elucidate the morphogenesis of *Saccharina latissima*'s embryos from descriptive and mechanistic point of view. First, we identified three main phases based on the body axes of the embryo. Phase I follows the formation of the polarised zygote, characterised by a sequence of anticlinal transverse divisions perpendicular to the main growth axis. Then, longitudinal anticlinal divisions take place during Phase II, leading to the formation of a monostromatic grid made of cross-aligned cuboid cells. The third growth axis is introduced during Phase III, together with the emergence of different types of tissue, a process defined as polystromatisation. Then (Paper I), a morphometric study was performed in Phase II. Morphometric quantitative parameters like cell division rate and orientation as well as cell shape and direction of expansion were collected and combined with hyperosmotic treatments to test simulations derived from vertex modelling. Simulations suggest that anisotropic patterns on cell wall (CW) stiffness explain the 2D morphogenesis of the embryo. Next (Paper II), we postulated that these patterns could be underlied by a specific organisation of the cytoskeleton. Observations on actin labelling show an anisotropic actin filaments (AFs) organisation at the cortex below the anticlinal CWs. Specifically, the cortical AFs are parallel to the future third growth axis. In contrast, the AFs below the walls of the front and rear surfaces seem isotropic. Drug treatments did not assist to establish a functional link between the CW stiffness and AF patterns. However, AFs potentially restrict cell growth along a 2D plane. We postulate that this pattern of AFs organisation needs to be rearranged for allowing cell growth and division along the three spatial axes, and therefore, to allow thickening of the so far monolayer lamina. Furthermore, we focused on the cellular and molecular events leading lamina thickening (Phase II – to – Phase III transition). At the molecular level (Paper IV), transcriptomic analysis during the initiation of Phase III detected a downregulation of most of the differentially expressed genes. In addition, GO analysis indicates a switch of gene expression towards signaling and post-translational modifications. However, a direct relation between the patterns of gene expression and the addition of a third growth axis has not been established. At the cellular level (Paper III), semithin sections elucidated the patterns of 3D growth and cell differentiation. Specifically, polystromatisation (thickening) and cell differentiation occurs centripetally from an external epidermal meristem and propagates acropetally from the base of the embryo. Different regions of the developing thallus present different morphometries and abundance of the different cell types. For example, the older polystroma is rich in medullary elements and poor in cortical cells, and the inverse is observed in younger polystroma.

My project formulates a morphogenetic model for *Saccharina*'s embryos, based on simple cellular mechanics. Anisotropic patterns explain how the embryos acquire their initial shape which is the scaffold for the late 3D growth accompanied by tissue emergence and a superficial meristem.

French Summary

Saccharina latissima est un organisme photosynthétique multicellulaire parenchymateux du groupe des algues brunes (Phaeophyceae). Elle appartient spécifiquement au groupe des kelps (Laminariales), qui a récemment fait l'objet d'un intérêt croissance au niveau économique et écologique. Nos connaissances sur *Saccharina* et les autres laminaires sont limitées à leurs caractéristiques physiologiques et écologiques, et notre compréhension de leur développement est pour la plupart ancienne ou incomplète. Leur cycle de vie est diplobiontique avec des générations hétéromorphes. Plus précisément, la phase du cycle la plus grande et la plus visible est le sporophyte et le stade microscopique est représenté par deux gamétophytes dioïques. Le développement précoce du sporophyte est un processus largement inconnu.

Le but de ma thèse était d'identifier les mécanismes impliqués dans la morphogenèse des embryons de *Saccharina latissima* , essentiellement sur le plan mécanique. Tout d'abord, nous avons identifié trois phases principales basées sur les axes de croissance des embryons. La Phase I correspond la formation de l'axe apico-basal (X) du zygote, puis du jeune embryon par une séquence de divisions transversales anticlinales perpendiculaires à l'axe longitudinal du zygote. Ensuite, des divisions longitudinales anticlinales ont lieu pendant la Phase II, établissant le deuxième axe de croissance (Y) perpendiculaire au premier. La succession de divisions dans les axes X et Y conduit à la formation d'une grille monostromatique composée de cellules cuboïdes alignées en lignes et en colonnes. Le troisième axe de croissance (Z) est introduit au début de la Phase III, au cours de laquelle l'embryon s'épaissit – un processus nommé polystromatisation – et différents types de tissus se différencient.

Dans un deuxième temps de ma thèse, une étude morphométrique a été réalisée au stade Phase II (Paper I). Des paramètres quantitatifs morphométriques tels que le taux et l'orientation des divisions cellulaires ainsi que la forme des cellules et la direction de la croissance cellulaire ont été collectés. De plus, des traitements hyperosmotiques ont été effectués sur les embryons de *S. latissima* pour estimer d'éventuelles anisotropies mécaniques. Ces données quantitatives biologiques ont « nourri » un modèle de type « vertex model » bidimensionnel (2-VM). Le résultat des simulations suggère que l'anisotropie de la rigidité de la paroi cellulaire (CW) dans les axes X et Y peut rendre compte de la morphogenèse 2D de l'embryon. Ensuite (Paper II), nous avons caractérisé l'organisation du cytosquelette pour évaluer dans quelle mesure elle pouvait jouer un rôle dans la morphogenèse de l'embryon. Les observations sur le marquage de l'actine montrent une organisation anisotrope des filaments d'actine (AFs) au niveau du cortex le long des parois anticlinales. Notamment, les AFs corticaux sont parallèles au futur et troisième axe de croissance. En revanche, l'organisation des AFs localisés le long des parois cellulaires « avant » et « arrière » semble isotropes. Les traitements aux drogues déstabilisant les AFs n'ont pas permis d'établir un lien fonctionnel entre la rigidité des MC et l'organisation des AFs. Cependant, les AFs limitent potentiellement la croissance cellulaire le long d'un plan 2D. Nous postulons que la croissance et la division cellulaires dans les trois axes de l'espace, et en particulier l'épaississement de la lame monocouche, nécessitent une ré-organisation des AFs.

Tester cette hypothèse nécessite de mieux comprendre les événements cellulaires et moléculaires à l'origine de la polystromatisation. Ainsi, dans un troisième temps de ma thèse, j'ai entamé une analyse transcriptomique pendant la transition de la Phase II à la Phase III de l'embryogenèse (Paper IV). J'ai détecté une régulation négative de la plupart des gènes différentiellement exprimés. En outre, l'analyse GO indique un changement de l'expression des gènes vers la signalisation et les modifications post-traductionnelles. Cependant, une relation directe entre les modèles d'expression génique et l'ajout d'un troisième axe de croissance n'a pas été établie. Par ailleurs, j'ai effectué des coupes semi-fines dans le but d'élucider les patrons de croissance 3D et de différenciation cellulaire au moment du

changement d'axes de croissance de la monocouche (X-Y) à son épaississement (X-Y-Z) (Paper III). J'ai décrit que la polystromatisation et la différenciation cellulaire se produisent de manière centripète à partir d'un méristème épidermique externe et se propagent de manière acropète à partir de la base de l'embryon. Des différences dans la forme et l'abondance des différents types cellulaires sont observées en fonction des régions de l'embryon. Par exemple, le polystroma le plus ancien est riche en éléments médullaires et pauvre en cellules corticales, et l'inverse est observé dans le polystroma le plus jeune.

En résumé, mon projet apporte les premiers éléments sur le rôle potentiel des forces mécaniques dans le patron de croissance de la lame monocouche de l'embryon *S. latissima* et sur le changement d'orientation de croissance cellulaire au moment de la polystromatisation. La mise en place d'anisotropies mécaniques au niveau de la paroi et d'anisotropie dans l'organisation du cytosquelette apparaît globale et homogène à l'échelle de l'embryon.

Norwegian Summary

Saccharina latissima (sukkertare) er en flercellet parenkymatisk fotosyntetiserende organisme i gruppen brunalger (divisjon Phaeophyceae). Sukkertare er en såkalt kelp i ordenen Laminariales, som er økologisk viktig og som nylig har fått økt økonomisk interesse. Vår kunnskap om *Saccharina* og andre stortarer er hovedsakelig knyttet til deres fysiologiske og økologiske egenskaper, mens vår forståelse av deres utviklingsbiologi er utdatert og ufullstendig. Plantens livssyklus består av en dominerende stor sporofytt og de små adskilte (toboede) gametofyttene. Den tidlige utviklingen av sporofytten er hovedsakelig ukjent.

Prosjektets mål var kartlegging av embryo utvikling i sukkertare. Først identifiserte vi embryoets tre hovedfaser basert på dets kroppsakser. Fase I følger den polariserte zygoten, karakterisert av antiklinale tverrdelinger i forhold til hovedaksen. Deretter følger antiklinale lengdedelinger i fase II (alternerende celledelinger parallelt og vinkelrett på lengdeaksen), som danner det monostromatiske cellenettet som utgjøres av kryssliggende kubiske celler. Den tredje aksen settes i fase III, samtidig som ulike vev differensieres, en prosess som defineres av polystromatisering. Vår første artikkel (Artikkel I) presenterer en morfometrisk studie av fase II med morfometriske kvantitative parametre som celledelingsrate og celleorientering, samt celle form og retning av ekspensjonen. Dette er kombinert med hyperosmotisk behandling for å teste simuleringer fra vertex modellering. Simuleringene indikerer at anisotropiske stive celleveggsmønstre kan forklares av det todimensjonale (2D) embryoet. I artikkel II (Artikkel II) postulerer vi at disse mønstrene kan underbygges av spesifikk cytoskjelett organisering. Observasjoner fra aktinmerking viser en anisotropisk aktinfilament (AF) organisering i cortex under antiklinale cellevegger (CWs). De kortikale AFs er parallelle til den fremtidige tredje aksen, mens derimot de AFs under veggene i de fremre og bakre overflatene syntes isotropiske. Kjemisk behandling kunne ikke etablere en funksjonell kobling mellom CW stivhet og AF mønstre. LIkevel kan AFs potensielt begrense cellevekst langs det todimensjonale planet. Vi postulerer at denne organiseringen av AFs må reorganiseres for å muliggjøre celleekspansjon og celledeling langs alle tre aksene, og dermed utviklingen av en tykkere lamina (fase II til fase III overgangen). På det molekylære nivået (Artikkel **IV**) syntes det å være en nedregulering av gener mer avgjørende enn oppregulering. I tillegg indikerer GO analysen en endring av genuttrykk mot signaltransduksjon og post-transkripsjonelle modifikasjoner i dette stadiet. En direkte sammenheng mellom ett genuttrykksmønster og etableringen av 3D identitet er som forventet ikke etablert. Videre viste semitynne snitt 3D vekst og celledifferensiering (Artikkel I**II**), med polystromatisering (fortykning) og celledifferensiering i basalenden av embryoet i motsetning til et eksternt epidermalt meristem. Ulike regioner består av ulike celletyper og i ulike relative forhold, som f eksempel at eldre polystroma hovedsakelig består av medullære elementer men få kortikale celler, og motsatt i yngre polystroma. Mitt prosjekt formulerer en morfologisk model for *Saccharina*'s embryo, basert på enkle cellulære mekanismer. Anisotropiske mønstre forklarer hvordan embryoene oppnår sin opprinnelige form, som er ett mønster for senere 3D vekst sammen med en overfladisk meristoderm.

List of papers

Paper I: Making a monolayer lamina with aligned cuboid cells: the case of the embryo of the brown alga *Saccharina*

Paper II: Organisation of the cytoskeleton in the early embryo of the kelp *Saccharina latissima*

Paper III: Outside in: how kelp embryos shift to 3D growth, an atlas of cell division and differentiation

Paper IV: The first transcriptomic analysis of *S. latissima* embryo development with possible connections between cell divisions, the cytoskeleton and eukaryotic phylogeny

Paper V: Preparation of Zygotes and Embryos of the Kelp *Saccharina latissima* for Cell Biology Approaches

List of figures

List of abbreviations

4WJ	Four cell wall Junction
AF	Actin filaments
azp	After zygote polarisation
BCV	Biological coefficient of variation
BSA	Bovine serum albumin
CMF	Cellulose microfibrils
CW	Cell wall
DAF	Days after fertilization
DAPI	4',6-diamidino-2-phenylindole
DMSO	Dimethyl sulfoxide
ECM	Extracellular matrix
GTA	glutaraldehyde
LatB	Latrunculin B
MBS	m-maleimido benzoic acid N-hydroxy succinimide ester
MT	microtubule
MTB	Microtubule stabilisation buffer
Noc	Nocodazole
PBS	Phosphate buffered saline
PD	plasmodesmata
PES	Provasoli Enriched Seawater
PF	Pit-fields
PFA	paraformaldehyde
Ph-Alexa488	Alexa-fluor™ 488 conjugated phalloidine
Ph-Rh	Rhodamine conjugated phalloidine
ROI	Region of interest
ROS	Reactive oxygen species
RT	Room temperature
TF	Transcription factor
TZ	Transition zone

1. Introduction

1.1. Developmental differences of animals and plants

Multicellular organisms can vary from colonial forms like *Volvox*, to complex cell arrangements with specialized tissues shaping whole body plans and organs (Niklas and Newman 2013) like metazoans or land plants. The development and emergence of the different tissues in parenchymatic Eukaryota is dependent on cell differentiation and cell communication (Niklas 2014) as well as the physical and biochemical properties of their extracellular matrix (ECM) (Karamanos et al. 2021) or cell wall (Charrier et al. 2019; Kloareg et al. 2021). During the embryogenesis of metazoans like *Drosophila* (fig. 1 a), their cells reside on a fluidic substrate, especially at the initial steps, offering much freedom of movements from cell migration to forming furrows and folds (Hannezo and Heisenberg 2019). A collective example of this tissual freedom is found during gastrulation (Leptin 1999) with the mesodermal ventral furrow in *Drosophila*. First, the ventral mesoderm will fold inwards, then the internalized cells will break from the epithelial tissue, divide and migrate forming one cell layer on top of the ectoderm. For the described tissue changes, there are necessary cell shape changes and tissue mechanics driven by the structure of actinomyosin systems in interaction with their ECM (LeGoff and Lecuit 2016). Actinomyosin structure and dynamics control cell shape and movement as well as the stiffness of animal cell borders (LeGoff and Lecuit 2016; Heer and Martin 2017; Hannezo and Heisenberg 2019). During the ventral furrow, topological variation takes places between two tissue populations on actinomyosin dynamics in contractility. In case of the ventral region, there is a gradient of contractility with the tissue away from the future furrow to be gradually unbending along a dorsal ventral axis, this arrangement leads to the selective position of the furrow.

Land plants on the other hand like *Arabidopsis thaliana* (fig. 1 b) have a rigid and restrictive cell wall as ECM (Charrier et al. 2019; Kloareg et al. 2021), their cells cannot migrate or change their shape like animal cells. Therefore, the different shapes of organs and embryos are driven mainly from cell shape and size as well as division frequency and orientation (Sinnott 1960 chap. 3). However, cell division and changes in size (cell growth) are also important for the morphogenesis of animal tissues (LeGoff and Lecuit 2016). Key difference between animal and plant development is the potential of stem cells activity, which in animals is finite taking place mainly during development (Gilbert and Barresi 2018). In plants, there are low differentiation regions with increased potential in cell division, localized at the apex of the shoot and the root where the plant stem cells reside (Heidstra and Sabatini 2014; Moody 2020). The apical meristems (ap, fig. 1 b) have the potential of infinite primary growth and production of aerial organs (lp, fig. 1 b) , a big developmental difference with the finite animal development.

1.2. Morphogenetic mechanisms in land plants

Land plants are not the only cell walled organisms with complex multicellularity and parenchymatic body plan (Grosberg and Strathmann 2007; Popper et al. 2011; Niklas and Newman 2013, 2020). However, they are the best studied group regarding tissue morphogenesis and development. There is great amount of works and reviews on the genetic background and transcriptional regulation during different stages of development (e.g. embryo: (Verma et al.

2022) ,apical meristem: (Chang et al. 2020)) as well as structures (flower; (Alvarez-Buylla et al. 2010)) and organs (lateral root;(Banda et al. 2019)). The main model of these works is *Arabidopsis* (Koornneef and Meinke 2010), however other species like *Cardamine hirsuta* (Vlad et al. 2014) and *Antirrhinum* (Xu et al. 2021) have been on the focus too. One example comes from the evolution of MADs MIKC transcription factors (TF) (Theißen et al. 2016) and how their combinatory function controls the development of the flowers and the variety of different shapes and sizes. Another example is the evolution and development of leaf shape (Sarvepalli et al. 2019).

However, shape changes (morphogenesis) are not simply induced by transcriptional regulation or biochemical control. Mechanical properties based on traits of cells, tissues, or organs as well as the forces applied from turgor pressure are at the base of any morphogenetic mechanism (Trinh et al. 2021). Specifically, morphogenesis of any plant tissue or organ is based on cell mechanics, which are features that are quantifiable on cellular level (Sinnott 1960; Geitmann and Ortega 2009; Autran et al. 2021). Cell division plane and rate, cell expansion direction and intensity as well as cell shape and size are the main quantifiable cell features related to morphogenesis. Changes to these traits depend on the cytoskeleton ultrastructure and cell wall physical properties while turgor pressure generates the necessary force on the apoplast as well as mechanical cues (Trinh et al. 2021). For example, an anisotropically stiffer cell wall directs turgor pressure, therefore, cell expansion towards a specific direction or axis (Lockhart 1965; Cosgrove 1987; Geitmann and Ortega 2009; Trinh et al. 2021), while cytoskeleton participates in setting up the anisotropy and cell division/cytokinesis plane determination (Lloyd 1991; Hamant et al. 2008). In addition, cytoskeleton underlies any cell trafficking therefore the transport of material that can modify the physical properties of the cell wall and participate in mechanical signalling.

1.3. Properties of cell wall and tissue morphogenesis

The main structural component of growing undifferentiated plant cell walls (CWs) is microfibrils of cellulose (CMF) embedded in an amorphous matrix of pectins, interconnected with hemicellulose (Cosgrove 2000a). The orientation of CMF is essential for the constrain of cellular growth and direction to the work of turgor pressure (Szymanski and Cosgrove 2009). An isotropic CW has identical properties on every orientation in contrast with an anisotropic CW that is stiffer or more plastic to some regions. Stiffness and plasticity are key physical properties of an extending material. A stiff CW presents higher resistance to extension, while a plastic CW when extended keeps to some level that change in shape (Geitmann and Ortega 2009). The current model is that biochemical changes of pectins (e.g. methylesteration), hemicelluloses and the other components of the CW can modulate its stiffness and/or plasticity (Cosgrove 1987, 2022; Peaucelle et al. 2011). These changes control the direction and intensity of cellular growth as well as the cell shape, both of them depending on the applied forces from turgor pressure (Cosgrove 2018). However, cells are not isolated and their neighboring cells can affect their growth potential when their turgor collides on the same CWs, generating mechanical conflicts (Trinh et al. 2021). Depending on the scale of the conflicts (a few cells or whole tissues) these conflicts lead to different organ or tissue shapes.

1.4. Mechanical stress and the role of cytoskeleton

In developing organs, turgor and the physical properties of CW generate tensile stress (also mechanical stress), that is the pulling force perpendicular to any of the cell surfaces. Tensile stress is perceived by the cells and can be instructive for cell expansion and morphogenesis of the organ through mechanoperception and mechanical impact. In isotropically stressed tissues like apical meristems or *Coleochaete* algae, the lay down of new CWs during cytokinesis takes place according to the empirical rule of Errera (Besson and Dumais 2011; Louveaux et al. 2016a). Specifically, microtubules (MTs) perceive the geometrical cues of the cells and then cytoskeleton and associated proteins lead the development of phragmoplast and hence, of cytokinesis through the centroid and the shortest path possible (Lloyd 1991; Besson and Dumais 2011; Livanos and Müller 2019). In anisotropically stressed tissues like the margins between apical meristem and organs primordia, cytokinesis takes place along the direction of the maximal tensile stress which coincides with the stress generated by the tissue (Louveaux et al. 2016a). Nevertheless, cell division plane can be predicted in both isotropically and anisotropically stressed tissues with area minimization passing through or approximately through the centroid, suggesting a more potential role of cell geometry to cell division (Moukhtar et al. 2019).

Cortical MTs are usually perpendicular to the main growth axis of a cell, often parallel to the axis of maximal tensile stress from growing organs or tissues, like in the shoot apical meristem (Williamson 1990; Hamant et al. 2008; Landrein and Hamant 2013). The organisation of cortical MTs guides cellulose synthase complexes (Baskin et al. 2004; Paredez et al. 2006; Sampathkumar et al. 2019), which results in the alignment of CMFs with cortical MTs. From a mechanistic point of view, growth anisotropy and shape determination depend mostly on CMFs orientation (Geitmann and Ortega 2009; Sampathkumar et al. 2014b). Therefore, cortical MTs orientation regulates cell shape and growth direction (isotropic, anisotropic) through the aligned CMFs. Cortical MTs orientation is the product of a mechanical feedback loop where cortical MTs organisation responds to the cell geometry, cell growth direction and maximal tensile stress axis generated either from the stressed CW or/and tissue physical properties (e.g. bulking or oriented growth) (Hamant et al. 2019; Trinh et al. 2021).

It is unclear how cells and cytoskeleton perceive mechanical stress but there are few candidate molecules. CW associated receptor kinases are potential CW integrity sensors therefore also mechanical stress sensors (Zhao et al. 2018). Kinases of the WAK and FER families interact with pectins (Kohorn 2016) either cross-linked or fragmented, which can lead to transcriptional changes in development or stress – related responses. Released Ca^{2+} from the pectins in combination with stretch sensing channels can further promote cytoskeletal changes based on the integrity of the CW. DEK1 is another potential primary mechanosensor of CW integrity that could turn on Ca^{2+} channels (Tran et al. 2017; Zhao et al. 2018). Then, Ca^{2+} interacts with Rho GTPases which can reorganise the cytoskeleton in both animals (Marston et al. 2019) and plants (Craddock et al. 2012). Alternatively, there are a few hypotheses coupling cortical MTs organisation and their function as sensor of CW mechanical heterogeneities (Hamant et al. 2019) then, stress will lead to structural and gene expressional changes to maintain or alter the feedback loop.

1.5. Early development of leaves as morphogenetic model

Ideal models on the mechanical approach of morphogenesis is leaf and sepal organogenesis (Zhao et al. 2020; Trinh et al. 2021). First auxin promotes the organ initiation at the shoot apical meristem, involving the induction of expansins via pH changes (Nakahori et al. 1991; Cosgrove 2000b; Arsuffi and Braybrook 2018) and pectin demethylesteration leading to decrease CW stiffness and increased CW expansion (Peaucelle et al. 2011). Cortical MTs at the top of the initiated organ have random orientation following the isotropic nature of the predicted tensile stress (Hamant et al. 2008; Sampathkumar et al. 2014b), in contrast with the margins where anisotropic tensile stress occurs. During early stages of blade development and specifically shortly after the organ initiation, margin determination genes *WOX1* and *PRS* shape the leaf primordium to a flat ellipsoid (Zhao et al. 2020; Zhang et al. 2020). This initial shape is enhanced during leaf development through mechanical feedback between tensile stress along the abaxial-adaxial axis and the cortical MTs of the inner anticlinal CWs. Cortical MTs are orientated parallel to the abaxial-adaxial axis, restricting cell growth along two axes thus promoting the flat shape of the early blade (Zhao et al. 2020). The predicted axis of maximum tensile stress is along the abaxial-adaxial axis being part of a mechanical feedback loop with the restriction on cell growth from the cortical MTs and the parallel CMFs. In short, the cortical MTs and CMFs of the inner CWs are aligned to the axis of maximal tension as observed in other systems (Hamant et al. 2008; Sampathkumar et al. 2014a, 2019). In addition, cell divisions are stress-driven following the previously mentioned rule of Louveaux et al. (2016), therefore, they are mostly anticlinal, parallel to the abaxial-adaxial axis. Sepals early development follows the same principles as the leaves (Zhao et al. 2020).

1.6. Robustness and stochasticity

Stochasticity and robustness are two important principles of morphogenesis. Stochasticity is the quality of unpredictability to the outcome of a process or event, expressed in biological context as variability and noise in gene expression for example or cell growth and shape (Meyer and Roeder 2014). Another example comes from cell division plane probabilities. Since plant cells have no simple cuboid shape but are mostly hexagonal, there can be up to three even four optimal division planes going through the centroid in tissues stressed isotropically (Besson and Dumais 2011). Surface area minimisation designates that one division plane is more probable than the other. However, all four division planes may be observed on the growing tissue. Similarly, there is great variability in cell growth and shape in the developing sepals epidermis due to the chance that an epidermal cell exits the mitotic cell cycle and enters endo-reduplication (Roeder et al. 2010). This leads to heterogeneity in cells mechanical properties like shape and growth as well as local conflicts (Hong et al. 2016). This heterogeneity has genetic background. However, it remains mostly probabilistic. Additionally, reactive oxygen species (ROS) in sepals act as termination and maturation signal highly concentrated at the maturation zone of the sepals while inhibiting variability. Nevertheless, this variability is essential for the high robustness shown in sepal development (Hong et al. 2016). As robustness is defined the reproducibility in the morphogenetic and developmental processes, in essence, how much identical are the products of development. The sepals of *Arabidopsis* are almost identical between them despite the stochasticity that leads to variability of cell growth

and cell size (Hong et al. 2016). In sepals, variable growth occurs through all the developing organs, while stomata differentiation introduces local growth variability on epidermis of developing leaves (Le Gloanec et al. 2022). To result to the robust final shape of leaves, the neighbouring cells of stomata buffer the effect of local growth variability in contrast to sepals where spatiotemporal averaging takes place.

In summary, the morphogenesis of plants can be quantified and followed on simple morphometrical parameters like cell size, shape, division plane and rate as well as direction of growth or expansion. These are basically the motors for any morphogenetic mechanism. These mechanisms are underlined by properties of cytoskeleton and CW being together part of a mechanical feedback loop based on the tensile stress (pulling forces) generated by the turgor and the resistance or stiffness of the CW.

1.7. Brown algae cell and thallus organisation

Brown algae (Phaeophyceae) is a group of photosynthetic cell walled, mostly marine, organisms in the protist group of Heterokonta (Bringloe et al. 2020). That means that their last common ancestor with land plants and generally the Archaeplastida lineage dates more than 1.5 billion years ago (Yoon et al. 2004), while as group they are relatively recent, diverged from the rest of heterokonts 252 - 266 million years ago. They have the same in-finite growth potential as land plants and share many cytological traits (Bogaert et al. 2013) like CW plasmodesmata enabling communication between cells (Terauchi et al. 2015) as well as sieve elements for long distance transports and potentially signalling (Drobnitch et al. 2015). However, they have centrioles, lack preprophase band and cortical MTs (Katsaros et al. 2006), and only a very small percentage of cellulose at their cell wall which is mainly con-sisted of alginates and fucose containing sulfated polysaccharides (Charrier et al. 2019).

Brown algae demonstrate a great variety of thallus (body plan) morphologies and growth strategies. Their thalli can be uniseriate filaments like *Ectocarpus* (fig. 1 (f)) with typical tip growth though dependent on different cell wall mechanics than pollen tube or root hairs (Rabillé et al. 2019a). Filamentous thalli can often be consisted of two different types of filaments depending if they are upright or prostrate (Charrier et al. 2008). In many cases, like some species of Tilopteridales, the prostrate part forms discs that can hibernate through tough environmental conditions (Kuhlenkamp 1996). Filamentous thalli can also result from diffused growth and trichothallic growth (e.g. the polystichous species *Tilopteris mertensii* (Kuhlenkamp 1996)*)*. This differs from Sphacelariales, that are polystichous growing apically with cell differentiation based on cell position (Ducreux 1984). Desmarestiales are pseudoparenchymatic with complex filamentous aggregations around one axial filament (Fritsch 1945). Many brown algae are parenchymatous, and most studies in tissue organisation and development focused on the orders of Fucales, Dictyotales and Laminariales (Fritsch 1945; Charrier et al. 2012).

1.8. Development in parenchymatic brown algae

Parenchymatic brown algae demonstrate some functional similarities on meristematic growth with land plants. The primary growth of both Fucales and Dictyotales depend on apical meristems. In Fucales, the apical meristem of *Fucus* is made of a single cell that divides rarely

(Moss 1967, 1969, 1970). That differs from *Sargassum* (fig. 1d) (Linardić and Braybrook 2017) and *Cystophora* (Klemm and Hallam 1987) where the apical cells divides regularly like the apical cell of *Physcomitrium*'s gametophore (Harrison et al. 2009). Dictyotales have active apical cells, which divide asymmetrically into a monolayer tissue (*Dictyopteris*, 8 apical initial cells (Katsaros and Galatis 1988)) or divide into a three-dimensional lamina in two steps (*Dictyota,* one or two apical cells, fig. 1c) (Katsaros and Galatis 1985; Gaillard et al. 1986). In comparison, the apical meristem of land plants produces new tissues while the central zone divides infrequently (Steeves and Sussex 1989), like the apical cells of the Fucales *Fucus* (Moss 1967) and *Ascophyllum* (Moss 1970). In Fucales and Dictyotales, a big proportion of the apical meristem functions and it is completed by the lateral growth that depends on a unique meristematic tissue, the meristoderm. The meristoderm is an external epidermal meristem found in all parenchymatic lineages of brown algae (Fritsch 1945).

In Laminariales, like *Saccharina latissima* (fig. 1 e) there is no apical meristem, the main growth site is an intercalary region between the blade and the stipe called the transition zone (TZ) (fig. 2)(Smith 1939; Fritsch 1945) where the meristoderm and the underlying tissues are particularly active division wise. Derivatives of the periclinal (parallel to the surface) divisions of meristoderm differentiate into cortical cells and form the cortex. The inner cortex re-differentiates into medulla cells (Smith 1939; Fritsch 1945). The tissues below the meristoderm are actively growing and expand acropetally and medio laterally. Therefore, to accompany the underlying growth, the meristoderm divides anticlinally on both possible directions, as the peripheral layer L1 in land plants does (Sinnott and Bloch 1941). Therefore, the meristoderm is highly active both anticlinally and periclinally in the TZ and the base of blade (Smith 1939). As a result, kelps display intercalary growth that is dependent on the high division activity of the meristoderm and on the growth of the tissues below it.

The meristoderm in Fucales is structurally and functionally similar to that of kelps (Fritsch 1945; Moss 1950, 1969, 1970; Clayton et al. 1985; Sokhi and Vijayaraghavan 1987; Linardić and Braybrook 2017). At the apical meristem, it surrounds the infrequently or frequently dividing apical cell(s) (Klemm and Hallam 1987; Linardić and Braybrook 2017) and it covers all the surface of the alga from apical meristem to base. It contributes to lateral and vertical growth with anticlinal and periclinal division resulting in cortical cells that differentiate into medulla. In *Ascophyllum*, two different pathways of branching exist. One way is dichotomous, from division of the apical meristem and the second is with lateral nodes which are essentially apical grooves produced by meristoderm (Moss 1970).

In *Dictyopteris* (Dictyotales), the growth of its branches depends on an apical meristem with four to eight central cells, that are named apical initials (Katsaros and Galatis 1988). The initial medio-lateral axis and the maintenance of the meristem depend on symmetric longitudinal anticlinal divisions of the apical initials. Asymmetric perpendicular anticlinal divisions contribute to the growth along the long axis of the branches. The first periclinal divisions of these derivatives are symmetric. However, the next periclinal divisions which take place at the center of the tissue of *Dictyopteris* are asymmetric and self-replacing, giving first medullary elements and then cortical cells (Katsaros and Galatis 1988). This is the opposite of *Saccharina*'s meristoderm which gives only cortical cells and these then differentiate to medulla (Smith

1939). The differentiation of the meristodermatic cells coincides with the formation of a midrib (Katsaros and Galatis 1988). The midrib is surrounded laterally by two bistromatic regions, defined as “wings”. The mature midrib has a photosynthetic epidermal tissue instead of a meristoderm but the base of *Dictyopteris* thallus has an active meristoderm dividing periclinally toproduce cortical cells.

Land plants leaf development begins in the apical meristem with three different layers in which the rate of cell division and cell expansion is increased (Steeves and Sussex 1989). In brown algae, aerial organs result from primarily increased meristematic activity of meristoderm. Its derivatives at the surface of the apical meristem differentiate and in a second step divide and grow (Moss 1967, 1970; Linardić and Braybrook 2017). This is a non-intuitive way for building aerial organs. Nevertheless, this is not so different from how a vascular cambium functions (Steeves and Sussex 1989; Crang et al. 2018), one layer tissue performing anticlinal and periclinal division on both sides. The meristoderm is similar only with one way divisions and in Laminariales, it can even have many layers (Smith 1939).

Parenchymatic brown algae have a variety of growth strategies. However, only Fucales were subject of a functional approach on the morphogenetic mechanisms taking place at the apical meristem. Linardić et al. (2017) found that the three faced apical cell of *Sargassum* (fig. 1 (d)) is actively dividing by following a golden angle spiral patterning similar to that of *Physcomitrium pattens* (Harrison et al. 2009). In *Physcomitrium*, the division pattern is projected on the phyllotaxis, in contrast with *Sargassum* where the pattern of buds developing into new organs seems to diverge from the division pattern of the apical cell. In addition, the emergence of new buds does not seem correlated with auxin and the alginates deposition patterns could not predict any cell wall loosening events (Linardić and Braybrook 2017). Nevertheless, the established growing buds seem to have softer CWs. Comparing with land plants apical meristems, there are possibly different mechanisms occurring during the organogenesis of *Sargassum.* That is characterised by the absence of three or more distinct layers (Steeves and Sussex 1989) and instead, the presence of a meristoderm and its periclinal derivatives that differentiate and then divide. This means that the different tissues are already set while the new organ is forming.

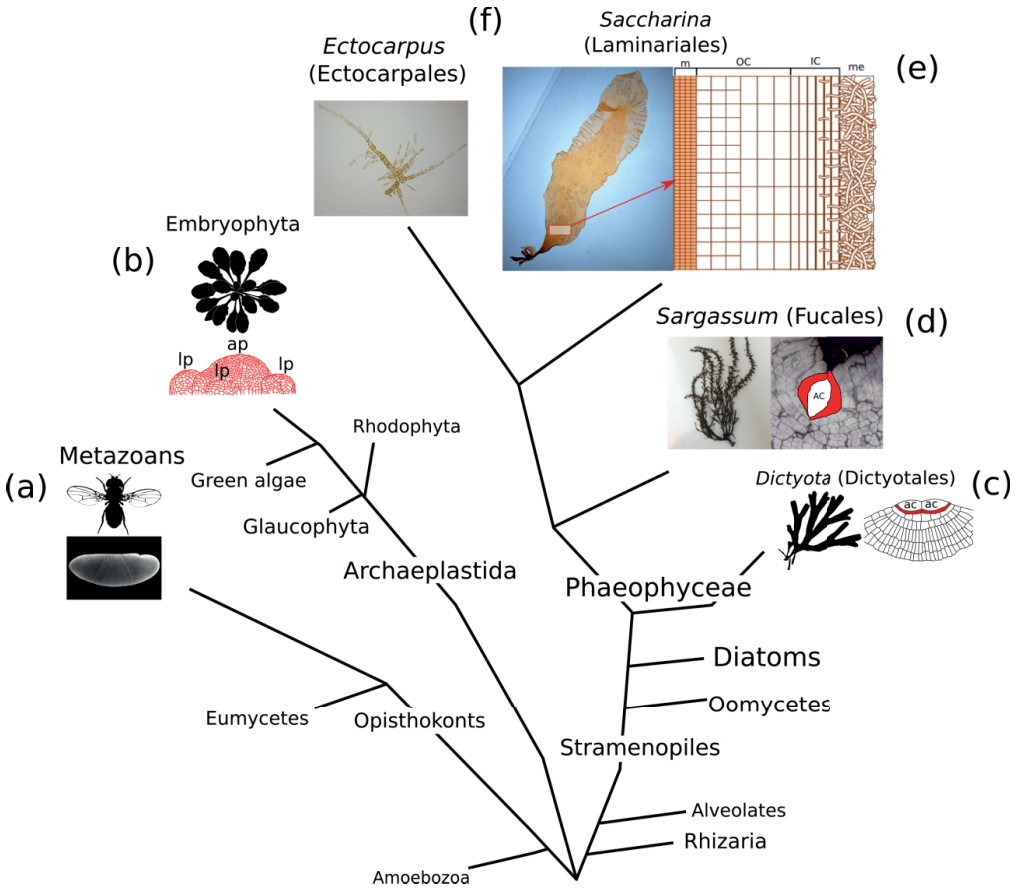

Figure 1: Meristems and body plans among different multicellular groups. (a) Metazoan development is based on free moving tissues (furrowing, folding etc) and finite embryonic cells activity. (b) Land plants (Embryophyta) are cell walled organisms with restricted tissue movement. Development of new organs and tissues is possible after embryogenesis and is based on meristematic areas like shoot apical meristems (Steeves and Sussex 1989). The apex of *Arabidopsis* (ap) includes the outer layers of tunica, dividing exclusively anticlinally, while the corpus includes tissues with more random division modes. Surrounding the main apex are the leaf primordia (lp), initiates of aerial organs. In Phaeophyceae there are few groups of the parenchymatic species well studied in anatomy and structure. Dictyotales (Katsaros and Galatis 1988; Bogaert et al. 2020) (c) are characterised by a main apical meristem with one or more apical cells (ac), some times in lenticular shape. Species like *Dictyopteris* base their in-width growth on meristoderm while it is absent in *Dictyota* (c). Fucales (d) like *Sargassum* have a main apical meristem consisted of a frequently (*Sargassum*, (Linardić and Braybrook 2017)) or infrequently (*Fucus*, (Moss 1967)) dividing anticlinally apical cell (ac) and the derived meristoderm (red color, pre-peristoderm). Meristoderm is also active at the shunks of the apical meristem, responsible for growth in length and width. Kelps (e) have no main meristems and the growth of their blades is dependent on the division activity of the meristoderm (m) and the growth of the cortex (outer cortex: OC, inner cortex: IC) and medulla (me) below it. *Ectocarpus* (f) and most uniseriate filamentous brown algae are tip growing. The phylogenetic tree is rootless and does not represent any actual evolutionary distances among the presented groups. The phylogenetic relationships between the groups of brown algae are presented in detail from Bringloe et al. (2020), here the placement of the different representative geni per order are based on their phylogenetic tree. Photographs of *Sargassum* come from the archive of Marina Linardić.

1.9. The brown alga Saccharina latissima

Saccharina latissima is a simple morphologically Laminariales species (Starko et al. 2019) consisted of a simple blade, a stipe and the holdfast (fig. 2). As already mentioned, the main growth region of *Saccharina*'s thallus is between the blade and the stipe (Sykes 1908; Smith 1939; Fritsch 1945; Parke 1948), called transition zone (TZ). Like all Laminariales, *Saccharina* has an heteromorphous haplodiplobiotic life cycle (Bartsch et al. 2008) (fig. 2). Meiospores are formed on the surface of the mature blade inside the sporangia, which, after release to the medium, sink and then germinate to either a male or female microscopic gametophyte. When the conditions are favorable, then the male gamete fertilises the female and the diploid generation begins.

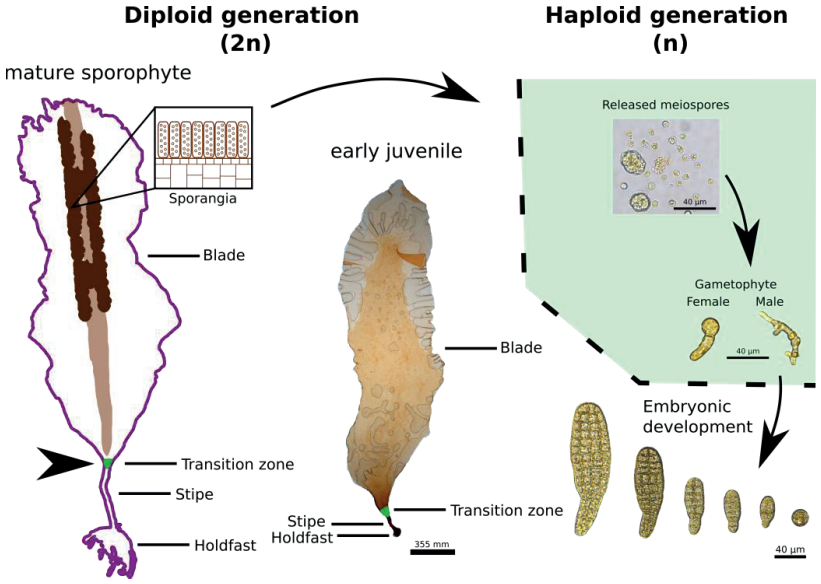

Figure 2: Life history and basic anatomy in *Saccharina latissima.* The thallus of the diploid sporophyte consists of a blade, a stipe and a holdfast. The transition zone (intercalary growth region) is located between the blade and the stipe (green area). The basic anatomy of juvenile and the mature sporophytes is the same. On mature sporophytes, a midrib is distinguished (light brown area) and sori (dark brown area). Sori are regions containing the sporangia, placed laterally and on the midrib. The haploid meiospores are released from the sporangia to the surrounding medium. Their germination gives a male or a female haploid gametophyte. Fertilisation of the female gamete begins the diploid generation and the embryonic development.

The mature sporophyte can be several meters long and has great ecological importance. Together with other kelp species they form the kelp forests (Starko et al. 2019) which are unique ecosystems in the cold-temperate coasts of the north Atlantic and north Pacific oceans. In Asia (Hwang et al. 2019) and most recently also in Europe (Forbord et al. 2012; Broch et al. 2019) Saccharina latissima is cultivated for uses in nutrition (FAO 2018; Barbier et al. 2019) and other applications like the reduction of the impact of fisheries (Fossberg et al. 2018) and the production of anti-inflammatory and anticoagulant pharmacological agents (Cumashi et al. 2007).

2. Aim of this study

The sporophyte of *Saccharina* is an interesting developmental model for three reasons. First, the embryogenesis takes place outside any maternal tissue making the growing tissue amenable to cytological manipulation and mechanically uncoupled to surrounding tissues (Fritsch 1945; Bogaert et al. 2013; Theodorou and Charrier 2021). Therefore, any microscopic and modelling approaches take place directly on the developing embryo. Second reason, the early embryo of *Saccharina* (and most kelps) is a growing undifferentiated tissue thick of one cell layer (monostromatic) (Drew 1910; Killian 1911; Yendo 1911; Fritsch 1945; Theodorou and Charrier 2021). The monostromatic growing tissue is consisted of simple cuboid cells, whose description in literature indicates frequent four cell wall junctions. This cell arrangement is uncommon and often avoided in developing tissues of land plants due to increased shearing stress (Sinnott and Bloch 1941; Lloyd 1991). When it occurs, it is related with the later opening of large intercellular spaces like during the development of spongy photosynthetic parenchyma in leaves (Zhang and Ambrose 2022). Thirdly, the early embryo of Saccharina is a poorly investigated system regarding developmental biology, with great comparative value due to the evolutionary position of brown algae, distant from both animals and plants (Theodorou and Charrier 2021).

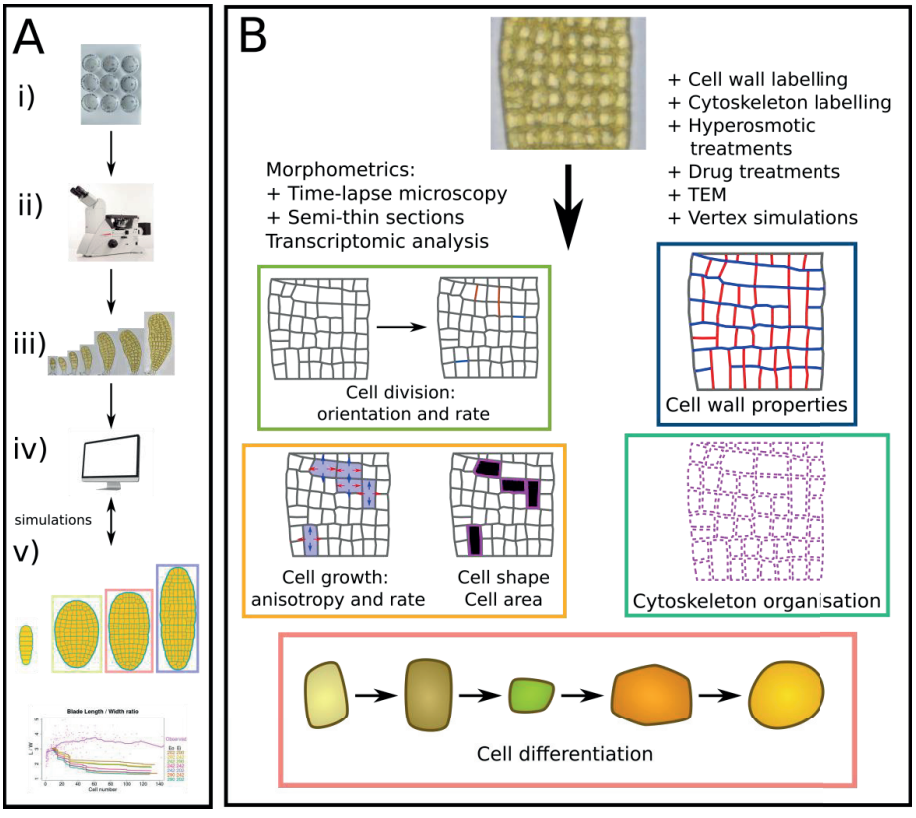

Figure 3. Thesis project summary. (A) The main experimental pipeline (i – iii) wet lab and rudimentary image analysis tasks. (iv – v) Simulations and in silico analysis were performed from the bionformatician Bernard Billoud based on the microscopy data. The project begins with optimizing a cultivation protocol (i) and have lab grown embryos for microscopical observations (ii) and image analysis (iii). Further image analysis (iv) is performed to formulate potential models and compare with vertex simulations (v). (B) The focus of the project. The morphogenesis of a tissue depends on cellular traits or mechanics. While cell division, growth and shape are dependent on CW properties and cytoskeleton organisation, the last two have their own additional additional effects on tissue morphogenesis and mechanics. (+) The techniques that were used to study the different cell mechanics.

The presented project (summarized at figure 3) is the first approach on the embryonic development of *Saccharina latissima* focusing on the morphogenetic mechanisms related to cell and tissue patterning. Through microscopical studies, morphometrical analysis, simulation and modelling, we aimed to shed light on the morphogenesis of *Saccharina*'s embryos. Therefore, the following presented investigation is multidisciplinary, and parts of the work are still in progress due to the intrinsic complexity that these developmental models possess. In the end, we establish the emergence of a new developmental model easily distinguished from other better studied organisms.

3. Materials and methods

3.1. Algal material

3.1.1. Stock cultures

Saccharina latissima sporophytes were collected from the Perharidy beach, close to Roscoff, France (48°43'33.5"N, 4°00'16.7"W). Beach stranded fertile individuals were transferred to the lab for further process. The detail manipulation of this foundation material is described in (Theodorou et al. 2021). In summary, there are dark areas on the blade of fertile *Saccharina* were the meiosporiangia reside (sori; singular: sorus). The sori are dissected from the rest of the blade and cleaned from epiphytes. Spore release was induced over-night in a humid chamber at 4 °C. The next day, the pieces of the sori were sinked in autoclaved and filtered at 0.2 µm seawater. With a counting chamber the released meiospores' density in the medium was monitored until it reaches 300,000-400,000 cells ml^{-1}. The rest of the work and material manipulation took place under a laminar hood. Small volumes of the medium (5-7 ml) were filtered with a strainer and diluted to optimal density (30-40 spores ml^{-1}) in half-strength Provasoli enriched seawater (half-PES) for the meiospores germination and gametophytic growth. These were the first stock cultures kept at red light conditions: 3 µmol photons m^{-2} s^{-1} light intensity and 14:10 light:dark photoperiod at 13 °C. The medium was replaced completely every month. Gametophytic density was monitored which is crucial for their vegetative growth (Yabu, 1965).

3.1.2. Gametogenesis induction for production of zygotes and embryos

The process of gametogenesis induction as well as the optimal conditions for normal embryonic development are described in (Theodorou et al. 2021). As a short mention, gametophytic stock material was fragmented and diluted in full strength PES medium (full-PES). The fragments are transferred in white low light conditions: 16 µmol photons m^{-2} s^{-1} light intensity and 14:10 light:dark photoperiod at 13 °C. After approximately 5 days, the first zygotes were present. The material is then transferred to normal light conditions: 50 µmol photons m^{-2} s^{-1}.

The developing embryos need enough space for their normal growth, therefore, their cultures are transferred in 2-L Nalgene bottles a month after gametogenesis induction. As the growth of the later embryos and juveniles progresses, the material should be transferred in larger containers and increasing light intensity, better detailed and presented in (Forbord et al. 2018). It is noted that gametophytic density is crucial for successful gametogenesis and proper embryonic development ((Zhang et al. 2008; Ebbing et al. 2020). The stock cultures are kept in half-PES because increased concentrations of chelated iron like in full-PES, (present in PES as Fe-EDTA), can induce unplanned gametogenesis (Motomura and Sakai 1984; Lewis et al. 2013). The used recipe for the provasoli medium is described in Theodorou et al. 2021. The stock solutions except the vitamin mix, were autoclaved before storing at 4 ^{o}C.

3.1.3. Establishing monogenic cultures

The establishment of one genotype gametophytic cultures was shout out for crosses and controlling the genotype of the produced embryos. Using sterile home-made glass tools, small individual females and males were isolated into separate petri dishes and left to grow for about a year (Theodorou et al. 2021). Before the production of one genotype embryos, their parents were crossed and left to vegetatively grow together for three months at red light conditions, after fragmentation and dilution to optimal gametophytic density (Ebbing et al. 2020).

3.1.4. Drug treatments

Cultures of Phase 2 emryos were treated with either latrunculin B (LatB; Sigma-Aldrich) at 100 nM or nocodazole (Sigma-Aldrich) at 13 μM. Both drugs were stored in dimethyl sulfoxide (DMSO) at 1mM and -20 oC, before their dilution in PES medium The medium with either of the two drugs was changed every 3 days. Cultures treated with DMSO ran together with the drug treatments to verify no side effects from the compound in the amount added in the drug treatments which is 0,04%. As additional control, normal full PES cultures were run in parallel. A picture of the state of selected specimen was taken every 24 h for 7 d. The specimens were selected if possible, according to their position and an as clear as possible bright field acquisition.

3.2. Microscopical methods

3.2.1. Timelapse set up

Embryos were followed under a bright field inverted microscope from the zygote stage and up to 10 days of development. The clearer and most detailed image data were used for further image analysis on the cell morphometrics, division and growth patterns. The acquisitions were done all manually, each culture containing the followed specimen was placed and observed under the Bright field, every 8, 12 and 24 hours. Three time-lapse experiments followed mixed genotype cultures and two took place on one-genotype cultures. The mixed genotype experiments resulted in 14 specimens with extractable data, and the one genotype timelapse produced extractable data from four specimen.

3.2.2. Hyperosmotic treatment: preparation and observation

Phase II embryos were brought under the confocal microscope, a z-stack was acquired for each specimen before the treatment. For the treatment, the PES medium was replaced with sucrose in sterile seawater solution of 2660 mOsm like in *Ectocarpus* and pollen tube experiments (Zonia et al. 2006; Zonia and Munnik 2007; Rabillé 2018; Rabillé et al. 2019a). One minute after the replace of the medium, a new acquisition is taken with the effect of the hyperosmotic treatment. The specimen were stained with Fluorescent Brightener 28 (Calcofluor white: Sigma-Aldrich®) (final concentration 20 µM in filtered and autoclaved seawater, one hour incubation at 14 °C and three washes, five minutes each). The stain was excited during the acquisitions with the 405 nm laserline and a photomultiplier tube (PMT) as detector at 440 nm – 480 nm wavelength, it is combined with a PMT transmission channel for the verification of plasmolysis during the treatment. 13 specimen had extractable data, their image analysis is described later.

3.2.3. Preparation of samples for transmission electron microscopy and semi-thin sections

The following protocol is based on (Raimundo et al. 2018). Phase 3 embryos were fixed in 1% glutaraldehyde (GTA) and 1% PFA in filtered and autoclaved seawater, incubated for two hours at 14 oC. The medium of the fixed tissue was gradually changed from seawater to 0.1 M cacodylate -Na. A post fixation step took place with 1% OsO4 at 4 oC, overnight. After washes with cacodylate-Na, the material was gradually dehydrated with an increasing ratio of ethanol/cacodylate-Na up to 100% ethanol. Spurr resin (Spurr 1969) was used for the infiltration step, gradually replacing ethanol with the resin with incubations on a rocking table and changing the 100% solution four times. Before polymerization and embedding of the material, fresh Spurr resin was prepared and used for the embedding. Spurr polymerises at 60 °C. For the handling and preparation of the resin, the manual from Electron Microscopy Sciences© was followed. Ultra-thin Sections of 50-70 nm thickness, mounted on copper grids (Formvar 400 mesh; Electron Microscopy Science©) were stained with 2% uranyl acetate for 10 min and 2% lead citrate for 3 min, and observed with the transmission electron microscope. Semi-thin sections of 500 - 750 nm stained with 1 % w/v toluidine blue in 1% w/v borax (sodium tetraborate) water solution or Stevenel's Blue (del Cerro et al. 1980) were observed under a bright field microscope.

3.2.4. Microtubule immunolocalisation and actin labeling

For the **microtubule immunolocalisation** the protocols from Tsirigoti et al. (2014) and Rabillé (2018) were combined, Phase II embryos were fixed in 2% paraformaldehyde (PFA) in microtubule stabilising buffer (50 mM PIPES, 5 mM ethyleneglycolbis(aminoethyl ether)-tetraacetic acid (EGTA), 5 mM $MgSO_4.7H_2O$, 25 mM KCl, 4% NaCl, 2.5% polyvinylpyrrolidone 25 (PVP), 1 mM DL-dithiothreitol (DTT),pH7.4) at 4 oC. The material was then washed and gradually changed from MTB to phosphate buffered saline (PBS; 137 mM NaCl, 0.7 mM KCl, 5.1 mM Na_2HPO_4, 1.7mM KH_2PO_4, 0.01% NaN_3, pH 7.4). The cell wall of the fixed material was digested with cell wall lysis buffer (Enzymes composition in PBS: 2% w/v Cellulase Onozuka R-10 (Yakult Pharmaceutical industry Co., Ltd.), 2% w/v Hemi-Cellulase (Sigma-Aldrich®), 1% driselase (Sigma-Aldrich®), 1.5% Macerozyme R-10 (Yakult Pharmaceutical industry Co., Ltd.) and 50 $U.ml^{-1}$ Alginate lyases-G (Station Biologique de Roscoff)). The lyophilized extracts of the

enzymes were dissolved in PBS and then centrifuged for 10 mins at 5000 rpm. The supernatant was kept and mixed with the alginate lyases G extract which were stored in their own buffer at -20 oC. Incubation too place in room temperature (RT) for 10 mins. After washes with PBS, pigments are removed and the cell membrane becomes permeable to antibodies with incubation at 4% Triton X-100 (Sigma-Aldrich®) in PBS for 15 min at RT. A blocking step follows with 1% Bovine Serum Albumine (BSA; Sigma-Aldrich®) for 10 min, RT. The primary antibody, Rat Anti tubulin-α IgG clone: YL 1/2 (mca77g, BioRad) was diluted in 1% BSA in PBS, 1/80 dilution factor. Incubation took place overnight, RT. The secondary antibody, fluorescein isothiocyanate (FITC)-conjugated IgG (polyclonal, Sigma-Aldrich®), was diluted 1/40 in 1% BSA in PBS and incubated for 2 h in the dark at 37 oC. The nucleus was stained with DAPI at 15 $\mu g.ml^{-1}$ but for this series of experiments, it didn't give any proper signal. The samples were mounted on Vectashield H-1000-10 (Vector®) before observation. At the confocal microscope, a 488 nm laserline was used in combination with a 515-535 nm PMT detector and the 100x lense.

The **actin labelling protocol** followed modified version of Rabillé (2018). The material was prefixed at 300 µM m-maleimido benzoic acid N-hydroxy succinimide ester (MBS; Sigma-Aldrich®), 0.2 % Triton X-100 and 2 % DMSO in MTB for 30 min in the dark and RT. Fixation took place without washes for 1:30 hr in the dark and RT (Fixation solution: 2% PFA, 0.2% GTA and 2 U of Rhodamine conjugated phalloidine (Ph-Rh; R415, Invitrogen™) or Alexa-fluor™ 488 conjugated phalloidine (Ph-Alexa488; A12379, Invitrogen™). After washes with MTB:PBS 1:1. the cell wall was digested with cell wall lysis buffer in MTB:PBS 1:1, its composition is described above but it included additionally 5 U Ph-Rh/ Ph-Alexa488 and 0.15 % Triton X-100. The phalloidine conjugates were dissolved in methanol, which is an inhibitor for cell wall enzymes. To avoid any disturbance, a solution was made with the phalloidine conjugates and the Triton X-100 dissolved in 1:1 MTB:PBS and left at RT for 45 min before dissolving the enzymes as described before. The incubation in the modified cell wall lysis buffer takes place for 10 min in the dark at RT. For permeabilisation and pigments removal, the material is incubated in extraction solution (5% DMSO, 3% Triton X-100 and one of the Phalloidin conjugates (2U) in PBS) for 10 min in dark and RT. The actin finally was stained with 15 U of the chosen phalloidin conjugate in MTB:PBS 1:1, overnight at 4 oC in the dark. The nucleus was stained with DAPI as previously described, this time with decent results. Finally, the material was mounted in Vectashield H-1000-10 (Vector®) before observation. Note that when a phalloidin conjugate is chosen, the same conjugate is used for the rest of the protocol, no combination of conjugates is implied. For the acquisition, the laserlines 561 nm (for Ph-RH; PMT: 566 nm – 637 nm) or 488 nm (for Ph-Alexa488; PMT: 501 nm – 557 nm) was used depending the conjugate. For the DAPI, the 405 nm laser line was chosen and a PMT of 436 nm – 482 nm.

3.2.5. Microscope equipment

For bright field and epifluorescence microscopy the inverted microscopes used were: 1) the DMI8 (Leica Microsystems ©) equipped with the color camera DMC4500 (Leica Microsystems ©) and controlled with LAS X v3.0 (Leica Microsystems ©). 2) the DMI6000B inverted optical microscope (Leica Microsystems ©) equipped with a motorized stage and the color camera

DFC450C, controlled by the LASX version 3.0 software. Both microscopes were equipped with the Leica CTR electronics box and the the Leica EL6000 compact light source.

The confocal microscope was the TCS SP5 AOBS inverted confocal microscope (Leica Microsystems ©) controlled by the LASAF v2.2.1 software (Leica Microsystems ©).

The transmission electron microscope was a JEM-1400Flash (JEOL Ltd.)

3.3. Image analysis

The acquired image data from the timelapse and hyperosmotic treatment were processed for manual segmentation via using Inkscape 1.2 (Inkscape 2022) and FIJI (Schindelin et al. 2012), the process is similar with Vőfély et al. (2019). First, the acquired Z-stacks were projected in different types of Z-projections for example average, standard deviation and sum slices. The plugin stack-focuser was also used. These projections assisted the manual segmentation process. Programs designed and run by Bernard Billoud (MMA group), were used for the extraction of detailed morphometric data like area, length and width, division plane, cell lineage from the drawn skeletons of the embryos and their cells. The various measurements on images were done via FIJI and processed with R or Excel (Microsoft Office 365 ©), more details are given to each article. The simulations also were run from Bernard Billoud and Cristophe Godin (more details at Paper I).

3.4. RNA sampling and preparation

Embryos from different timepoints of Phase II were fixed in RNAlater™(AM7021, Invitrogen™) for 24 hours and then microdissected using homemade glass tools and an inverted bright field microscope, like for the gametophyte isolation above, to remove any gametophytic material. The isolated tissue was stored in fresh RNAlater before further processing. The RNA was extracted from this tissue samples using the RNAqueous™ Micro total RNA isolation kit (AM1931, Invitrogen™) The quality of the RNA was measured with the Agilent 2100 Bioanalyzer (Agilent Technologies. Inc.) and the Agilent RNA 6000 Pico assay (Agilent Technologies. Inc.). Samples with RNA integrity index (RIN) ≥7 were processed further. The extracted RNA was sent to Novogene Co. Ltd. for further processing before sequencing. The cDNA from polyA tail containing RNA was synthesized using the SMART-Seq® v4 Ultra® Low Input RNA Kit for Sequencing (Takara Bio USA, Inc). The resulting cDNA was processed further for generating libraries for illumina high throughput next generation sequencing with 150 bp pair-end reads, specifically utilizing the NovaSeq 6000 system. The depth of sequencing (or read depth) was 22.1 - 32.6 million reads per sample, resulting to approximately 60 Gb of gzip compressed data.

3.5. De novo transcriptomics

The quality control of the raw reads, was calculated with FastQC v. 0.11.9 from Babraham Bioinformatics and MultiQC v. 1.9 (Ewels et al. 2016) for grouped comparisons. With Trimommatic v. 0.39 (Bolger et al. 2014) on paired-end mode, and options: a) remove the adapters, seed mismatches = 2, palindrome clip threshold= 30, simple clip threshold = 10, b) sliding

window 4 nt size, required quality 28 and c) with minimum length at 50 nt. Trinity v. 2.13 (Grabherr et al. 2011) was used for the assembly of the reads to transcripts. Classification of the trimmed reads for removing any human, fungi and prokaryote contamination was performed with Kraken2 (Wood et al., 2019) to paired-end and confidence 0.05 settings prior the assembly with Trinity v2.13 (Haas et al. 2013). The trimmed reads were mapped on the denovo transcriptome with Bowtie2 v.2.4.5, (Langmead and Salzberg 2012) while RSEM (Li and Dewey 2011) was used for estimating transcript abundance. Corset v. 1.09, (Davidson and Oshlack 2014) was used to cluster the denovo transcripts (default parameters) and generate counts per cluster

3.6. Gene expression analysis

The package edgeR v. 3.38.1 (Robinson et al. 2010; McCarthy et al. 2012) from Bioconductor together with various statistical and table sorting packages from R were used for the differential gene expression analysis. The clusters were filtered with minimum 12 counts and then normalized with a trimmed mean of M values for every group of samples. The correlation between the samples was calculated and their biological co-efficient of variance. The general lineal mode based tagwise, common and trended dispersions were calculated. These then were used for testing for differential expression above a fold-change threshold ($log_2FC > log_21.2$)based on TREAT method(McCarthy and Smyth 2009; McCarthy et al. 2012). For the differentially expressed genes (DEGs). Significant DEGs were those that had a p-value adjusted with FDR method below 0.05 (p.adj.<0.05).

3.7. Image analysis

The acquired image data from the timelapse and hyperosmotic treatment were processed for manual segmentation via using Inkscape 1.2 (Inkscape 2022) and FIJI (Schindelin et al. 2012), the process is similar with Vőfély et al. (2019). First, the acquired Z-stacks were projected in different types of Z-projections, for example average, standard deviation and sum slices. The plugin stack-focuser was also used. These projections assisted the manual segmentation process. Programs, designed and run by Bernard Billoud (MMA group), were used for the extraction of detailed morphometric data like area, length and width, division plane, cell lineage from the drawn skeletons of the embryos and their cells. The various measurements on images were done via FIJI and processed with R or Excel (Microsoft Office 365 ©), more details are given in each article. The simulations were run by Bernard Billoud and Christophe Godin (more details at **Paper I**)

3.8. RNA sampling and preparation

Embryos from different time points of Phase II were fixed in RNAlater™ (AM7021, Invitrogen™) for 24 hours and then microdissected using homemade glass tools and an inverted bright field microscope, like for the gametophyte isolation above, to remove any gametophytic material. The isolated tissue was stored in fresh RNAlater before further processing. The RNA was extracted from this tissue samples using the RNAqueous™ Micro total RNA isolation kit (AM1931, Invitrogen™) The quality of the RNA was measured with the Agilent 2100 Bioanalyzer (Agilent Technologies. Inc.) and the Agilent RNA 6000 Pico assay (Agilent Technologies. Inc.). Samples with RNA integrity index (RIN) ≥7 were processed further. The

extracted RNA was sent to Novogene Co. Ltd. for further processing before sequencing. The cDNA from polyA tail containing RNA was synthesized using the SMART-Seq® v4 Ultra® Low Input RNA Kit for Sequencing (Takara Bio USA, Inc). The resulting cDNA was processed further for generating libraries for Illumina high throughput next generation sequencing with 150 bp pair-end reads, specifically utilizing the NovaSeq 6000 system. The depth of sequencing (or read depth) was 22.1 - 32.6 million reads per sample, resulting to approximately 60 Gb of gzip compressed data.

3.9. De novo transcriptomics

The quality control of the raw reads, was calculated with FastQC v. 0.11.9 from Babraham Bioinformatics and MultiQC v. 1.9 (Ewels et al. 2016) for grouped comparisons. With Trimommatic v. 0.39 (Bolger et al. 2014) on paired-end mode, and options: a) remove the adapters, seed mismatches = 2, palindrome clip threshold= 30, simple clip threshold = 10, b) sliding window 4 nt size, required quality 28 and c) with minimum length at 50 nt. Trinity v. 2.13 (Grabherr et al. 2011) was used for the assembly of the reads to transcripts. Classification of the trimmed reads for removing any human, fungi and prokaryote contamination was performed with Kraken2 (Wood et al., 2019) to paired-end and confidence 0.05 settings prior the assembly with Trinity v2.13 (Haas et al. 2013). The trimmed reads were mapped on the denovo transcriptome with Bowtie2 v.2.4.5, (Langmead and Salzberg 2012) while RSEM (Li and Dewey 2011) was used for estimating transcript abundance. Corset v. 1.09, (Davidson and Oshlack 2014) was used to cluster the denovo transcripts (default parameters) and generate counts per cluster

3.10. Gene expression analysis

The package edgeR v. 3.38.1 (Robinson et al. 2010; McCarthy et al. 2012) from Bioconductor together with various statistictical and table sorting packages from R were used for the differential gene expression analysis. The clusters were filtered with minimum 12 counts and then normalized with a trimmed mean of M values for every group of samples. The correlation between the samples was calculated and their biological co-efficient of variance. The general lineal mode based tagwise, common and trended dispersions were calculated. These then were used for testing for differential expression above a fold-change threshold ($log_2FC > log_21.2$)based on TREAT method(McCarthy and Smyth 2009; McCarthy et al. 2012). For the differentially expressed genes (DEGs). Significant DEGs were those that had a p-value adjusted with FDR method below 0.05 (p.adj.<0.05).

3.11. Annotation, Gene ontology and KEGG

To annotate the DEGs, we used DIAMOND v. 2.0.15 (Buchfink et al. 2021) against a database of proteins coming from three good annotated genomes: *Ectocarpus siliculosus* v2 (https://bioinformatics.psb.ugent.be/orcae/, (Cormier et al. 2016)), *Saccharina japonica* (https://bioinformatics.psb.ugent.be/orcae/, (Liu et al. 2019)) and *Undaria pinnatifida* (http://www.magic.re.kr/portal/main, (Graf et al. 2021)). The ones without a hit on the custom database, were reblasted with DIAMOND against a database of Phaeophyceae proteins generated from UniProt (release 2022_03). The totally matchless sequences were blasted on tremble, Swiss prot and NCBI databases. The best hits (lowest e-value) were the

representatives of their clusters. Interproscan v. 5.57-90.0 ((Jones et al. 2014; Blum et al. 2021)) was used to functionally characterize the DEGs (gene ontology or GO ID) and Kofam-KOALA v. 2022-09-01 for KEGG IDs (Aramaki et al. 2020), both on the protein sequence of the best blast hit for each cluster. In the end, 152 out of 644 annotated DEGs have no GO id and 362 have no KEGG id. Further decontamination took place for high percentage and low evalue sequences aligned with human or other mammalian proteins that do not have biological meaning to be part of a brown algal transcriptome (e.g albumin serum). Sequences aligned with uncharacterised proteins with no GO id and different taxonomy from brown algae were removed too. In the end, 623 DEGs were used for our analysis. This difficulty on functional annotation is not a big surprise since the development of brown algae is not well studied on molecular level, there are few annotated genomes and in general stramenopiles are mostly studied for their metabolism so there is a gap of knowledge. In addition, our study is on an organismic level never mentioned or approached and our dependency for annotation is on adult plants or juveniles that rarely express these proteins or at a differential level. The R packages topGO v. 2.48.0 (Adrian Alexa and Jörg Rahnenführer 2022) and clusterProfiler v 4.4.4 (Wu et al. 2021) were used for the GO and KEGG analysis, without a chosen p-adjust method.

4. Results & Discussion

4.1. Cultivation of kelp embryos

The first step to study the morphogenesis of *Saccharina*'s embryos is to observe and follow the different stages that its embryogenesis goes through. Therefore, the most basic step is to establish a cultivation protocol that can keep standard conditions for an optimal development. Ebbing et al. (2020) had a recent approach on establishing the parameters necessary for an efficient reproduction out of culture stock of gametophytes. Key parameter and one often omitted is the density of the material in the medium and based on their observations and our experience with stock cultures a protocol on cultivating embryos was set (Theodorou et al. 2021), **Paper V**). We defined two necessary precautions for an efficient production of zygotes and embryos from a stock culture: i) the use of full-provasoli medium (Provasoli and Carlucci 1974; Le Bail and Charrier 2013; Theodorou et al. 2021) for gametogenesis induction ii) the maintenance of a distance of about 300 µm between gametophytes in contact with the substrate of the petri dish . Regularly, most of the gametophytes will form gametes. However, often an increased light intensity (>5 µmol photons m^{-2} s^{-1}) even of the red inhibiting spectrum (Lüning and Dring 1972; Ebbing et al. 2020) or an increased amount of chelated iron (Lewis et al. 2013) to the filtered seawater can trigger gametogenesis. For reducing spontaneous gametogenesis, we propose a change of half strength medium every month at the stock (table 1). In addition, we prefer inducing gametogenesis at low white light intensity simply for convenience. An overview of the medium and culture conditions necessary for each stage of small-scale lab cultures is given in table 1 as established for microscopical studies (Theodorou et al. 2021), **Paper V**) and followed during our following investigations.

Table 1. Overview of different culture conditions. Each ontogenic stage need different culture conditions for optimal development. Temperature is the same for all, at 13°C, while the photoperiod is 14:10 (light:dark). (Paper V)

Ontogenic stage	Light quality and intensity	Medium composition	Medium changes
Vegetative gametophytic growth	Red, 3 µmol photons m^{-2} s^{-1}	Half-Provasoli enriched medium	Once every month
Gametogenesis	White, 16 µmol photons m^{-2} s^{-1}	Full-Provasoli enriched medium	
Embryogenesis	White, 50 µmol photons m^{-2} s^{-1}	Full-Provasoli enriched medium	After 20-30 days together with glassware and plasticware
Juveniles and young sporophytes	White, 50 µmol photons m^{-2} s^{-1}	Full-Provasoli enriched medium	Once every four to seven days

4.2. Growth axis and division plane changes during the different Phases of embryogenesis

With timelapse microscopy, we observed three distinct Phases of embryogenesis (**Paper I, Paper III**) which are summed up on figure 4 and table 2. Each Phase has distinct traits regarding cell division plane and growth axes. The first step of Phase I is taking place with the polarisation of the zygote and the subsequent cell divisions, still attached to the maternal gametangium. These divisions are perpendicular to the longitudinal growth axis (X-axis); therefore they are defined as transversal anticlinal divisions (fig. 4A-C). This sequence of cell divisions makes a short uniseriate filament of cells usually up to 8 cells. A 90° shift to the cell division plane leads to Phase II and the establishment of a second medio-lateral growth axis (Y-axis) (fig. 4D-G). These new cell divisions are parallel to the longitudinal axis (X-axis), thus the name longitudinal anticlinal divisions.

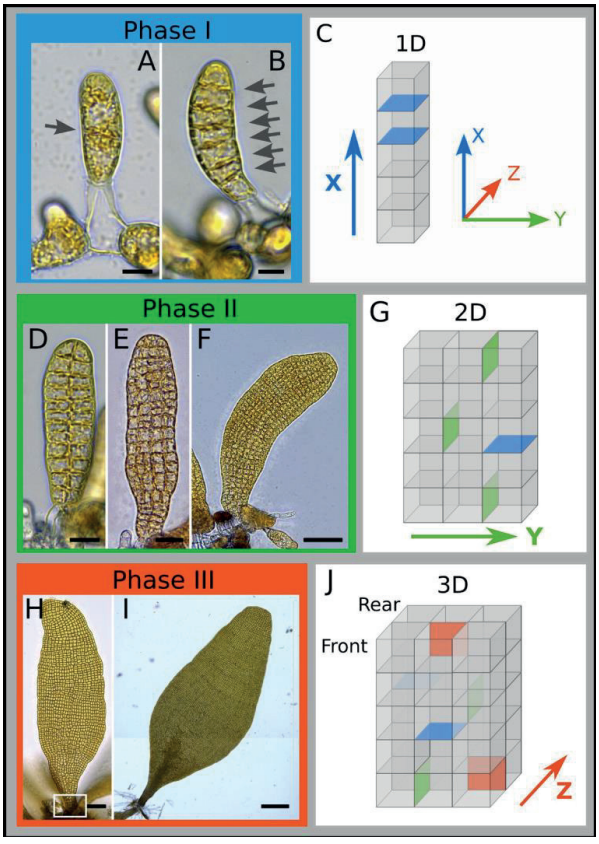

Figure 4. Phases of *Saccharina*'s embryogenesis. (A-C) Phase I is characterised from perpendicular division to the X-axis (longitudinal axis) forming one-dimensional filament like thallus, (grey arrows): transversal to the X axis anticlinal (perpendicular to surface) cell divisions. (D-G) Phase II is characterised from an alternation of division plane between transversal (blue) and longitudinal (green) cell divisions resulting to a growing monostroma (one cell layer tissue). The longitudinal anticlinal divisions are perpendicular to the Y-axis and the surface of the tissue. (H-J) The first periclinal cell divisions of phase III take place at the base of the embryo (white box). The addition of cell layers (polystromatisation) is observed as darkened areas in I. As periclinal divisions are defined the parallel to the surface divisions (red color), perpendicular to the Z-axis. Bars: A,B: 10 µm; D,E, F: 15 µm, 25 µm, 70 µm; H, I: 90 µm, 300 µm (**Paper III**)

There is a series of alternation between transverse and longitudinal anticlinal cell divisions which leads to the formation of a monostromatic lamina. Almost each new cell division plane is perpendicular to the previous one (**Paper I**). Therefore, an anisotropy is observed along the Z-axis where cell growth is absent. The first periclinal division and sign of growth along Z-axis occurs at approximately 14 days old embryos (fig. 4H). An increase to cell layers

(polystromatisation) is therefore observed starting from the base of the embryos next to the rhizoids (fig. 4H, white box), this is the beginning of Phase III. Our current theory regarding the initiation of polystromatisation is based on what has been observed in *Saccorhiza bulbosa* (currently *S. polyschides*) (Fritsch 1945) and *Chorda filum* (Kogame and Kawai 1996). Specifically, at the base of the embryo a few cells divide periclinally, establishing a polystromatic region with diffused growth along X-axis both acropetally and basipetally while polystromatisation proceeds. This region will be the future transition zone (TZ) situated between the blade and the future stipe. During the establishment of TZ, the rest of the tissue is polystromatised. After approximately 20 days (fig. 4 I, **Paper III**), polystromatisation is visible as the embryo starts thickening and the polystroma appears darker than the monostroma or bistroma. On table 2 the different Phases of *Saccharina*'s embryogenesis are summarised with their traits regarding axes of growth and cell division mode.

Table. 2 Phases of embryogenesis in *Saccharina latissima* and their characteristics regarding axes of growth, cell division mode and age. (Paper III)

Phases of embryogenesis	Axes of growth	Cell division mode		End (days after zygote polarisation)
		Initiated by	Maintained by	
Phase I	X-axis: 1D growth, apico-basal	Anticlinal transversal		3
Phase II	X- and Y-axes: 2D growth, medio-lateral (monostromatic tissue)	Anticlinal longitudinal	Anticlinal (transversal and longitudinal)	15
Phase III	X-, Y- and Z-axes: 3D growth, in thickness (polystromatisation)	Periclinal	Anticlinal (transversal and longitudinal) and periclinal	50

Regarding the overall embryogenesis of *Saccharina*, it is a unique process where two (apico-basal, medio-lateral or X and Y respectively) of the three growth axes (X, Y, Z) are first established. In brown algae, most zygotes of parenchymatic species (and filamentous, like *Ectocarpus*) (Bogaert et al. 2022) demonstrate an initial polarisation and an asymmetric division. Asymmetric division(s) can occur at later stage without any polarisation, like in *Himanthalia elongata* (Ramon 1973) or some *Cystoseira* species (Guern 1962; Lardi et al. 2022). In *Saccharina* we observed and verified that an apico-basal polarity is established, and an asymmetric division takes place. Big differences with the *Fucus* and *Dictyota* paradigms, are 1) the presence of flagella at the egg of *Saccharina*, that remains during zygote stage 2) the attachement to the empty oogonium 3) and also the maternally set apico-basal axis (Klochkova et al. 2019; Bogaert et al. 2022). That means that the polarisation axis and apico-basal cell fates are already set from the maternal empty oogonium, expressed during zygote stage. In *Fucus* the polarity axis is set together with the apico-basal differentiation from envinronmental cues

(Kropf et al. 2001; Bogaert et al. 2015) while in *Dictyota* there are two poles like in *Saccharina*, and the general axis is maternally set but the apico-basal differentiation is decoupled (Bogaert et al. 2017).

The maternally set apico-basal axis is enhanced with a series of anticlinal transverse divisions, then the second growth axis, horizontal (medio-lateral), is set with the first anticlinal longitudinal divisions parallel to the main growth axis. Like in Fucales (Moss and Lacey 1963; Moss 1970; Clayton et al. 1985; Klemm and Hallam 1987; Lardi et al. 2022) or Dictyotales (Fritsch 1945) or land plant embryos (Steeves and Sussex 1989), we would then except a periclinal division parallel to the surface of the established two growth axis systems (X-,Y- axes). This occurs when the basic thallus of the embryo is developed, at around 800 cells, and specifically at the base next to the rhizoids (our observations, (Yendo 1911; Fritsch 1945). This is a unique developmental plan.

In land plants, comparable structures with the embryo of *Saccharina* are the leaves of mosses like *Physcomitrium patens*. Its leaves are monostromatic but demonstrate heteroblasty, the upper leaves have midrib and different overall morphology from the basal leaves which are simpler (Barker and Ashton 2013). The formation of a leaf initial in *Physcomitrium* begins with an outgrowth from the shoot apical cell followed by an asymmetric division resulting in the leaf apical cell (Harrison et al. 2009; Lin et al. 2021). Like the shoot apical cell, the leaf apical cell (ex-leaf initial) divides asymmetrically and retains its meristematic activity until its activity stops and it becomes the tip of the leaf. Then, diffused cell divisions and growth broaden the developing leaf. This is a developmental plan different from a monostromatic structure; however, diffused cell divisions seem to be a common tactic between *Physcomitrium* and *Saccharina* for broadening the developing tissue. Another common trait with *Saccharina* is how the leaf of *Physcomitrium* remains monostromatic, this is realised with division planes restricted to one plane (X-,Y-axes) which are forming approximately 90° with each other (Harrison et al. 2009) (check also **Paper I** and next section).

4.3. Morphogenesis during Phase II

4.3.1. CW elastic modulus anisotropy and stochasticity and during phase II

Analysing the timelapse of 14 developing embryos several interesting patterns appear (**Paper I**). First, the alignment of the cells is a grid of four CW junctions (4WJ) shown by mean number of neighbouring cells per cell (fig. 5A) while the area of sister cells is approximately equal after a division (fig. 5B). Together these results and an alternation of division plane of 90 ° point towards a geometrical rule of cell division, specifically an application of Errera's rule, through the centroid and shortest possible distance (Besson and Dumais 2011; Minc and Piel 2012). In addition, the distribution of the small range of cell shape and size as well as division activity indicates a diffused growth and is expected from the microscopical observations (Paper I). Furthermore, blade morphometrics indicate isotropic growth maintaining the initial anisotropic shape of phase I, while cells have an anisotropic shape. The above parameters together with the calculation of ratio perimeter/area (exchange ratio) for each dividing cell are used in 2D vertex models.

The advantage that this approach offers, is that we can explore mechanical parameters that are necessary for building an *in silico* developing tissue with the traits of *Saccharina*'s Phase II. Furthermore, we can add modifications on an established model to investigate further its potential morphogenetic mechanisms. The first step included finding the necessary elastic modulus (E) that would allow the simulated tissue to grow with the same rate with the *in vivo* material. E=2905 MPa gave the best result based on a turgor pressure of 0.5 MPa as calculated in *Ectocarpus* (Rabillé et al. 2019a). The simulations started from a stereotypical embryo of 8 cells. The previous exercise of the first vertex model resulted in an oval shaped embryo far from the real specimens (fig. 5C ii) but presenting 4WJs. However, this model, did not take into account any anisotropies on the physical properties of cells or tissue. Hyperosmotic treatment experiments indicated higher retraction of the blade and the cells (regardless of the long cell axis orientation) along the X-axis (longest blade axis) of the blade. Further exploration with the vertex models on E anisotropic patterns indicates that the outer CW even though thicker than the inner CW, needs to have a lower E than the inner CW to approach the shape of developing phase II embryos. In addition, the longitudinal (parallel to X-axis) inner CWs have to be softer (lower E) than the transverse CWs (parallel to Y-axis). Specifically, the angular anisotropy between longitudinal and transverse inner CWs has to be in the range of 2.25 (**Paper I**) and the ratio of outer to inner CWs elastic modulus (E_o/E_i) equal to 0.45.

So on figure 5 C (iii), the optimal 2D vertex model is presented which is then tested for its robustness under different levels of stochasticity on key parameters: (a) turgor pressure, (b) exchange-ratio threshold, (c) division plane position, (d) division plane orientation (**Paper I**). Tests with different level of randomness, which means the values of the developing embryos could increase or drop within a set range, were run to examine the changes on the model. Regarding the turgor pressure and the exchange ratio, stochasticity on both cell features did not affect the shape of the blade but only the grid pattern and that partially as the number of neighbouring cells remains within range. However, higher randomness at the exchange ratio leads to a considerate increase in the number of neighbouring cells, and hence, in the disruption of the grid. Disruption of the grid was also observed when the division plane was positioned randomly away from the centroid, allowing increased inequality to cell divisions. Similar effect has Stochasticity of the division plane orientation had similar results. When separated, these stochastic parametershave a small effect on the *in silico* development of Phase II, mostly focused on disrupting the grid. When combined, the shape of the blade was unchanged but the grid was severely disturbed with high number of neighbouring cells already from low levels of stochasticity (Paper I). Notable is the small

Regarding the observations on cell growth and division as well as exchange ratio thershold, these cellular traits show little heterogeneity along the developing phase II embryo (**Paper I**). Therefore, it raises questions as to how the the grid is affected with combined stochastic parameters, and not the blade but this is actually in agreement with works in land plants. In sepals (Hong et al. 2016) and leaves (Le Gloanec et al. 2022), cell growth variabilities are buffered by averaging or local variability in cell growth resulting in robust shaped organs. The small fluctuations in low stochasticity seem to even allow maintenance of the grid, however, increased stochasticity has a profound negative effect on 4WJs. The most obvious effect comes from modifying the canonical cell division mode plane wise and orientation (**Paper I**)

This indicates that the maintenance of Errera's rule of division is essential for the morphogenesis of the grid and only small variation is allowed. This, leads to assume that a control mechanism ensures the proper positioning of cytokinesis plane with little stochasticity. This mechanism should integrate three parameters: cell geometry, CW stiffness and mechanical stress from cell and tissue shape. In land plants, the organisation of MTs is such an integrating mechanism (Sampathkumar et al. 2014a; Louveaux et al. 2016b; Robinson 2021). Support to this notion gives the cytokinesis in brow algae which is determined by the positioning of centrosomes and their extending MTs
(Motomura et al. 2010). The geometry of the cells could be "read" by the two daughter centrosomes leading to their correct allingment (along the longest axis or maximal tension).

4.3.2. Actin filaments organisation and blade morphogenesis in Phase II

On **Paper II**, we look into the cytoskeleton organisation Phase II embryos using immunolocalisation on microtubules (MTs) and actin labelling for actin filaments (AFs). The interest on cytoskeleton stems from its properties on morphogenesis of land plants and brown algae. As we looked already in the introduction, MTs and cell wall (CW) constitute the core of a

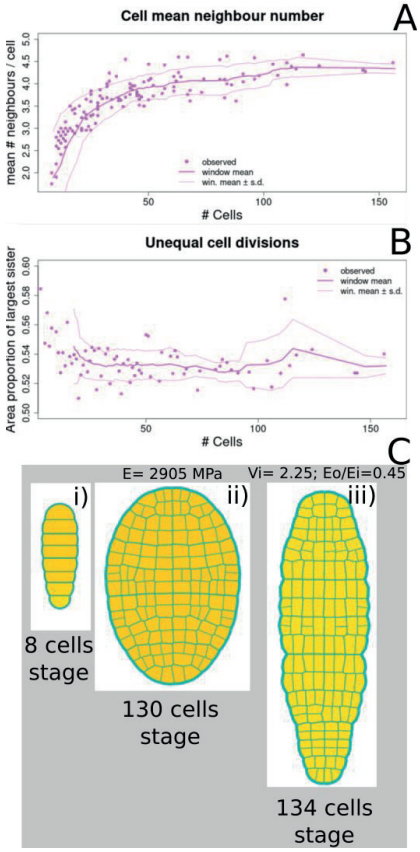

Figure 5. Timelapse extracted data and 2D vertex simulations. (A) Mean number of neighbour cells per cell plotted against the number of cells. The number begins with 2 neighbours per cell during the uniseriate Phase I. Longitudinal divisions of Phase II increase the number of neighbouring cells and around 70 cells the number of neighbours is stabilised at 4. (B) Area of the largest sister cell as proportion plotted against the number cells. The first few divisions of Phase I are a bit anisotropic reaching up to 0.58 of area proportion for the largest derivative. However, the proportion falls at around 0.54 and stabilizes. Therefore, we considere these divisions equal in size, and that the division plane passes through the centroid following the least distance possible, otherwise on a cuboid shape that would result in different area proportions. In conclusion, Errera's rule is followed for the divisions. (C) Vertex simulations. i) the start of every simulation presented in **Paper I**, is the 8 cells embryo, ii) isotropic mechanical properties and elastic modulus 2905 MPa, iii) anisotropic mechanical properties at the internal CWs (Vi = 2.25, stiffer horizontal cell walls) and between outer and internal CWs (Eo/Ei = 0.45, higher E for inner cell walls), note that the stiffnes of a CW takes in consideration also the thickness of a CW not only its elastic modulus and the outer CW is several times thicker.

mechanical feedback loop driven by geometrical cues and tensile stress. Cell division plane and cell growth direction are regulated by this loop. In *Saccharina*, we didn't observe cortical MT organisation, which is in agreement with previous observations (fig. 6A and B) (Katsaros et al. 2006). However, their organisation resembles that of *Dictyota*'s epidermal and medullary cells (Katsaros and Galatis 1992). Specifically, we can observe a cage alike structure surrounding the perinuclear region, resembling a spindle. MTs radiate from the poles of the cage extending through cytoplasm and cortex.

On the other hand, actin filaments (AFs) are cortical and tightly pressed like sheets. With the Fibriltool (Boudaoud et al. 2014) I measured the AFs orientation in reference to the thallus surface. The resultssupported our qualitative estimations (fig. 6C-J). The AFs of the lateral (anticlinal) cortex have a specific orientation compared to the random orientation of the cortical AFs below the surface of the thallus (surface, fig. 6D, I). The orientation (fig. 6E, I) of AFs below the lateral CWs are mostly aligned along the Z-axis (77.69 ° ± 10.43). To test the impact of disturbed AFs, a timelapse with latrunculin B (LatB) treatment took place for seven days (Paper II). Even though the sample was small and highly heterogenous, there was a conspicuous effect on the treated specimen compared to the control. Overall tissue growth was hindered but more specifically the Y-axis and in which less longitudinal divisions were observed. Also, the treated specimen had a sigmoid shape and potentially an irregular cell expansion, making the tissue look thicker than the control embryos. These observations need additional verification with cellular stains and actin labelling to estimate the magnitude of disturbance. In conclusion, the LatB treatment indicates a potentially restricting role for the AFs against cell growth along the Z-axis and maybe a control over the Y-axis cell growth and divisions. These observations need to be investigated further. When compared with the early leaf morphogenesis (Zhao et al. 2020), we observed a similar pattern for the cortical MT bundles below the internal anticlinal CWs. Zhao et al. (2020) showed that the parallel MTs to adaxial-abaxial axis (Z-axis) of the early developing leaf are aligned with: 1) cellulose microfibrils (CMF) and 2) the axis of the maximal tensile stress. In addition, most of the cell divisions are also aligned along the maximal tension axis. Furthermore, oryzalin treatments cause a significant increase in the number of periclinal divisions and decreased growth in the medio-lateral axis of the blade (Y-axis), an effect that is similar to that of LatB on *Saccharina*.

The model of the early developing leaf is considered similar to the developing Phase II because, with the exception of the amount of cell layers, it is a flat organ with diffused cell divisions. This means there is no specific active region like a meristem. However, cell divisions cease at later stages of leaf development and only cell expansion takes place. Therefore, a hypothesis is suggested, yet to be tested. Since there are indications that CMF in brown algae align with the AFs

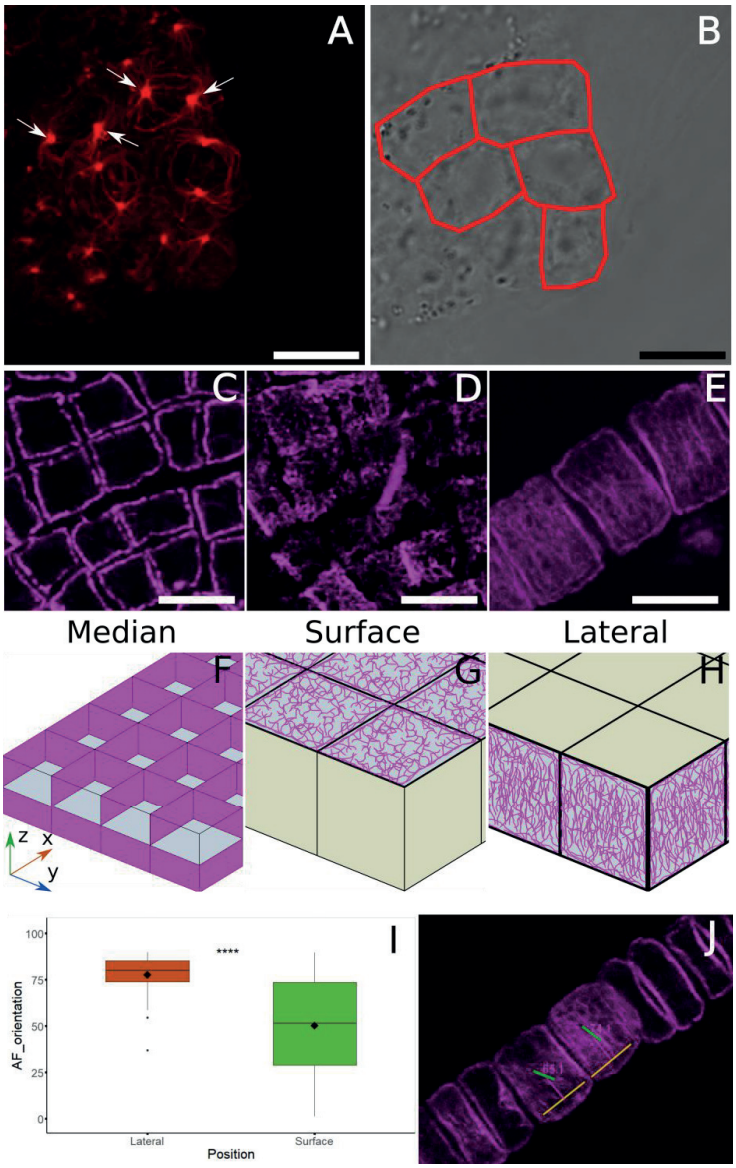

Figure 6. Cytoskeleton organisation of Phase II embryos. (A) Maximal projection of α-tubulim immunofluorescence in blade cells. Cage like structures are visible with two focus points (arrows). The microtubules extend through cytoplasm and cortex. (B) Transmission channel of A. (C, F) Median confocal section from Ph-Rh labelling and simple sketch with the axes system. (D, G) Surface confocal section and simple sketch. (E, H) Lateral confocal section and simple sketch. Comparing the lateral with surface section, a certain orientation of the AFs is visible. (I) Box-blots of AFs from measurements with the MT_Angle2Ablation workflow, **** = p-value < 0.0001. N= 54 for the lateral (horizontal and vertical) cell walls, N=315 for the surface cell walls measurements. (J) Example of measurements, the angle (°) is measured between the green line that follows the average orientation of the AFs projected and the yellow parallel line to the surface. Bars: 10µm

(Katsaros et al. 2002), then potentially a mechanical feedback loop between AFs and CW properties, similar to that in plants (Hamant et al. 2008; Sampathkumar et al. 2019; Trinh et al. 2021), is present in *Saccharina'*s Phase II cells. However, cellulose is at a very small percentage in brown algae (Charrier et al. 2019). Patterns of alginates deposition could contribute to the modulation on stiffness of CW (Torode et al. 2016; Rabillé et al. 2019b). Potential organisator of AFs could be RAC1 present in both animals (Marston et al. 2019) and plants (Craddock et al. 2012), as well as in the zygote polarisation of *Fucus* (Hable 2014), promoting the organisation of distinct structures of AF, an actin patch in the case of *Fucus.* However, RAC1 does not seem to be related with the AF organisation at the tip growth of *Ectocarpus* (Nehr et al. 2021).

4.4. Morphogenesis during Phase III

4.4.1. Polystromatisation: process

The first divisions parallel to the surface of the embryonic thallus of *Saccharina* take place two weeks after the polarisation of the zygote, 800-1000 cells. In about one week, big part of the embryo is polystromatised (Phase III) and different types of cells and tissues emerge (**Paper III**). A gradient of cell layers appears at the blade, observed similarly from Yendo (1911). This gradient has a specific direction with the polystromatisation moving acropetally.

This kind of arrangement is not completely unique in brown algae. It is unique at an embryogenesis level. However, there are mature thalli growing in a similar way. The thallus of *Dictyopteris mebranacea* is flat (like kelps) and branched with a midrib in the middle of the branches (Katsaros and Galatis 1988). Tthe upper leaves of *Physcomitrella patens* exhibit a similar morphology, with the exception of the presence of serrated edges (Barker and Ashton 2013). The apical ends of *Dictyopteris*' branches are monostromatic (Katsaros and Galatis 1988). After a short monostromatic region, the thallus of *Dictyopteris* becomes bilayered and gradually turns thicker and polystromatic while a polystromatic midrib is established (Katsaros and Galatis 1988). On the sides of the midrib, two bilayered "wings" are formed similar with the monostromatic and bistromatic sides of the developing Phase III (**Paper III**). In contrast with *Saccharina,* polystromatisation moves basipetally during *Dictyopteris*' apical growth, and lateral growth occurs via meristoderm. A common point between the two species and stages is the midrib, which is a similar case with *Saccharina*'s embryo, as the lateral expansion of polystromatisation on the blade occurs from the center of the tissue to the sides (Paper III).

On figure 7, the process of polystromatisation at a monostromatic region of the blade is depicted as observed and perceived (**Paper III**). The observations come from 20 days old Phase III embryos, and semi-thin lateral longitudinal sections along the polystromatic region. Initially, periclinal symmetric cell divisions take place at the one cell layer tissue (monostroma) (fig. 7A) followed cell growth. Then, a second periclinal, equal but assymmetrical division takes place resulting in initials of meristoderm and cortex (fig. 7B). Anticlinal symmetric divisions of the meristodermatic initial establish the meristoderm (fig. 7C). The cortical initial expands considerably in volume, while symmetrical divisions of equal or unequal size occur with random orientation (fig. 7C, D). The same process takes place for the second cell of the bistroma, either delayed or concurrently with the first cell. Polystromatisation results to four cell

layers (fig. 7E). In the center of the young polystroma, there are four or more layers of cortex surrounded by a layer of meristoderm on each external side (fig. 7E). The process is not homogenous and can be interrupted from different stages of polystromatisation until a region is fully polystromatic (**Paper III**).

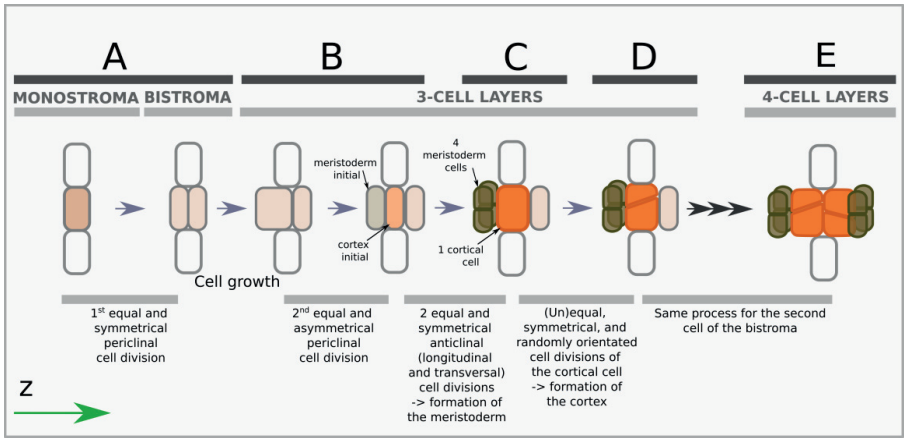

Figure 7. Series of events during polystromatisation. (A) The first periclinal division is equal (same volume) and symmetrical (same fate) results to bistromatic region. (B) Cell expansion and a second equal but asymmetric division (different cell fate of the deriatives) is the first step on distinguishing between internal and external tissues. (C-D) Series of divisions of the initials of meristoderm and cortex, establish the different tissues. (E) The process from the second derivative of the first equal division (A) can be delayed or occur at the same time. The series is presented from a transversal section point of view, the Z-axis is depicted at the left corner of the figure.

4.4.2. Polystromatisation: initiation

The transition from a 2D growth to 3D growth process seems to be resolved early in the embryonic development of Fucales (Moss and Lacey 1963; Moss 1970; Clayton et al. 1985; Klemm and Hallam 1987; Lardi et al. 2022) and Dictyotales (Fritsch 1945; Gaillard et al. 1986; Bogaert et al. 2020). Outside the group of brown algae, land plants, green and red algae are capable to form complex 3D structures (Knoll 2011), while simpler multicellular bodies can be found in green algae like *Volvox* (Umen 2020), *Ulva* (Spoerner et al. 2012) and most of the Charophycean lineage (Leliaert et al. 2012). Interestingly, 3D growth is also preferred under selection pressure from unicellular eukaryotes and prokaryotes alike (Herron et al. 2019; Bozdag et al. 2021; Márquez-Zacarías et al. 2021). These even more add up to the question about the late introduction of the third axis, and potentially indicates that a suppression mechanism is present in *Saccharina* expressed by the potential mechanical feedback loop along the Z-axis (**Paper II**).

Regarding potential signals for initiation of polystromatisation, there are two possibilities. Firstly, apical cells and meristems in brown algae have long been proven as culprits of morphogenesis regulation through apical dominance (Katsaros 1995; Tanaka et al. 2017). However, *Saccharina* does not grow apically. If a supressing signal exists at the tip of the blade of Phase II embryo, then increased distance between the tip and the base of the blade would decrease until a threshold is reached; where the polystromatisation inhibitor cannot reach

the base of the embryo anymore, thus promoting polystromatisation. A second possibility is that polystromatisation is promoted by a signal diffusing from the base to the tip of the embryo, similar to the sporogenesis inhibitor of kelps (Buchholz and Lüning 1999; Pang and Lüning 2004), which is potentially auxin (Kai et al. 2006).

Regarding the cascade triggered by the emitted signal, transcriptomic data (**Paper IV**) on whole 12- and 14-days after fertilisation (DAF) embryos compared with 10 DAF embryos, indicate a prominent downregulation pattern for the differentially expressed genes (DEGs) during initiation of polystromatisation. More than half of the DEGs are down regulated with increased abundance to the gene ontology terms (GO terms) related to cell communication and signal transduction for the 14 DAF. In addition, 14 DAF embryos show upregulation to key genes like calmodulin, mannuronan C-5-epimerase, MYB transcription factors (TFs), phospolipases and several kinases and signalling related genes (**Paper IV**). Although direct connection cannot be established with re-organisation of actin filaments or the initiation of polystromatisation at the base of the embryo, Paper IV points towards a switch of expression with four times more DEGs at 14 DAF embryos in comparison with the 12 DAF embryos (475 vs 111 DEGs). We estimate that the first periclinal division will take place after the previous potential mechanical feedback loop along the Z-axis (**Paper II**) is cancelled via AFs reorganisation and cell modifications. This initial hypothesis is based on a similar phenomenon with the initiation of organogenesis at the apical meristem of land plants followed by reorganisation of cortical MTs to isotropic arrangement and softening of the CW (Hamant et al. 2008; Peaucelle et al. 2011; Sampathkumar et al. 2014b; Arsuffi and Braybrook 2018). Firstly, increased amounts of calmodulin can be related with spikes to Ca^{2+} concentrations (Izadi et al. 2018) which can lead to reorganisation of the AFs through RAC1 and generally Rho-GTPases (Fowler et al. 2004; Craddock et al. 2012; Hable 2014; Marston et al. 2019). Therefore, calmodulin could function as secondary messenger after the promoting signal for polystromatisation. Similarly, phospholipases D have been associated with AFs dynamics (Pleskot et al. 2013) as part of signalling pathways. Secondly, mannuronan C-5-epimerases are enzymes related to alginate modifications at the cell wall of brown algae (Fischl et al. 2016), therefore potentially related with modulation of CW stiffness (Rabillé et al. 2019b; Yonamine et al. 2021). Their role could be similar with that of expansins and pectinases on CW properties modification, promoting growth along Z-axis and the first periclinal divisions. But as mentioned already, “soft” and “stiff” alginates patterns during initiation of organogenesis in *Sargassum* did not align with predictions of softer cell wall (Linardić and Braybrook 2017). Lastly, MYB TFs are related with cell proliferation and differentiation (Zeng et al. 2022), therefore, they potentially contribute to the polystromatisation process and first cell differentiations. Better experimental design focused on the spatial localisation of the observed differential expression is needed to mechanistically explore the different molecules and their functional value that contribute to initiation of polystromatisation.

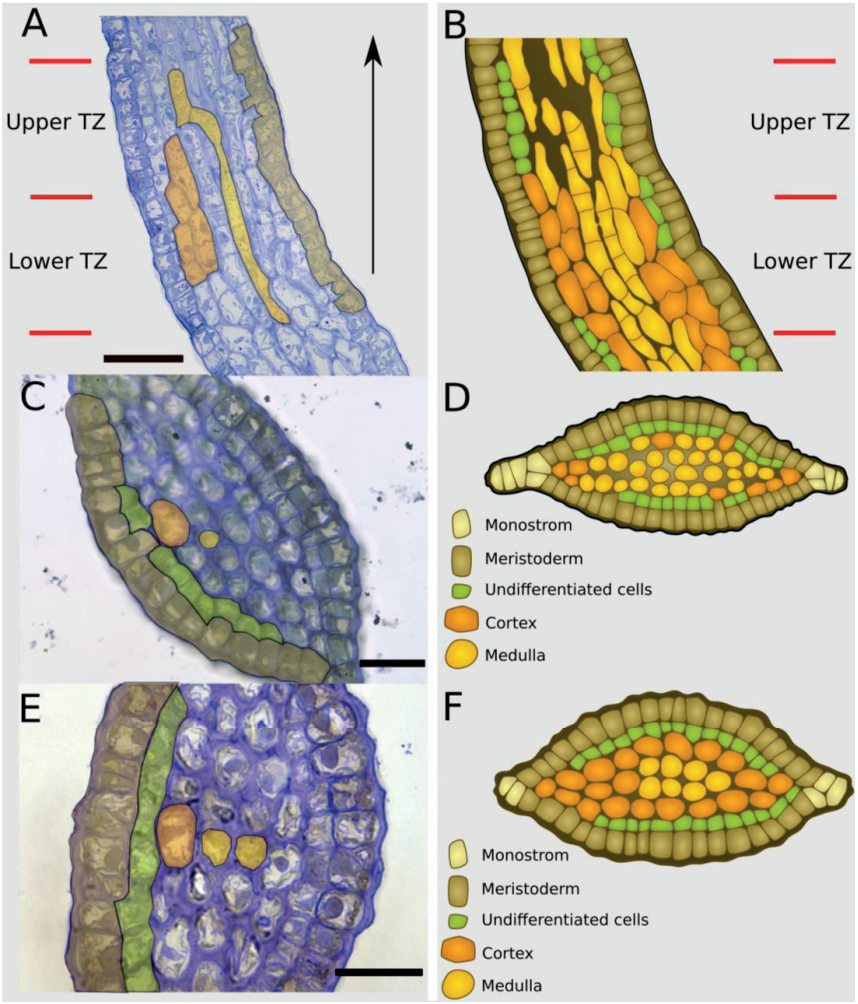

Figure 8. Semithin sections at the transition zone of Phase III embryos. (A, B) Longitudinal section and graphical depiction of the TZ. The rough limits of the upper and lower TZ are indicated. (C, D) Transversal section of upper TZ and its graphical depiction. An increased abundance of medullary cells is visible with only few cortical cells while there is a layer of undifferentiated cells, just below the meristoderm. (E, F) Transversal section of lower TZ and its graphical depiction. An increased abundance of cortical cells is visible with only few medullary cells while there is a layer of undifferentiated cells, just below the meristoderm. Bars: (A) 50, (C, E) 25 µm.

4.4.3. Tissue structure and differentiation in different regions of Phase III thallus

Polystromatisation is an ongoing process during Phase III (**Paper III**). At the same time, the already polystromatic regions depend on the growth of the meristodermatic cells which divides symmetrically along the X-axis and the Y-axis to follow the growth of the underlying tissues, while periclinal asymmetric divisions supply internal tissues with undifferentiated cells. These are abundant in TZ and base of blade but mostly absent from the younger polystroma. In mature plants they form additional layers of meristoderm (Smith 1939), though in phase III polystroma they are mostly responsible for furnishing the interior with additional cortical cells that, then, differentiate into medullary cells. Medullary cells are long sinuous

cells, occasionally branching, replacing the cortical cells at the base of the blade and older polystroma. Specifically, medulla and cortex are both present in older polystroma but the first is dominant at the base of blade and the second is dominant at the younger polystroma and stipe. At the stipe, a few non-branching medulla cells can be found close to the TZ, however, they are forming a dense meshwork in mature plants all along the thallus (Sykes 1908; Smith 1939; Fritsch 1945). In conclusion, different polystromatic regions of varying levels of maturity present different cellular composition. Interestingly, common cellular types between the different regions can have significantly different morphometrics potentially related to shape or role (**Paper III**).

In figure 8, we can observe that at the TZ, the region between blade and stipe, is practically consisted of the same cell types as the stipe and the base of blade (**Paper III**). In addition, lower and upper TZ differ on the abundance of the different cell types projecting the composition of the region directly next to them. Specifically, lower TZ has more cortical cells than medullary elements like the stipe below it, while the upper TZ is richer in medulla like the base of blade. Both sub-regions have a high amount of asymmetric undifferentiated cells. This indicates that the TZ could function indeed as the main growth region (Smith 1939; Parke 1948; Steinbiss and Schmitz 1974) or alternatively be a quiscent center from whic all the different tissues grow in thickness and along the two haxes (X- and Y- axes) while the meristoderm supplies with undifferentiated cells. However, growth is not restricted to TZ and its surroundings during Phase III. There is diffuse growth along the polystroma and the monostroma which is observable from the size and shape of the meristodermatic cells along the X axis of the longitudinal semi-thin sections (**Paper III**). As a result, like the epidermal tissues of land plants, the cells of the meristoderm need to divide anticlinally along both X- and Y- axes to follow the growth of the internal tissues (Sinnott and Bloch 1941; Sinnott 1960).

4.4.4. Meristoderm, cell differentiation and growth in brown algae

Meristoderm is a unique meristematic tissue of brown algae. Apical meristem-based growth orders like Fucales and Dictyotales, base their apical meristem function and lateral growth on the function of meristoderm. As mentioned before, the main growth axis of the branches of *Dictyopteris* depends on apical meristems of up to nine initial cells while the differentiation of the meristodermatic cells coincides with the formation of the midrib (Katsaros and Galatis 1988). The process is similar with *Saccharina*'s polystromatisation and meristoderm function, however, *Dictyopteris*' first asymmetric cells differentiates into medullary cells. After the establishment of the meristoderm, the next batch of asymmetric cells of *Dictyopteris* differentiates into cortical cells which can differentiate further to medulla (Katsaros and Galatis 1988) like in *Saccharina*. This indicates two potential pathways for the periclinal derivatives of the meristoderm. Similarly, in *Saccharina*, a second pathway of direct differentiation of the meristodermatic asymmetric derivatives to medulla can explain the conspicuous abundance of medulla at the base of blade (**Paper III**). Alternatively, a fast-track differentiation from cortical to medulla cells could occur. In Fucales, the meristoderm complements the function of the apical meristem (Fritsch 1945; Moss 1950, 1969, 1970; Clayton et al. 1985; Sokhi and Vijayaraghavan 1987; Linardić and Braybrook 2017) and is responsible for organogenesis and growth in

thickness. Further activity of the meristoderm below the apical meristem supports thickness growth. However, the differentiation rate does not seem as intensive as in kelps.

To summarise, axial growth and lateral or thickness growth are decoupled in Fucales and Dictyotales. However, in the case of *Saccharina* and kelps, these two growth directions occur in the same region and at the same time. This region is the transition zone and parts of the tissue surrounding it (Smith 1939; Fritsch 1945; Parke 1948; Steinbiss and Schmitz 1974). Periclinal cell divisions potentially take place mostly in the TZ and the base of the blade (**Paper III**, (Smith 1939; Fritsch 1945). Periclinal cell divisions become rarer away from the two active regions, but, the meristoderm should follow the growth of internal tissues like the L1 layer of developing organs (Sinnott and Bloch 1941; Sinnott 1960; Steeves and Sussex 1989). Therefore, anticlinal divisions become abundant away from TZ. In essence, 3D intercalary growth in mature plants of *Saccharina* and most kelps is a result of cell division and differentiation activity of the meristoderm at the active region of TZ and base of blade.

5. Conclusions and future remarks

During the morphogenesis of *Saccharina*'s embryos we observed an alternative strategy on parenchymatic development. Usually, parenchymatic organisms develop from early stages along a three-axial system. However, the embryos of *Saccharina* have a general 2D-shape setup during Phases I and II (**Paper I**), while the third growth axis is delayed in comparison to other brown algal species and parenchymatic organisms (**Paper III**). The 2D tissue morphogenesis during the earlier stages is potentially a result of anisotropic patterns on the elastic modulus of the outer and inner cell walls (**Paper I**). The proposed model is robust with low levels of stochactisity on the model parameters. In addition, AFs organisation seems to play an essential role to the monostromatic nature of Phase II blade (**Paper II**) when comparing with the mechanism that holds the leaf of land plants flat (Zhao et al. 2020). Further drug treatments combined with AFs and MTs labelling are necessary to support our theory, coupled also with CW disintegrating approaches like laser ablation or chemical treatments. Open remaining questions for phase II are the establishment and maintenance of the apico-basal axis along *Saccharina*'s embryogenesis (ongoing work from Samuel Boscq, PhD student in MMA team, Roscoff). In addition, a mechanistic approach is necessary for investigating how the observed anisotropies in AFs organisation and CW properties are established and which are the key molecules. Preliminary data (not presented) from immunolocalisation of alginates deposition, RAC1 and myosin already seem to form a picture, but it is still incomplete.

During Phase III (**Paper III**), polystromatisation proceeds like a wave along all the body of the developing embryo following a series of periclinal cell divisions of different orientation (symmetric, asymmetric) resulting in the essential meristoderm and the first cortical cells. Polystromatisation as a process practically results in the establishment of the third growth axis (i.e., growth in thickness) (**Paper III**). However, the mature blade remains flat besides its large size (up to 5 meters length). It is interesting to look into the mechanics that hold the blade flat and compare with the aerial organs of land plants.

There is an insight on the necessary steps for initiation of polystromatisation (**Papers III, IV**) beginning with a cascade that promotes downregulation to genes mostly associated to signalling and post-translational modification. The few upregulated proteins, like calmodulin, phospholipases and mannuronan C-5-epimerase have a potential role in breaking the feedback loop established during Phase II, however, direct connection with the events of polystromatisation cannot be established yet. Further spatial exploration of transcriptomic changes coupled to auxin and alginates immunolocalisation is needed for locating the potential signal and its effects on cytoskeleton organisation and CW properties. Laser capture microdissection can be an essential tool for this above approach, already optimised for another brown algal species, *Ectocarpus siliculosus* (Saint-Marcoux et al. 2015).

The observations on the structure and dynamics of Phase III tissues come from static acquisitions of semi thin sections. Then a detailed description and conceptualisation follows on how the meristoderm supplies the cortex and the medulla with new cells. However, it is recognisable that the situation is more dynamic, and this is especially conspicuous from the different cellular composition of each region of the Phase III thallus and its morphometrics (**Paper III**). In the future, confocal imaging coupled to non-toxic stains or even genome edited fluorophores, could assist a more detailed imaging and investigation of the events taking place in the meristoderm and the underlying tissues.

Further works are ongoing on the apico basal axis establishment, coupled with advanced microscopic methods like laser ablation (Boscq et al. 2022) and cultivation of *Saccharina* embryos in microfluidic chips (Clerc et al. 2022). These will assist more detailed image acquisitions and accurate manipulations on cellular level for the earliest stages of Phases I and II. During this PhD I contributed to answer the questions about which events and mechanisms take place, from a cellular and tissue properties perspective. In the end, a new comparative model is established to study morphogenetic forces on a mechanically isolated context.

6. References

Adrian Alexa and Jörg Rahnenführer. 2022. topGO: Enrichment Analysis for Gene Ontology. R.

Alvarez-Buylla, E.R., Benítez, M., Corvera-Poiré, A., Cador, Á.C., Folter, S. de, Buen, A.G. de, Garay-Arroyo, A., García-Ponce, B., Jaimes-Miranda, F., Pérez-Ruiz, R.V., Piñeyro-Nelson, A., and Sánchez-Corrales, Y.E. 2010. Flower Development. arbo.j **2010**(8). The American Society of Plant Biologists. doi:10.1199/tab.0127.

Aramaki, T., Blanc-Mathieu, R., Endo, H., Ohkubo, K., Kanehisa, M., Goto, S., and Ogata, H. 2020. KofamKOALA: KEGG Ortholog assignment based on profile HMM and adaptive score threshold. Bioinformatics **36**(7): 2251–2252. doi:10.1093/bioinformatics/btz859.

Arsuffi, G., and Braybrook, S.A. 2018. Acid growth: an ongoing trip. Journal of Experimental Botany **69**(2): 137–146. doi:10.1093/jxb/erx390.

Autran, D., Bassel, G.W., Chae, E., Ezer, D., Ferjani, A., Fleck, C., Hamant, O., Hartmann, F.P., Jiao, Y., Johnston, I.G., Kwiatkowska, D., Lim, B.L., Mahönen, A.P., Morris, R.J., Mulder, B.M., Nakayama, N., Sozzani, R., Strader, L.C., Tusscher, K. ten, Ueda, M., and Wolf, S. 2021. What is quantitative plant biology? Quantitative Plant Biology **2**. Cambridge University Press. doi:10.1017/qpb.2021.8.

Banda, J., Bellande, K., von Wangenheim, D., Goh, T., Guyomarc'h, S., Laplaze, L., and Bennett, M.J. 2019. Lateral Root Formation in *Arabidopsis*: A Well-Ordered LRexit. Trends in Plant Science **24**(9): 826–839. doi:10.1016/j.tplants.2019.06.015.

Barbier, M., Charrier, B., Araujo, R., Holdt, S.L., Jacquemin, B., and Rebours, C. 2019. PEGASUS -PHYCOMORPH European Guidelines for a Sustainable Aquaculture of Seaweeds. COST Action FA1406, Roscoff, France. Available from https://doi.org/10.21411/2c3w-yc73.

Barker, E.I., and Ashton, N.W. 2013. Heteroblasty in the moss, *Aphanoregma patens* (*Physcomitrella patens*), results from progressive modulation of a single fundamental leaf developmental programme. Journal of Bryology **35**(3): 185–196. doi:10.1179/1743282013Y.0000000058.

Bartsch, I., Wiencke, C., Bischof, K., Buchholz, C.M., Buck, B.H., Eggert, A., Feuerpfeil, P., Hanelt, D., Jacobsen, S., Karez, R., Karsten, U., Molis, M., Roleda, M.Y., Schubert, H., Schumann, R., Valentin, K., Weinberger, F., and Wiese, J. 2008. The genus *Laminaria* sensu lato : recent insights and developments. European Journal of Phycology **43**(1): 1–86. doi:10.1080/09670260701711376.

Baskin, T.I., Beemster, G.T.S., Judy-March, J.E., and Marga, F. 2004. Disorganization of Cortical Microtubules Stimulates Tangential Expansion and Reduces the Uniformity of Cellulose Microfibril Alignment among Cells in the Root of *Arabidopsis*. Plant Physiol **135**(4): 2279–2290. doi:10.1104/pp.104.040493.

Besson, S., and Dumais, J. 2011. Universal rule for the symmetric division of plant cells. Proceedings of the National Academy of Sciences **108**(15): 6294–6299. doi:10.1073/pnas.1011866108.

Blum, M., Chang, H.-Y., Chuguransky, S., Grego, T., Kandasaamy, S., Mitchell, A., Nuka, G., Paysan-Lafosse, T., Qureshi, M., Raj, S., Richardson, L., Salazar, G.A., Williams, L., Bork, P., Bridge, A., Gough, J., Haft, D.H., Letunic, I., Marchler-Bauer, A., Mi, H., Natale, D.A., Necci, M., Orengo, C.A., Pandurangan, A.P., Rivoire, C., Sigrist, C.J.A., Sillitoe, I., Thanki, N., Thomas, P.D., Tosatto, S.C.E., Wu, C.H., Bateman, A., and Finn, R.D. 2021. The InterPro protein families and domains database: 20 years on. Nucleic Acids Research **49**(D1): D344–D354. doi:10.1093/nar/gkaa977.

Bogaert, K.A., Arun, A., Coelho, S.M., and De Clerck, O. 2013. Brown Algae as a Model for Plant Organogenesis. *In* Plant Organogenesis: Methods and Protocols. *Edited by* I. De Smet. Humana Press, Totowa, NJ. pp. 97–125. doi:10.1007/978-1-62703-221-6_6.

Bogaert, K.A., Beeckman, T., and Clerck, O.D. 2017. Two-step cell polarization in algal zygotes. Nature Plants **3**(2): 1–7. doi:10.1038/nplants.2016.221.

Bogaert, K.A., Beeckman, T., and De Clerck, O. 2015. Photopolarization of *Fucus* zygotes is determined by time sensitive vectorial addition of environmental cues during axis amplification. Front. Plant Sci. **6**: 26. doi:10.3389/fpls.2015.00026.

Bogaert, K.A., Delva, S., and De Clerck, O. 2020. Concise review of the genus *Dictyota* J.V. Lamouroux. J Appl Phycol **32**(3): 1521–1543. doi:10.1007/s10811-020-02121-4.

Bogaert, K.A., Zakka, E.E., Coelho, S.M., and De Clerck, O. 2022. Polarization of brown algal zygotes. Seminars in Cell & Developmental Biology. doi:10.1016/j.semcdb.2022.03.008.

Bolger, A.M., Lohse, M., and Usadel, B. 2014. Trimmomatic: a flexible trimmer for Illumina sequence data. Bioinformatics **30**(15): 2114–2120. doi:10.1093/bioinformatics/btu170.

Boscq, S., Dutertre, S., Theodorou, I., and Charrier, B. 2022. Targeted Laser Ablation in the Embryo of *Saccharina latissima*. JoVE (Journal of Visualized Experiments) (181): e63518. doi:10.3791/63518.

Boudaoud, A., Burian, A., Borowska-Wykręt, D., Uyttewaal, M., Wrzalik, R., Kwiatkowska, D., and Hamant, O. 2014. FibrilTool, an ImageJ plug-in to quantify fibrillar structures in raw microscopy images. Nat Protoc **9**(2): 457–463. Nature Publishing Group. doi:10.1038/nprot.2014.024.

Bozdag, G.O., Zamani-Dahaj, S.A., Kahn, P.C., Day, T.C., Tong, K., Balwani, A.H., Dyer, E.L., Yunker, P.J., and Ratcliff, W.C. 2021, August 5. De novo evolution of macroscopic multicellularity. bioRxiv. doi:10.1101/2021.08.03.454982.

Bringloe, T.T., Starko, S., Wade, R.M., Vieira, C., Kawai, H., Clerck, O.D., Cock, J.M., Coelho, S.M., Destombe, C., Valero, M., Neiva, J., Pearson, G.A., Faugeron, S., Serrão, E.A., and Verbruggen, H. 2020. Phylogeny and Evolution of the Brown Algae. Critical Reviews in Plant Sciences **39**(4): 281–321. Taylor & Francis. doi:10.1080/07352689.2020.1787679.

Broch, O.J., Alver, M.O., Bekkby, T., Gundersen, H., Forbord, S., Handå, A., Skjermo, J., and Hancke, K. 2019. The Kelp Cultivation Potential in Coastal and Offshore Regions of Norway. Front. Mar. Sci. **5**. Frontiers. doi:10.3389/fmars.2018.00529.

Buchfink, B., Reuter, K., and Drost, H.-G. 2021. Sensitive protein alignments at tree-of-life scale using DIAMOND. Nat Methods **18**(4): 366–368. Nature Publishing Group. doi:10.1038/s41592-021-01101-x.

del Cerro, M., Cogen, J., and del Cerro, C. 1980. Stevenel's Blue, an excellent stain for optical microscopical study of plastic embedded tissues. Microsc Acta **83**(2): 117–121.

Chang, W., Guo, Y., Zhang, H., Liu, X., and Guo, L. 2020. Same Actor in Different Stages: Genes in Shoot Apical Meristem Maintenance and Floral Meristem Determinacy in *Arabidopsis*. Frontiers in Ecology and Evolution **8**. Available from https://www.frontiersin.org/articles/10.3389/fevo.2020.00089 [accessed 25 September 2022].

Charrier, B., Coelho, S.M., Bail, A.L., Tonon, T., Michel, G., Potin, P., Kloareg, B., Boyen, C., Peters, A.F., and Cock, J.M. 2008. Development and physiology of the brown alga *Ectocarpus siliculosus*: two centuries of research. New Phytologist **177**(2): 319–332. doi:10.1111/j.1469-8137.2007.02304.x.

Charrier, B., Le Bail, A., and de Reviers, B. 2012. Plant Proteus: brown algal morphological plasticity and underlying developmental mechanisms. Trends in Plant Science **17**(8): 468–477. doi:10.1016/j.tplants.2012.03.003.

Charrier, B., Rabillé, H., and Billoud, B. 2019. Gazing at Cell Wall Expansion under a Golden Light. Trends in Plant Science **24**(2): 130–141. doi:10.1016/j.tplants.2018.10.013.

Clayton, M.N., Hallam, N.D., Luff, S.E., and Diggins, T. 1985. Cytology of the apex, thallus development and reproductive structures of *Hormosira banksii* (Fucales, Phaeophyta). Phycologia **24**(2): 181–190. doi:10.2216/i0031-8884-24-2-181.1.

Clerc, T., Boscq, S., Attia, R., Kaminski Schierle, G.S., Charrier, B., and Läubli, N.F. 2022. Cultivation and Imaging of *S. latissima* Embryo Monolayered Cell Sheets Inside Microfluidic Devices. Bioengineering **9**(11): 718. Multidisciplinary Digital Publishing Institute. doi:10.3390/bioengineering9110718.

Cormier, A., Avia, K., Sterck, L., Derrien, T., Wucher, V., Andres, G., Monsoor, M., Godfroy, O., Lipinska, A., Perrineau, M.-M., Van De Peer, Y., Hitte, C., Corre, E., Coelho, S.M., and Cock, J.M. 2016. Re-annotation, improved large-scale assembly and establishment of a catalogue of noncoding

loci for the genome of the model brown alga *Ectocarpus*. New Phytol. **214**: 219–232. doi:10.1111/nph.14321.

Cosgrove, D.J. 1987. Wall Relaxation and the Driving Forces for Cell Expansive Growth. Plant Physiology **84**(3): 561–564. American Society of Plant Biologists. doi:10.1104/pp.84.3.561.

Cosgrove, D.J. 2000a. Expansive growth of plant cell walls. Plant Physiology and Biochemistry **38**(1): 109–124. doi:10.1016/S0981-9428(00)00164-9.

Cosgrove, D.J. 2000b. Loosening of plant cell walls by expansins. Nature **407**(6802): 321. doi:10.1038/35030000.

Cosgrove, D.J. 2018. Diffuse Growth of Plant Cell Walls. Plant Physiology **176**(1): 16–27. doi:10.1104/pp.17.01541.

Cosgrove, D.J. 2022. Building an extensible cell wall. Plant Physiology **189**(3): 1246–1277. doi:10.1093/plphys/kiac184.

Craddock, C., Lavagi, I., and Yang, Z. 2012. New insights into Rho signaling from plant ROP/Rac GTPases. Trends Cell Biol. **22**(9): 492–501. doi:10.1016/j.tcb.2012.05.002.

Crang, R., Lyons-Sobaski, S., and Wise, R. 2018. Vascular Cambium. *In* Plant Anatomy. Springer International Publishing, Cham. pp. 479–507. doi:10.1007/978-3-319-77315-5_14.

Cumashi, A., Ushakova, N.A., Preobrazhenskaya, M.E., D'Incecco, A., Piccoli, A., Totani, L., Tinari, N., Morozevich, G.E., Berman, A.E., Bilan, M.I., Usov, A.I., Ustyuzhanina, N.E., Grachev, A.A., Sanderson, C.J., Kelly, M., Rabinovich, G.A., Iacobelli, S., Nifantiev, N.E., and Consorzio Interuniversitario Nazionale per la Bio-Oncologia, Italy. 2007. A comparative study of the anti-inflammatory, anticoagulant, antiangiogenic, and antiadhesive activities of nine different fucoidans from brown seaweeds. Glycobiology **17**(5): 541–552. doi:10.1093/glycob/cwm014.

Davidson, N.M., and Oshlack, A. 2014. Corset: enabling differential gene expression analysis for de novo assembled transcriptomes. Genome Biol. **15**(7): 410. doi:10.1186/PREACCEPT-2088857056122054.

Drew, G.H. 1910. The Reproduction and early Development of *Laminaria digitata* and *Laminaria saccharina*. Annals of Botany **24**(1): 177–189. doi:10.1093/oxfordjournals.aob.a089253.

Ducreux, G. 1984. Experimental Modification of the Morphogenetic Behavior of the Isolated Sub-Apical Cell of the Apex of Sphacelaria *Cirrosa* (Phaeophyceae). Journal of Phycology **20**(4): 447–454. doi:https://doi.org/10.1111/j.0022-3646.1984.00447.x.

Ebbing, A., Pierik, R., Bouma, T., Kromkamp, J.C., and Timmermans, K. 2020. How light and biomass density influence the reproduction of delayed *Saccharina latissima* gametophytes (Phaeophyceae). Journal of Phycology **56**(3): 709–718. doi:10.1111/jpy.12976.

Ewels, P., Magnusson, M., Lundin, S., and Käller, M. 2016. MultiQC: summarize analysis results for multiple tools and samples in a single report. Bioinformatics **32**(19): 3047–3048. doi:10.1093/bioinformatics/btw354.

FAO. 2018. The global status of seaweed production, trade and utilization. Rome, Italy.

Fischl, R., Bertelsen, K., Gaillard, F., Coelho, S., Michel, G., Klinger, M., Boyen, C., Czjzek, M., and Hervé, C. 2016. The cell-wall active mannuronan C5-epimerases in the model brown alga *Ectocarpus*: From gene context to recombinant protein. Glycobiology **26**(9): 973–983. doi:10.1093/glycob/cww040.

Forbord, S., Skjermo, J., Arff, J., Handå, A., Reitan, K., Bjerregaard, R., and Lüning, K. 2012. Development of *Saccharina latissima* (Phaeophyceae) kelp hatcheries with year-round production of zoospores and juvenile sporophytes on culture ropes for kelp aquaculture. J Appl Phycol **24**(3): 393–399. doi:10.1007/s10811-011-9784-y.

Forbord, S., Steinhovden, K.B., Rød, K.K., Handå, A., Skjermo, J., Steinhovden, K.B., Rød, K.K., Handå, A., and Skjermo, J. 2018. Cultivation protocol for *Saccharina latissima*. *In* Protocols for Macroalgae Research. doi:10.1201/b21460-2.

Fossberg, J., Forbord, S., Broch, O.J., Malzahn, A.M., Jansen, H., Handå, A., Førde, H., Bergvik, M., Fleddum, A.L., Skjermo, J., and Olsen, Y. 2018. The Potential for Upscaling Kelp (*Saccharina*

latissima) Cultivation in Salmon-Driven Integrated Multi-Trophic Aquaculture (IMTA). Front. Mar. Sci. **5**. Frontiers. doi:10.3389/fmars.2018.00418.

Fowler, J.E., Vejlupkova, Z., Goodner, B.W., Lu, G., and Quatrano, R.S. 2004. Localization to the rhizoid tip implicates a *Fucus distichus* Rho family GTPase in a conserved cell polarity pathway. : 11.

Fritsch, F.E. 1945. The Structure And Reproduction Of The Algae. Cambridge University Press, Cambridge.

Gaillard, J., L'Hardy-Halos, M.Th., and Pellegrini, L. 1986. Morphogenèse du *Dictyota dichotoma* (Huds.) Lamouroux (Phaeophyta). II. Ontogenèse du thalle et cytologie ultrastructurale des différents types de cellules. Phycologia **25**(3): 340–357. doi:10.2216/i0031-8884-25-3-340.1.

Geitmann, A., and Ortega, J.K.E. 2009. Mechanics and modeling of plant cell growth. Trends in Plant Science **14**(9): 467–478. doi:10.1016/j.tplants.2009.07.006.

Gilbert, S.F., and Barresi, M.J.F. 2018. Developmental biology. *In* Eleventh edition. Sinauer Associates, Inc., Sunderland, Massachusetts.

Grabherr, M.G., Haas, B.J., Yassour, M., Levin, J.Z., Thompson, D.A., Amit, I., Adiconis, X., Fan, L., Raychowdhury, R., Zeng, Q., Chen, Z., Mauceli, E., Hacohen, N., Gnirke, A., Rhind, N., di Palma, F., Birren, B.W., Nusbaum, C., Lindblad-Toh, K., Friedman, N., and Regev, A. 2011. Full-length transcriptome assembly from RNA-Seq data without a reference genome. Nat Biotechnol **29**(7): 644–652. Nature Publishing Group. doi:10.1038/nbt.1883.

Graf, L., Shin, Y., Yang, J.H., Choi, J.W., Hwang, I.K., Nelson, W., Bhattacharya, D., Viard, F., and Yoon, H.S. 2021. A genome-wide investigation of the effect of farming and human-mediated introduction on the ubiquitous seaweed *Undaria pinnatifida*. Nat Ecol Evol **5**(3): 360–368. Nature Publishing Group. doi:10.1038/s41559-020-01378-9.

Grosberg, R.K., and Strathmann, R.R. 2007. The Evolution of Multicellularity: A Minor Major Transition? Annu. Rev. Ecol. Evol. Syst. **38**(1): 621–654. doi:10.1146/annurev.ecolsys.36.102403.114735.

Guern, M. 1962. EMBRYOLOGIE DE QUELQUES ESPÈCES DU GENRE *CYSTOSEIRA* Agardh 1821 (FUCALES). : 33.

Haas, B.J., Papanicolaou, A., Yassour, M., Grabherr, M., Blood, P.D., Bowden, J., Couger, M.B., Eccles, D., Li, B., Lieber, M., MacManes, M.D., Ott, M., Orvis, J., Pochet, N., Strozzi, F., Weeks, N., Westerman, R., William, T., Dewey, C.N., Henschel, R., LeDuc, R.D., Friedman, N., and Regev, A. 2013. De novo transcript sequence reconstruction from RNA-seq using the Trinity platform for reference generation and analysis. Nat Protoc **8**(8): 1494–1512. Nature Publishing Group. doi:10.1038/nprot.2013.084.

Hable, W.E. 2014. Rac1 signaling in the establishment of the fucoid algal body plan. Front. Plant Sci. **5**: 690. doi:10.3389/fpls.2014.00690.

Hamant, O., Heisler, M.G., Jönsson, H., Krupinski, P., Uyttewaal, M., Bokov, P., Corson, F., Sahlin, P., Boudaoud, A., Meyerowitz, E.M., Couder, Y., and Traas, J. 2008. Developmental Patterning by Mechanical Signals in *Arabidopsis*. Science **322**(5908): 1650–1655. American Association for the Advancement of Science. doi:10.1126/science.1165594.

Hamant, O., Inoue, D., Bouchez, D., Dumais, J., and Mjolsness, E. 2019. Are microtubules tension sensors? Nat Commun **10**(1): 2360. doi:10.1038/s41467-019-10207-y.

Hannezo, E., and Heisenberg, C.-P. 2019. Mechanochemical Feedback Loops in Development and Disease. Cell **178**(1): 12–25. doi:10.1016/j.cell.2019.05.052.

Harrison, C.J., Roeder, A.H.K., Meyerowitz, E.M., and Langdale, J.A. 2009. Local Cues and Asymmetric Cell Divisions Underpin Body Plan Transitions in the Moss *Physcomitrella patens*. Current Biology **19**(6): 461–471. doi:10.1016/j.cub.2009.02.050.

Heer, N.C., and Martin, A.C. 2017. Tension, contraction and tissue morphogenesis. Development **144**(23): 4249–4260. doi:10.1242/dev.151282.

Heidstra, R., and Sabatini, S. 2014. Plant and animal stem cells: similar yet different. Nat Rev Mol Cell Biol **15**(5): 301–312. Nature Publishing Group. doi:10.1038/nrm3790.

Herron, M.D., Borin, J.M., Boswell, J.C., Walker, J., Chen, I.-C.K., Knox, C.A., Boyd, M., Rosenzweig, F., and Ratcliff, W.C. 2019. De novo origins of multicellularity in response to predation. Scientific Reports **9**(1): 2328. Nature Publishing Group. doi:10.1038/s41598-019-39558-8.

Hong, L., Dumond, M., Tsugawa, S., Sapala, A., Routier-Kierzkowska, A.-L., Zhou, Y., Chen, C., Kiss, A., Zhu, M., Hamant, O., Smith, R.S., Komatsuzaki, T., Li, C.-B., Boudaoud, A., and Roeder, A.H.K. 2016. Variable Cell Growth Yields Reproducible Organ Development through Spatiotemporal Averaging. Developmental Cell **38**(1): 15–32. doi:10.1016/j.devcel.2016.06.016.

Hwang, E.K., Yotsukura, N., Pang, S.J., Su, L., and Shan, T.F. 2019. Seaweed breeding programs and progress in eastern Asian countries. Phycologia **58**(5): 484–495. doi:10.1080/00318884.2019.1639436.

Inkscape. 2022. Inkscape Project. Available from https://inkscape.org.

Izadi, M., Hou, W., Qualmann, B., and Kessels, M.M. 2018. Direct effects of Ca2+/calmodulin on actin filament formation. Biochemical and Biophysical Research Communications **506**(2): 355–360. doi:10.1016/j.bbrc.2018.07.159.

Jones, P., Binns, D., Chang, H.-Y., Fraser, M., Li, W., McAnulla, C., McWilliam, H., Maslen, J., Mitchell, A., Nuka, G., Pesseat, S., Quinn, A.F., Sangrador-Vegas, A., Scheremetjew, M., Yong, S.-Y., Lopez, R., and Hunter, S. 2014. InterProScan 5: genome-scale protein function classification. Bioinformatics **30**(9): 1236–1240. doi:10.1093/bioinformatics/btu031.

Karamanos, N.K., Theocharis, A.D., Piperigkou, Z., Manou, D., Passi, A., Skandalis, S.S., Vynios, D.H., Orian-Rousseau, V., Ricard-Blum, S., Schmelzer, C.E.H., Duca, L., Durbeej, M., Afratis, N.A., Troeberg, L., Franchi, M., Masola, V., and Onisto, M. 2021. A guide to the composition and functions of the extracellular matrix. The FEBS Journal **288**(24): 6850–6912. doi:10.1111/febs.15776.

Katsaros, C., and Galatis, B. 1992. Immunofluorescence and electron microscopic studies of microtubule organization during the cell cycle of *Dictyota dichotoma* (Phaeophyta, Dictyotales). Protoplasma **169**(1): 75–84. doi:10.1007/BF01343372.

Katsaros, C., Karyophyllis, D., and Galatis, B. 2006. Cytoskeleton and Morphogenesis in Brown Algae. Ann Bot **97**(5): 679–693. doi:10.1093/aob/mcl023.

Katsaros, Chr., and Galatis, B. 1985. Ultrastructural studies on thallus development in *Dictyota dichotoma* (Phaeophyta, Dictyotales). British Phycological Journal **20**(3): 263–276. Taylor & Francis. doi:10.1080/00071618500650271.

Katsaros, Chr., and Galatis, B. 1988. Thallus development in *Dictyopteris membranacea* (Phaeophyta, Dictyotales). British Phycological Journal **23**(1): 71–88. doi:10.1080/00071618800650091.

Katsaros, C.I. 1995. Apical cells of brown algae with particular reference to Sphacelariales, Dictyotales and Fucales. Phycological Research **43**(1): 43–59. doi:https://doi.org/10.1111/j.1440-1835.1995.tb00004.x.

Katsaros, C.I., Karyophyllis, D.A., and Galatis, B.D. 2002. Cortical F-actin underlies cellulose microfibril patterning in brown algal cells. Phycologia **41**(2): 178–183. doi:10.2216/i0031-8884-41-2-178.1.

Killian, K. 1911. Beiträge zur Kenntnis der Laminarien. Zeitschr. Bot. **3**: 433–494.

Klemm, M.F., and Hallam, N.D. 1987. Branching pattern and growth in *Cystophora* (Fucales, Phaeophyta). Phycologia **26**(2): 252–261. doi:10.2216/i0031-8884-26-2-252.1.

Kloareg, B., Badis, Y., Cock, J.M., and Michel, G. 2021. Role and Evolution of the Extracellular Matrix in the Acquisition of Complex Multicellularity in Eukaryotes: A Macroalgal Perspective. Genes **12**(7): 1059. Multidisciplinary Digital Publishing Institute. doi:10.3390/genes12071059.

Klochkova, T.A., Motomura, T., Nagasato, C., Klimova, A.V., and Kim, G.H. 2019. The role of egg flagella in the settlement and development of zygotes in two *Saccharina* species. Phycologia **58**(2): 145–153. Taylor & Francis. doi:10.1080/00318884.2018.1528804.

Knoll, A.H. 2011. The Multiple Origins of Complex Multicellularity. Annu. Rev. Earth Planet. Sci. **39**(1): 217–239. doi:10.1146/annurev.earth.031208.100209.

Kogame, Y., and Kawai, H. 1996. Development of the intercalary meristem in *Chorda filum* (Laminariales, Phaeophyceae) and other primitive Laminariales. Phycological Research **44**(4): 247–260. doi:10.1111/j.1440-1835.1996.tb00054.x.

Kohorn, B.D. 2016. Cell wall-associated kinases and pectin perception. Journal of Experimental Botany **67**(2): 489–494. doi:10.1093/jxb/erv467.

Koornneef, M., and Meinke, D. 2010. The development of *Arabidopsis* as a model plant. The Plant Journal **61**(6): 909–921. doi:10.1111/j.1365-313X.2009.04086.x.

Kropf, D.L., Bisgrove, S.R., and Hable, W.E. 2001. Establishing a Growth Axis in Fucoid Algae. *In* Branching in Nature. *Edited by* V. Fleury, J.-F. Gouyet, and M. Léonetti. Springer, Berlin, Heidelberg. pp. 87–97. doi:10.1007/978-3-662-06162-6_5.

Kuhlenkamp, R. 1996. New observations on the Tilopteridaceae (Phaeophyceae). II. Culture studies determine *Phaeosiphoniella* as an arctic species and crusts as systems for perennation and propagation. Phycologia **35**(3): 225–233. Taylor & Francis. doi:10.2216/i0031-8884-35-3-225.1.

Landrein, B., and Hamant, O. 2013. How mechanical stress controls microtubule behavior and morphogenesis in plants: history, experiments and revisited theories. The Plant Journal **75**(2): 324–338. doi:10.1111/tpj.12188.

Langmead, B., and Salzberg, S.L. 2012. Fast gapped-read alignment with Bowtie 2. Nat Methods **9**(4): 357–359. Nature Publishing Group. doi:10.1038/nmeth.1923.

Lardi, P.I., Varkitzi, I., Tsiamis, K., Orfanidis, S., Koutsoubas, D., Falace, A., and Salomidi, M. 2022. Early development of *Gongolaria montagnei* (Fucales, Phaeophyta) germlings under laboratory conditions, with a view to enhancing restoration potential in the Eastern Mediterranean. Botanica Marina. De Gruyter. doi:10.1515/bot-2021-0105.

Le Bail, A., and Charrier, B. 2013. Culture Methods and Mutant Generation in the Filamentous Brown Algae *Ectocarpus siliculosus*. *In* Plant Organogenesis: Methods and Protocols. *Edited by* I. De Smet. Humana Press, Totowa, NJ. pp. 323–332. doi:10.1007/978-1-62703-221-6_22.

Le Gloanec, C., Collet, L., Silveira, S.R., Wang, B., Routier-Kierzkowska, A.-L., and Kierzkowski, D. 2022. Cell type-specific dynamics underlie cellular growth variability in plants. Development **149**(14): dev200783. doi:10.1242/dev.200783.

LeGoff, L., and Lecuit, T. 2016. Mechanical Forces and Growth in Animal Tissues. Cold Spring Harb Perspect Biol **8**(3): a019232. doi:10.1101/cshperspect.a019232.

Leliaert, F., Smith, D.R., Moreau, H., Herron, M.D., Verbruggen, H., Delwiche, C.F., and De Clerck, O. 2012. Phylogeny and Molecular Evolution of the Green Algae. Crit. Rev. Plant Sci. **31**(1): 1–46. doi:10.1080/07352689.2011.615705.

Leptin, M. 1999. Gastrulation in *Drosophila*: the logic and the cellular mechanisms. The EMBO Journal **18**(12): 3187–3192. John Wiley & Sons, Ltd. doi:10.1093/emboj/18.12.3187.

Lewis, R.J., Green, M.K., and Afzal, M.E. 2013. Effects of chelated iron on oogenesis and vegetative growth of kelp gametophytes (Phaeophyceae). Phycological Research **61**(1): 46–51. doi:10.1111/j.1440-1835.2012.00667.x.

Li, B., and Dewey, C.N. 2011. RSEM: accurate transcript quantification from RNA-Seq data with or without a reference genome. BMC Bioinformatics **12**(1): 323. doi:10.1186/1471-2105-12-323.

Lin, W., Wang, Y., Coudert, Y., and Kierzkowski, D. 2021. Leaf Morphogenesis: Insights From the Moss *Physcomitrium patens*. Frontiers in Plant Science **12**. Available from https://www.frontiersin.org/article/10.3389/fpls.2021.736212 [accessed 5 May 2022].

Linardić, M., and Braybrook, S.A. 2017. Towards an understanding of spiral patterning in the *Sargassum muticum* shoot apex. Sci Rep **7**(1): 1–10. doi:10.1038/s41598-017-13767-5.

Liu, T., Wang, X., Wang, G., Jia, S., Liu, G., Shan, G., Chi, S., Zhang, J., Yu, Y., Xue, T., and Yu, J. 2019. Evolution of Complex Thallus Alga: Genome Sequencing of *Saccharina japonica*. Front. Genet. **10**. doi:10.3389/fgene.2019.00378.

Livanos, P., and Müller, S. 2019. Division Plane Establishment and Cytokinesis. Annu. Rev. Plant Biol. **70**(1): 239–267. doi:10.1146/annurev-arplant-050718-100444.

Lloyd, C.W. 1991. How does the cytoskeleton read the laws of geometry in aligning the division plane of plant cells? Development **113**(Supplement 1): 55–65.

Lockhart, J.A. 1965. An analysis of irreversible plant cell elongation. Journal of Theoretical Biology **8**(2): 264–275. doi:10.1016/0022-5193(65)90077-9.

Louveaux, M., Julien, J.-D., Mirabet, V., Boudaoud, A., and Hamant, O. 2016a. Cell division plane orientation based on tensile stress in *Arabidopsis thaliana*. Proc Natl Acad Sci USA **113**(30): E4294–E4303. doi:10.1073/pnas.1600677113.

Louveaux, M., Rochette, S., Beauzamy, L., Boudaoud, A., and Hamant, O. 2016b. The impact of mechanical compression on cortical microtubules in Arabidopsis: a quantitative pipeline. The Plant Journal **88**(2): 328–342. doi:10.1111/tpj.13290.

Lüning, K., and Dring, M.J. 1972. Reproduction induced by blue light in female gametophytes of *Laminaria saccharina*. Planta **104**(3): 252–256. doi:10.1007/BF00387080.

Márquez-Zacarías, P., Conlin, P.L., Tong, K., Pentz, J.T., and Ratcliff, W.C. 2021. Why have aggregative multicellular organisms stayed simple? Curr Genet **67**(6): 871–876. doi:10.1007/s00294-021-01193-0.

Marston, D.J., Anderson, K.L., Swift, M.F., Rougie, M., Page, C., Hahn, K.M., Volkmann, N., and Hanein, D. 2019. High Rac1 activity is functionally translated into cytosolic structures with unique nanoscale cytoskeletal architecture. PNAS **116**(4): 1267–1272. National Academy of Sciences. doi:10.1073/pnas.1808830116.

McCarthy, D.J., Chen, Y., and Smyth, G.K. 2012. Differential expression analysis of multifactor RNA-Seq experiments with respect to biological variation. Nucleic Acids Research **40**(10): 4288–4297. doi:10.1093/nar/gks042.

McCarthy, D.J., and Smyth, G.K. 2009. Testing significance relative to a fold-change threshold is a TREAT. Bioinformatics **25**(6): 765–771. doi:10.1093/bioinformatics/btp053.

Meyer, H.M., and Roeder, A.H.K. 2014. Stochasticity in plant cellular growth and patterning. Frontiers in Plant Science **5**. Available from https://www.frontiersin.org/articles/10.3389/fpls.2014.00420 [accessed 14 November 2022].

Minc, N., and Piel, M. 2012. Predicting division plane position and orientation. Trends in Cell Biology **22**(4): 193–200. doi:10.1016/j.tcb.2012.01.003.

Moody, L.A. 2020. Three-dimensional growth: a developmental innovation that facilitated plant terrestrialization. J Plant Res **133**(3): 283–290. doi:10.1007/s10265-020-01173-4.

Moss, B. 1967. The Apical Meristem of Fucus. New Phytologist: 67–74.

Moss, B. 1969. Apical Meristems and Growth Control in *Himanthalia elongata* (s. F. Gray). New Phytologist **68**(2): 387–397. doi:10.1111/j.1469-8137.1969.tb06451.x.

Moss, B. 1970. Meristems and Growth Control in *Ascophyllum nodosum* (l.) Le Jol. New Phytologist **69**(2): 253–260. doi:10.1111/j.1469-8137.1970.tb02423.x.

Moss, B., and Lacey, A. 1963. The Development of *Halidrys siliquosa* (L.) Lyngb. The New Phytologist **62**(1): 67–74. [Wiley, New Phytologist Trust].

Moss, B.L. 1950. Studies in the Genus Fucus : II. The Anatomical Structure and Chemical Composition of Receptacles of *Fucus vesiculosus* from Three Contrasting Habitats. Annals of Botany **14**(3): 395–410. doi:10.1093/oxfordjournals.aob.a083254.

Motomura, T., Nagasato, C., and Kimura, K. 2010. Cytoplasmic inheritance of organelles in brown algae. J Plant Res **123**(2): 185–192. doi:10.1007/s10265-010-0313-x.

Motomura, T., and Sakai, Y. 1984. Ultrastructural studies of gametogenesis in *Laminaria angustata* (Laminariales, Phaeophyta) regulated by iron concentration in the medium. null **23**(3): 331–343. Taylor & Francis. doi:10.2216/i0031-8884-23-3-331.1.

Moukhtar, J., Trubuil, A., Belcram, K., Legland, D., Khadir, Z., Urbain, A., Palauqui, J.-C., and Andrey, P. 2019. Cell geometry determines symmetric and asymmetric division plane selection in *Arabidopsis* early embryos. PLOS Computational Biology **15**(2): e1006771. doi:10.1371/journal.pcbi.1006771.

Nakahori, K., Katou, K., and Okamoto, H. 1991. Auxin Changes Both the Extensibility and the Yield Threshold of the Cell Wall of *Vigna* Hypocotyls. Plant Cell Physiol **32**(1): 121–129. doi:10.1093/oxfordjournals.pcp.a078046.

Nehr, Z., Chenivesse, S., Billoud, B., Genicot, S., Desban, N., Theodorou, I., Nasir, A., Bail, A.L., Rabillé, H., Godfroy, O., Katsaros, C., and Charrier, B. 2021, August 28. Tip growth in the brown alga *Ectocarpus* is controlled by a RHO-GAP-BAR domain protein independently from F-actin organisation. bioRxiv. doi:10.1101/2021.08.28.458042.

Niklas, K.J. 2014. The evolutionary-developmental origins of multicellularity. Am. J. Bot. **101**(1): 6–25. doi:10.3732/ajb.1300314.

Niklas, K.J., and Newman, S.A. 2013. The origins of multicellular organisms. Evolution & Development **15**(1): 41–52. doi:10.1111/ede.12013.

Niklas, K.J., and Newman, S.A. 2020. The many roads to and from multicellularity. Journal of Experimental Botany **71**(11): 3247–3253. doi:10.1093/jxb/erz547.

Paredez, A.R., Somerville, C.R., and Ehrhardt, D.W. 2006. Visualization of Cellulose Synthase Demonstrates Functional Association with Microtubules. Science **312**(5779): 1491–1495. American Association for the Advancement of Science. doi:10.1126/science.1126551.

Parke, M. 1948. Studies on British Laminariaceae. I. Growth in *Laminaria saccharina* (L.) Lamour. J. Mar. Biol. Ass. **27**(3): 651–709. doi:10.1017/S0025315400056071.

Peaucelle, A., Braybrook, S.A., Le Guillou, L., Bron, E., Kuhlemeier, C., and Höfte, H. 2011. Pectin-Induced Changes in Cell Wall Mechanics Underlie Organ Initiation in *Arabidopsis*. Current Biology **21**(20): 1720–1726. doi:10.1016/j.cub.2011.08.057.

Pleskot, R., Li, J., Žárský, V., Potocký, M., and Staiger, C.J. 2013. Regulation of cytoskeletal dynamics by phospholipase D and phosphatidic acid. Trends in Plant Science **18**(9): 496–504. Elsevier. doi:10.1016/j.tplants.2013.04.005.

Popper, Z.A., Michel, G., Hervé, C., Domozych, D.S., Willats, W.G.T., Tuohy, M.G., Kloareg, B., and Stengel, D.B. 2011. Evolution and Diversity of Plant Cell Walls: From Algae to Flowering Plants. Annual Review of Plant Biology **62**(1): 567–590. doi:10.1146/annurev-arplant-042110-103809.

Provasoli, L., and Carlucci, A.F. 1974. Vitamins and growth regulators. *In* Algal physiology and biochemistry. *Edited by* W. Stewart. Blackwell, Oxford. pp. 741–787.

Rabillé, H. 2018. Biophysical and cellular mechanisms of tip-growth in the brown alga *Ectocarpus* sp. Cellular Biology. Sorbonne Université (NNT : 2018SORUS597.): 242. doi:tel-02489811.

Rabillé, H., Billoud, B., Tesson, B., Panse, S.L., Rolland, É., and Charrier, B. 2019a. The brown algal mode of tip growth: Keeping stress under control. PLOS Biology **17**(1): e2005258. doi:10.1371/journal.pbio.2005258.

Rabillé, H., Koutalianou, M., Charrier, B., Katsaros, C., Koutalianou, M., Charrier, B., and Katsaros, C. 2018. Actin fluorescent staining in the filamentous brown alga *Ectocarpus siliculosus*. *In* Protocols for Macroalgae Research. Available from http://doi.org/10.1201/b21460-24 [accessed 23 January 2020].

Rabillé, H., Torode, T.A., Tesson, B., Le Bail, A., Billoud, B., Rolland, E., Le Panse, S., Jam, M., and Charrier, B. 2019b. Alginates along the filament of the brown alga *Ectocarpus* help cells cope with stress. Sci Rep **9**(1): 12956. doi:10.1038/s41598-019-49427-z.

Raimundo, S.C., Domozych, D.S., and Domozych, D.S. 2018. Probing the subcellular topography of seaweeds : Transmission electron microscopy, immunocytochemistry, and correlative light microscopy. *In* Protocols for Macroalgae Research. CRC Press. pp. 391–410. Available from DOI: 10.1201/b21460-26 [accessed 7 September 2020].

Ramon, E. 1973. Germination and Attachment of Zygotes of *Himanthalia elongata* (l.) S. F. Gray1. Journal of Phycology **9**(4): 445–449. doi:10.1111/j.1529-8817.1973.tb04119.x.

Robinson, M.D., McCarthy, D.J., and Smyth, G.K. 2010. edgeR: a Bioconductor package for differential expression analysis of digital gene expression data. Bioinformatics **26**(1): 139–140. doi:10.1093/bioinformatics/btp616.

Robinson, S. 2021. Mechanobiology of cell division in plant growth. New Phytologist **231**(2): 559–564. doi:10.1111/nph.17369.

Roeder, A.H.K., Chickarmane, V., Cunha, A., Obara, B., Manjunath, B.S., and Meyerowitz, E.M. 2010. Variability in the Control of Cell Division Underlies Sepal Epidermal Patterning in *Arabidopsis thaliana*. PLOS Biology **8**(5): e1000367. Public Library of Science. doi:10.1371/journal.pbio.1000367.

Saint-Marcoux, D., Billoud, B., Langdale, J.A., and Charrier, B. 2015. Laser capture microdissection in *Ectocarpus siliculosus*: the pathway to cell-specific transcriptomics in brown algae. Front Plant Sci **6**: 54. doi:10.3389/fpls.2015.00054.

Sampathkumar, A., Krupinski, P., Wightman, R., Milani, P., Berquand, A., Boudaoud, A., Hamant, O., Jönsson, H., and Meyerowitz, E.M. 2014a. Subcellular and supracellular mechanical stress prescribes cytoskeleton behavior in *Arabidopsis* cotyledon pavement cells. eLife **3**: e01967. doi:10.7554/eLife.01967.

Sampathkumar, A., Peaucelle, A., Fujita, M., Schuster, C., Persson, S., Wasteneys, G.O., and Meyerowitz, E.M. 2019. Primary wall cellulose synthase regulates shoot apical meristem mechanics and growth. Development **146**(10): dev179036. doi:10.1242/dev.179036.

Sampathkumar, A., Yan, A., Krupinski, P., and Meyerowitz, E.M. 2014b. Physical Forces Regulate Plant Development and Morphogenesis. Current Biology **24**(10): R475–R483. doi:10.1016/j.cub.2014.03.014.

Sarvepalli, K., Das Gupta, M., Challa, K.R., and Nath, U. 2019. Molecular cartography of leaf development — role of transcription factors. Current Opinion in Plant Biology **47**: 22–31. doi:10.1016/j.pbi.2018.08.002.

Schindelin, J., Arganda-Carreras, I., Frise, E., Kaynig, V., Longair, M., Pietzsch, T., Preibisch, S., Rueden, C., Saalfeld, S., Schmid, B., Tinevez, J.-Y., White, D.J., Hartenstein, V., Eliceiri, K., Tomancak, P., and Cardona, A. 2012. Fiji: an open-source platform for biological-image analysis. Nat Methods **9**(7): 676–682. Nature Publishing Group. doi:10.1038/nmeth.2019.

Sinnott, E.W. 1960. Plant morphogenesis. McGraw-Hill Book Compary, INC.

Sinnott, E.W., and Bloch, R. 1941. The Relative Position of Cell Walls in Developing Plant Tissues. American Journal of Botany **28**(7): 607–617. doi:10.1002/j.1537-2197.1941.tb10984.x.

Smith, A.I. 1939. The Comparative Histology of Some of the Laminariales. American Journal of Botany **26**(8): 571–585.

Sokhi, G., and Vijayaraghavan, M.R. 1987. Meristoderm in *Turbinaria conoides* (Fucales, Sargassaceae). Aquatic Botany **28**(2): 171–177. doi:10.1016/0304-3770(87)90038-6.

Spoerner, M., Wichard, T., Bachhuber, T., Stratmann, J., and Oertel, W. 2012. Growth and Thallus Morphogenesis of *Ulva mutabilis* (Chlorophyta) Depends on A Combination of Two Bacterial Species Excreting Regulatory Factors. J. Phycol. **48**(6): 1433–1447. doi:10.1111/j.1529-8817.2012.01231.x.

Spurr, A.R. 1969. A low-viscosity epoxy resin embedding medium for electron microscopy. Journal of Ultrastructure Research **26**(1): 31–43. doi:10.1016/S0022-5320(69)90033-1.

Starko, S., Soto Gomez, M., Darby, H., Demes, K.W., Kawai, H., Yotsukura, N., Lindstrom, S.C., Keeling, P.J., Graham, S.W., and Martone, P.T. 2019. A comprehensive kelp phylogeny sheds light on the evolution of an ecosystem. Molecular Phylogenetics and Evolution **136**: 138–150. doi:10.1016/j.ympev.2019.04.012.

Steeves, T.A., and Sussex, I.M. 1989. Patterns in plant development. *In* 2nd ed. Cambridge University Press, Cambridge [England] ; New York.

Steinbiss, H.-H., and Schmitz, K. 1974. Zur Entwicklung und funktionellen Anatomie des Phylloids von *Laminaria hyperborea*. Helgolander Wiss. Meeresunters **26**(2): 134–152. BioMed Central. doi:10.1007/BF01611380.

Sykes, M.G. 1908. Anatomy and Histology of *Macrocystis pyrifera* and *Laminaria saccharina*. Annals of Botany **os-22**(2): 291–325. doi:10.1093/oxfordjournals.aob.a089171.

Szymanski, D.B., and Cosgrove, D.J. 2009. Dynamic Coordination of Cytoskeletal and Cell Wall Systems during Plant Cell Morphogenesis. Current Biology **19**(17): R800–R811. doi:10.1016/j.cub.2009.07.056.

Tanaka, A., Hoshino, Y., Nagasato, C., and Motomura, T. 2017. Branch regeneration induced by sever damage in the brown alga *Dictyota dichotoma* (Dictyotales, Phaeophyceae). Protoplasma **254**(3): 1341–1351. doi:10.1007/s00709-016-1025-4.

Theißen, G., Melzer, R., and Rümpler, F. 2016. MADS-domain transcription factors and the floral quartet model of flower development: linking plant development and evolution. Development **143**(18): 3259–3271. doi:10.1242/dev.134080.

Theodorou, I., and Charrier, B. 2021. Brown Algae: *Ectocarpus* and *Saccharina* as Experimental Models for Developmental Biology. *In* Handbook of Marine Model Organisms in Experimental Biology. *Edited by* A. Boutet and B. Schierwater. CRC Press. pp. 27–46. Available from https://doi.org/10.1201/9781003217503.

Theodorou, I., Opsahl-Sorteberg, H.-G., and Charrier, B. 2021. Preparation of Zygotes and Embryos of the Kelp *Saccharina latissima* for Cell Biology Approaches. Bio-101: e4132. Bio-protocol LLC. doi:10.21769/BioProtoc.4132.

Torode, T.A., Siméon, A., Marcus, S.E., Jam, M., Le Moigne, M.-A., Duffieux, D., Knox, J.P., and Hervé, C. 2016. Dynamics of cell wall assembly during early embryogenesis in the brown alga *Fucus*. Journal of Experimental Botany **67**(21): 6089–6100. doi:10.1093/jxb/erw369.

Tran, D., Galletti, R., Neumann, E.D., Dubois, A., Sharif-Naeini, R., Geitmann, A., Frachisse, J.-M., Hamant, O., and Ingram, G.C. 2017. A mechanosensitive Ca 2+ channel activity is dependent on the developmental regulator DEK1. Nat Commun **8**(1): 1009. doi:10.1038/s41467-017-00878-w.

Trinh, D.-C., Alonso-Serra, J., Asaoka, M., Colin, L., Cortes, M., Malivert, A., Takatani, S., Zhao, F., Traas, J., Trehin, C., and Hamant, O. 2021. How Mechanical Forces Shape Plant Organs. Current Biology **31**(3): R143–R159. doi:10.1016/j.cub.2020.12.001.

Tsirigoti, A., Küpper, F.C., Gachon, C.M.M., and Katsaros, C. 2014. Cytoskeleton organisation during the infection of three brown algal species, *Ectocarpus siliculosus*, *Ectocarpus crouaniorum* and *Pylaiella littoralis*, by the intracellular marine oomycete *Eurychasma dicksonii*. Plant Biology **16**(1): 272–281. doi:10.1111/plb.12041.

Umen, J.G. 2020. Volvox and volvocine green algae. EvoDevo **11**(1): 13. doi:10.1186/s13227-020-00158-7.

Verma, S., Attuluri, V.P.S., and Robert, H.S. 2022. Transcriptional control of *Arabidopsis* seed development. Planta **255**(4): 90. doi:10.1007/s00425-022-03870-x.

Vlad, D., Kierzkowski, D., Rast, M.I., Vuolo, F., Dello Ioio, R., Galinha, C., Gan, X., Hajheidari, M., Hay, A., Smith, R.S., Huijser, P., Bailey, C.D., and Tsiantis, M. 2014. Leaf Shape Evolution Through Duplication, Regulatory Diversification, and Loss of a Homeobox Gene. Science **343**(6172): 780–783. doi:10.1126/science.1248384.

Vőfély, R.V., Gallagher, J., Pisano, G.D., Bartlett, M., and Braybrook, S.A. 2019. Of puzzles and pavements: a quantitative exploration of leaf epidermal cell shape. New Phytologist **221**(1): 540–552. doi:10.1111/nph.15461.

Williamson, R.E. 1990. Alignment of Cortical Microtubules by Anisotropic Wall Stresses. Functional Plant Biol. **17**(6): 601–613. CSIRO PUBLISHING. doi:10.1071/pp9900601.

Wu, T., Hu, E., Xu, S., Chen, M., Guo, P., Dai, Z., Feng, T., Zhou, L., Tang, W., Zhan, L., Fu, X., Liu, S., Bo, X., and Yu, G. 2021. clusterProfiler 4.0: A universal enrichment tool for interpreting omics data. Innovation **2**(3). Elsevier. doi:10.1016/j.xinn.2021.100141.

Xu, X., Smaczniak, C., Muino, J.M., and Kaufmann, K. 2021. Cell identity specification in plants: lessons from flower development. Journal of Experimental Botany **72**(12): 4202–4217. doi:10.1093/jxb/erab110.

Yendo, K.R. 1911. The Development of *Costaria*, *Undaria*, and *Laminaria*. Ann Bot **os-25**(3): 691–716. Oxford Academic. doi:10.1093/oxfordjournals.aob.a089349.

Yonamine, R., Ichihara, K., Tsuyuzaki, S., Hervé, C., Motomura, T., and Nagasato, C. 2021. Changes in Cell Wall Structure During Rhizoid Formation of *Silvetia babingtonii* (Fucales, Phaeophyceae) Zygotes. Journal of Phycology **57**(4): 1356–1367. doi:10.1111/jpy.13178.

Zeng, Q., Liu, H., Chu, X., Niu, Y., Wang, C., Markov, G.V., and Teng, L. 2022. Independent Evolution of the MYB Family in Brown Algae. Frontiers in Genetics **12**. Available from https://www.frontiersin.org/article/10.3389/fgene.2021.811993 [accessed 1 June 2022].

Zhang, L., and Ambrose, C. 2022. CLASP balances two competing cell division plane cues during leaf development. Nat. Plants: 1–12. Nature Publishing Group. doi:10.1038/s41477-022-01163-5.

Zhang, Q.S., Qu, S.C., Cong, Y.Z., Luo, S.J., and Tang, X.X. 2008. High throughput culture and gametogenesis induction of *Laminaria japonica* gametophyte clones. J Appl Phycol **20**(2): 205–211. doi:10.1007/s10811-007-9220-5.

Zhang, Z., Runions, A., Mentink, R.A., Kierzkowski, D., Karady, M., Hashemi, B., Huijser, P., Strauss, S., Gan, X., Ljung, K., and Tsiantis, M. 2020. A WOX/Auxin Biosynthesis Module Controls Growth to Shape Leaf Form. Current Biology **30**(24): 4857-4868.e6. doi:10.1016/j.cub.2020.09.037.

Zhao, F., Chen, W., and Traas, J. 2018. Mechanical signaling in plant morphogenesis. Current Opinion in Genetics & Development **51**: 26–30. doi:10.1016/j.gde.2018.04.001.

Zhao, F., Du, F., Oliveri, H., Zhou, L., Ali, O., Chen, W., Feng, S., Wang, Q., Lü, S., Long, M., Schneider, R., Sampathkumar, A., Godin, C., Traas, J., and Jiao, Y. 2020. Microtubule-Mediated Wall Anisotropy Contributes to Leaf Blade Flattening. Current Biology **30**(20): 3972-3985.e6. doi:10.1016/j.cub.2020.07.076.

Zonia, L., Müller, M., and Munnik, T. 2006. Hydrodynamics and cell volume oscillations in the pollen tube apical region are integral components of the biomechanics of *Nicotiana tabacum* pollen tube growth. Cell Biochem Biophys **46**(3): 209–232. doi:10.1385/CBB:46:3:209.

Zonia, L., and Munnik, T. 2007. Life under pressure: hydrostatic pressure in cell growth and function. Trends in Plant Science **12**(3): 90–97. Elsevier. doi:10.1016/j.tplants.2007.01.006.

Related Publications

Boscq S, Dutertre S, **Theodorou I**, Charrier B. (2022). Targeted Laser Ablation in the Embryo of *Saccharina latissima*. JoVE (Journal of Visualized Experiments) e63518. DOI: 10.3791/63518

Theodorou I, Kovi MR, Liang Z, Opsahl-Sorteberg H-G. (2022). Genetic and Genomic Approaches for Improved and Sustainable Brown Algal Cultivation. In: "Sustainable Global Resources of Seaweeds Volume 2: Food, Pharmaceutical and Health Applications". *Springer International Publishing*. DOI: 10.1007/978-3-030-92174-3_33

Theodorou I, Charrier B. (2021) Brown algae *Ectocarpus* and *Saccharina* as experimental models for developmental biology. In: "Established and emerging marine organisms in experimental biology". *CRC Press*. DOI: 10.1201/9781003217503

Nehr, Z, Chenivesse, S, Billoud, B, Genicot, S, Desban, N, **Theodorou, I.**, et al. (2021) Tip growth in the brown alga *Ectocarpus* is controlled by a RHO-GAP-BAR domain protein independently from F-actin organisation. *bioRxiv* 2021.08.28.458042; DOI: 10.1101/2021.08.28.458042

Theodorou I, Opsahl-Sorteberg H-G, Charrier B. (2021) Preparation of zygotes and embryos of the kelp *Saccharina latissima* for cell biology approaches. *Bio-101*: e4132. DOI: 10.21769/BioProtoc.4132

Conferences and meetings

Theodorou I, Milstein R, Boscq S, Charrier B. (2022) Cell structure during grid morphogenesis in the brown alga species *Saccharina latissima*, **2nd International Symposium on quantitative Plant Morphodynamics Plant Growth & Form 2022**, Heidelberg, Germany. (Poster)

Theodorou I, Billoud B, Boscq S, Opsahl-Sorteberg H-G, Charrier B. (2022) Key cell and tissue features during embryogenesis in brown alga *Saccharina latissima* **29th Scandinavian Plant Physiology Society Conference**, Longyearbyen, Svalbard, Norway. (Poster)

Theodorou I, Lian Z, Fletcher J.C, Cock J. M, Opsahl-Sorteberg H-G. (2022) Brown algae as models to study multicellularity and the evolutionary origin of meristems **29th Scandinavian Plant Physiology Society Conference**, Longyearbyen, Svalbard, Norway. (Poster)

Boscq S, Dutertre S, Billoud B, **Theodorou I**, Charrier B. (2022) Role of the maternal tissue in the establishment of the polarity axes in the early embryo of the brown alga *Saccharina latissima*, **Euro Evo Devo conference 2022**, Napoli, Italy. (Short talk)

Theodorou I, Canto P-Y, Charrier B. (2022) Laser capture microdissection of key regions in the embryonic blade of the brown alga *Saccharina latissima*. **Journées du réseau André Picard** (JAP2022), Villefranche/Mer, 24-25 March 2022 (Short talk)

Billoud B, **Theodorou I**, Boscq S, Sellin G, Godin C, Charrier B. (2022) Modelling the force-driven early morphogenesis in the brown alga *Saccharina latissima,* **Journées du réseau André Picard** (JAP2022), Villefranche/Mer, 24-25 March 2022 (Short talk)

Boscq S, **Theodorou I**, Billoud B, Le Panse S., Opsahl-Sorteberg H-G, Charrier B (2021) Establishment of growth and polarity axes in the early embryo of the brown alga *Saccharina latissima*, **Shaping Life 2**, SFBD conference. (Poster)

Theodorou I, Billoud B, Le Panse S Opsahl-Sorteberg H-G, Charrier B. (2021) Grid patterning on the embryonic lamina of the brown alga *Saccharina latissima*, **Shaping Life 2**, SFBD conference. (Web Short talk)

Theodorou I, Billoud B, Boscq S, Le Panse S., Opsahl-Sorteberg H-G., Charrier B. (2021) Grid patterning on the embryonic lamina of the brown alga *Saccharina latissima*, **Journées du reseau André Picard** (JAP2021). (Web Short talk)

Boscq S, **Theodorou I**, Billoud B, Le Panse S, Charrier B**.** (2021) Establishment of growth and polarity axes in the early embryo of the brown alga *Saccharina latissima* **Journées du reseau André Picard** (JAP2021). (Web Short talk)

Charrier B., **Theodorou I**., Billoud B., Boscq S, Opsahl-Sorteberg H-G. (2020) Embryo patterning in the brown alga *Saccharina*. **Laboratory Plant Reproduction & Developmen**t (RDP), ENS-Lyon, France (Webinar)

Theodorou I, Billoud B, Rolland E, Opsahl-Sorteberg H-G, Charrier B (2019) Planar patterning in the brown alga *Saccharina latissima*. **CENTURI Scientific meeting 2019**, Cargèse, France. (Poster)

Papers

Paper I: Making a monolayer lamina with aligned cuboid cells: the case of the embryo of the brown alga *Saccharina*

State of publication: In preparation

Contributions: This manuscript was written mainly by B. Charrier and B. Billoud; I acquired all the experimental data and participated in their analysis and interpretation as well as in the writing of the article, especially concerning the experimental part and the figures.

Title: Making a monolayered lamina with aligned cuboid cells: the case of the embryo of the brown alga *Saccharina*

Authors: Ioannis Theodorou[1,2]*, Bernard Billoud[1]*, Samuel Boscq[1], Christophe Godin[3], Sophie Le Panse[4], Bénédicte Charrier[1$]

* co-first author

[$]author for correspondence

Affiliations

[1] Laboratory of Integrative biology of marine models (LBI2M), UMR8227, CNRS and Sorbonne University, 29 680, Roscoff, France

[2] Plant Sciences Department, Faculty of Biosciences, Norwegian University of Life Sciences, Ås, Norway

[3] Merimage Platform, FR2424, Station Biologique, 29680 Roscoff, France

[4] Laboratory of Plant reproduction and development, Univ Lyon, ENS de Lyon, UCB Lyon1, CNRS, INRAE, INRIA, 69342 Lyon, France

Abstract

The embryo of the brown alga *Saccharina* develops a monolayer lamina in the early stages. This lamina emerges at the ~ 20-cell stage and thickens at the ~ 500-cell stage. During the monolayer stage, the cells are cuboids arranged in rows and columns, forming a cellular grid. Using a 2D vertex model, we aimed to simulate the development of this monolayer lamina up to the 128-cell stage. The model was based on the visco-plastic properties of the cell wall for cell expansion, and on Errera's rule for cell division. Continuous monitoring of embryo development provided quantitative parameters on cell shape, size and growth dynamics. The results showed that while the arrangement of cells in a grid emerged from the simulation with isotropic mechanical properties, the simulation of the embryo shape required mechanical anisotropy in the apico-basal *vs* medio-lateral axes of the embryo. The model was robust to stochastic turgor and timing of cell division induction, as well as stochastic position and orientation of the cell division plane, in a range consistent with the live observations. This study provides a mechanistic model explaining the dynamic formation of the shape and tissue pattern of a kelp embryo that involves longitudinal and transverse mechanical anisotropy. We discuss the potential underlying cellular organisation that could support both mechanical anisotropy and the Errera's cell division rule in the context of brown algae cells.

Introduction

Brown algae are conspicuous marine organisms thriving along all the coastlines of our planet, where they serve as food sources and shelters for many marine animals, and structure the coastal ecosystem in which they are the main primary producers (Pessarrodona et al., 2022). Kelps are large brown algae of the order Laminariales, making most of this brown coastal bar often real forests up to 40-50 meters high. Surprisingly, knowledge about the mechanisms of embryogenesis of these brown algae is very scarce. Early 20th century phycologists Harold Drew (1910) and Karl Killian (1911) provided preliminary descriptions of the main characteristics of a kelp embryo: the kelp embryo is a lamina (also named a blade) that that has two main characteristics: 1) the lamina consists of a monolayered, pear shaped cell sheet that grows vertically in the sea water. In the early stages, it is attached to the maternal gametophyte in its lower part, from which the egg was produced. 2) The lamina consists of cuboid cells aligned in rows and columns, forming a grid where each cell corner is shared by three other cells, creating what are called four-way junctions (4WJ) (Fig. 1A,B).

This original tissue patterning is extremely rare in the tree of life. Typically, a sheet of isotropic cells spontaneously tends towards 5- to 7- sided polygons (e.g. Staple et al. 2010 for *Drosophil*a, and Corson et al. 2009 for *Arabidopsi*s) of angles 51-72° angles. Viewed in a plane, these polygons connect to each other by 3-way junctions (3WJ; Fig. 1B). However, other patterns can be observed if mechanical forces constrain the formation and maintenance of a cell shape different from a 6-sided polygon. For example, 4WJ are formed in the *Drosophila* epidermis with altered myosin dynamics (mutant PTEN, Bardet *et al.*, 2013). Due to the presence of a cell wall preventing tissue sliding or cell migration, plant tissues correspond to an extreme case where cell wall mechanics is a prevailing parameter impacting cell expansion and cell division, and ultimately, the resulting sheet pattern. In these organisms, 3WJ of 5-7 sided cells are also the norm of cell layers. However, in some tissues such as those in plant roots, the cells are cuboids organised in staggered rows, connected by “T”-shaped 3WJs (Fig. 1B). Interestingly, D’Arcy Thompson (1942) (Thompson and Thompson, 1942) observed that this conformation is not even maintained and that the “T”-shaped junction gradually drifts into a “Y”-shape 3WJ as the side walls of the cell fold (Fig. 1B) (Lloyd, 1991). A reason why plants do not possess 4WJs is the selection by plants of a specific mechanism avoiding their formation, called 4WJ avoidance (Lloyd, 1991; Rasmussen & Bellinger, 2018).

The question of the formation of 4WJs takes on a particular twist in the context of brown algae, which have unique characteristics. First, in the group of Stramenopiles, brown algae are the only complex multicellular organisms and they emerged relatively recently, 250 millions years ago, compared to animals and plants (Starko, 2019). Secondly, the Stramenopiles diverged at the root of the eukaryotic tree. As a result, brown algae evolved independently from the Opisthokonta (animals and fungi) and the Archaeplastida (land plants, red and green algae). Then, thanks to this particular evolution, the cells of brown algae acquired an original cellular organisation and composition : their cell wall is largely made of alginates and fucans, two polysaccharides that engulf a low percentage of cellulose (Charrier *et al.*, 2019).

In addition, they display intracellular components specific to animal cells, such centrosomes, cortical actin filaments (Katsaros et al., 2006) and integrins (Cock *et al.*, 2010). Thirdly, they generally grow in a fairly buffered fluid environment, limiting the mechanical stresses applied to their bodies, especially at the embryogenic stage. For example, the monolayered blade of *Saccharina* grows vertically in the sea water and therefore, planar growth is independent of any contact with a solid surface. In addition, the lamina is symmetrical on both sides, which consequently perceive the same external cues.

Therefore, overall, the monolayer cell sheet of *Saccharina* embryo is an exceptional opportunity to attempt to identify the basic mechanisms linking the orientation of cell division to the shape of an embryo. Here, we aimed to identify the intrinsic mechanical constraints that can account for the shape of the embryo together with the correct tissue pattern of the kelp *Saccharina latissima*.

Results

The development of the Saccharina embryo begins with a long period of diffuse and undifferentiated growth in a single plane

Since the static observation of H. Drew more than one century ago (Drew, 1910), no one has looked into the formation of 4WJs in the embryo of the kelp *Saccharina*. Therefore, we grew and monitored 14 embryos of *S. latissima* every 12 or 24 hours for up to 10 days (Suppl Fig. 1). All embryos were included in the analysis, even those that stopped growing or were out of focus before the end of the monitoring period. Based on this experience and the literature, we divided *Saccharina* embryogenesis into four main phases, all related to the orientation of cell divisions (Fig. 2). After fertilisation (Fig. 2, left), embryogenesis is initiated by the elongation of the zygote and a first anticlinal, transverse cell division. Each of the two daughter cells divides again with cell divisions parallel to the first one. As each daughter cell divides again, a stack of ~ 8 cells is formed. This defines Phase I, which extends from fertilisation of the egg to the formation of a stack of ~ 8 cells aligned along a longitudinal apico-basal axis (1D). Phase II is initiated by the tilting of the division plane by 90° (Fig. 2, centre). As a result, the embryo establishes a second – medio-lateral – axis (2D). The cells continue to divide transversely and longitudinally, until an embryo of about 1000 cells is formed. It consists of a monolayer cell sheet with a pear-shaped body. Cell patterning within this sheet depicts a grid pattern with 4WJs (Fig. 1A and Fig. 2, centre). At the end of Phase II, the lamina starts to thicken in the Z-axis by periclinal cell divisions (Theodorou & Charrier, in prep; Chapter IV of this thesis) while growth continues in the X and Y axes. Further variation in the orientation of the cell divisions leads to the loss of the grid pattern. At the same time, cells start to differentiate and specific tissues emerge. This is Phase III (Fig. 2). After that stage, the development of the embryo becomes more complex, with the emergence of specific tissues and organs. Phase IV is characterised by a fully polystromatised thallus and the emergence of a holdfast. It leads juvenile embryos of about 3 mm in length to the adult stage of up to 3 meters in length (Fig. 2, right). Phases I and II define early embryogenesis in which most cells are undifferentiated and align in rows and columns to form a monolayered lamina.

The length (X-axis), width (Y-axis) and surface area of these laminae were measured over time from time-lapse photographs. Interestingly, while the number of cells and the surface area of the embryos increase with time (Fig. 3A), the shape, expressed as the Length / Width ratio (*LWR*), is constant at a value of about 3 until at least the 128 cell stage (Fig. 3B). This indicates that the elongated shape of the embryo is maintained over time, and that growth is isotropic. Longer observations showed that this property is maintained even further into development (not shown).

The embryogenetic Phase II is monotonous

Bright field photographs shown in Suppl Fig. 1 were segmented manually to obtain the cell contours (Suppl Fig. 2). The length, width and surface area of the cells were measured from these segmented embryos. The Length / Width ratio was used as an indicator of cell shape. Fig. 4A shows that most of the cells are rectangular cuboids, the shape of which varies within the embryos. Ratios range from 1 (square cells) to ~ 3 (very elongated cells), with an average of 1.47, and it is reasonable to assume that this range reflects the alternation of shapes resulting from successive cycles of cell division. Whatever the reason, all possible cell shapes in this range are distributed homogeneously within the lamina, reflecting homogeneous cell growth and cell division dynamics in the embryo at that stage. A similar distribution of cell shapes was observed in earlier stages of Phase II embryos (not shown). The distribution of cell sizes within the blade is also monotonous, although it varies significantly between embryos. Nevertheless, all cells occupy a surface area of ~ 89 ± 32.3 μm^2(Fig. 4B). Finally, cells divide in average once every 12 hours with little variation within and between embryos (Fig. 4C). Therefore, cell shape, size and mitotic activities are very homogeneous within and between embryos (with the exception of cell size, where two embryos differ significantly). This reflects a monotonous cell growth behaviour characteristic of diffuse growth.

Segmentation of bright-field photos also displayed that in Phase II embryos, the monolayer cell sheet is arranged with cells aligned in rows and columns (Fig. 1A; Suppl Fig. 2). To quantitatively characterise the grid, we counted the number of neighbouring cells surrounding each cell. The average number of neighbouring cells starts with a low value close to 2 (Fig. 4D), because in Phase I, each cell has two neighbouring cells, unless it is located at the ends of the 8-cell stack where it has only one. Further cell divisions result in a larger number of cells located inside the lamina and without contact with the edges. In this case, if the inner cells were arranged in a perfect grid, the number of neighbouring cells sharing a common edge would be 4. If the cells were staggered or honeycombed, each inner cell would have 6 neighbours. Fig. 4D shows that most of the embryos have cells with 4 neighbours, yet with variations. This is in agreement with the microscopy pictures showing a grid in most of the laminas but also some 3WJs in the most apical and basal areas (Fig. 1A; Suppl Figs 1 & 2).

Interestingly, the analysis of the position of the cell division planes shows that, on average, the cell division is almost equal (Fig. 4E), with a slight shift of about 0.04 unit from 0.5 which corresponds to the middle of the cell. The dispersion around this value is small as it belongs to the interval [0.51; 0.56].

Finally, to assess when, in terms of size, the cells divide, we calculated the Perimeter / Area ratio (called here Exchange ratio) of each cell before and after cell division. We observed that this ratio, which depends not only on the cell size (a large cell has a smaller ratio than a small cell of the same shape), but also on the cell shape (for cells of same volume, an elongated cell has a smaller ratio than a spherical cell), tends towards 0.35 (Fig. 4F). This value indicates when a cell enters cell division at the latest in its growth curve.

In summary, during Phase II, the lamina grows isotropically, with anisotropic cuboid cells of similar shape, surface area and growth rate within each lamina. They divide almost equally and enter cell division when they have grown sufficiently to reach a Perimeter / Surface area ratio close to 0.40. Although these parameters are fairly evenly distributed within a lamina, they vary between embryos.

To complete our mapping of the cell features, we assessed the thickness of the cell wall over time. We measured the thickness at different locations on TEM sections of *Saccharina* embryos cut along longitudinal axes (both frontal and median). We observed that the outer cell wall was thicker than the inner walls. This is expected as the outer cell wall forms immediately after egg fertilisation whereas the inner walls form successively as the zygote begins to divide and the Phase I embryos continue to develop. We plotted cell wall measurements against time to infer the dynamics of outer and inner cell wall thickening (Fig. 5). When the embryo was large of 2 cells, the outer cell wall was already ~ 300 nm thick, and its thickness increased at a rate of 3 $nm \cdot h^{-1.}$ In contrast, the first inner cell walls were ~ 150 nm thick and increased by 0.6 $nm \cdot h^{-1}$. Therefore, during embryo growth, the outer cell wall seems to thicken more rapidly than the inner walls.

An isotropic 2D vertex models simulates the grid pattern in the lamina

A widely used class of models for embryogenesis studies is the Vertex Models (VM) (Ali *et al.*, 2014; Fletcher *et al.*, 2013). In plant tissues, VMs explicitly represent cell wall segments as edges, connecting nodes that mostly represent 3WJs or 4WJs. VMs implement tissue dynamics through the integration of forces and vertex displacements, intended to model the natural energy minimisation performed by tissues, as a result of their structure and expansion/division mechanisms. We implemented a 2D VM to simulate the growth of the embryo monolayer cell sheet of *Saccharina.* Complete description, equations and assumptions of the model are given in Supplementary material – A. Vertex Model.

All the characteristics of the blade that could be measured were used as model parameters: the thickness of the blade was estimated to be 12 µm from 3D reconstruction of microscopy experiments (not shown). Time-lapse observations showed that the blades reached 128 cells after 168 h. Turgor was considered to be re-equilibrated every hour to its basal value. A value of 0.5 MPa was given based on the measurement in the brown alga *Ectocarpus* (Rabillé et al., 2019a). The dynamics of cell wall thickening (Fig. 5 described above) was included in the model. Based on our observation of the distribution of the cell exchange ratios over time (Fig. 4F), we set the threshold for cells to enter cell division at 0.35 μm^{-1}. The starting point for all the simulations is an 8-cell embryo designed from the average

dimensions observed at this stage (Suppl Figs 1 & 2). In particular, this embryo had a *LWR* of 3.05.

The elastic modulus of the cell walls was used as a free parameter adjusted so that the cell growth rate could match the observations. Test runs of the simulation using various values showed that *E* = 2905 MPa allowed to render the proper growth rate (Fig. 6A-C, and Movie 1). However, compared to the observations, the shape and architecture of the simulated blade were not correctly rendered (Fig. 6D): while in the observed blades, the LWR was kept above 3, in the simulations it dropped rapidly, independently of the value of *E*. The grid pattern, characterised by the average number of neighbouring cells, was better reproduced with all values of *E* tested (Fig. 6E). Therefore, a majority of 4WJs have emerged from this physical model without the need for a promoting mechanism. However, it cannot be stated that the grid arrangement of the cells is independent of the overall shape of the blade. Therefore, in order to ensure that the grid pattern also emerges in the more elongated blades, the model had to be refined.

The embryos are mechanically anisotropic

To improve the shape of the simulated embryo, we first investigated whether living embryos display mechanical anisotropy. In seawater, cells of brown algae are under turgor (Hurd et al., 2014; Wright & Reed, 1988; Rabillé et al., 2019a) and the cells are expected to shrink when immersed in a solution with a much higher osmotic pressure than the sea water. We investigated whether, when immersed in a solution of seawater (1100 mosmol ~ 2.4 MPa) supplemented with 1660 mosmol of sucrose, laminas shrink homogeneously in the X-orientation compared to the Y- orientation, or if instead, they retract differently in one of the two axes. We first addressed this question at the tissue level, i.e at the level of the lamina. We measured the length and width of 13 embryos before and after immersion in the hyper-osmotic solution (Fig. 7A), and observed that in response to this treatment, the embryos shrank in average 8.0% in the X-axis while only of 6.4% in the Y-axis (t-test, P-value 0.022). Among the 13 embryos, only 11 shrank, while two expanded (Fig. 7B). This illustrates that the response of the embryos to this treatment is heterogeneous. The percentage of shrinkage of the laminas of these 11 specimen was 8.4% in X- vs 6.1 in Y- axis (t-test P value 0.004).

We then verified that this response was similar at the cellular level. The X and Y dimensions of each cell in three embryos were measured. We observed that, like whole laminas, the cells shrink more in the X orientation than in the Y orientation (Fig. 7C). The cells are rectangular cuboids that can be oriented vertically or horizontally in the vertical lamina (i.e. with their longest axis either along the X axis or the Y-axis of the lamina respectively). Interestingly, the anisotropic shrinkage response was independent of the orientation of the cells in the blade (Fig. 7C). Furthermore, although some heterogeneity in the shrinkage response was observed among the cells, it was not related to specific areas of the lamina, such as bottom versus top or margin versus centre (not shown). It is not known whether this response is due to the mechanical anisotropy of the outer or the inner cell walls. This question will be investigated by simulation.

The mechanical anisotropy of the embryos accounts for the shape of the lamina

The observed mechanical anisotropy can be explained by introducing an angular anisotropy of E on the cell walls. This is done by tuning the Elastic Modulus *E* in (i) the outer wall or (ii) the inner walls, depending on their angle with the main axis of the blade.

The angular anisotropy for the outer cell wall *E* (E_o) was obtained by adding to the central value of *E* a local offset proportional to the cosine of the angle of the piece of cell wall with the blade main axis. The amplitude of this variation was set by a parameter called V_O, computed so that $V_O > 1$ (respectively $V_O < 1$) means that the longitudinal outer walls (along the X-axis of the lamina) are softer (respectively stiffer) than the transversal outer walls (along the Y-axis of the lamina). Results showed that in the range 1/5 - 5, V_O did not significantly increase the *LWR* of the blade (Fig. 8A,B, and Movie 2). The mean number of neighbouring cells was also not affected (Fig. 8C), except for the lowest value $V_O = 1/5$ which fluctuates beyond the standard deviation of the observed values.

Similarly to the outer cell wall, we applied an angular variation to the inner cell walls, tuned by the parameter V_I. In this case, high values of V_I allow the simulated blade to reach a high LWR, although not sufficient to mimic the observations (Fig. 8D,E, and Movie 3). For the extreme value $V_I = 1/5$, the grid pattern was affected, but for all other values, the average number of neighbouring cells remained close to the observations (Fig. 8F).

We also tested the impact of a difference in *E* between the outer and the inner walls by modulating the ratio E_O/E_I, E_O and E_I being the *E* of the outer and the inner cell walls respectively. In the same time, both values were adjusted to match the chosen ratio while keeping a correct growth rate. Results showed that the softer the outer cell wall with respect to the inner cell walls (*i.e.* lower E_O/E_I ratio), the higher the *LWR* of the blade (Fig. 9A,B, and Movie 4). For $E_O/E_{I\,\text{ratio}} = 1/5$, the *LWR* has reached the expected level. Note that in this case, the very low E_O results in a local deformation of the blade with protruding cells. Except for the highest value of the ratio ($E_O/E_I = 5$), the average number of neighbouring cells remained close to the observations (Fig. 9C).

As two unequal distributions of Elastic Modulus resulted in a change in the blade shape, we used them simultaneously to find an optimal combination. We compared the outcome of the pairs (V_I, E_O/E_I), and challenged their ability to reproduce the observations. Each simulation was evaluated using a combination of three parameters: (i) Blade *LWR*, (ii) Mean *LWR* of all cells in each blade and (iii) Blade convexity (see Supplementary material – A. Vertex Model for computation details). Minimisation of the discrepancy between simulations and observations was done in three steps (see Suppl. Figs. 3-5) to obtain an optimal combination of parameters: $V_I = 2.25$ and $E_O/E_I = 0.45$ (Suppl Fig. 5, Fig. 10 and Movie 5).

The model is robust to a low level of stochasticity

Although adjusting the Elastic Modulus led to satisfactory results in terms of blade shape and dynamics, the deterministic nature of the model did not allow to account for inter-individual variability in development. To explore the effect of less tightly tuned physical conditions, we included stochasticity in the simulation. We used the parameters defined above for the Elastic Modulus, and added variations for four different cellular parameters: (i) turgor pressure, (ii) exchange-ratio threshold, (iii) position and (iv) orientation of the cytokinetic plane. Three levels of randomness were tested for each parameter: 0.05, 0.1 and 0.2 (see Supplementary material – A. Vertex Model for a formal definition). First, the stochastic behaviour of each parameter was examined separately. When cells were given a random turgor at birth, they tended to grow at different rates (Fig. 11 and Movie 6). The blade aspect was not strongly affected except for the highest level of stochasticity (Fig. 11A). *LWR* remained similar to the observations (Fig. 11B), but regardless of the stochasticity level, the inter-individual variability (standard deviation, n=7) remained low compared to the natural diversity. Similarly, the deviation around the mean number of neighbouring cells did not reach the amplitude observed in blades (Fig. 11C). The mean value increased with stochasticity, but this effect remained lower than the standard deviation of the observations, showing that unequal turgor can only very partially affect the grid.

Adding randomness to the threshold of the exchange ratio resulted in differences in the size at which cells divided. Some cells divided early when they were small (having a high exchange ratio), so their daughter cells were small. Other cells were able to grow longer before dividing, resulting in large cells (Fig. 12A and Movie 7). This diversity did not drastically affect the shape of the blade (Fig. 12A). Similarly to turgor stochasticity, exchange ratio threshold stochasticity did not result in a change in the *LWR* of the blade, and did not allow for large inter-individual variations in this parameter (Fig. 12B). In contrast, the mean number of neighbouring cells increased more than with turgor stochasticity, meaning that the grid pattern was affected (Fig. 12C).

The two other stochastic parameters that we tested were geometrical parameters of cell division. Randomly changing the position and the orientation of the cytokinetic plane should lead to changes in the relative positions of the cell walls, and thus in the arrangement of the cells within the lamina. Firstly, we have increased the inequality in cell division by allowing the cytokinetic plane to move from the centroid to an other point. The sister cells will therefore have different cell cycles kinetics due to their different initial size (Fig. 13A and Movie 8). We observed that, although the shape of the blade remained similar to observations (Fig. 13A,B), the grid pattern was strongly affected, as the average number of neighbouring cells increased significantly with a stochastic level of 0.1 and 0.2 (Fig. 13C).

Finally, we tested the impact of the orientation of the cytokinetic plane. We expect that the stochasticity of the division plane angle will have an impact on the shape of the cell, and result in a change in the tissue pattern and potentially in the shape of the blade. Fig. 14 and Movie 9 show similar results to those obtained with the position of the cytokinetic plane, in that the shape of the blade is not impacted (Fig. 14A,B) but the tissue pattern is, as the stochasticity levels of 0.1 and 0.2 partially disrupt the grid (Fig. 14C).

Considering that cells are subject to many variable factors in the natural environment, we

combined the stochasticity of the four parameters. To account for the cumulative effects of stochasticity on different parameters, we tested values up to 0.1. Fig. 15A,B and Movie 10 show that the overall blade shape is preserved for all stochasticity levels tested. However, the average number of neighbouring cells increases with a level of stochasticity as low as 0.05 (Fig. 15C), which contrasts with the results obtained when each parameter is taken individually.

In summary, the model is robust to stochasticity levels < 0.1 for each of the parameters tested when considered individually and < 0.05 when combined.

Discussion

Placed in a biological context, how cells must spatially arrange themselves and ensure the integrity of the sheet (tissue) while complying with inherent physical forces is a key and timely question in both animals and plants (Uroz et al., 2018; Sampathkumar et al., 2014; Du and Jiao 2020).

Here, we aimed to identify the mechanisms underlying the formation of a monolayer cell sheet whose cells are mainly connected through 4WJs. We used the embryo lamina of the brown alga *Saccharina latissima* as a case study.

Requirement for a mechanical anisotropy, of what nature?

We managed to simulate the growth of the embryo lamina with the correct shape and tissue patterning by using a 2D vertex model based on the visco-elastic properties of the cell wall. The grid emerged spontaneously from the simulation, with no requirement for mechanical anisotropy. In contrast, rendering the shape of the lamina required mechanical anisotropy. In particular, the cell walls of the lamina had to be stiffer along the medio-lateral axis than along the apico-basal axis. This mechanical anisotropy was supported by experimental evidence showing that, in response to a hyper-tonic treatment, living embryos shrank more along their apico-basal axis than along their medio-lateral axis, as do their cells. However, the origin of this mechanical growth anisotropy is unknown, and it remains possible that the intrinsic stiffness of the cell wall that is assessed when cells are subjected to a hyper-osmotic shock, is in fact not related to the growth potential of the cell walls.

Brown algal cells are surrounded by a cell wall composed of 90% of unique polysaccharides distinct from those found in land plants (Popper et al., 2011; Charrier et al., 2019). Also, cellulose is scarce and structured in ribbons, unlike in plants where it is abundant and in the form of thread-like fibrils (Tsekos, 1999). While, as in plants, cell growth requires cell wall yielding in response to turgor, the low percentage of cellulose and the different nature of the polysaccharides in brown algae make the mechanisms of cell wall growth in *Saccharina* most likely different from those identified in land plants (e.g. Rabillé et al., 2019a). In addition to this particular chemical composition, the cocktails of biosynthetic and catalytic enzymes characteristic of the brown algal cell wall (Salgado et al., 2009; Michel et al., 2010) are very likely largely involved in the regulation of the mechanical properties of the cell wall. Taking this specific composition into account, where could the axial anisotropy originate from? As in plants, growth may rely on cell wall remodelling mechanisms depending on the

maturation stage of maturation (Cosgrove, 2018; Charrier et al., 2019). Interestingly in *Saccharina* embryo, the age of the cell walls correlates to their position within the lamina. In embryogenesis Phase I, all the inner cell walls are oriented along the medio-lateral axis. As the embryo grows, these transverse cell walls may acquire higher stiffness properties, first by their continuous thickening, as observed in this work, but also possibly through an increase in their Elastic Modulus with time. Oxidation is one of the cellular mechanisms that could result in higher cell wall stiffness, as it promotes the cross-linking of phenolic compounds present in the cell wall of brown algae (Berglin et al., 2004). Interactions of phenolic compounds with alginate, an abundant cell wall polysaccharide in brown algae, decrease the viscosity of alginates, and consequently, have an impact the cell wall stiffness (Salgado et al., 2009, La Barre et al., 2010). A second mechanism that could promote an increase in the Elastic Modulus of the cell wall over time is a continuous secretion of fucose-containing sulfated polysaccharides, or of mannuronan C-5 epimerase, both of which have been reported to confer stiffness to brown algal cell walls (reviewed in Beuder and Braybrook, 2023). Therefore, the cell walls could increase their Elastic Modulus by a process reminiscent of cell wall lignification in land plants, which strengthens the primary cell walls of stem parenchyma (Barros et al., 2015) or the methyl-esterification of pectin (Hocq et al., 2017). The different cell wall layers of kelp lamina observed in TEM (Katsaros et al., 2021) confirm that the structure and possibly the chemical composition of the cell wall varies with time.

Alternatively, the mechanical anisotropy could be due to an anisotropic organisation of the alginate fibers or of the cellulose microfibrils in the different cell axes, as reported in the brown algae *Ectocarpus* (Terauchi et al., 2016) and *Sphacelaria* (Karyophyllis et al., 2000) respectively. Observation of the orientation of cellulose microfibrils in the different cell walls of the lamina of *Saccharina* embryos could be done by atomic force microscopy on extracted cell walls as performed in *Ectocarpus* (Rabillé et al., 2019a). This work showed that microfibrils were distributed isotropically in the apical cell of the prostrate filaments.

To which extent can the model buffer variable parameters?

The model is robust to stochasticity, yet of different levels depending on the parameters. Variation in turgor did not impact the shape and tissue pattern of the embryo, even with a stochasticity of 0.2. This level means that 96% of the turgor values vary between 0.3 to 0.7 MPa. These values are well below the value of 1.5 MPa measured in the blade disks of the mature kelp *Laminaria digitata* (Wright & Reed, 1988), which is phylogenetically and morphologically closely related to *Saccharina latissima.* However, in this study, we focused on turgor values measured in young tissues, like the *Ectocarpus* embryos and its turgor at 0.5 MPa. Whatever its value, the interval of turgor variations tested in this study is well larger than the variations in osmotic pressures expected in *S. latissima'*s natural environment. Indeed, this alga is immersed most of the year (Luttikhuizen et al. 2018) and the salinity where the parental line was collected prior to this study varies between ~ 0.58 and 0.61 M salts (34.0 and 35.5 psu; environmental data collection from SOMLIT https://www.somlit.fr/en/). This stable salinity cannot induce large turgor variations in submerged algae. Therefore, the range of turgor variations tested in the simulation is much higher than that experienced by algal embryos in nature.

In contrast, variations in the exchange ratio threshold above 0.1 stochasticity resulted in the loss of the grid pattern. The levels below which the grid is conserved corresponds to an interval of [0.28;0.42[which includes 96% of the values. This interval includes most of the lowest exchange ratio values observed in living embryos. For the position and orientation of the cytokinetic plane, the level of stochasticity maintaining the grid was even lower, down to 0.05. This translate into values for the position of the cytokinetic plane in the range [0.4; 0.6] with 0.5 being the centre of the cell. Although we were unable to capture the exact time at which cells divide, we could measure the relative size of the daughter cells in embryos up to the 150-cell stage. From the results, we observed that deviation from cell size equality was largely contained within this interval. Finally, the fluctuations in the orientation of the cytokinetic plane that the model could buffer (stochasticity level of 0.05) were of the order of +/- 4.5° with respect to the orientation of the shortest path (set to 0°). Permitted deviation of 9° might seem small compared to what cells can afford (Nestor-Bergmann et al., 2019) but the lack of precise captures of cell division events does not allow us to assess whether this is compatible with the live observations.

Therefore, to reproduce the grid, the model is able to buffer most of the physiological and environmental variations.

However, it failed to reproduce the diversity of shapes that was observed in living embryos and instead simulated the isotropic growth of the stereotypical 8-cell embryo that is the starting point for the simulations. In our monitoring experiment, the embryos were siblings of a single parental sporophyte and therefore they had different genetic backgrounds. This could account for the diverse morphologies observed, which simulations could not reproduce even with a high level of stochasticity. Nevertheless, since the model simulates isotropic lamina growth, we predict that it is also able to reproduce the morphological diversity of early stage embryos with different shapes, when they substitute for the stereotyped 8-cell embryo that we used in this work. Preliminary data support this prediction (not shown).

Which cellular mechanisms underlie the robustness of the model?

In all organisms, cell geometry results from the repeated application of rules setting the position of the cytokinetic plane. And in animals and plants, these rules in turn, result from the shape of the cells. They are known as the “long-axis division rule”, where the spindle aligns along the longest cell axis and cell division occurs perpendicularly to it (Minc & Piel, 2012; Nestor-Bergmann et al., 2019). Initially described in purely geometric terms (Errera, 1888), the choice of the position of the cell division plane is now understood in both animals and plants, as a mechanical process involving the cytoskeleton (Sallé and Minc, 2022; Smith 2001, Besson and Dumais, 2010, Louveaux and Hamant 2013) and its interaction with cortical proteins present at the cellular junctions (Nestor-Bergmann et al., 2019). The central concept is thus that an equilibrium in forces exerted by the dynamics of microtubules interacting with the cell periphery (e.g. cell corners in animal cells or PPB in plants) results in the positioning of the nucleus near the cell centroid from which the cytokinetic plane is selected. Noticeably, this process was shown to be intrinsically prone to stochasticity (Besson and Dumais, 2014).

Can these rules also account for the formation of the grid in *Saccharina* embryos? The cells are rectangular cuboids, in which the division plane can easily be centred as the result of a balance of forces due to the distribution of spindle and astral microtubules along the longest cell axis. Then, depending on the cell shape of the daughter cells, the orientation of the divisions would alternate from vertical to horizontal in the vertical lamina, accounting for the grid pattern. In this regard, it is worth noting that the *LWR* of cells in *Saccharina* Phase II embryos is close to √2 and that this ratio perpetuates the alternation of the cell division plane by 90° at each cell division. Interestingly, similar modelling work has been carried out in the monolayer disc of the green alga *Coleochaete* (Charophyta, Coleochaetophyceae), where 4WJs were also observed (Dupuy et al., 2010). In this alga, the tissues are not parenchymatous like in *Saccharina* lamina, but are polystichous, i.e. composed of a a juxtaposition of cell lines radiating from the centre of the disk. Moreover, cell growth is limited to the margin of the algal disc and is not diffuse as in *Saccharina*. Finally, finite element modelling based on the isotropic mechanical properties of the cells, showed that the formation of 4WJs in this species relies mainly on the synchronisation of cell divisions, a process that does not apply to *Saccharina*, both in the live embryos and in the model.

Notwithstanding these differences, in both cases the cells must be able to develop a cell shape-dependent mechanisms on which the cytokinetic plane will set its position and which can dampen stochastic variations. Brown algae lack pre-prophase bands (Katsaros et al., 2006) that, in land plants, orient the cell division plane (Mills et al., 2022). They also lack the PAR proteins, cadherins and LGN/NuMA complexes that anchor microtubules to the cortex and thus contribute to the orientation of the mitotic spindle through the length-dependent microtubule mechanism (Lechler & Mapelli, 2021; Zhong et al., 2022).

Despite the absence of these molecular complexes identified in land plants and animals, brown algal cells are subject to mechanical stress like all other cells. At minima, the stress can result from their own anisotropic shape. At the end of embryogenesis Phase I, the cells are very anisotropic (*LWR* ~ 3) and the first cell division of Phase II reduces this anisotropy by tilting the cell division plane by 90°. Daughter cells are then more 'square' than their Phase I mother cell, and have a *LWR* close to 1.4 (~ √2) characteristic of Phase II cells. However, these cells are still anisotropic and as turgid cells, they should tend towards *LWR* =1 if their mechanical properties happened to be isotropic. Interestingly, we observed that instead, these cells maintain – and even tend towards – *LWR* = √2 (not shown). What compels them to do so is unclear, as we have shown that the stiffness anisotropy that *Saccharina* Phase II cells display in response to hyper-osmotic shock, 1) is not related to cell shape but to their position relative to the lamina axes (only the cell walls in the Y-axis are stiffer than those in the X-axis) and 2) is not required for the formation of the grid. Therefore, and in summary, rather than depending on cell growth in response to intrinsic mechanical forces, cell shape appears to depend primarily on the orientation of cell division, which itself depends on cell shape. Therefore, the establishment of highly anisotropic cells at the end of Phase I could be the starting point for a self-organising process undertaken in Phase II and based solely on cell shapes.

An additional fact supports an original mechanism in brown algae. Most of the DAPI-stained nuclei are observed stuck in the corners of fixed *Saccharina* lamina cells, and not in the centre of the cells (not shown). This suggests that nuclei are unlikely to determine the

center of mass through which the division plane is set. Instead, in brown algae the position of the centrosomes would control the position of the division plane (Katsaros et al., 2012). This is even more interesting when one considers that two centrosomes are present during the majority of the cell cycle and that the formation of the cytokinetic plane can take place long after the two daughter nuclei are well separated. This opens the door to possible new mechanisms for controlling the position of the cytokinetic plane.

Why such an isotropic growth and a monotonous pattern?

It is striking that despite the observed biological noise, the growth of the embryo lamina is isotropic (both *in vivo* and *in silico*) for about 20 days and more than 250 cell divisions from Phase I to the end of Phase II. Furthermore, the cellular patterns of growth rate, cell area and shape are monotonous during the whole Phase II. Planar plant organs like sepals, petals and leaves display heterogeneous cell growth rates and shapes (Hong et al., 2016; Le Gloanec et al., 2022) and examples of symmetry-breaking events, triggered by stochastic cell behaviours, abound in animals and plants (Green & Sharpe, 2015). We have shown that in the multiple stochasticity range of 0.02, the morphogenetic homeostasis observed in *Saccharina* lamina is maintained. This could be explained by a process of spatio-temporal averaging process as described in plants (Hong et al., 2016), which would maintain the monotony of the pattern for a long period of time, until a new parameter is introduced into the system. Interestingly, the loss of the monotonous pattern coincides with polystromatisation, i.e. the thickening of the lamina due to the first periclinal cell divisions (see paper III of this thesis). As actin filaments (AFs) are oriented along the Z- axis during Phase II (paper II of this thesis), a disruption of these AFs could lead to both the tilting of the division plane in the Z- axis and the loss of the grid pattern. Preliminary results confirm that the two events are concomitant, but with a time scale that needs to be clarified.

In summary, we have simulated the formation of a grid pattern during the development of a pear-shaped monolayer embryo of the brown alga *Saccharina*, using a robust mechanical model with simple rules of cell division and cell growth. *Saccharina* is thus an original case illustrating how isotropic growth relies on anisotropic mechanical properties and how a grid-like cellular arrangement can emerge from cell shape resulting solely from cell division. Many future experiments are needed to identify the underlying cellular mechanisms involved in this developmental pattern. The spatio-temporal distribution of centrosomes and microtubules in relation to cell shape, as well as the structure and composition of the cell wall in relation to the growth axes of the embryo, will be the main targets of these studies.

Material & Methods

Algal material and time-lapse monitoring

The production of the embryos of *Saccharina latissima* (Arthrothamnaceae, Laminariales, Phaeophyceae; Theodorou & Charrier, 2021) was optimised as reported in (Theorodou et

al., 2021). In brief, the embryos were produced from the fertilisation of eggs hatched from the oogonium differentiated from vegetative cells of female gametophytes, by sperm cells released by filamentous male gametophytes. Both gametophytes are filamentous, and they were grown from a single mature sporophyte collected in the wild. The egg remains attached to the female gametophyte, through the cell wall of the empty oogonium. Gametogenesis was induced under 16 µmol photons $m^{-2} \cdot s^{-1}$ light intensity and 14:10 light:dark photoperiod at 13 °C. Five to 7 days after, polarised zygotes were transferred to 50 µmol photons $m^{-2} \cdot s^{-1}$ intensity with same photoperiod and temperature. Fourteen developing embryos were monitored under bright field microscope, with intervals of 12 or 24 hours depending on the specimen.

Manual segmentation

Acquired images were segmented using Inkscape 1.2 (Inkscape 2022) and FIJI (Schindelin et al. 2012), as described in Vőfély et al. (2019). The images consisted of both single plane and Z-stacks acquisitions. To help draw the cell contours manually, images were first projected in different types of Z-projections, e.g. average, standard deviation and sum slices mode (plug-in stack-focuser). The resulting drawings were analysed by a in-house software. In addition to the complete cell lineage, the program output various quantitative lamina and cellular parameters : 1) length and width, perimeter, area and cell number in each lamina. In addition, shape parameters like convexity were calculated to describe the lamina shape more accurately; 2) length, width, perimeter, area, perimeter/area ratio at which cells divide (called in this study “exchange ration threshold”), and the orientation of their division plane (transversal along the Y axis or longitudinal along the X axis) of each cell. Finally, the number of cell neighbours was counted. All these parameters were used to assess the adequacy of the simulation with regards to the growth dynamics of the embryo.

Assessment of mechanical anisotropy in the embryo lamina and cells through measurement of the response to hyper-osmotic treatments

Phase II specimens were stained with 20 µM filtered and sterile Brightener 28 (Calcofluor white; Sigma-Aldrich) for one hour in seawater, at 14 °C and in the dark. After three 5 min washes in seawater, the embryos were immersed in 2660 mOsmoles of sterile seawater supplemented with sucrose (28.3g in 50mL seawater) as described in Rabillé et al. (2019b). Z-stack under confocal microscopy (Leica) was acquired for each specimen prior to and 1 min after immersion. Control was immersion in sea water. Image acquisition used the 405 nm laser line for excitation of Calcofluor White and a photomultiplier tube (PMT) as a detector set at 440 nm - 480 nm wavelength for emission. Plasmolysis was checked with the Trans PMT.
Thirteen specimens were treated and tracked for each condition, from which manual segmentation and image analysis were performed using FIJI. Length and width of the laminas were measured and the percentage of lamina shrinkage was calculated as $x_{(before)} - x_{(after)} / x_{(before)}$, where x is the lamina or the cell. For each cells of the embryos responding to the hyper-osmotic shock, the Length / Width ratio was calculated after measurement with FIJI.

Model and simulation software

The developing *Saccharina latissima* blade was modelled by a 2D vertex model (Fozard et al. 2013). In such model, cells are depicted as polygons, the edges of which represent the cell wall, made of an elastic / plastic material. The cell interior is subject to turgor pressure (T) which, by pushing the walls, tends to increase the cell size. The cell edges resist lengthening which results from this cell enlargement. Details of the model are given in the Supplementary Material – A. Vertex Model section. The model was implemented as an object-oriented python 3.10 program, making use of standard libraries: numpy, matplotlib, scipy, opencv. The code was developed in an Ubuntu environment, and simulations ran on a HPC/Cluster infrastructure based on the scheduler SLURM.

Acknowledgement

We are very grateful to Philippe Andrey (INRAE Versailles, France) and Floris Bosveld (Institut Curie, Paris, France) for their valuable advice in this work. We are grateful to the ABiMS bioinformatics platform in Roscoff (https://abims.sb-roscoff.fr), which is part of the French Institute of Bioinformatics (ANR-11-INBS-0013) and of the BioGenouest network, for the provision of computing resources. This work has been funded by the CNRS MITI (project name "Lame Brune", 2020-2022). I.T was funded by the Region Bretagne (ARED, project "PUZZLE") and the NMBU.

References

Ali, O., Mirabet, V., Godin, C., and Traas, J. 2014. Physical Models of Plant Development. *In* Annual Review of Cell and Developmental Biology, Vol 30. *Edited by* R. Schekman and R. Lehmann. Annual Reviews, Palo Alto. pp. 59–78.

Bardet, P.-L., Guirao, B., Paoletti, C., Serman, F., Léopold, V., Bosveld, F., Goya, Y., Mirouse, V., Graner, F., and Bellaïche, Y. 2013. PTEN Controls Junction Lengthening and Stability during Cell Rearrangement in Epithelial Tissue. Dev. Cell **25**(5): 534–546. doi:10.1016/j.devcel.2013.04.020.

Berglin, M., Delage, L., Potin, P., Vilter, H., and Elwing, H. 2004. Enzymatic cross-linking of a phenolic polymer extracted from the marine alga Fucus serratus. Biomacromolecules **5**(6): 2376–2383. doi:10.1021/bm0496864.

Besson, S., and Dumais, J. 2011. Universal rule for the symmetric division of plant cells. Proc. Natl. Acad. Sci. **108**(15): 6294–6299. doi:10.1073/pnas.1011866108.

Besson, S., and Dumais, J. 2014. Stochasticity in the symmetric division of plant cells: when the exceptions are the rule. Front. Plant Sci. **5**. doi:10.3389/fpls.2014.00538.

Beuder, S., and Braybrook, S.A. 2023. Brown algal cell walls and development. Semin. Cell Dev. Biol. **134**: 103–111. doi:10.1016/j.semcdb.2022.03.003.

Charrier, B., Rabillé, H., and Billoud, B. 2019. Gazing at Cell Wall Expansion under a Golden Light. Trends Plant Sci. **24**(2): 130–141. doi:10.1016/j.tplants.2018.10.013.

Cock, J.M., Sterck, L., Rouzé, P., Scornet, D., Allen, A.E., Amoutzias, G., Anthouard, V.,

Artiguenave, F., Aury, J.-M., Badger, J.H., Beszteri, B., Billiau, K., Bonnet, E., Bothwell, J.H., Bowler, C., Boyen, C., Brownlee, C., Carrano, C.J., Charrier, B., Cho, G.Y., Coelho, S.M., Collén, J., Corre, E., Da Silva, C., Delage, L., Delaroque, N., Dittami, S.M., Doulbeau, S., Elias, M., Farnham, G., Gachon, C.M.M., Gschloessl, B., Heesch, S., Jabbari, K., Jubin, C., Kawai, H., Kimura, K., Kloareg, B., Küpper, F.C., Lang, D., Le Bail, A., Leblanc, C., Lerouge, P., Lohr, M., Lopez, P.J., Martens, C., Maumus, F., Michel, G., Miranda-Saavedra, D., Morales, J., Moreau, H., Motomura, T., Nagasato, C., Napoli, C.A., Nelson, D.R., Nyvall-Collén, P., Peters, A.F., Pommier, C., Potin, P., Poulain, J., Quesneville, H., Read, B., Rensing, S.A., Ritter, A., Rousvoal, S., Samanta, M., Samson, G., Schroeder, D.C., Ségurens, B., Strittmatter, M., Tonon, T., Tregear, J.W., Valentin, K., von Dassow, P., Yamagishi, T., Van de Peer, Y., and Wincker, P. 2010. The Ectocarpus genome and the independent evolution of multicellularity in brown algae. Nature **465**(7298): 617–621. doi:10.1038/nature09016.

Corson, F., Hamant, O., Bohn, S., Traas, J., Boudaoud, A., and Couder, Y. 2009. Turning a plant tissue into a living cell froth through isotropic growth. Proc. Natl. Acad. Sci. U. S. A. **106**(21): 8453–8458. doi:10.1073/pnas.0812493106.

Cosgrove, D.J. 2018. Diffuse Growth of Plant Cell Walls1[OPEN]. Plant Physiol. **176**(1): 16–27. doi:10.1104/pp.17.01541.

Drew, G.H. 1910. The Reproduction and early Development of *Laminaria digitata* and *Laminaria saccharina*. Ann. Bot. **24**(1): 177–189. doi:10.1093/oxfordjournals.aob.a089253.

Du, F., and Jiao, Y. 2020. Mechanical control of plant morphogenesis: concepts and progress. Curr. Opin. Plant Biol. **57**: 16–23. doi:10.1016/j.pbi.2020.05.008.

Dupuy, L., Mackenzie, J., and Haseloff, J. 2010. Coordination of plant cell division and expansion in a simple morphogenetic system. Proc. Natl. Acad. Sci. U. S. A. **107**(6): 2711–2716. doi:10.1073/pnas.0906322107.

Errera, L. 1888. Über Zellformen und Siefenblasen. Bot. Cent. **34**: 395–399.

Fletcher, A.G., Osborne, J.M., Maini, P.K., and Gavaghan, D.J. 2013. Implementing vertex dynamics models of cell populations in biology within a consistent computational framework. Prog. Biophys. Mol. Biol. **113**(2): 299–326. doi:10.1016/j.pbiomolbio.2013.09.003.

Green, J.B.A., and Sharpe, J. 2015. Positional information and reaction-diffusion: two big ideas in developmental biology combine. Dev. Camb. Engl. **142**(7): 1203–1211. doi:10.1242/dev.114991.

Hocq, L., Pelloux, J., and Lefebvre, V. 2017. Connecting Homogalacturonan-Type Pectin Remodeling to Acid Growth. Trends Plant Sci. **22**(1): 20–29. doi:10.1016/j.tplants.2016.10.009.

Hofmeister, W. 1863. Zusatze und Berichtigungen zu den 1851 veroffentlichen Untersuchungen der Entwicklung hoherer Kryptogamen. Jahrb Wiss Bot **3**: 259–193.

Hong, L., Dumond, M., Tsugawa, S., Sapala, A., Routier-Kierzkowska, A.-L., Zhou, Y., Chen, C., Kiss, A., Zhu, M., Hamant, O., Smith, R.S., Komatsuzaki, T., Li, C.-B., Boudaoud, A., and Roeder, A.H.K. 2016. Variable Cell Growth Yields Reproducible Organ Development through Spatiotemporal Averaging. Dev. Cell **38**(1): 15–32. doi:10.1016/j.devcel.2016.06.016.

Hurd, C.L., Harrison, P.J., Bischof, K., and Lobban, C.S. 2014. Seaweed Ecology and

Physiology. Cambridge University Press.
Inkscape. 2022. Inkscape Project. Available from https://inkscape.org.
Karyophyllis, D., Katsaros, C., Dimitriadis, I., and Galatis, B. 2000. F-Actin organization during the cell cycle of Sphacelaria rigidula (Phaeophyceae). Eur. J. Phycol. **35**(1): 25–33. doi:10.1080/09670260010001735591.
Katsaros, C., Karyophyllis, D., and Galatis, B. 2006. Cytoskeleton and morphogenesis in brown algae. Ann. Bot. **97**(5): 679–693. doi:10.1093/aob/mcl023.
Katsaros, C., Nagasato, C., Terauchi, M., and Motomura, T. 2013. Cytokinesis in brown algae. *In* Advances in Algal Cell Biology, Kirsten Heimann and Christos Katsaros. De Gruyter, Berlin, Boston. p. 224. Available from https://doi.org/10.1515/9783110229615.
Katsaros, C., Panse, S.L., Milne, G., Carrano, C.J., and Küpper, F.C. 2021. New insights on Laminaria digitata ultrastructure through combined conventional chemical fixation and cryofixation. Bot. Mar. **64**(3): 177–187. De Gruyter. doi:10.1515/bot-2021-0005.
Killian, K. 1911. Beiträge zur Kenntnis der Laminarien. Z. Für Bot. **3**: 433–494.
La Barre, S., Potin, P., Leblanc, C., and Delage, L. 2010. The halogenated metabolism of brown algae (Phaeophyta), its biological importance and its environmental significance. Mar. Drugs **8**(4): 988–1010. doi:10.3390/md8040988.
Le Gloanec, C., Collet, L., Silveira, S.R., Wang, B., Routier-Kierzkowska, A.-L., and Kierzkowski, D. 2022. Cell type-specific dynamics underlie cellular growth variability in plants. Dev. Camb. Engl. **149**(14): dev200783. doi:10.1242/dev.200783.
Lechler, T., and Mapelli, M. 2021. Spindle positioning and its impact on vertebrate tissue architecture and cell fate. Nat. Rev. Mol. Cell Biol. **22**(10): 691–708. Nature Publishing Group. doi:10.1038/s41580-021-00384-4.
Lloyd, C.W. 1991. How does the cytoskeleton read the laws of geometry in aligning the division plane of plant cells? Development **113**(Supplement 1): 55–65.
Louveaux, M., and Hamant, O. 2013. The mechanics behind cell division. Curr. Opin. Plant Biol. **16**(6): 774–779. doi:10.1016/j.pbi.2013.10.011.
Luttikhuizen, P.C., Heuvel, F.H.M. van den, Rebours, C., Witte, H.J., Bleijswijk, J.D.L. van, and Timmermans, K. 2018. Strong population structure but no equilibrium yet: Genetic connectivity and phylogeography in the kelp *Saccharina latissima* (Laminariales, Phaeophyta). Ecol. Evol. **8**(8): 4265–4277. doi:10.1002/ece3.3968.
Michel, G., Tonon, T., Scornet, D., Cock, J.M., and Kloareg, B. 2010. The cell wall polysaccharide metabolism of the brown alga Ectocarpus siliculosus. Insights into the evolution of extracellular matrix polysaccharides in Eukaryotes. New Phytol. **188**(1): 82–97. doi:10.1111/j.1469-8137.2010.03374.x.
Mills, A.M., Morris, V.H., and Rasmussen, C.G. 2022. The localization of PHRAGMOPLAST ORIENTING KINESIN1 at the division site depends on the microtubule-binding proteins TANGLED1 and AUXIN-INDUCED IN ROOT CULTURES9 in Arabidopsis. Plant Cell **34**(11): 4583–4599. doi:10.1093/plcell/koac266.
Minc, N., and Piel, M. 2012. Predicting division plane position and orientation. Trends Cell Biol. **22**(4): 193–200. doi:10.1016/j.tcb.2012.01.003.
Nestor-Bergmann, A., Stooke-Vaughan, G.A., Goddard, G.K., Starborg, T., Jensen, O.E., and Woolner, S. 2019. Decoupling the Roles of Cell Shape and Mechanical Stress in Orienting and Cueing Epithelial Mitosis. Cell Rep. **26**(8): 2088-2100.e4. doi:10.1016/j.celrep.2019.01.102.

Pessarrodona, A., Assis, J., Filbee-Dexter, K., Burrows, M.T., Gattuso, J.-P., Duarte, C.M., Krause-Jensen, D., Moore, P.J., Smale, D.A., and Wernberg, T. 2022. Global seaweed productivity. Sci. Adv. **8**(37): eabn2465. American Association for the Advancement of Science. doi:10.1126/sciadv.abn2465.

Popper, Z.A., Michel, G., Hervé, C., Domozych, D.S., Willats, W.G.T., Tuohy, M.G., Kloareg, B., and Stengel, D.B. 2011. Evolution and Diversity of Plant Cell Walls: From Algae to Flowering Plants. Annu. Rev. Plant Biol. **62**(1): 567–590. doi:10.1146/annurev-arplant-042110-103809.

Rabillé, H., Billoud, B., Tesson, B., Le Panse, S., Rolland, É., and Charrier, B. 2019a. The brown algal mode of tip growth: Keeping stress under control. PLoS Biol. **17**(1): e2005258. doi:10.1371/journal.pbio.2005258.

Rabillé, H., Torode, T.A., Tesson, B., Le Bail, A., Billoud, B., Rolland, E., Le Panse, S., Jam, M., and Charrier, B. 2019b. Alginates along the filament of the brown alga Ectocarpus help cells cope with stress. Sci. Rep. **9**(1): 12956. doi:10.1038/s41598-019-49427-z.

Rasmussen, C.G., and Bellinger, M. 2018. An overview of plant division-plane orientation. New Phytol. **219**(2): 505–512. doi:10.1111/nph.15183.

Sachs, J. 1878. Arbeiten des Botanischen instituts in Würzburg /. Wilhelm Engelmann, Leipzig : doi:10.5962/bhl.title.81722.

Salgado, L.T., Cinelli, L.P., Viana, N.B., Tomazetto de Carvalho, R., De Souza Mourão, P.A., Teixeira, V.L., Farina, M., and Filho, A.G.M.A. 2009. a vanadium bromoperoxidase catalyzes the formation of high-molecular-weight complexes between brown algal phenolic substances and alginates(1). J. Phycol. **45**(1): 193–202. doi:10.1111/j.1529-8817.2008.00642.x.

Sallé, J., and Minc, N. 2021. Cell division geometries as central organizers of early embryo development. Semin. Cell Dev. Biol. doi:10.1016/j.semcdb.2021.08.004.

Sampathkumar, A., Yan, A., Krupinski, P., and Meyerowitz, E.M. 2014. Physical Forces Regulate Plant Development and Morphogenesis. Curr. Biol. **24**(10): R475–R483. doi:10.1016/j.cub.2014.03.014.

Schindelin, J., Arganda-Carreras, I., Frise, E., Kaynig, V., Longair, M., Pietzsch, T., Preibisch, S., Rueden, C., Saalfeld, S., Schmid, B., Tinevez, J.-Y., White, D.J., Hartenstein, V., Eliceiri, K., Tomancak, P., and Cardona, A. 2012. Fiji - an Open Source platform for biological image analysis. Nat. Methods **9**(7). doi:10.1038/nmeth.2019.

Smith, L.G. 2001. Plant cell division: building walls in the right places. Nat. Rev. Mol. Cell Biol. **2**(1): 33–39. Nature Publishing Group. doi:10.1038/35048050.

Staple, D.B., Farhadifar, R., Röper, J.-C., Aigouy, B., Eaton, S., and Jülicher, F. 2010. Mechanics and remodelling of cell packings in epithelia. Eur. Phys. J. E Soft Matter **33**(2): 117–127. doi:10.1140/epje/i2010-10677-0.

Starko, S. 2019. Morphological and functional diversification during kelp evolution. University of British Columbia. doi:10.14288/1.0378025.

Terauchi, M., Nagasato, C., Inoue, A., Ito, T., and Motomura, T. 2016. Distribution of alginate and cellulose and regulatory role of calcium in the cell wall of the brown alga Ectocarpus siliculosus (Ectocarpales, Phaeophyceae). Planta **244**(2): 361–377. doi:10.1007/s00425-016-2516-4.

Theodorou, I., and Charrier, B. 2021. Brown Algae: Ectocarpus and Saccharina as Experimental Models for Developmental Biology. *In* Handbook of Marine Model

Organisms in Experimental Biology, 1st edition. CRC Press, Boca Raton. pp. 27–47.
Theodorou, I., Opsahl-Sorteberg, H.-G., and Charrier, B. 2021. Preparation of Zygotes and Embryos of the Kelp Saccharina latissima for Cell Biology Approaches. Bio-Protoc.: e4132–e4132.
Thompson, D.W., and Thompson, D.A.W. 1942. On growth and form. *In* Cambridge university press. Cambridge.
Tsekos, I. 1999. The Sites of Cellulose Synthesis in Algae: Diversity and Evolution of Cellulose-Synthesizing Enzyme Complexes. J. Phycol. **35**(4): 635–655. doi:10.1046/j.1529-8817.1999.3540635.x.
Uroz, M., Wistorf, S., Serra-Picamal, X., Conte, V., Sales-Pardo, M., Roca-Cusachs, P., Guimerà, R., and Trepat, X. 2018. Regulation of cell cycle progression by cell-cell and cell-matrix forces. Nat. Cell Biol. **20**(6): 646–654. doi:10.1038/s41556-018-0107-2.
Vőfély, R.V., Gallagher, J., Pisano, G.D., Bartlett, M., and Braybrook, S.A. 2019. Of puzzles and pavements: a quantitative exploration of leaf epidermal cell shape. New Phytol. **221**(1): 540–552. doi:10.1111/nph.15461.
Wright, P.J., and Reed, R.H. 1988. Method for determination of turgor pressure in macroalgae, with particular reference to the Phaeophyta. Mar. Biol. **99**(4): 473–480. doi:10.1007/BF00392554.
Zhong, T., Gongye, X., Wang, M., and Yu, J. 2022. Understanding the underlying mechanisms governing spindle orientation: How far are we from there? J. Cell. Mol. Med. **26**(19): 4904–4910. doi:10.1111/jcmm.17526.

Figures

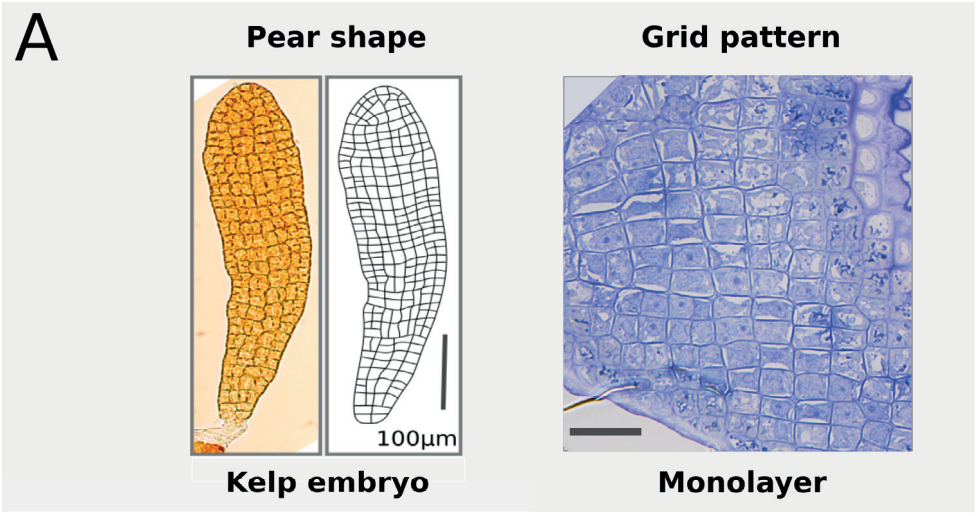

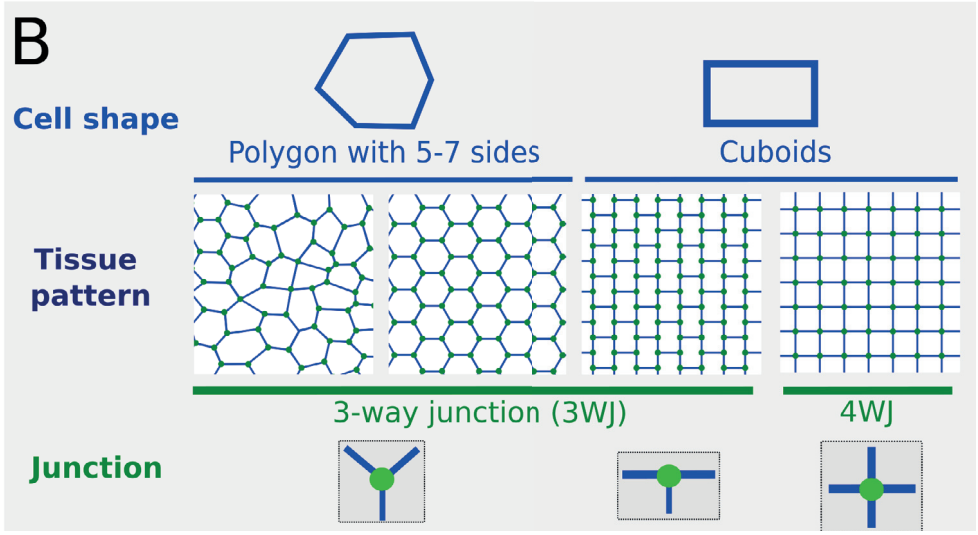

Figure 1. Cell sheet organisation. (A) *Saccharina* embryo lamina is rich in cuboid cells, which are joined to three other cells (when represented in 2D) by four-way junctions (4WJ) (left). This conformation leads to a tissue with a "grid" pattern observed in Phase II embryo stained with methylene blue (right). (B) Different cell arrangements within tissues, as observed in plants and algae. Whichever the cell shape (i.e. in 2D polygons with 5 to 7 sides or rectangles), most tissues display mainly 3-way junctions (3WJ; e.g. epidermis of land plants and red algae, shooty leaf of bryophytes). Scale bar: 25 µm.

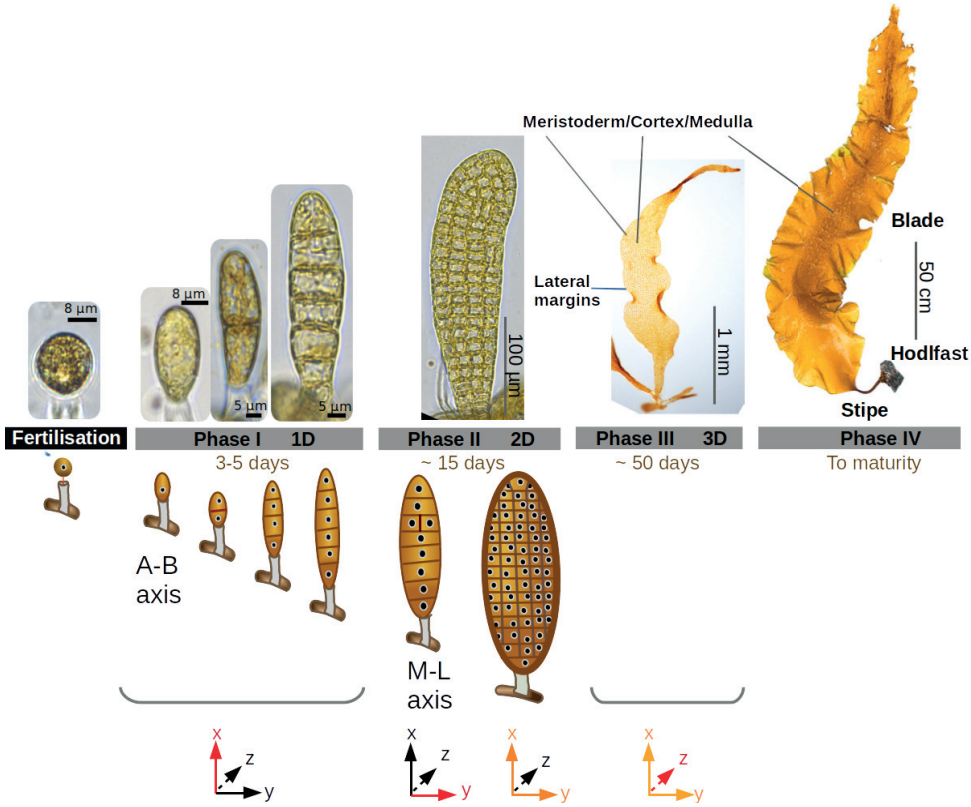

Figure 2. **Definition of four embryogenic phases in *S. latissima*.** (A) The development of *S. latissima* embryo was divided in four main phases, based on the orientation of the cell divisions. See main text for detailed descriptions. Schematics (bottom) illustrate the orientation of the cell walls in Phases I and II, along the apico-basal (A-P) and the medio-lateral (M-L) axes.

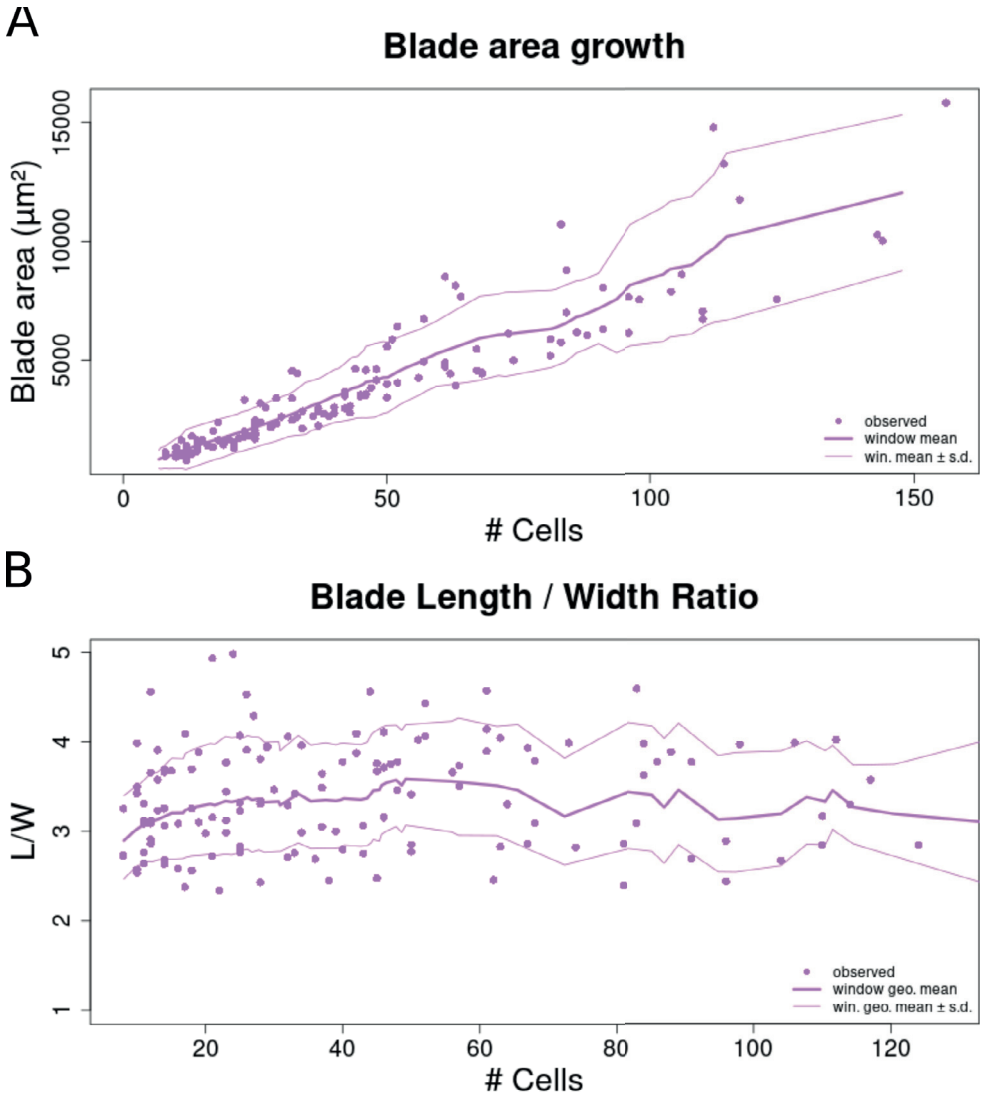

Figure 3: **Blade measures as a function of cell number.** (A) Blade Area. The dots represent the observations of the live embryos; the thick line represents the arithmetic mean in a sliding window of 16; the thin lines represent the mean ± standard deviation (s.d.). (B) Length / Width Ratio, computed as the ratio between length of main (X-) and secondary (Y-) axes. The meaning of dots and lines are similar to (A) except that the mean is geometric instead of arithmetic.

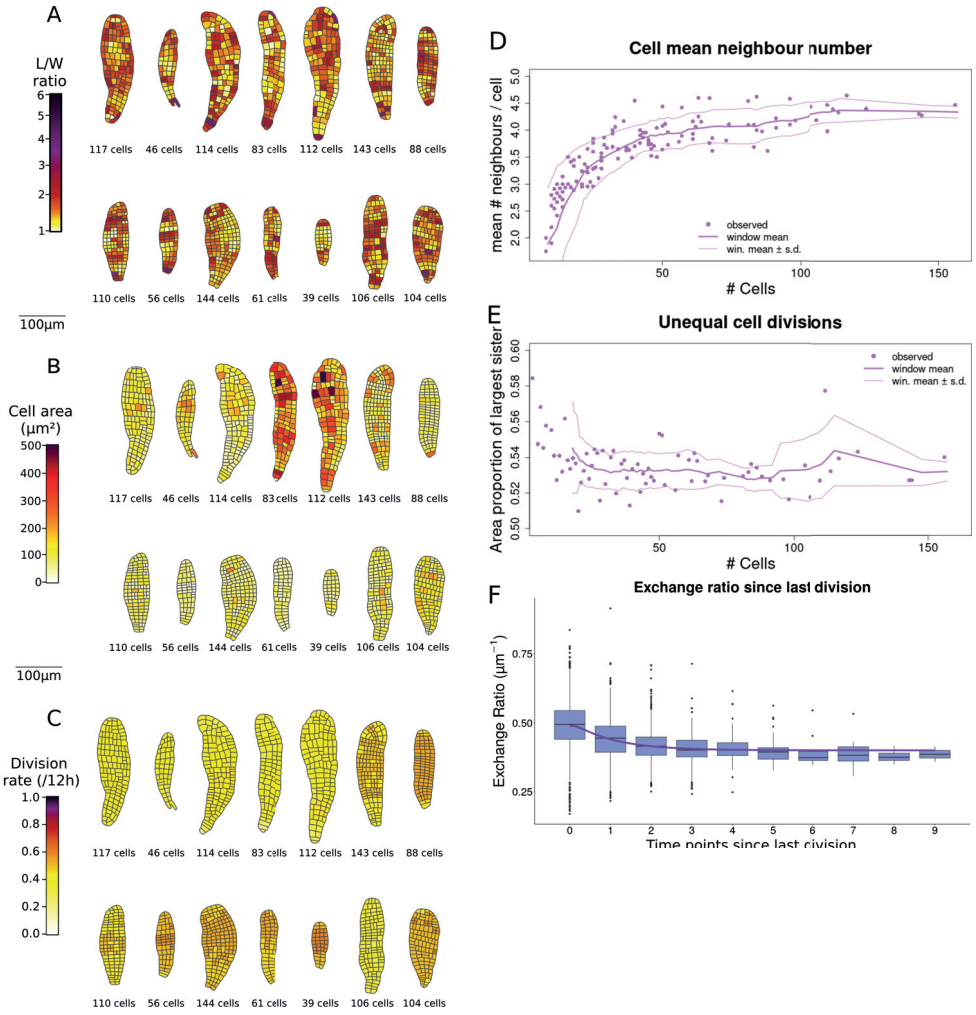

Figure 4. Cell morphometrics. For each specimen, the blade shown is the one for which the cell number (reported under each blade) is the closest to 128. (A) Cell Length / Width Ratio, computed as the ratio between main and secondary axes of the cell shape, regardless of the orientation of the cell within the lamina. (B) Cell area. Two embryos display much larger cells than the others. (C) Cell division rate, expressed as the number of cell divisions every 12 hours, averaged from the start of embryo growth. (D) Average number of neighbouring cells. The pink dots represent the average value for cells of each lamina at each time point. The thick line represents the arithmetic mean in a sliding window of 16; the thin lines represent the mean ± standard deviation. (E) Unequal division, shown as the area proportion of the largest of two sister cells just after cell division. Same description of dots, thin and thick lines as above. (F) Evolution of the Exchange ratio distribution after a division. The ratio decreases while the cell grows.

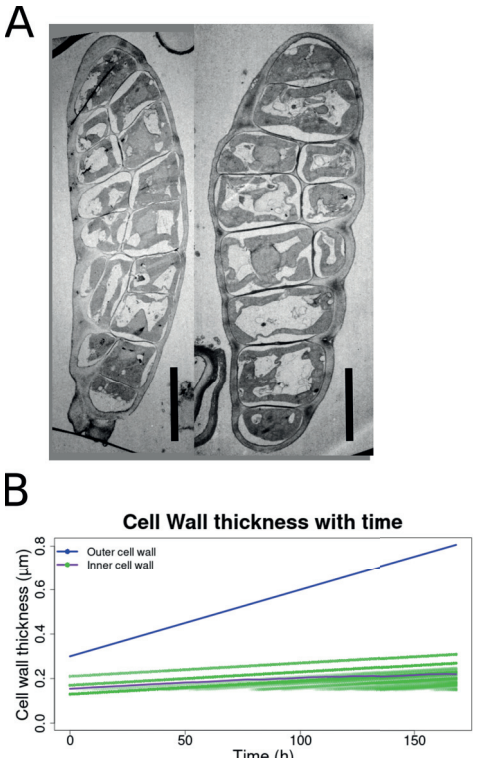

Figure 5. Model of cell wall thickening in the embryos of *S. latissima*. (A) Examples of TEM photos of longitudinal sections of early Phase II embryos used for the measurement of the cell wall thickness of the outer and the inner cell walls. Scale bar 10 µm. (B) Model of cell wall thickening inferred from the measurements. blue: outer cell wall, green: successive inner cell walls. Purple: curve of the average cell wall thickness of all the inner cell walls, giving the average dynamics of cell wall thickening over time. The first time point corresponds to 2-cell stage embryos (time 0). Last time point corresponds to ~ 10-15-cell embryos (160 hours).

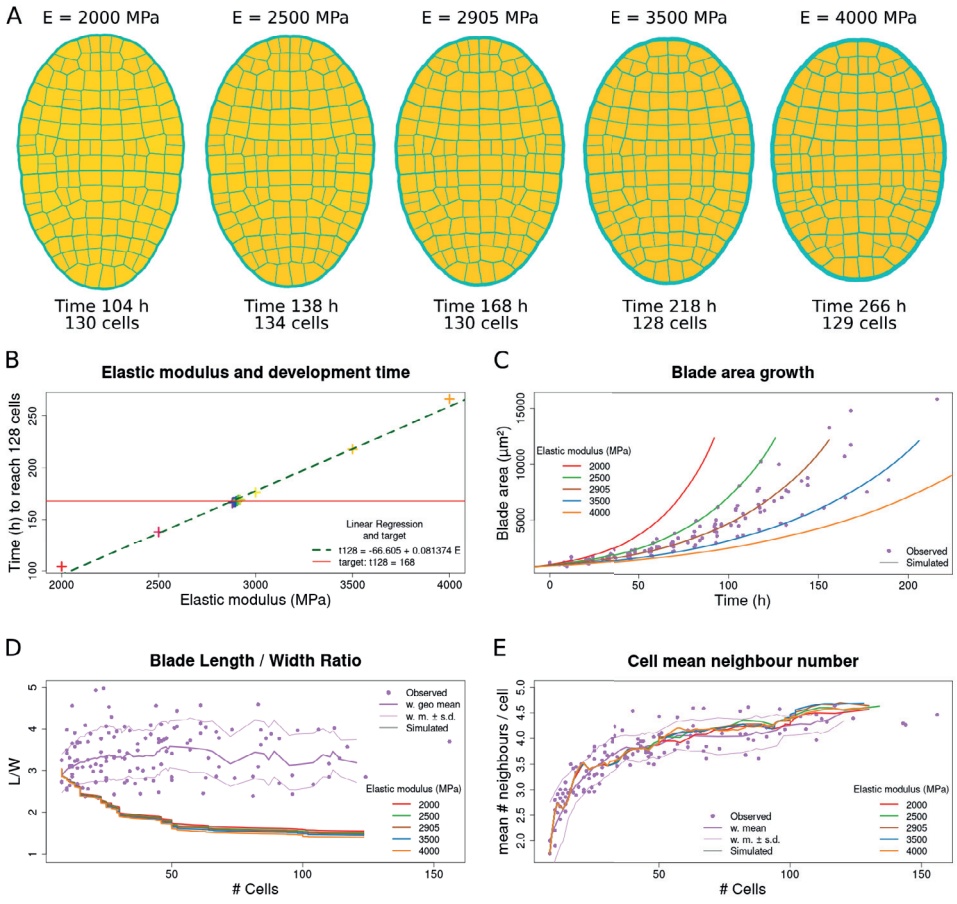

Figure 6: **Comparison of observed and simulated characteristics for various values of the Elastic Modulus (*E*) of the cell wall.**

(A) Final state of simulations for five values of *E*. (B) Time to reach 128 cells for various values of *E*. The linear regression (dashed line) meets the observed value (red horizontal line) at *E* = 2905 MPa. In (C,D,E) pink dots represent observations, thick line is their mean (M) by window and thin lines show their standard deviation (SD); lines with other colours show the simulation results for five values of *E*. (C) Growth (blade area as a function of time). The growth curve for *E* = 2905 MPa matches the observations. (D) For the five values of *E* tested, the blade Length / Width ratio (LWR) decreases rapidly during the simulation, which means that the simulated blade tends to become rounder, instead of keeping its elongated shape. However (E), the grid pattern, here depicted by the average number of neighbouring cells, is close to the observations as it is mainly in the M ± SD interval.

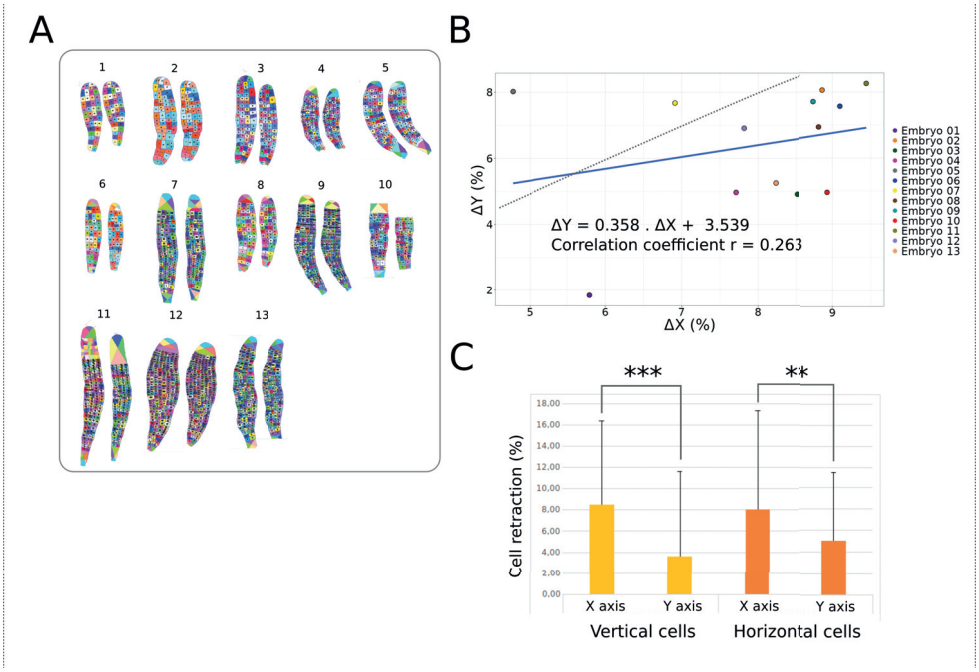

Figure 7. Lamina and cell response to a hyper-osmotic shock. (A) Lamina and cell outlines of 13 embryos, before and after the osmotic treatment. Each cell is represented by a different colour. (B) Distribution of the % of lamina retraction along the apico-basal (X-) axis *vs* the medio-lateral (Y-) axis for 13 embryos in response to the hyper-osmotic treatment. The linear regression curve (blue line) shows that in response to the osmotic shock, laminas retract more in the X than in the Y orientation (slope = 0.358). Dashed grey line: curve for the isotropic shrinkage. (C) Histogram of the % of the cell retraction in embryos responding to the hyper-osmotic shock.

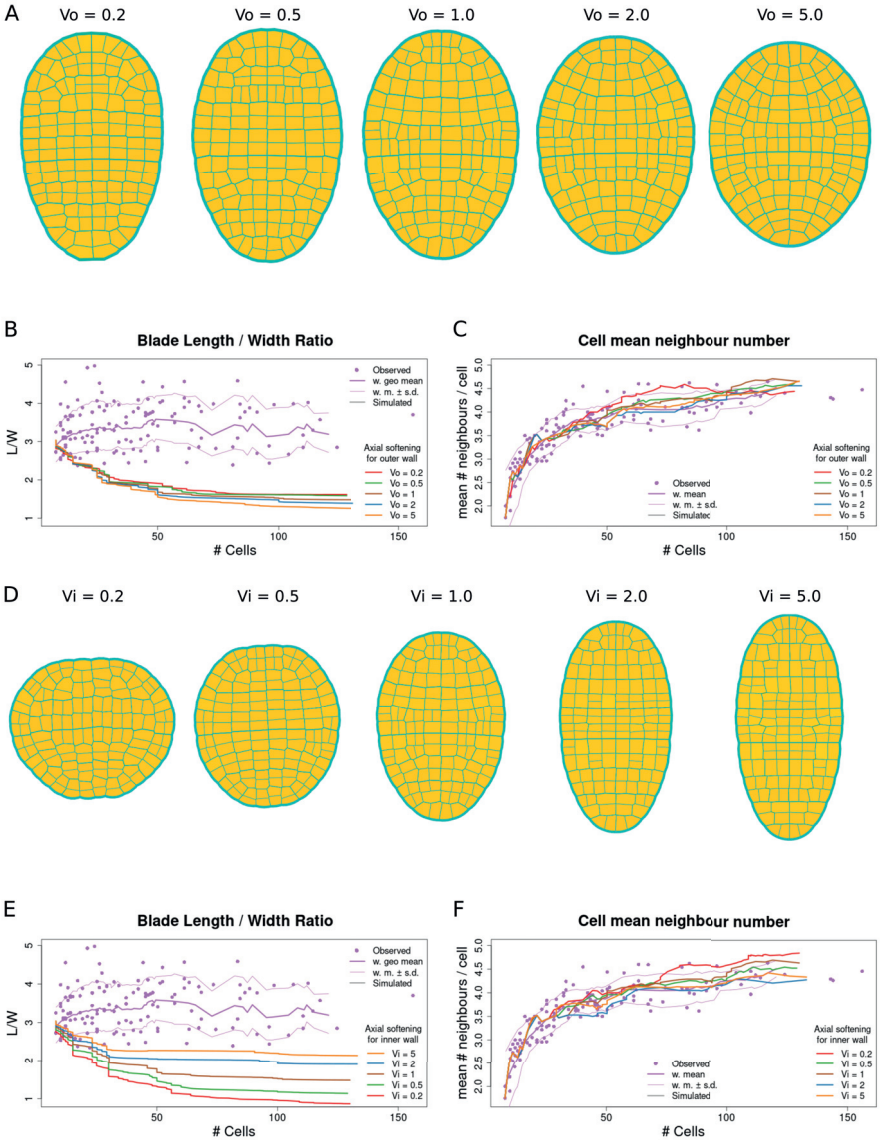

Figure 8. Effects of anisotropic elastic modulus (*E*). (A) Final aspect of simulated blades for five values of outer wall anisotropy (V_o): a low value of V_o means that longitudinal walls are stiffer than transversal walls. With V_o = 1 (centre), there is no anisotropy and the simulation is identical to the one shown in the central position of Fig. 6A. (B) For all values of V_o (lines with various colours), the Length / Width Ratio (*LWR*) of the blade falls below the expected (observed) value, shown here in pink. (C) The mean number of neighbouring cells is most of

the time above the expected average for all values of V_o, but usually remains within the range [mean ± standard deviation]. (D) Final aspect of simulated blades for five values of inner wall anisotropy (V_I). Meaning of the parameter is like in (A). (E) For high values of V_I, the blade shape remains more elongated than without anisotropy (V_I = 1) but not as much as the observed blades. (F) Except for V_I = 0.2, the average number of neighbouring cells is similar to the observations.

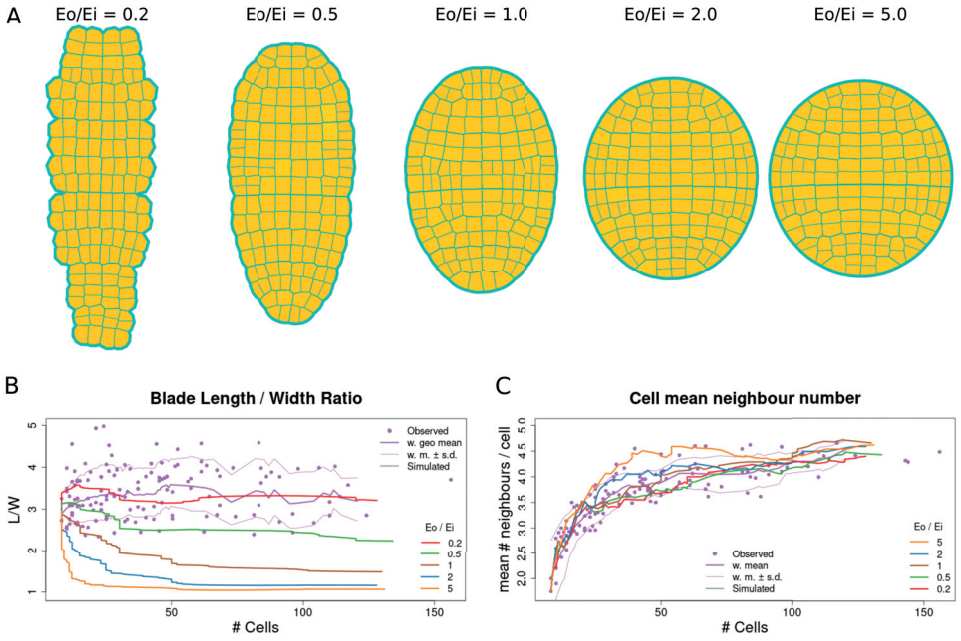

Figure 9: Effect of differential Elastic Modulus between cell walls of the outer wall envelope (E_o) and the inner ones, separating cells (E_I). (A) Final aspect of the simulated blades for five values of the E_o/E_I ratio. (B) Only the lowest value of E_o/E_I (0.2) results in a correct blade elongation, while the Length / Width Ratio is too low for all other values. (C) All values of E_o/E_I result in a correct value for the average number of neighbouring cells per cell, except the extremely high value of 5.

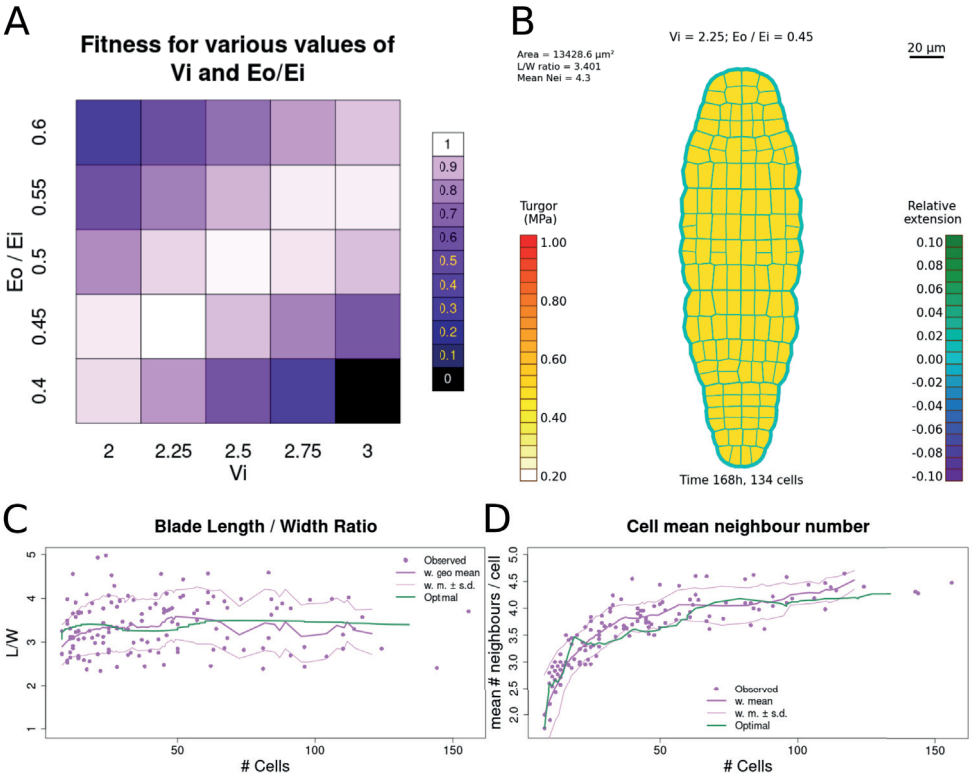

Figure 10: Optimised distribution of Elastic Modulus in the simulation. (A) Heat-map showing how the simulation fitness depends on E_0/E_I and V_I. The optimal is found for the values V_I = 2.25 and E_0/E_I = 0.45. (B) Final state of the simulation using optimal values for V_I and E_0/E_I. (C) Blade *LWR* for the optimal combination, as compared to the observations. (D) Average neighbouring cell number for the optimal combination, as compared to the observations.

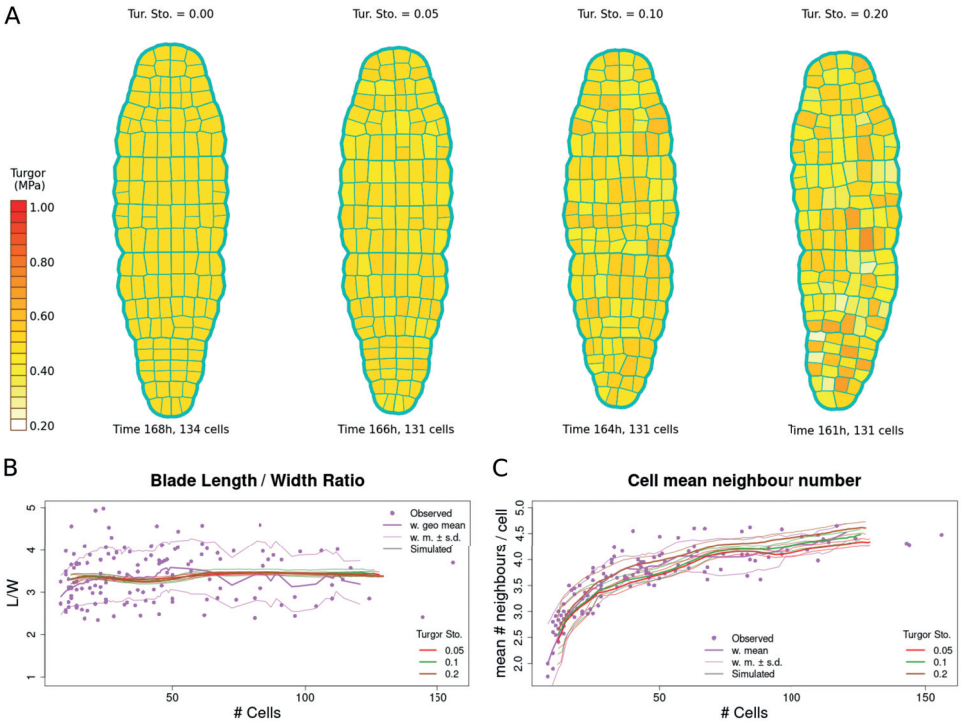

Figure 11: Effect of turgor stochasticity on simulations. (A) Final state of the blade for Turgor stochasticity levels 0.00 (no stochasticity), 0.05, 0.10 and 0.20. High level of stochasticity resulted in variable cell sizes, which alter the shape of the blade. (B) The *LWR* of the blade was not affected by turgor stochasticity. (C) Increasing turgor stochasticity caused an increase in the mean number of neighbouring cells per cell. However the effect remains lower than natural inter-individual variability.

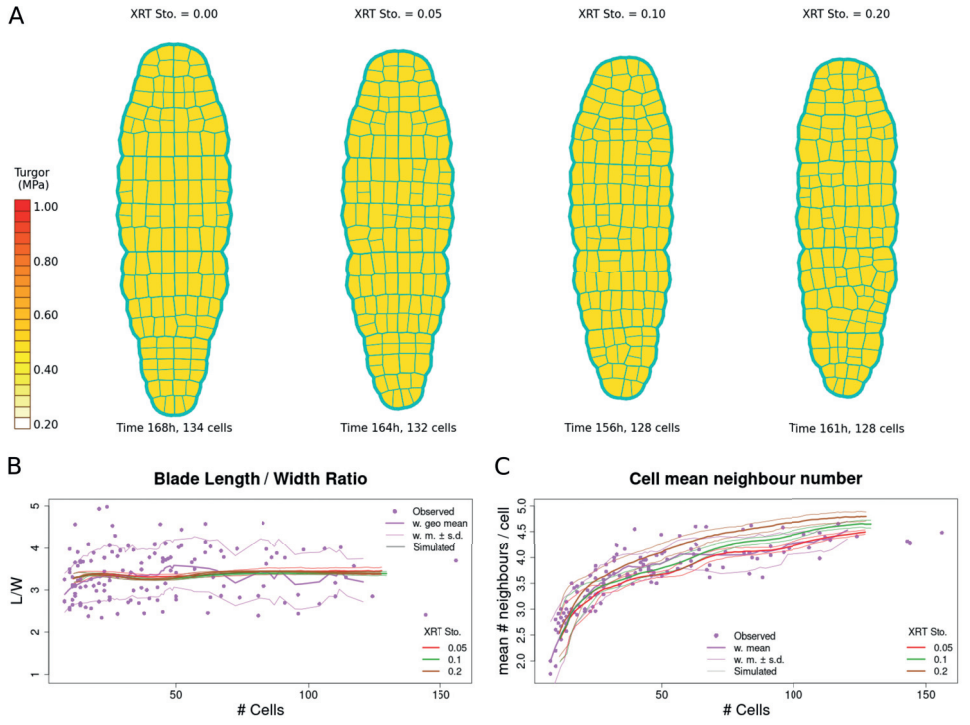

Figure 12: Effect of stochastic exchange ratio threshold on simulations. (A) Final shape of the blade for exchange ratio stochasticity levels 0.00 (no stochasticity), 0.05, 0.10 and 0.20. A high level of stochasticity affected the tissue pattern. (B) Blade *LWR*. The *LWR* of the blade was not affected by exchange ratio stochasticity. (C) Neighbouring cells. Increasing the exchange ratio stochasticity to 0.20 caused an increase in the average number of neighbouring cells (above the standard deviation).

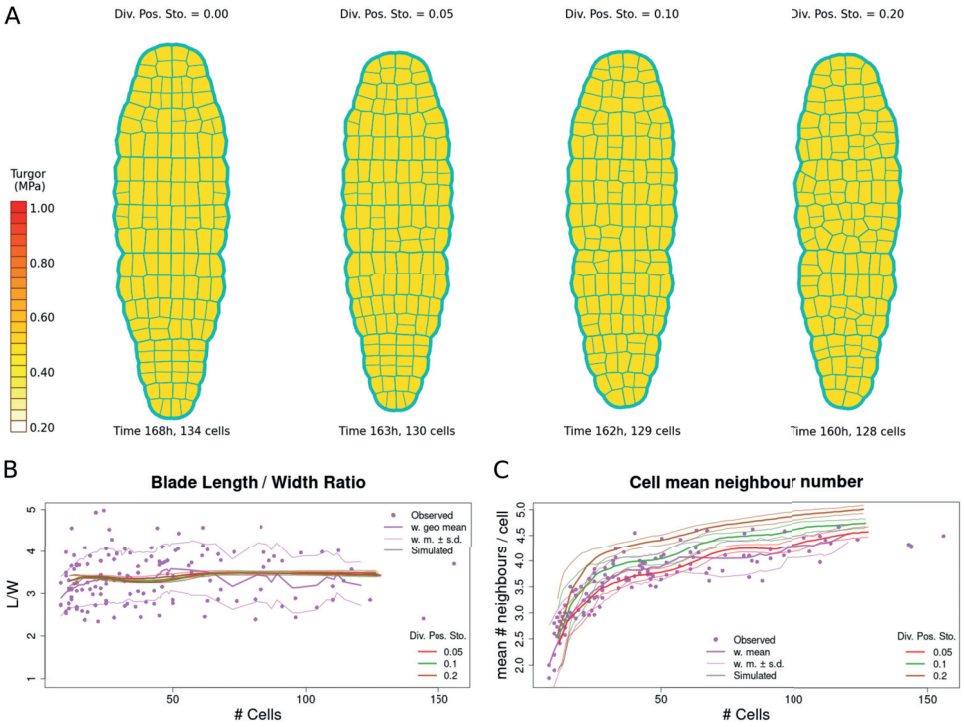

Figure 13: Effect of stochastic division plane position on simulations. (A) Final shape of the blade for stochasticity levels on the position of the division plane of 0.00 (no stochasticity), 0.05, 0.10 and 0.20. High levels of stochasticity affected the tissue pattern. (B) Blade *LWR*. The *LWR* of the blade was not affected by position stochasticity. (C) Neighbouring cells. Increasing the stochasticity of the cell division plane position to 0.10 caused an increase in the average number of neighbouring cells (above the standard deviation).

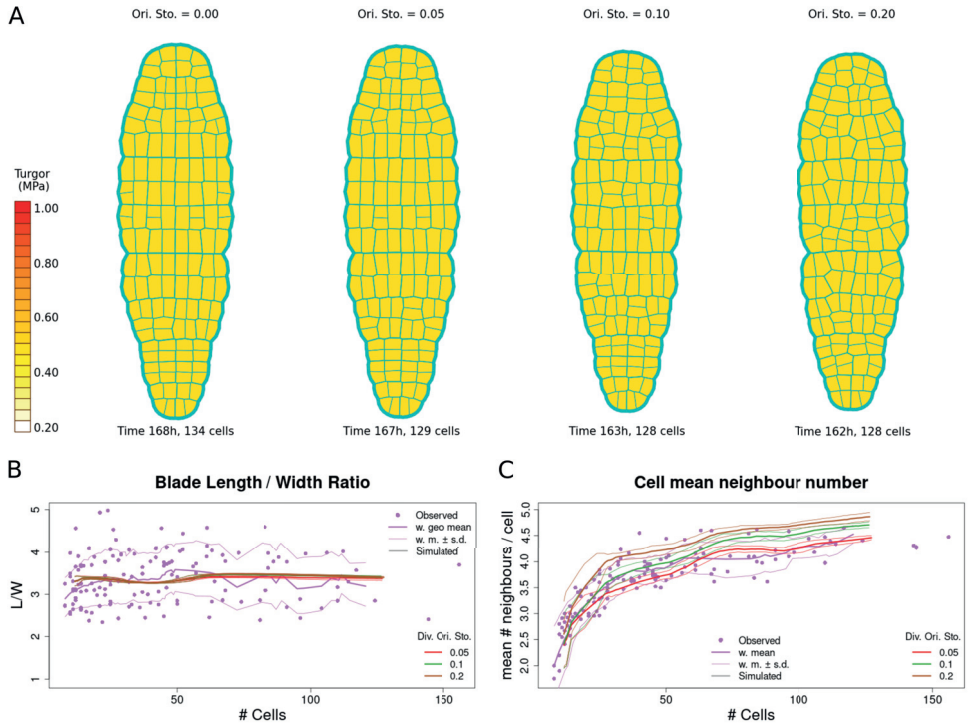

Figure 14: **Effect of stochastic division plane orientation on simulations.** (A) Final shape of the blade for stochasticity levels on the orientation of the division plane of 0.00 (no stochasticity), 0.05, 0.10 and 0.20. High levels of stochasticity affected the tissue pattern. (B) Blade *LWR*. The *LWR* of the blade was not affected by orientation stochasticity. (C) Neighbouring cells. Increasing the stochasticity of the orientation of the division plane to 0.10 caused an increase in the average number of neighbouring cells (above the standard deviation).

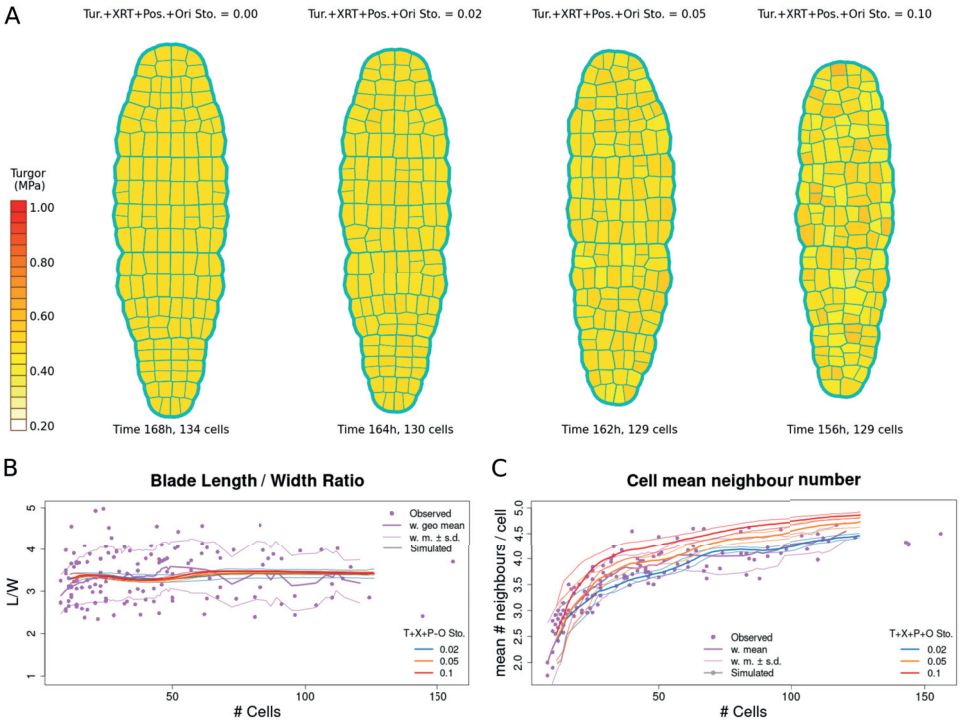

Figure 15: Effect of four stochastic parameters on simulations. (A) Final shape of the blade for stochasticity levels on the four parameters together: turgor (T), exchange ratio threshold (X), position (P) and orientation (O) of the division plane of 0.00 (no stochasticity), 0.02, 0.05 and 0.10. Note that the levels of stochasticity tested here are lower than in the previous figures. (B) Blade *LWR*. The average *LWR* of the blade was not affected by any of the stochasticity levels tested. Dispersion among samples remains low compared to the natural variability between observed specimen. (C) Counting neighbouring cells. The simultaneous application of increasing stochasticity levels to the four parameters resulted in an increase in the number of neighbouring cells. With stochasticity level = 0.1, the number of neighbouring cells is significantly higher than the mean + standard deviation of the observations.

Movies

Movie 1 : *Saccharina* blade simulation for various values of Elastic Modulus (*E*).
https://dropsu.sorbonne-universite.fr/s/jzjcc2MXYF8DZsB

Movie 2 : *Saccharina* blade simulation for various values of outer wall anisotropy (*VO*).
https://dropsu.sorbonne-universite.fr/s/dsPbgnFBi2sj6a6

Movie 3 : *Saccharina* blade simulation for various values of inner wall anisotropy (*VI*).
https://dropsu.sorbonne-universite.fr/s/gPwy3scFwqAxDJb

Movie 4 : *Saccharina* blade simulation for various values of outer *vs* inner wall ratio (*EO/EI)*.
https://dropsu.sorbonne-universite.fr/s/iXQNT9eQSAEE6B7

Movie 5 : *Saccharina* blade simulation for optimised values of inner wall anisotropy (*VI*) and outer *vs* inner wall ratio (*EO / EI)*.
https://dropsu.sorbonne-universite.fr/s/ZMLgQQRk9GKCYkN

Movie 6 : *Saccharina* blade simulation for various values Turgor stochasticity.
https://dropsu.sorbonne-universite.fr/s/o8KTkDjFyHdXKT2

Movie 7 : *Saccharina* blade simulation for various values of exchange ratio threshold (XRT) stochasticity.
https://dropsu.sorbonne-universite.fr/s/opwwCkcH45KqLq4

Movie 8 : *Saccharina* blade simulation for various values of division position stochasticity.
https://dropsu.sorbonne-universite.fr/s/SnDyKxK7bCDyfKZ

Movie 9 : *Saccharina* blade simulation for various values of division orientation stochasticity.
https://dropsu.sorbonne-universite.fr/s/fSDCW4kRNoQ7wA5

Movie 10 : *Saccharina* blade simulation for various values of turgor, exchange ratio threshold, division position and orientation stochasticity.
https://dropsu.sorbonne-universite.fr/s/yxi9F5yEDtmzCBb

Supplementary data

Supplementary figures

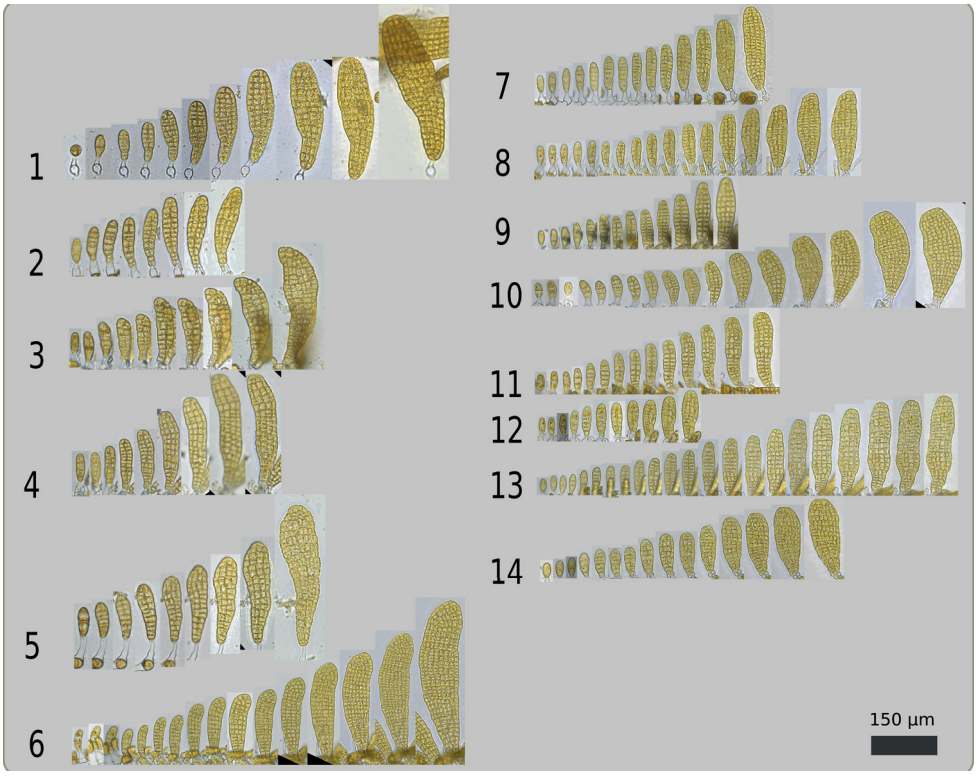

Suppl Fig. 1: Time lapse monitoring of 14 embryos of *S. latissima*. Bright field images of 14 embryos were recorded every 12 or 24 hours. Some embryos stopped being recorded before the end of the time-lapse experiment when they grew out of focus. Embryos 1-5: one time point every 24 hours; Embryos 6-14: one time point every 12 hours. Scale bar 150 µm.

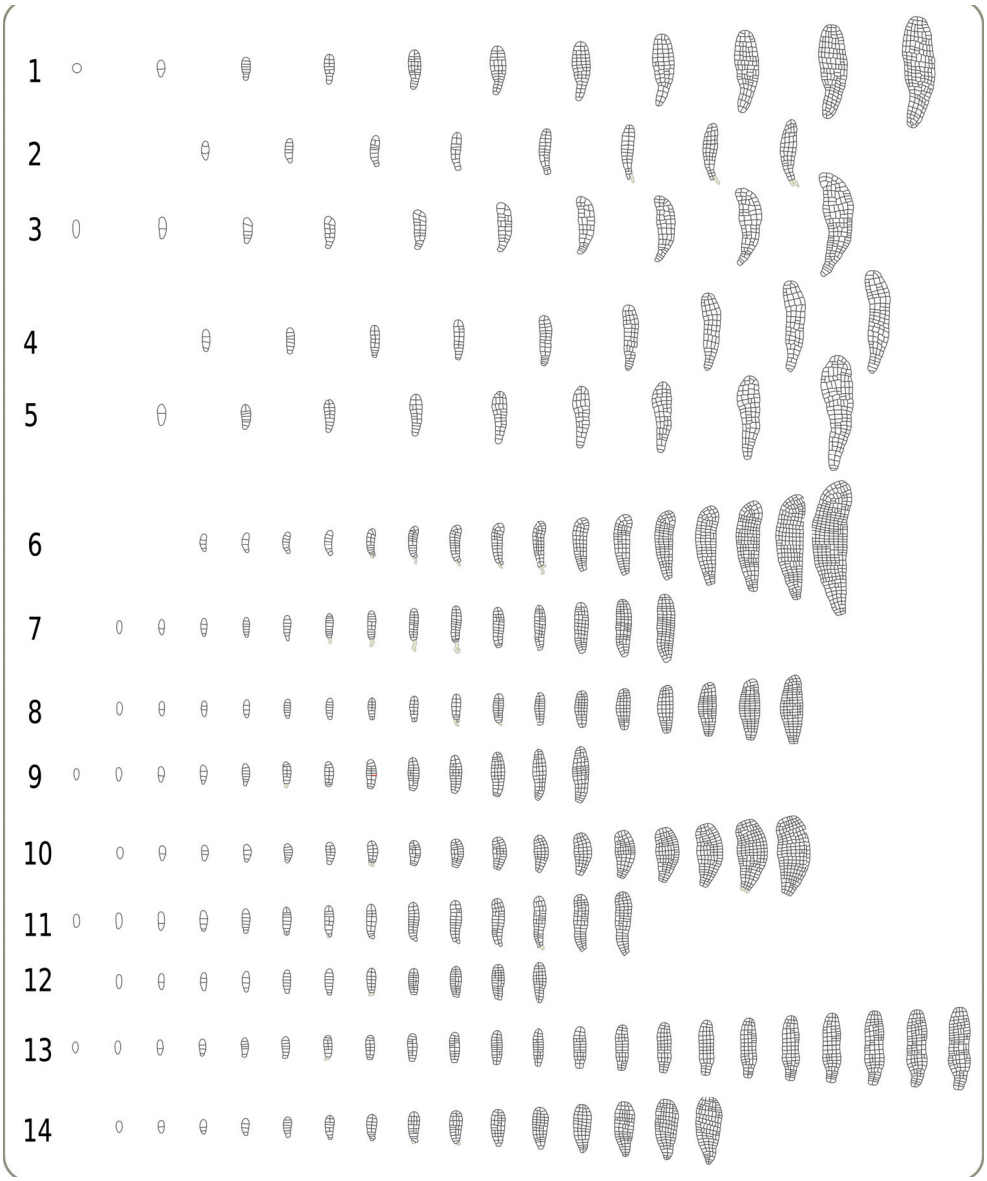

Suppl Fig. 2: Segmentation of 14 embryos of *Saccharina latissima*. The bright field images of Suppl Fig. 1 were segmented manually to display the cell contours. Embryos were not at the same developmental stage at the onset of the time-lapse. Therefore, the series were aligned to the two-cell stage, which is the most reliable benchmark because egg elongation and fertilisation are events of high temporal variability. Embryos 1-5: one time point every 24 hours; embryos 6-14: one time point every 12 hours. Scale bar 150 µm.

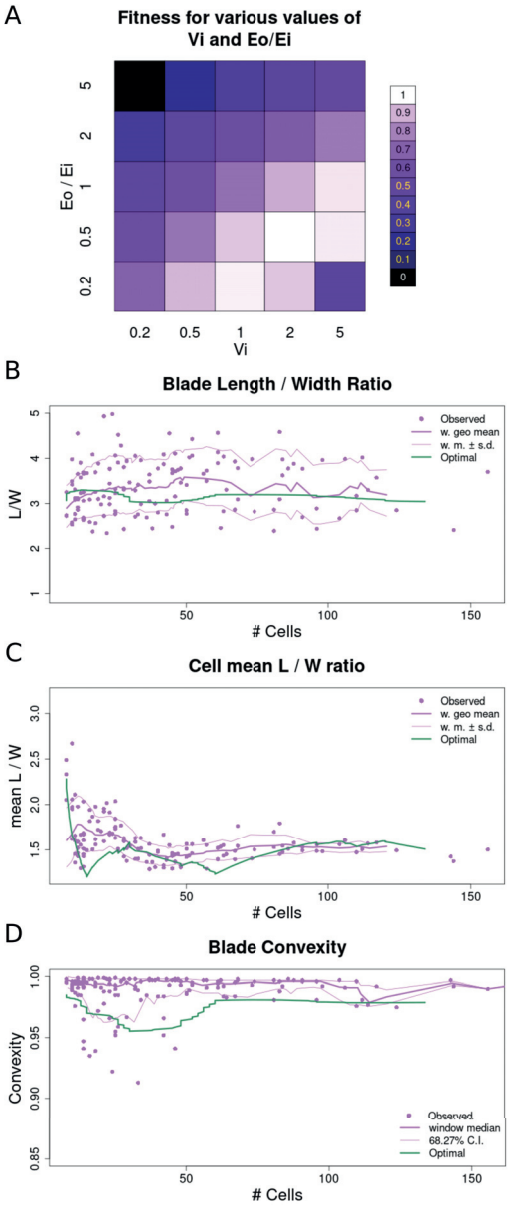

Suppl. Figure 3: First optimisation step. (A) twenty-five simulations are run, each for a combination of values of V_I and E_O/E_I. The best combination is for $V_I = 2.0$ and $E_O/E_I = 0.5$. (B-D): Behaviour of the simulation using the optimal combination, for the three optimization parameters, compared to the observations. (B) Blade Length/Width Ratio. (C) Cell Mean Length/Width Ratio. (D) Blade Convexity.

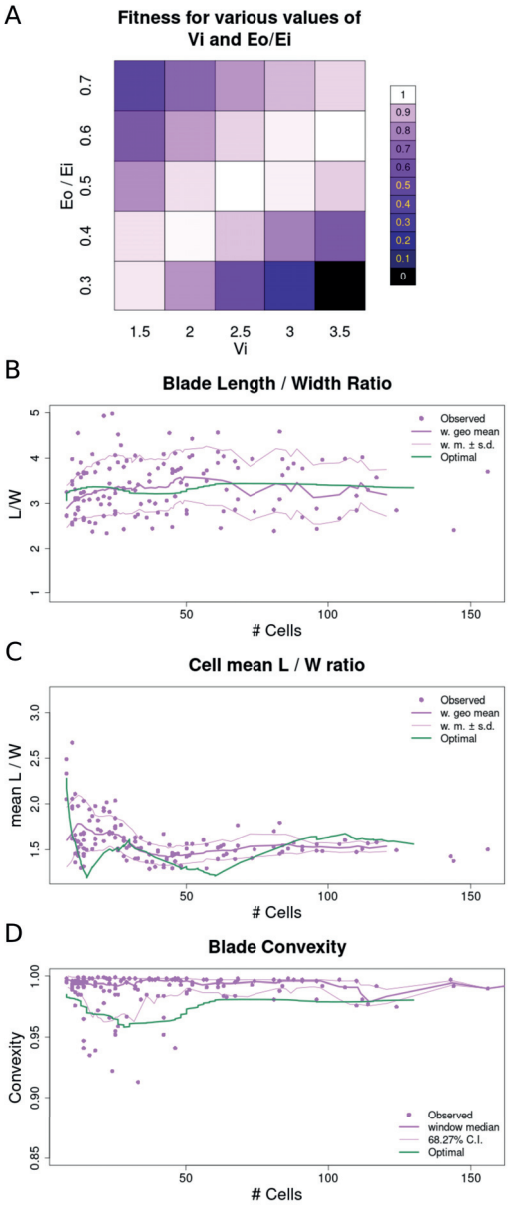

Suppl. Figure 4: Second optimisation step. (A) Results for twenty-five simulations for parameters V_I and E_O/E_I in narrower intervals than in Suppl Fig. 3. The best combination is found for $V_I = 2.5$ and $E_O/E_I = 0.5$. (B) Blade Length/Width Ratio for the optimal combination so far. (C) Cell Mean Length/Width Ratio for the optimal combination so far. (D) Blade Convexity for the optimal combination so far.

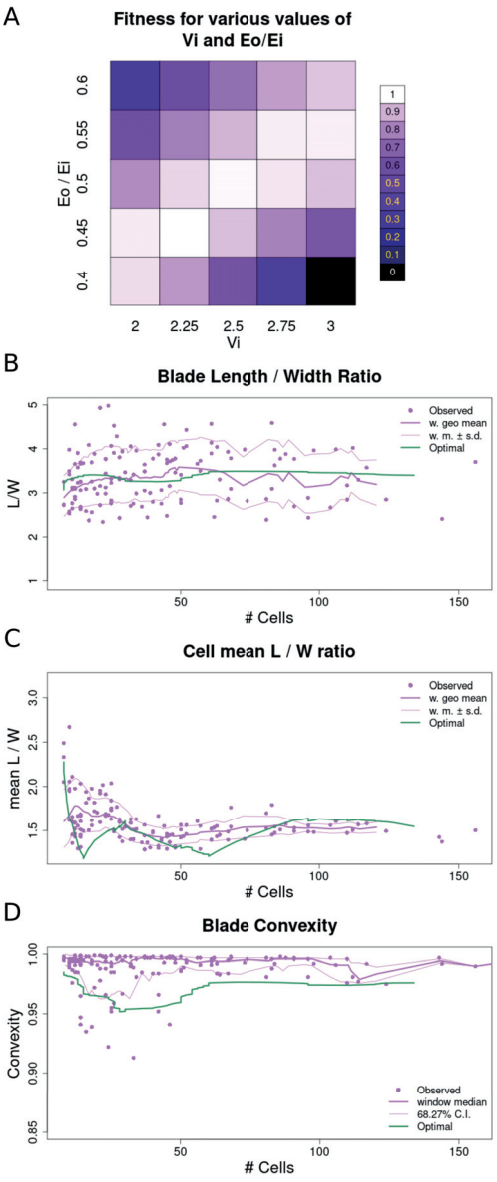

Suppl. Figure 5: Third optimisation step. (A) Results for twenty-five simulations for parameters V_I and E_O/E_I in narrower intervals than in Suppl Fig. 4. The best combination is found for $V_I = 2.25$ and $E_O/E_I = 0.45$, which is further used as a standard. (B) Blade Length/Width Ratio for the final optimal combination. (C) Cell Mean Length/Width Ratio for the final optimal combination. (D) Blade Convexity for the final optimal combination.

Supplementary Material

Ioannis Theodorou, Bernard Billoud, Samuel Boscq,
Christophe Godin, Sophie Le Panse, Bénédicte Charrier

A Vertex Model

A.1 Cell wall

Each wall is assimilated to a series of small pieces with a rectangular parallelepiped geometry. This piece, projected in the 2D vertex model as an edge e has dimensions: (i) length l (ii) wall thickness δ (iii) blade height h, the latter being assumed as identical for all edges and constant throughout all the development phase studied. From these dimensions, we compute the section area of an edge as $A = h \times \delta$.

In addition, the cell wall material is characterised by its physical properties: (i) elastic modulus (Young modulus) E; and (ii) viscosity η. Thus, the spring constant (stiffness) k of an edge is computed as:

$$k = \frac{EA}{l_0}$$

where l_0 is its resting length, *i.e.* length in the absence of any mechanical constraint.

A.2 Turgor

In cell C, turgor T_C pushes on each edge e with force:

$$\vec{F}_{Ce} = T_C \times l_e \times h \times \vec{n}_{Ce}$$

where $\vec{n}_{Ce}$ is a unit vector normal to the edge e and pointing out of cell C.
In the 2D representation, this force is assigned to both vertices defining the edge. So, the total force due to Turgor from several cells (usually 1 to 4) acting on a single vertex v shared by several edges (usually 2 to 4) is:

$$\vec{F}_{v,T} = \frac{1}{2} \sum_{e,C} T_C \times l_e \times h \times \vec{n}_{Ce}$$

Due to this force, during an infinitesimal time interval $\mathrm{d}t$, the vertex moves with velocity:

$$\frac{\mathrm{d}\vec{X}_{v,T}}{\mathrm{d}t} = \frac{1}{\eta_e} \vec{F}_{v,T}$$

A.3 Cell wall elasticity

As vertices move, length and/or orientation of edges change. An edge e which in rest has length l_{0e} and is extended up to l_e resists with:

$$\vec{F}_{Re} = -k_e \left(l_e - l_{0e}\right) \vec{u}_e$$

where $\vec{u}_e$ is a unit vector oriented in the direction of edge elongation.

Each vertex v receives one half of this force from each edge it belongs to:

$$\vec{F}_{v,R} = \frac{1}{2} \sum_{e} -k_e \left(l_e - l_{0e}\right) \vec{u}_e$$

If this force was alone, it would move the vertex with velocity:

$$\frac{\mathrm{d}\vec{X}_{v,R}}{\mathrm{d}t} = \frac{1}{\eta_e} \vec{F}_{v,R}$$

A.4 Integrating over time

The actual displacement of the vertex is:

$$\frac{\mathrm{d}\vec{X}_v}{\mathrm{d}t} = \frac{\mathrm{d}\vec{X}_{v,T}}{\mathrm{d}t} + \frac{\mathrm{d}\vec{X}_{v,R}}{\mathrm{d}t}$$

Notice that when vertices move, the cell shape changes, and in particular, its volume (area in the 2D model) increases, and Turgor decreases. Similarly, the vector directions change.

After a time interval Δt, the vertex displacement is:

$$\Delta\vec{X} = \frac{1}{\eta_e}\int_{\Delta t}\left(\vec{F}_{v,T} + \vec{F}_{v,R}\right)\,\mathrm{d}t$$

N.B. Both $\vec{F}_{v,T}$ and $\vec{F}_{v,R}$ are functions of time, but t has been omitted to lighten the notation.

A.5 Specific features

From observations, we established the following specific features:

- As cell growth tends to decrease Turgor, cells are assumed to periodicaly restore a basal value.
- Cell walls become thicker with time. To follow observations, the wall thickness after a time interval Δt, is $\delta_{t+\Delta t} = \delta_t + \min(\Delta\delta, (\delta_{max} - \delta_t)/\tau) \times \Delta t$ where $\Delta\delta$ is the linear increase rate, δ_{max} the maximum thickness, and τ the time constant for the asymptotic thickening towards δ_{max}.
- Outer cell wall is thicker than inner cell walls, so the above computation involves different parameters depending on the cell wall position.
- A cell divides when its exchange ratio ϵ = Perimeter/Area has decreased below a given threshold ϵ_{min}.
- Cells divide according to Errera's rule: the new wall passes through the cell centroid and orients so that its length is minimal.

A.6 Observed parameter values

The following values were observed (see main text) and are used as default parameters in simulations, or central values when stochasticity is used (see below):

Parameter	symbol	value	unit
Blade thickness (normal to the 2D representation)	h	12	µm
Basal Turgor	T_0	0.5	MPa
Outer wall initial thickness	$\delta_{O,0}$	0.300	µm
Outer wall thickness linear increase	$\Delta\delta_O$	0.003	µm·h^{-1}
Outer wall maximum (asymptotic) thickness	$\delta_{O,max}$	3	µm
Inner wall initial thickness	$\delta_{I,0}$	0.15	µm
Inner wall thickness linear increase	$\Delta\delta_I$	0.0006	µm·h^{-1}
Inner wall maximum (asymptotic) thickness	$\delta_{I,max}$	1	µm
Asymptotic wall increase time constant	τ	200	hour
Exchange ratio threshold	ϵ_{min}	0.35	µm^{-1}

A.7 Model assumptions

For all simulations, we assume the following features:

- At time $t = 0$, the blade is made of 8 cells arranged as a column. This initial embryo was designed as an average of the observed embryos of the same stage. The geometric mean of the measured ratios between main and secondary axis length (3.05), together with the average blade area (740 µm^2) were used to build an equivalent ellipsis. We also estimated, for each blade, how wider was its upper part

vs lower part (the bottom being considered at the attachment to the maternal tissue), by computing the ratio between the width at 3/4 of the height and the width at 1/4 of the height. We applied a geometrical deformation to the ellipsis to reproduce this ratio. We positioned the transversal cell walls to reproduce the respective mean areas of the observed cells at the same place in the stack.

- Cells are considered to re-equilibrate their turgor to T_0 every hour.
- Also every hour, most of cell wall elastic elongation is converted into plasticity, *i.e.* for each edge, l_0 is replaced by $l_0 + \lambda(l - l_0)$. By default, we set $\lambda = 0.8$.
- Simulations run up to the moment when the cell number in blade reaches at least 128.
- Elastic modulus E is set to a value allowing the blade to grow at the expected rate, that is to reach 128 cells after 168h.

Other parameters are tuned in order to maximize fitness between the outcome of a simulation and the expected features of a blade.

A.8 parameter optimization

As a target for optimization, we build an index combining three parameters:

$bLWR$: Blade L/W ratio computed as $\sqrt{\lambda_1/\lambda_2}$ where λ_1 and λ_2 are respectively the first and second eigenvalues of the inertial tensor matrix T[1]

$$T = \begin{pmatrix} I_{xx} & -I_{xy} \\ -I_{xy} & I_{yy} \end{pmatrix}$$

with $I_{xx} = 1/12 \sum_{i=1}^{n} (x_i y_j - x_j y_i)(y_i^2 + y_i y_j + y_j^2)$, $I_{yy} = 1/12 \sum_{i=1}^{n} (x_i y_j - x_j y_i)(x_i^2 + x_i x_j + x_j^2)$, $I_{xy} = 1/12 \sum_{i=1}^{n} (x_i y_j - x_j y_i)(x_i y_j + 2x_i y_i + 2x_j y_j + x_j y_i)$ for the coordinates (x_i, y_i) and (x_j, y_j) of two successive points ($j = i + 1$, $j = n + 1$ loops on $j = 1$) of the counter-clockwise list of n vertices of the blade perimeter.

$cLWR$: geometric mean of the L/W ratios (computed as above) of all cells in the blade;

$bCvx$: Blade convexity measured as the ratio between the length of the blade's convex hull and the blade perimeter[2].

Out of a simulation, at each time point we extract one couple: $(n, p_s(n))$ where n is the number of cells and p_s the simulated value for parameter P (where $P \in \{bLWR, cLWR, bCvx\}$). We estimate the average values in simulation by computing them from observed data in a sliding window of width 16. This results in a series of couples $(n, p_o(n))$ for the same values of n as the simulations. The difference between simulation and observations for N time points for parameter P is:

$$d_P^2 = \frac{1}{N} \sum_n \left(\frac{p_s(n) - p_o(n)}{p_o(n)} \right)^2$$

For the three considered parameters, we compute a unique difference by summing:

$$D^2 = \sum_P d_P^2$$

This metrics are used to compare, and optimize the values for one or more parameters.

To visually compare a series of simulations, we set a graphic representation where the D^2 index of simulation s is shown as a color, representing a relative fitness factor F with value between 0 (less fitted) and 1 (most fitted):

$$F(s) = \frac{\max(D^2) - D^2(s)}{\max(D^2) - \min(D^2)}$$

[1] see Fletcher *et al.* (2013) *Progress in Biophysics and Molecular Biology* 113:2, pp 299–326, doi: 10.1016/j.pbiomolbio.2013.09.003

[2] see Lobo *et al.* (2016) *J Tissue Eng Regen Med*, **10**: 539–553, doi: 10.1002/term.1994

A.9 Stochasticity

Various parameters are subject to stochasticity, the level of which is set by parameter S. Implementation is as follows:

Turgor : whenever a cell is created, its basal turgor $T_0^{[S]}$ is drawn from a truncated normal distribution:

$$T_0^{[S]} \mapsto N(\mu = T_0, \sigma = S \times T_0); \quad T_0^{[S]} > 0$$

Exchange Ratio Threshold : a value of $\epsilon_{min}^{[S]}$ is set in each new cell, following a truncated normal law:

$$\epsilon_{min}^{[S]} \mapsto N(\mu = \epsilon_{min}, \sigma = S \times \epsilon_{min}); \quad \mu - 1.96\sigma < \epsilon_{min}^{[S]}\mu + 1.96\sigma$$

Cell Division Position : instead of passing through the centroid C, the division axis is shifted so as to pass by a point $C^{[S]}$ for which the angle α of $\overrightarrow{CC^{[S]}}$ with the horizontal follows a random uniform distribution in $[0, 2\pi]$, and the distance $CC^{[S]}$ is drawn from a truncated normal distribution:

$$CC^{[S]} \mapsto N(\mu = 0, \sigma = S \times r_\alpha); \quad CC^{[S]} < r_\alpha$$

where r_α is the radius, in the direction α, of the ellipsis having the length and width of the cell as main radiuses.

Cell Division Orientation : The angle of the division axis with the horizontal $\theta^{[S]}$ follows a normal distribution around the direction θ chosen using the Errera rule:

$$\theta^{[S]} \mapsto N(\mu = \theta, \sigma = S \times \pi/4)$$

Paper II: Organisation of the cytoskeleton in the early embryo of the kelp *Saccharina latissima*

State of publication: In preparation, not yet submitted

Contributions: The manuscript was written by me and B. Charrier. I acquired the experimental data and interpreted them together with her.

Title: Organisation of the cytoskeleton in the early embryo of the kelp *Saccharina latissima*

Authors: Ioannis Theodorou[1,2] and Bénédicte Charrier[1]

Affiliations:

[1:] Laboratory of integrative marine models, Station Biologique de Roscoff, UMR8227, CNRS, Sorbonne University, Place Georges Teissier, 29680 Roscoff, France

[2:] Plant Sciences Department, Faculty of Biosciences, Norwegian University of Life Sciences, Ås, Norway

KW: brown algae, cytoskeleton, kelp, embryogenesis, morphogenesis, tissue, grid, actin filaments

Abstract

Saccharina latissima is a brown alga. Its sporophyte is a large organism and essential for the formation of marine forests along most coasts of the northern hemisphere. However, little is known on their early development and specifically which mechanisms govern over their morphogenesis. morphogenesis for *Saccharina*'s embryogenesis, we look into the cytoskeleton structure at its different cell types with focus on the organisation of actin filaments. Microtubules are organised as a cage with two poles surrounding the nucleus. The actin filaments form sheets at the anticlinal cell walls with specific orientation of the filaments. In addition, drugs targeting the actin cytoskeleton affect the cell and tissue shape, indicating an essential role of actin to the morphogenesis of embryonic cells. We hypothesise that the specific organisation of actin filaments, guides growth of the cells along a two-axial system, while they are orientated parallel to the tensile stresses generated by the tissue growth.

Introduction

Actin filaments (AFs) and microtubules (MTs) are essential part of every eukaryotic cell. They play important roles in morphogenesis (Fletcher and Mullins 2010; Munjal et al. 2015; Szymanski and Staiger 2018; Elliott and Shaw 2018; Röper 2020) by contributing to signalling and endomembrane trafficking (Drøbak et al. 2004; Rahman et al. 2007; Zhu and Geisler 2015) as well as cell wall biogenesis (Baskin et al. 2004; Chen et al. 2007) and more special cases of cell physiology like gravitropism (Pozhvanov et al. 2013). Particularly interesting is how the organisation of cytoskeleton is connected to cell shape changes and maintenance in the different multicellular lineages. For instance, animals have a well-developed cortical system consisted of AFs and myosin (Chugh and Paluch 2018). This cytoskeletal system generates tension in many different occasions (e.g. cell migration, cell division, constriction). The

changes in tension, their localisation and intensity are what give shape to the animal cells (Salbreux et al. 2012).

Plant cells and, in general, cell walled organisms are enclosed into a rigid extracellular matrix (ECM) which, however, exhibits flexibility and is susceptible to changes in its chemical composition and structural organisation (Charrier et al. 2019; Zhang et al. 2021). .

Plant protoplasts interact directly with the cell wall via the cellulose synthases which are connected to the cortical MTs (Baskin et al. 2004; Paredez et al. 2006; Landrein and Hamant 2013). The orientation of the cellulose microfibrils plays an important role in the physical attributes of the CW, hence in cell shape and tissue development (Geitmann and Ortega 2009). Many works establish that the MTs respond to mechanical stress and are guiding the orientation of cellulose microfibrils for tissue and cell morphogenesis (Landrein and Hamant 2013; Sampathkumar et al. 2014; Louveaux et al. 2016; Robinson and Kuhlemeier 2018; Hamant et al. 2019; Stöckle et al. 2022; Schneider et al. 2022). In essence, the cortical MTs organisation depends on cell geometry, direction of growth and applied tension as well as the tissue properties, interacting in a feedback loop with these parameters. On the other hand, AFs are an important part of plant cytoskeleton and often interacting with MTs, participating in the determination of the cell division plane (Kojo et al. 2013), morphogenesis of stomata complexes (Panteris et al. 2018), root cells elongation at the transition zone (Takatsuka et al. 2018), trichome morphogenesis (Tian et al. 2015) and in tip-growth (Cheung et al. 2008; Szymanski and Staiger 2018). However, they are not as stable as MTs and are subject to high remodelling dynamics (Staiger et al. 2009).

Brown algae are a distinct multicellular group of photosynthetic organisms (Bringloe et al. 2020). Their cytoskeleton structures are mostly studied on filamentous algae and zygotes and only a few on parenchymatic tissues (Katsaros et al. 2006). Common characteristic is the cortical AFs and central positioning of MTs structures. Our model *Saccharina latissima* is a parenchymatic brown alga consisted of a several meters long lamina attached to a much shorter stipe. Its development is divided into three Phases according to its growth axes and its cell division mode (Theodorou & Charrier, in prep, Paper III). During Phase I, cell divisions take place perpendicularly along the longest growth axis, these are defined as anticlinal transverse divisions, and during this Phase an apico-basal polarity is established. On Phase II, divisions shift from anticlinal transverse to anticlinal longitudinal in a sequential way following the empirical division rule of Errera, with the division plane passing through the centroid of the cells and along the shortest possible path. This results in a monostromatic tissue growing along two axes; the apico-basal axis and the medio-lateral axis. The third axis is introduced at Phase III together with the emergence of different tissue types.

During Phase II, cells align to form a grid in which the cells connect to each other through 4-way junctions shared by each cell vertex (Paper I, Paper III). To better understand the mechanisms underlying the formation of the grid, we aimed to investigate the role played by the cytoskeleton in this tissue patterning. We first described in detail the organisation of the cytoskeleton, especially AFs, in Phase II embryos, and initiated a discussion for its potential morphogenetic functions during the grid morphogenesis.

Materials and methods

Algal material

Phase II, embryos displaying a grid tissue pattern were used for this study. They developed from gametophytic cultures prepared according to Theodorou et al. (2021). In short, gametogenesis was induced under white light conditions at 16 µmol photons m^{-2} s^{-1}, 14:10 light:dark photoperiod and 13 °C and full provasoli enriched seawater (PES) (Le Bail and Charrier 2013; Theodorou et al. 2021). Then, the embryos were transferred to white light.

Microtubule immunolocalisation and actin labelling

For the microtubule immunolocalisation a combination of protocols from Tsirigoti et al. (2014) and Rabillé (2018) was used. Phase II embryos were fixed in 2% paraformaldehyde (PFA) in microtubule stabilising buffer (MTB, 50 mM PIPES, 5 mM ethyleneglycolbis(aminoethyl ether)-tetraacetic acid (EGTA), 5 mM $MgSO_4.7H_2O$, 25 mM KCl, 4% NaCl, 2.5% polyvinylpyrrolidone 25 (PVP), 1 mM DL-dithiothreitol (DTT),pH7.4) at 4 °C. The material was then washed and gradually changed from MTB to phosphate buffered saline (PBS; 137 mM NaCl, 0.7 mM KCl, 5.1 mM Na_2HPO_4, 1.7 mM KH_2PO_4, 0.01% NaN_3, pH 7.4). The cell wall of the fixed material was digested with cell wall lysis buffer (enzymes composition in PBS: 2% w/v Cellulase Onozuka R-10 (Yakult Pharmaceutical industry Co., Ltd.), 2% w/v Hemi-Cellulase (Sigma-Aldrich®), 1% driselase (Sigma-Aldrich®), 1.5% Macerozyme R-10 (Yakult Pharmaceutical industry Co., Ltd.) and 50 U/ml Alginate lyases-G (Station Biologique de Roscoff)) in 1:1 MTB:PBS, prepared according to Rabille (2018), with last addition the solution of alginates. Incubation took place for 10 min at room temperature (RT). Then, the cells were permeabilised and emptied of any pigments with 4% Triton X-100 (Sigma-Aldrich®) in PBS for 15 min at RT. A Blocking step took place with 1% Bovine Serum Albumine (BSA; Sigma-Aldrich®) for 10 min at RT. The primary antibody, Rat Anti tubulin-α IgG clone: YL 1/2 (mca77g, BioRad) was diluted in 1% BSA in PBS. Incubation overnight at RT was followed by adding the secondary antibody, fluorescein isothiocyanate (FITC)-IgG (polyclonal, Sigma-Aldrich®) diluted in 1% BSA in PBS and incubated for a couple of hours in the dark at 37 °C. The nucleus was stained with DAPI at 15 µg.mL^{-1} but for this series of experiments, it didn't give any proper signal. We mounted the samples on Vectashield H-1000-10 (Vector®) before observing at the confocal microscope. The images presented below are representative specimen out of a sample of 10 thalli.

The actin labelling protocol was a modified version of Rabillé et al. 2018. First, the material was prefixed at 300µM m-maleimido benzoic acid N-hydroxy succinimide ester (MBS; Sigma-Aldrich®), 0.2% Triton X-100 and 2% dimethyl sulfoxide (DMSO) in MTB for 30 min in the dark and at RT. Fixation took place without washes for 1:30 hr in the dark and at RT. Material was fixed at the same time as the actin labelling with 2% PFA, 0.2% glutaraldehyde (GTA) and 2 U of Rhodamine conjugated phalloidine (Ph-Rh; R415, Invitrogen™) or Alexa-fluor™ 488 conjugated phalloidine (Ph-Alexa488; A12379, Invitrogen™). After cells were washed with MTB : PBS 1:1, and the cell wall was digested with cell wall lysis buffer in 1:1 MTB : PBS and the same composition of enzymes as above with the addition of 5 U Ph-Rh/ Ph-Alexa488 and 0.15% Triton X-100. The incubation in the modified cell wall lysis buffer took place for 10 min

in the dark at RT. Extraction step took place with 5% DMSO, 3% Triton X-100 and one of the Phalloidin conjugates (2U) in PBS for 10 min in dark and at RT. The actin filaments were finally stained with 15U of the chosen phalloidin conjugate in MTB : PBS 1:1, overnight at 4 °C in the dark. The nucleus was stained with DAPI and before observation we mounted the material in Vectashield H-1000-10 (Vector®).

Image analysis

Image data are acquired with the bright field and epifluorescence microscope DMI8 (Leica Microsystems ©) equipped with the color camera DMC4500 (Leica Microsystems ©), Leica EL6000 compact light source and controlled with LAS X v3.0 (Leica Microsystems ©) and confocal microscope (TCS SP5 AOBS inverted confocal microscope (Leica Microsystems ©) controlled by the LASAF v2.2.1 software (Leica Microsystems ©). The data were analysed using FIJI (Schindelin et al. 2012). In addition, we used the MT_Angle2Ablation_Workflow (Verger Lab 2021) from github for measuring the orientation of actin microfilaments at the surface of the tissue. The measurements were plotted with R.

Drug treatments

We treated Phase II embryos with latrunculin B (LatB, 100 nM, Sigma Aldrich) or nocodazole (Noc, 13 µM, Sigma Aldrich) and then monitored their growth for 6 days with a bright field image acquisition every 24 h. Both drugs are stored in dimethyl sulfoxide (DMSO), therefore we added a 0.04% DMSO treatment as control, and full Provasoli enriched seawater (NSW) for additional control. Tissue morphometric data were collected from the acquired images and plotted with Excel (Microsoft Office 365 ©).

Results

Microtubules

The organisation of microtubules (MTs) in the cells of the embryo of *Saccharina latissima*'s in Phase II displays differences depending on the cell type. On figure 1A, we observe the MTs of the lamina cells to converge in dots, presumably centrioles surrounding a large empty area, probably filled by the nucleus as observed in Dictyota's vegetative cells (Katsaros and Galatis 1992). Specifically, the MTs grow from the two centrosomes and extend towards the cell peripheryforming on the one hand a cage-like structure visually similar to a large mitotic spindle (detail, S3 video) and on the other hand a mesh of astral MTs irradiating to the cortex. Interestingly, the long axis of this cage does not look to be systematically parallel to the longest cell axis (fig. 1B), but the deformation of the tissue during fixation does not allow us to affirm this.

In the rhizoid, MTs organise into long cable-like structures along the shanks of this very polarised cell (fig. 1C,D) and branch out before the dome of the cell tip. There, finer cortical MTs pass merge at several focused points to make an intricate structure (fig. 1E,F). The cortical placement of the MTs can be observed at different optical sections in confocal microscopy (fig. 1G i)-iii)). At the median (ii) plane, the MTs seem aligned parallel to the surface of the dome with two focused points at the very tip. At the front (i) and back (ii) sections, the MTs seem to form a mesh with many branches.

Actin filaments organisation and orientation

The organisation of actin filaments (AFs) differs among cell types of the Phase II embryos. In the rhizoids, AFs make a fine oriented meshwork at the shanks of the cell, localised mostly in the cortex (fig. 2A). At the apex of the tip, there is no specific filamentous organisation and we can observe spots of actin at the exit of the dome before the formation of the meshwork. At the base of the rhizoids (fig. 2B-E), the AFs meshwork seems to be a continuation of the cortical AFs from the previously cuboid cell while the nuclei are found further into the rhizoidal cytoplasm. This organisation contrasts with that of the cuboid cells of the lamina, where AFs are cortical and rarely extending through the cytoplasm (fig. 2F).

On more advanced Phase II specimens, we observe the same cortical organisation of AFs along all the embryonic tissue (compare fig. 3A and fig. 3C) while nuclei seem to occupy a large part of the cell volume (fig. 3A). The cuboid shape of the cells and their arragement as a grid are conspicuous (fig 3A-D). When the cells of the grid are observed at a median optical section, rarely any AFs extend through the cytoplasm (fig. 3E,F), so the AFs are rigidly packed along the cortex of the cells. There is a certain orientation to the AFs in the lateral (Z-orientation) cellular cortex compared with the AFs at the front and rear surfaces (X-Y planes) of the lamina (fig. 3G,H vs I,J), wherethey extend from the edges of the cells towards the center of the surface with random orientation (fig. 3G,H). The lateral AFs at both transversal (fig. 3I) and longitudinal sections (fig. 3K) are parallel to the Z-axis (axis system on fig. 3). However, the overall AFs structure remains a meshwork on both positions (surface and lateral). To quantify and verify this observation we measured the orientation of AFs with the fibril tool (Boudaoud et al. 2014; Verger Lab 2021) and reference line the parallels to the surface of the tissue (fig. 4). The orientation of the front and rear surface AFs (50.37 ° ± 26.41) is significantly different from that of the lateral AFs (77.69 ° ± 10.43; student T test, p-value < 0.0001, Table 1) (fig. 4). The dispersion from the average is lower for the lateral AFs than for the surface AFs, meaning that the orientation of the former is more constrained than that of the latter.

Morphological impairment under drug treatment

Embryos were treated with several drugs known to perturb the dynamics of the cytoskeleton. Depending on its concentration, the drug latrunculin B inhibits cell divisions and zygote polarity (Bisgrove and Kropf 2004; Nagasato and Motomura 2009; Nagasato et al. 2010), but also disrupts the polarity and/or morphogenesis of the embryos (Varvarigos et al. 2004; Bogaert et al. 2017). In land plants, nocodazole is considered to target mitotic microtubules (Hoffman and Vaughn 1994; Baskin et al. 2004) that are necessary for mitosis and cytokinesis and oryzalin is used to target cortical or structural microtubules (Morejohn et al. 1987; Baskin et al. 2004). However, *Dictyota* embryos did not respond morphologically to oryzalin (Bogaert et al. 2017) and therefore we used nocodazole.

Treatments of *Saccharina* embryos with nocodazole resulted in cell plasmolysis after 72 h (fig. 5 A, B, compared to DMSO control, fig. 5C)), . Plasmolysis was reversable for some of the cells; however, it often preceded a crashing incident from the turgor pressure of their neighbouring

cells leading to their death (fig. 5A at 48 h). Development overall seems arrested and longitudinal anticlinal divisions are blocked.

The phenotypic impact of Latrunculin B (latB) was less severe that that of nocodazole. After 72 h, most specimens tended to have a sigmoid tissue shape (fig. 6). Usually, the developing embryos are transparent to the bright field light source due to the one layer of cells, except when they are bullate or making an increased angle with the focal plane. In contrast, the LatB-treated specimens display an oblique conformation (e.g. timepoints 96 h and 144 h of LatB treated embryos vs NSW, fig. 6). In addition, the treated specimens look thicker than the control and the outlines of only a few cells are trully distinguishable, especially those positionned at the outer outline of the lamina. These led us to conclude that cells have grown in response to LatB treatment. The fact that the shape of the lamina has lost planarity suggests that cell growth in the Z-axis has taken place. In addition, the lamina looked particularly thick during the last timepoint of the sequential optical sections (fig. 6 LatB, 144 h, a-c) and the cells potentially have a rough surface. At the end of the timelapse most embryos seemed to be consisted of an outgrowth of the one cell layer, due to the lack of transparency and thicker looking tissue. However, this growth does not seem to follow the usual alignment of the cells and is potentially random. It is unclear if there is an addition of a cell layer. Nevertheless, the initial layer of cells remains morphologically as a grid (additional specimens are showed in fig. S2). Observations with non-toxic cellular stains could facilitate the observations. Overall, cell division was hindered, and the resulting size of the embryos was qualitatively smaller than the control.

In addition to the visual description, key morphometric parameters like the the length and width of the thallus as well as the number of cell rows (R) and columns (C) were measured. As quantitative parameters, R and C give an estimation of the transverse and longitudinal anticlinal divisions respectively. The product C x R provides a rough estimation for the number of the cells over time. Therefore, R and C are proxies for the cell division rate and orientation. The slope from linear regression of the morphometrics over time was calculated by giving the increasing rate (α) for each parameter over time.

For a population of different size and cell number specimens, results show a considerably varying α for nearly every parameter (Table S1). Arithmetic mean comparisons and student t-tests suggest that Noc impairs the growth of the embryos on both axes, which is supported by the low division rate over time (< 1 division h-1) and no division on rows or columns.

In response to LatB, α is 0.87 µm h^{-1} ± 0.33 µm h^{-1} for the length and 0.20 µm h^{-1} ± 0.10 µm h^{-1} for the width on average. The blade divides 0.60 divisions h^{-1} ± 0.42 and forms 0.02 columns h^{-1} ± 0.01 and 0.10 ± 0.06 (Table S1). The number of specimens is shown per treatment on table S1. These are smaller values than when the embryos grow in NSW, (Table S1). While the growth rate in length of specimens with similar sizes at t0 (fig. 7 A,B) is not so different between LatB and NSW, the width is significantly different (fig. 7B, student T-test p-value < 0.05, including all the specimen, check tables S1 and S2). The nearly invariant number of cell columns and rows in the embryos at the end of Noc treatment supports that cell division activity is impaired (fig. 7 C,D). For LatB, the columns are significantly different when

compared to NSW, supporting that the t impaired orientation of cell division for LatB treatment is longitudinal anticlinal (along the X-axis).

Discussion

Microtubules

In thallus cells, MTs are aligned as a cage around the central region of the cells extending through the cortex (fig. 8). Similar microtubular cages are observed in *Dictyota dichotoma* around the nucleus (Katsaros and Galatis 1992). In *Dictyota*'s cells, the centrioles are positioned at opposite poles, adjacent to the nuclei. In our case, radiating MTs from the centrioles extend almost to the whole width of the cells including most likely a larger volume than just the nucleus (the nuclei were not displayed in our experiment). This organisation is very different from the cortical MTs of land plants (Vavrdová et al. 2019). in the rhizoid, MTs are organised differently depending on their distance to the cell tip. A large cable like structure going through the cytoplasm up to the tip and then a fine network of cortical MTs were observed with several focal points at the apex. The last part close to the apex is similar to wha tis observed in the apical cell of in the filaments of the brown algae *Ectocarpus siliculosus* and *Sphacelaria rigidula* (Katsaros 1992). However, in the rhizoids, the nucleus is probably stationed away from the tip as we did not display any centrioles that would have indicated the presence of the nucleus in this cell area. There are focal points in both species like in *Saccharina*'s rhizoids. In the root hairs (Lloyd 1983) and pollen tube (Cai et al. 2005) of land plants, the apex of the cells is empty of MTs, while the shanks are rich in thick bundles of MT, especially close to the dome area. This constrast with *Saccharina*'s rhizoids where thicker MTs are localised at the base of the rhizoid. Interestingly, the organisation of MTs at *Saccharina*'s rhizoid is reminiscent of the organisation of MT in caulonemal tip cells of moss (Doonan et al. 1985), in which MTs form a network with longitudinal bundles. This network subsides towards the base of the caulonema like in *Saccharina*. However, there are more cytoplasmic MTs close to the apex of the moss cells in comparison with the cortical arrangement of *Saccharina*. The organisation of the MT cell network is very diverse in the tree of life, and *Saccharina* enriches this diversity, firstly by showing different organisations in the cuboid cells of its lamina and in the polarised rhizoids, which in both cases differ from those of land plants.

Treatment with nocodazole hindered significantly the growth of the embryos, by inhibiting cell division, and potentially the function of vacuoles which led to plasmolysis. The development of fucoidan zygotes is also impaired by nocodazole, which blocks the first cell division (Schoenwaelder and Clayton 1999). Similar results were obtained in the germinating zygote of *Ectocarpus*, in which the first 3 mitoses occurred with no cytokinesis, leading to multinucleated, elongated embryo (unpublished). This study shows that the inhibitory effect of nocodazole on cell division goes beyong the zygotic stage and expand to the embryonic stages where it blocks cell division.

Actin filaments

In the rhizoids, we do not observe any specific organisation like an actin fring or ring (Stephan 2017) as observed in land plant root hairs and pollen tube, but their depleted apical and

subapical regions are a common characteristic with *Saccharina*. Nevertheless, a well-organized MT cytoskeleton resides at the position of the dotted AF.

In the lamina of *Saccharina*, the AFs lamina are tightly packed forming sheets at the cellular cortex only rarely crossing through the cytoplasm (fig. 8). Cortical arrangement with distinct orientation of AF has been observed in *Sphacelaria* (Karyophyllis et al. 2000), *Macrocystis* (Varvarigos et al. 2004) and *Dictyota* (Katsaros et al. 2002). However, these species demonstrate additional organisations like radial spreading in developing protoplasts of *Macrocystis* and perinuclear and cytoplasmic localisation in *Sphacelaria* and *Dictyota*. Only in the meristematic epidermal cells of *Dictyota* there is a similar organisation of AFs packed in cortical sheets with a transverse orientation. An actin patch is also localised during cytokinesis in brown algal cells, between the two nuclei (Brawley and Robinson 1985; Karyophyllis et al. 2000; Bisgrove and Kropf 2004; Motomura et al. 2010) which is also observed in *Saccharina* (not shown).

Potential functions for the sheets of actin filaments in the embryogenesis of *Saccharina*

The cortical localisation of AFs inthe cells of the lamina is reminiscent of the cortical AFs also present in plants and animals. However, in animals, cortical actin forms together with myosin a dynamic partnership involved in cell migration, tissue folding, and withstanding any tissual tension (Chugh and Paluch 2018; Svitkina 2020), controlling cell shape and several cellular functions. In land plants, the cortical arrays of AFs are long filaments, often bundles, with great remodelling dynamics (Panteris 2008; Staiger et al. 2009). Interestingly, guarding cells of plant leaf stomata shared a similar organisation with *Saccharina* lamina cells, as AFs are packed at the lateral anticlinal cell walls of the guard mother cell (GMC), its derivatives and subsidiary cells (Apostolakos and Galatis 1999; Panteris et al. 2007, 2018). However, AFs at the periclinal cell walls of the GMC have specific orientation transversal to the long axis of the leaf (longest growth axis, X), while in *Saccharina*, the AFs along the longitudinal (X-axis of the lamina) and perpendicular (Y-axis of the lamina) CW are oriented almost parallel to the Z axis of the lamina (fig. 8). This organisation mostly resembles the cortical MTs organisation in vegetative plant cells. For example in the shoot apical meristem, cortical MT bundles are parallely oriented along the shortest path possible often perpendicularly to the main growth axis, responding to the generated mechanical stress of the tissue (Williamson 1990; Hamant et al. 2008; Landrein and Hamant 2013), while cellulose fibrils are often aligned to MTs (Baskin et al. 2004; Paredez et al. 2006; Sampathkumar et al. 2019). In *Sphacelaria*'s cells, cellulose fibrils follow AFs (Katsaros et al. 2002). Therefore, it is tempting to postulate that the AFs orientation along the Z-axis in *Saccharina* lamina cells, and the cellulose microfibrils whose the orientation they control, would act against cell growth at Z-axis. In our hypothesis, the Z-axis bears the highest tensile stress as these cells are restricted of expansion in this direction. How AFs would "read" the stress is unknown. This mechanical feedback loop is reminiscent of that described for cortical MTs at the inner anticlinal CWs during leaf development (Zhao et al. 2020). Specifically, Zhao et al. (2020) concluded that anisotropic MT orientation and stress-depended cell division are essential for the morphogenesis of a flat blade with directed growth along a two-axes system. We suggested that cellulose microfibrils follow the AF pattern, but cellulose consists only a small percentage at brown algal CW (Charrier et al.

2019). Additional compounds potentially contribute at CW stiffening and restriction of cell growth at Z-axis, possibly aligned with the AF orientation. Alginates are a such potential compound (Rabillé et al. 2019) and they can be modulated by C5-epimerase (Yonamine et al. 2021), reminiscent of the organ initiation model at the shoot apex (Peaucelle et al. 2011)

The pharmacological treatment with LatB supports this model: the lamina becomes thicker and wavier and its growth rate especially in the horizontal axis is impaired. Despite the low number of replicates, this result suggests that AFs dynamics is particularly necessary for the longitudinal anticlinal cell division (along the X axis).

Conclusions:

We have observed a unique cytoskeletal organisation for *Saccharina*'s embryonic cells. Further experiments can enrich these observations and investigate further their exact role on morphogenesis and test our theories. For instance, an important question is how the sheets are formed. First candidate is the Arp2/3 an actin nucleator present in brown algae responsible for the actin arrays during zygote polarisation in Fucales (Hable and Kropf 2005). Another candidate is RAC1 (Rho-gap protein) (Hable 2014; Marston et al. 2019) which is an organiser of AFs in animal cells while in brown algae Fucales it promotes the nucleation of AFs during the polarisation of the zygotes induced by environmental cues. However, the characterisation of a Rho-GAP mutant in Ectocarpus does not support a functional link between the Rho-GTPase pathway and the formation of AFs (Nehr et al. 2021). Another question is about the evolution of different sets of AFs. In plants and animals there are different isoforms of actin (Gunning et al. 2015; Kijima et al. 2018; Svitkina 2020) related with different cell types and AFs structures. *Saccharina japonica* a related species of *Saccharina latissima*, codes for three actin genes (Liu et al. 2019), which could suggest a similar functional distinction. Finally, we did not manage to directly answer the question whether AFs sheets are essential for the lamina to keep its monolayer conformation. A recent developed method on growing *Saccharina* embryos constrained in a narrow space (Clerc et al. in press) will enhance our studies on the AFs organisation. Also, more meticulous pharmacological treatments are needed with varying drugs for actin depolymerisation coupled with labelling approaches and cell segmentation analysis in 3D for fully evaluating their impact on morphogenesis. A similar approach should be followed for MTs to explore their potential dynamics beyond cell division and cytokinesis plane determination

References

Apostolakos, P., and Galatis, B. 1999. Microtubule and Actin Filament Organization during Stomatal Morphogenesis in the Fern *Asplenium nidus*. II. Guard Cells. The New Phytologist 141(2): 209–223. [Wiley, New Phytologist Trust].

Baskin, T.I., Beemster, G.T.S., Judy-March, J.E., and Marga, F. 2004. Disorganization of Cortical Microtubules Stimulates Tangential Expansion and Reduces the Uniformity of Cellulose Microfibril Alignment among Cells in the Root of *Arabidopsis*. Plant Physiol 135(4): 2279–2290. doi:10.1104/pp.104.040493.

Bisgrove, S.R., and Kropf, D.L. 2004. Cytokinesis in brown algae: studies of asymmetric division in fucoid zygotes. Protoplasma 223(2): 163–173. doi:10.1007/s00709-004-0038-6.

Bogaert, K.A., Beeckman, T., and De Clerck, O. 2017. Egg activation-triggered shape change in the *Dictyota dichotoma* (Phaeophyceae) zygote is actin–myosin and secretion dependent. Ann Bot 120(4): 529–538. doi:10.1093/aob/mcx085.

Boudaoud, A., Burian, A., Borowska-Wykręt, D., Uyttewaal, M., Wrzalik, R., Kwiatkowska, D., and Hamant, O. 2014. FibrilTool, an ImageJ plug-in to quantify fibrillar structures in raw microscopy images. Nat Protoc 9(2): 457–463. Nature Publishing Group. doi:10.1038/nprot.2014.024.

Brawley, S.H., and Robinson, K.R. 1985. Cytochalasin treatment disrupts the endogenous currents associated with cell polarization in fucoid zygotes: studies of the role of F-actin in embryogenesis. Journal of Cell Biology 100(4): 1173–1184. doi:10.1083/jcb.100.4.1173.

Bringloe, T.T., Starko, S., Wade, R.M., Vieira, C., Kawai, H., Clerck, O.D., Cock, J.M., Coelho, S.M., Destombe, C., Valero, M., Neiva, J., Pearson, G.A., Faugeron, S., Serrão, E.A., and Verbruggen, H. 2020. Phylogeny and Evolution of the Brown Algae. Critical Reviews in Plant Sciences 39(4): 281–321. Taylor & Francis. doi:10.1080/07352689.2020.1787679.

Cai, G., Del Casino, C., Romagnoli, S., and Cresti, M. 2005. Pollen cytoskeleton during germination and tube growth. Current Science 89(11): 1853–1860. Temporary Publisher.

Charrier, B., Rabillé, H., and Billoud, B. 2019. Gazing at Cell Wall Expansion under a Golden Light. Trends in Plant Science 24(2): 130–141. doi:10.1016/j.tplants.2018.10.013.

Chen, T., Teng, N., Wu, X., Wang, Y., Tang, W., Šamaj, J., Baluška, F., and Lin, J. 2007. Disruption of Actin Filaments by Latrunculin B Affects Cell Wall Construction in *Picea meyeri* Pollen Tube by Disturbing Vesicle Trafficking. Plant and Cell Physiology 48(1): 19–30. doi:10.1093/pcp/pcl036.

Cheung, A.Y., Duan, Q., Costa, S.S., de Graaf, B.H.J., Di Stilio, V.S., Feijo, J., and Wu, H.-M. 2008. The dynamic pollen tube cytoskeleton: live cell studies using actin-binding and microtubule-binding reporter proteins. Mol Plant 1(4): 686–702. doi:10.1093/mp/ssn026.

Chugh, P., and Paluch, E.K. 2018. The actin cortex at a glance. Journal of Cell Science 131(14): jcs186254. doi:10.1242/jcs.186254.

Clerc T., Boscq S., Attia R., Kaminski Schierle G.S., Charrier B., Näubli N.F. Cultivation and imaging of S. *latissima* embryo monolayered cell sheets inside microfluidic devices (in press in Bioengineering)

Doonan, J.H., Cove, D.J., and Lloyd, C.W. 1985. Immunofluorescence microscopy of microtubules in intact cell lineages of the moss, *Physcomitrella patens*. I. Normal and

CIPC-treated tip cells. Journal of Cell Science 75(1): 131–147. doi:10.1242/jcs.75.1.131.

Drøbak, B.K., Franklin-Tong, V.E., and Staiger, C.J. 2004. The role of the actin cytoskeleton in plant cell signaling. New Phytologist 163(1): 13–30. doi:10.1111/j.1469-8137.2004.01076.x.

Elliott, A., and Shaw, S.L. 2018. Update: Plant Cortical Microtubule Arrays. Plant Physiology 176(1): 94–105. doi:10.1104/pp.17.01329.

Fletcher, D.A., and Mullins, R.D. 2010. Cell mechanics and the cytoskeleton. Nature 463(7280): 485–492. Nature Publishing Group. doi:10.1038/nature08908.

Geitmann, A., and Ortega, J.K.E. 2009. Mechanics and modeling of plant cell growth. Trends in Plant Science 14(9): 467–478. doi:10.1016/j.tplants.2009.07.006.

Gunning, P.W., Ghoshdastider, U., Whitaker, S., Popp, D., and Robinson, R.C. 2015. The evolution of compositionally and functionally distinct actin filaments. Journal of Cell Science 128(11): 2009–2019. doi:10.1242/jcs.165563.

Hable, W.E. 2014. Rac1 signaling in the establishment of the fucoid algal body plan. Front. Plant Sci. 5: 690. doi:10.3389/fpls.2014.00690.

Hable, W.E., and Kropf, D.L. 2005. The Arp2/3 complex nucleates actin arrays during zygote polarity establishment and growth. Cell Motil Cytoskeleton 61(1): 9–20. doi:10.1002/cm.20059.

Hamant, O., Heisler, M.G., Jönsson, H., Krupinski, P., Uyttewaal, M., Bokov, P., Corson, F., Sahlin, P., Boudaoud, A., Meyerowitz, E.M., Couder, Y., and Traas, J. 2008. Developmental Patterning by Mechanical Signals in *Arabidopsis*. Science 322(5908): 1650–1655. American Association for the Advancement of Science. doi:10.1126/science.1165594.

Hamant, O., Inoue, D., Bouchez, D., Dumais, J., and Mjolsness, E. 2019. Are microtubules tension sensors? Nat Commun 10(1): 2360. doi:10.1038/s41467-019-10207-y.

Hoffman, J.C., and Vaughn, K.C. 1994. Mitotic disrupter herbicides act by a single mechanism but vary in efficacy. Protoplasma 179(1): 16–25. doi:10.1007/BF01360733.

Karyophyllis, D., Katsaros, C., Dimitriadis, I., and Galatis, B. 2000. F-Actin organization during the cell cycle of *Sphacelaria rigidula* (Phaeophyceae). European Journal of Phycology 35(1): 25–33. doi:10.1080/09670260010001735591.

Katsaros, C., and Galatis, B. 1992. Immunofluorescence and electron microscopic studies of microtubule organization during the cell cycle of *Dictyota dichotoma* (Phaeophyta, Dictyotales). Protoplasma 169(1): 75–84. doi:10.1007/BF01343372.

Katsaros, C., Karyophyllis, D., and Galatis, B. 2006. Cytoskeleton and Morphogenesis in Brown Algae. Ann Bot 97(5): 679–693. doi:10.1093/aob/mcl023.

Katsaros, C.I. 1992. Immunofluorescence Study of Microtubule Organization in Some Polarized Cell Types of Selected Brown Algae. Botanica Acta 105(6): 400–406. doi:10.1111/j.1438-8677.1992.tb00320.x.

Katsaros, C.I., Karyophyllis, D.A., and Galatis, B.D. 2002. Cortical F-actin underlies cellulose microfibril patterning in brown algal cells. Phycologia 41(2): 178–183. doi:10.2216/i0031-8884-41-2-178.1.

Kijima, S.T., Staiger, C.J., Katoh, K., Nagasaki, A., Ito, K., and Uyeda, T.Q.P. 2018. *Arabidopsis* vegetative actin isoforms, AtACT2 and AtACT7, generate distinct filament arrays in living plant cells. Sci Rep 8(1): 4381. Nature Publishing Group. doi:10.1038/s41598-018-22707-w.

Kojo, K.H., Higaki, T., Kutsuna, N., Yoshida, Y., Yasuhara, H., and Hasezawa, S. 2013. Roles of Cortical Actin Microfilament Patterning in Division Plane Orientation in Plants. Plant and Cell Physiology 54(9): 1491–1503. doi:10.1093/pcp/pct093.

Landrein, B., and Hamant, O. 2013. How mechanical stress controls microtubule behavior and morphogenesis in plants: history, experiments and revisited theories. The Plant Journal 75(2): 324–338. doi:10.1111/tpj.12188.

Le Bail, A., and Charrier, B. 2013. Culture Methods and Mutant Generation in the Filamentous Brown Algae *Ectocarpus siliculosus*. *In* Plant Organogenesis: Methods and Protocols. *Edited by* I. De Smet. Humana Press, Totowa, NJ. pp. 323–332. doi:10.1007/978-1-62703-221-6_22.

Liu, T., Wang, X., Wang, G., Jia, S., Liu, G., Shan, G., Chi, S., Zhang, J., Yu, Y., Xue, T., and Yu, J. 2019. Evolution of Complex Thallus Alga: Genome Sequencing of *Saccharina japonica*. Front. Genet. 10. doi:10.3389/fgene.2019.00378.

Lloyd, C.W. 1983. Helical microtubular arrays in onion root hairs. Nature 305(5932): 311–313. Nature Publishing Group. doi:10.1038/305311a0.

Louveaux, M., Rochette, S., Beauzamy, L., Boudaoud, A., and Hamant, O. 2016. The impact of mechanical compression on cortical microtubules in *Arabidopsis*: a quantitative pipeline. The Plant Journal 88(2): 328–342. doi:10.1111/tpj.13290.

Marston, D.J., Anderson, K.L., Swift, M.F., Rougie, M., Page, C., Hahn, K.M., Volkmann, N., and Hanein, D. 2019. High Rac1 activity is functionally translated into cytosolic structures with unique nanoscale cytoskeletal architecture. PNAS 116(4): 1267–1272. National Academy of Sciences. doi:10.1073/pnas.1808830116.

Morejohn, L.C., Bureau, T.E., Molè-Bajer, J., Bajer, A.S., and Fosket, D.E. 1987. Oryzalin, a dinitroaniline herbicide, binds to plant tubulin and inhibits microtubule polymerization in vitro. Planta 172(2): 252–264. doi:10.1007/BF00394595.

Motomura, T., Nagasato, C., and Kimura, K. 2010. Cytoplasmic inheritance of organelles in brown algae. J Plant Res 123(2): 185–192. doi:10.1007/s10265-010-0313-x.

Munjal, A., Philippe, J.-M., Munro, E., and Lecuit, T. 2015. A self-organized biomechanical network drives shape changes during tissue morphogenesis. Nature 524(7565): 351–355. Nature Publishing Group. doi:10.1038/nature14603.

Nagasato, C., Inoue, A., Mizuno, M., Kanazawa, K., Ojima, T., Okuda, K., and Motomura, T. 2010. Membrane fusion process and assembly of cell wall during cytokinesis in the brown alga, *Silvetia babingtonii* (Fucales, Phaeophyceae). Planta 232(2): 287–298. doi:10.1007/s00425-010-1188-8.

Nagasato, C., and Motomura, T. 2009. Effect of Latrunculin B and Brefeldin A on cytokinesis in the brown alga *Scytosiphon lomentaria* (Scytosiphonales, Phaeophyceae). Journal of Phycology 45(2): 404–412. doi:10.1111/j.1529-8817.2009.00655.x.

Nehr, Z., Chenivesse, S., Billoud, B., Genicot, S., Desban, N., Theodorou, I., Nasir, A., Bail, A.L., Rabillé, H., Godfroy, O., Katsaros, C., and Charrier, B. 2021, August 28. Tip growth in the brown alga *Ectocarpus* is controlled by a RHO-GAP-BAR domain protein independently from F-actin organisation. bioRxiv. doi:10.1101/2021.08.28.458042.

Panteris, E. 2008. Cortical actin filaments at the division site of mitotic plant cells: a reconsideration of the 'actin-depleted zone.' New Phytologist 179(2): 334–341. doi:10.1111/j.1469-8137.2008.02474.x.

Panteris, E., Achlati, T., Daras, G., and Rigas, S. 2018. Stomatal Complex Development and F-Actin Organization in Maize Leaf Epidermis Depend on Cellulose Synthesis. Molecules

23(6): 1365. Multidisciplinary Digital Publishing Institute. doi:10.3390/molecules23061365.

Panteris, E., Galatis, B., Quader, H., and Apostolakos, P. 2007. Cortical actin filament organization in developing and functioning stomatal complexes of *Zea mays* and *Triticum turgidum*. Cell Motility and the Cytoskeleton 64(7): 531–548.

Paredez, A.R., Somerville, C.R., and Ehrhardt, D.W. 2006. Visualization of Cellulose Synthase Demonstrates Functional Association with Microtubules. Science 312(5779): 1491–1495. American Association for the Advancement of Science. doi:10.1126/science.1126551.

Peaucelle, A., Braybrook, S.A., Le Guillou, L., Bron, E., Kuhlemeier, C., and Höfte, H. 2011. Pectin-Induced Changes in Cell Wall Mechanics Underlie Organ Initiation in *Arabidopsis*. Current Biology 21(20): 1720–1726. doi:10.1016/j.cub.2011.08.057.

Pozhvanov, G.A., Suslov, D.V., and Medvedev, S.S. 2013. Actin cytoskeleton rearrangements during the gravitropic response of *Arabidopsis* roots. Cell Tiss. Biol. 7(2): 185–191. doi:10.1134/S1990519X13020120.

Rabillé, H., Koutalianou, M., Charrier, B., Katsaros, C., Koutalianou, M., Charrier, B., and Katsaros, C. 2018. Actin fluorescent staining in the filamentous brown alga *Ectocarpus siliculosus*. *In* Protocols for Macroalgae Research. Available from http://doi.org/10.1201/b21460-24 [accessed 23 January 2020].

Rabillé, H., Torode, T.A., Tesson, B., Le Bail, A., Billoud, B., Rolland, E., Le Panse, S., Jam, M., and Charrier, B. 2019. Alginates along the filament of the brown alga *Ectocarpus* help cells cope with stress. Sci Rep 9(1): 12956. doi:10.1038/s41598-019-49427-z.

Rahman, A., Bannigan, A., Sulaman, W., Pechter, P., Blancaflor, E.B., and Baskin, T.I. 2007. Auxin, actin and growth of the *Arabidopsis thaliana* primary root. The Plant Journal 50(3): 514–528. doi:10.1111/j.1365-313X.2007.03068.x.

Robinson, S., and Kuhlemeier, C. 2018. Global Compression Reorients Cortical Microtubules in *Arabidopsis* Hypocotyl Epidermis and Promotes Growth. Current Biology 28(11): 1794-1802.e2. doi:10.1016/j.cub.2018.04.028.

Röper, K. 2020. Microtubules enter centre stage for morphogenesis. Philosophical Transactions of the Royal Society B: Biological Sciences 375(1809): 20190557. Royal Society. doi:10.1098/rstb.2019.0557.

Salbreux, G., Charras, G., and Paluch, E. 2012. Actin cortex mechanics and cellular morphogenesis. Trends in Cell Biology 22(10): 536–545. doi:10.1016/j.tcb.2012.07.001.

Sampathkumar, A., Krupinski, P., Wightman, R., Milani, P., Berquand, A., Boudaoud, A., Hamant, O., Jönsson, H., and Meyerowitz, E.M. 2014. Subcellular and supracellular mechanical stress prescribes cytoskeleton behavior in *Arabidopsis* cotyledon pavement cells. eLife 3: e01967. doi:10.7554/eLife.01967.

Sampathkumar, A., Peaucelle, A., Fujita, M., Schuster, C., Persson, S., Wasteneys, G.O., and Meyerowitz, E.M. 2019. Primary wall cellulose synthase regulates shoot apical meristem mechanics and growth. Development 146(10): dev179036. doi:10.1242/dev.179036.

Schindelin, J., Arganda-Carreras, I., Frise, E., Kaynig, V., Longair, M., Pietzsch, T., Preibisch, S., Rueden, C., Saalfeld, S., Schmid, B., Tinevez, J.-Y., White, D.J., Hartenstein, V., Eliceiri, K., Tomancak, P., and Cardona, A. 2012. Fiji: an open-source platform for biological-image analysis. Nat Methods 9(7): 676–682. Nature Publishing Group. doi:10.1038/nmeth.2019.

Schneider, R., Ehrhardt, D.W., Meyerowitz, E.M., and Sampathkumar, A. 2022. Tethering of cellulose synthase to microtubules dampens mechano-induced cytoskeletal organization in *Arabidopsis* pavement cells. Nat. Plants 8(9): 1064–1073. Nature Publishing Group. doi:10.1038/s41477-022-01218-7.

Schoenwaelder, M., and Clayton, M. 1999. The role of the cytoskeleton in brown algal physode movement. European Journal of Phycology 34(3): 223–229. doi:10.1080/09670269910001736282.

Staiger, C.J., Sheahan, M.B., Khurana, P., Wang, X., McCurdy, D.W., and Blanchoin, L. 2009. Actin filament dynamics are dominated by rapid growth and severing activity in the *Arabidopsis* cortical array. Journal of Cell Biology 184(2): 269–280. doi:10.1083/jcb.200806185.

Stephan, O.O.H. 2017. Actin fringes of polar cell growth. Journal of Experimental Botany 68(13): 3303–3320. doi:10.1093/jxb/erx195.

Stöckle, D., Reyes-Hernández, B.J., Barro, A.V., Nenadić, M., Winter, Z., Marc-Martin, S., Bald, L., Ursache, R., Fujita, S., Maizel, A., and Vermeer, J.E. 2022. Microtubule-based perception of mechanical conflicts controls plant organ morphogenesis. Science Advances 8(6): eabm4974. American Association for the Advancement of Science. doi:10.1126/sciadv.abm4974.

Svitkina, T.M. 2020. Actin Cell Cortex: Structure and Molecular Organization. Trends in Cell Biology 30(7): 556–565. Elsevier. doi:10.1016/j.tcb.2020.03.005.

Szymanski, D., and Staiger, C.J. 2018. The Actin Cytoskeleton: Functional Arrays for Cytoplasmic Organization and Cell Shape Control. Plant Physiol. 176(1): 106–118. doi:10.1104/pp.17.01519.

Takatsuka, H., Higaki, T., and Umeda, M. 2018. Actin Reorganization Triggers Rapid Cell Elongation in Roots. Plant Physiology 178(3): 1130–1141. doi:10.1104/pp.18.00557.

Theodorou, I., Opsahl-Sorteberg, H.-G., and Charrier, B. 2021. Preparation of Zygotes and Embryos of the Kelp *Saccharina latissima* for Cell Biology Approaches. Bio-101: e4132. Bio-protocol LLC. doi:10.21769/BioProtoc.4132.

Tian, J., Han, L., Feng, Z., Wang, G., Liu, W., Ma, Y., Yu, Y., and Kong, Z. 2015. Orchestration of microtubules and the actin cytoskeleton in trichome cell shape determination by a plant-unique kinesin. eLife 4: e09351. eLife Sciences Publications, Ltd. doi:10.7554/eLife.09351.

Tsirigoti, A., Küpper, F.C., Gachon, C.M.M., and Katsaros, C. 2014. Cytoskeleton organisation during the infection of three brown algal species, *Ectocarpus siliculosus*, *Ectocarpus crouaniorum* and *Pylaiella littoralis*, by the intracellular marine oomycete *Eurychasma dicksonii*. Plant Biology 16(1): 272–281. doi:10.1111/plb.12041.

Varvarigos, V., Katsaros, C., and Galatis, B. 2004. Radial F-actin configurations are involved in polarization during protoplast germination and thallus branching of *Macrocystis pyrifera* (Phaeophyceae, Laminariales). Phycologia 43(6): 693–702. doi:10.2216/i0031-8884-43-6-693.1.

Vavrdová, T., Šamajová, O., Křenek, P., Ovečka, M., Floková, P., Šnaurová, R., Šamaj, J., and Komis, G. 2019. Multicolour three dimensional structured illumination microscopy of immunolabeled plant microtubules and associated proteins. Plant Methods 15(1): 22. doi:10.1186/s13007-019-0406-z.

Verger Lab. 2021, December 8. MT_Angle2Ablation_Workflow. FIJI, Jupyter Notebook. Available from https://github.com/VergerLab/MT_Angle2Ablation_Workflow [accessed 4 October 2022].

Williamson, R.E. 1990. Alignment of Cortical Microtubules by Anisotropic Wall Stresses. Functional Plant Biol. 17(6): 601–613. CSIRO PUBLISHING. doi:10.1071/pp9900601.

Yonamine, R., Ichihara, K., Tsuyuzaki, S., Hervé, C., Motomura, T., and Nagasato, C. 2021. Changes in Cell Wall Structure During Rhizoid Formation of *Silvetia babingtonii* (Fucales, Phaeophyceae) Zygotes. Journal of Phycology 57(4): 1356–1367. doi:10.1111/jpy.13178.

Zhang, B., Gao, Y., Zhang, L., and Zhou, Y. 2021. The plant cell wall: Biosynthesis, construction, and functions. Journal of Integrative Plant Biology 63(1): 251–272. doi:10.1111/jipb.13055.

Zhao, F., Du, F., Oliveri, H., Zhou, L., Ali, O., Chen, W., Feng, S., Wang, Q., Lü, S., Long, M., Schneider, R., Sampathkumar, A., Godin, C., Traas, J., and Jiao, Y. 2020. Microtubule-Mediated Wall Anisotropy Contributes to Leaf Blade Flattening. Current Biology 30(20): 3972-3985.e6. doi:10.1016/j.cub.2020.07.076.

Zhu, J., and Geisler, M. 2015. Keeping it all together: auxin–actin crosstalk in plant development. Journal of Experimental Botany 66(16): 4983–4998. doi:10.1093/jxb/erv308.

Figures:

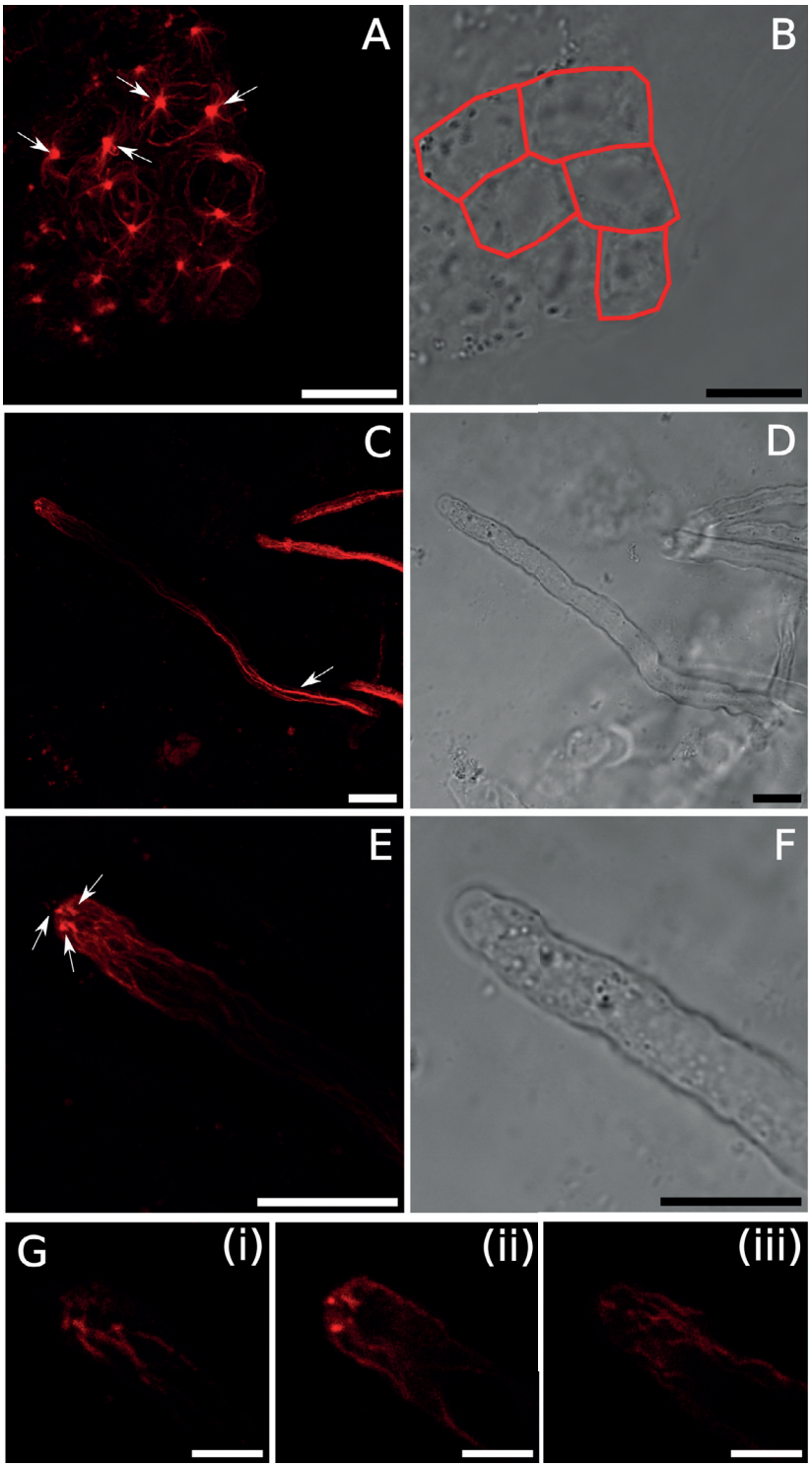

Figure 1. Microtubule organisation in different cell types of the embryo. A) Maximal projection of α-tubulin indirect immunofluorescence in lamina cells. MTs converge on two focus points (arrows) surrounding an empty space, presumably where the nucleus is. From these points, the MTs extend through the cytoplasm and the cell cortex. The convergence points are not present always at the same focal plane and the angle of the axis that they form can vary in each cell. B) Transmission channel of the stained tissue. The cell borders are visible to some extent. Lines have been added manually to assist the interpretation of (A). C) Maximal projection of α-tubulin indirect immunofluorescence in a rhizoid cell. Cable-like structures are present at the main stem of the cell (arrows). The cables seem to branch into finer structures before the tip of rizoid. D) Transmission channel of the rhizoid cell. E) The tip of the rhizoid through different sections. Fine MTs passing through mainly the cell cortex converge into several points (arrows). The signal of the MTs dissipates away from tip, but its intensity increases 30 μm below the tip (look C) where the MTs concentrate into cable-like organisation. F) Transmission channel of the tip. G) Different optical sections from E. (i) front, (ii) median, (iii) back. Bars: (A-F) 10 μm, G: 3 μm

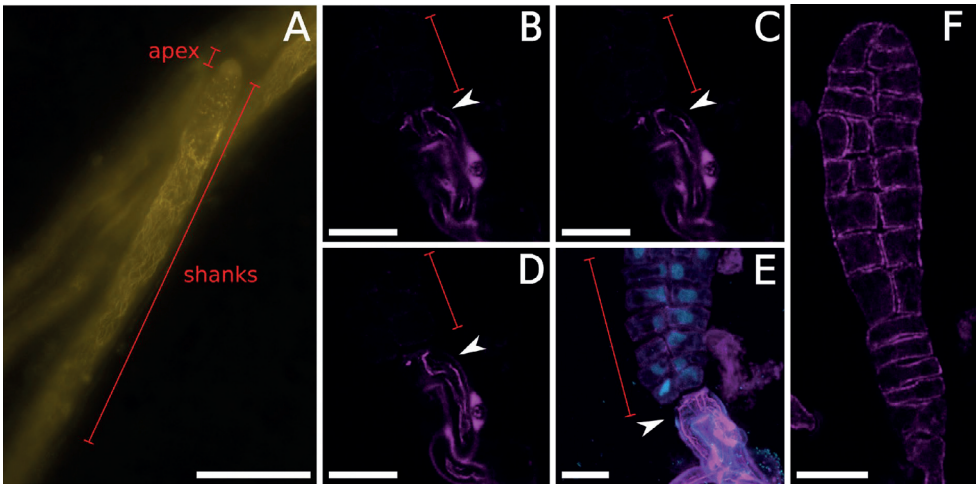

Figure 2. Actin cytoskeleton in different cell types of the embryo. A) Maximal projection of Phalloidin-Rhodamine (Ph-Rh) labelling on rhizoid at epifluorescence microscope. Notice the meshwork below the apex, while AFs are absent below the apex where 'dots' fill in the space. B-D) Sequence of confocal sections from Phalloidin - Alexafluor488 (Ph-Alexa488) labelled AFs at the base of two rhizoids, arrowhead: rhizoids, brackets: blade. E) Maximal projection of the base of rhizoid, same specimen with B-D, together with DAPI staining of the nuclei, arrowhead: rhizoids, brackets: blade. The nuclei of the differented cells have migrated further below the rhizoidal cells. F) Confocal microscopy median section of early Phase II embryo stained with Ph-Rh. Bars: A) 30 μm, B-F) 15 μm

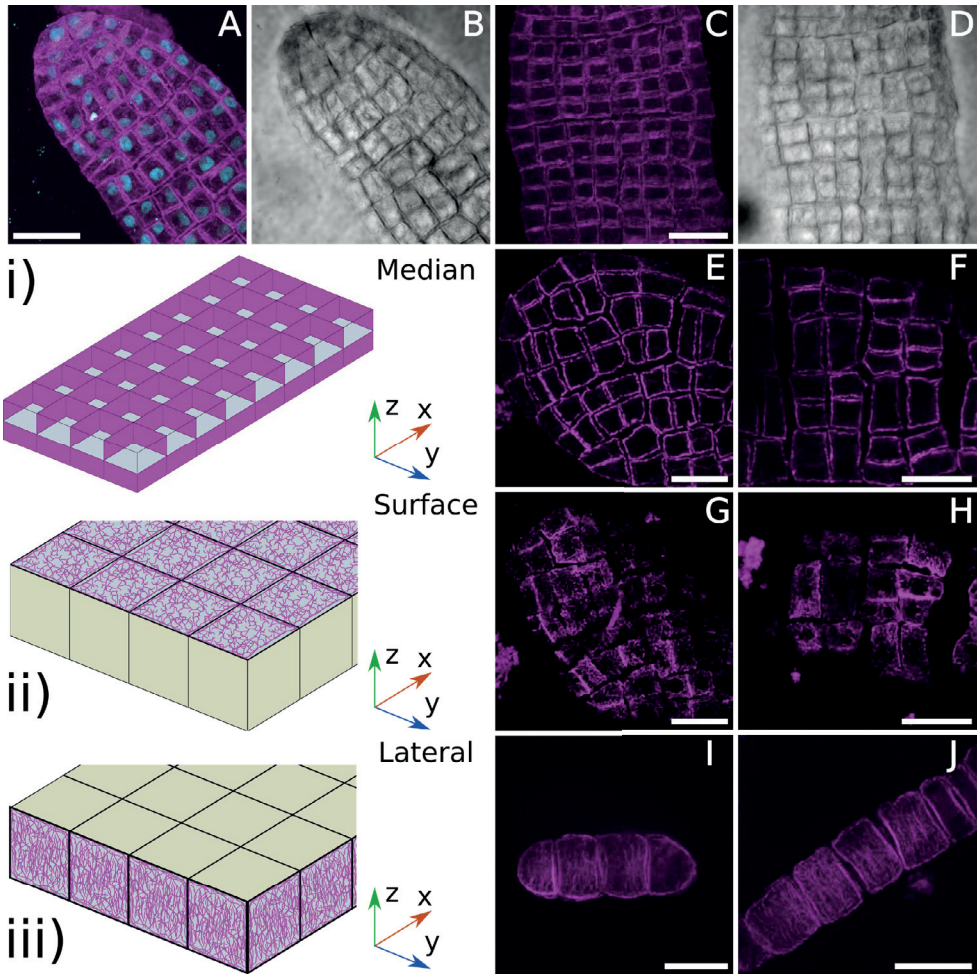

Figure 3. Actin filaments organisation and orientation. A) Maximal projection of Ph-Alexa488 labelling at the apex of a Phase II embryo together with DAPI stain. AFs are cortical while the nuclei are cytoplasmic occupying a big proportion of the cell volume. No AF was observed around the nuclei and rarely any extends through the cytoplasm. B) Transmission channel of A. C) Maximal projection from middle region of Phase II embryo labelled with Ph-Alexa488. The cuboidal shape of the cells was projected on the cortical organisation of the AFs together with several 4-cell junctions. D) Transmission channel of C. E) Median confocal section from Ph-Rh labelling at the apex of a Phase II specimen. AFs are tightly packed along the cortex of the cells and only rarely some filaments extend through the cell. F) Median section from a middle region of specimen at E. We observe the same organisation. G) Surface confocal section of E. The AFs demonstrate random orientation with strong signal at the cell edges. Some of the AFs seem like they are directing from the edges towards the center. H) Surface section of F. Similar with G, the AFs have random orientation and some of them extend from the edges towards the center. Big gaps are observed in both G and H, these are space

occupied by vacuoles. I) Transversal section of Ph-Alexa488 labelled Phase II embryo. A maximal projection of few sections is depicted. There is a specific orientation to the AFs, as they are extending from front to back along the Z axis. J) Longitudinal section of of Ph-Alexa488 labelled Phase II embryo. A maximal projection of few sections is depicted. The AFs are orientated parallel to Z axis of the tissue. i) Simplified depiction of median sections (E and F), ii) Simplified and magnified depiction of surface sections (G and H), iii) Simplified depiction of longitudinal and vertical section (I and J). Bars: A-D) 20 µm, E-J) 15 µm

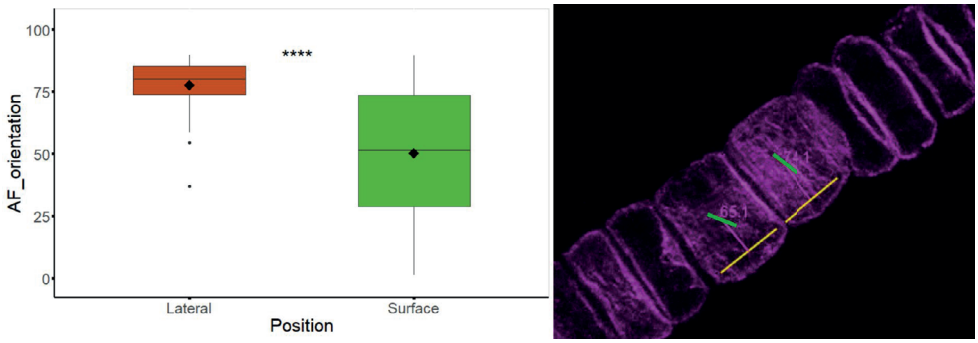

Figure 4. Box plots of actin filaments (AFs) orientation, measured with the MT_Angle2Ablation workflow. A measurement is shown, the angle (°) is measured with the green line that follows the average orientation of the AFs projected on the yellow reference line-parallel to the surface of the tissue. **** = p-value < 0.0001. N= 54 for the lateral (horizontal and vertical) cell walls, N=315 for the surface cell walls measurements.

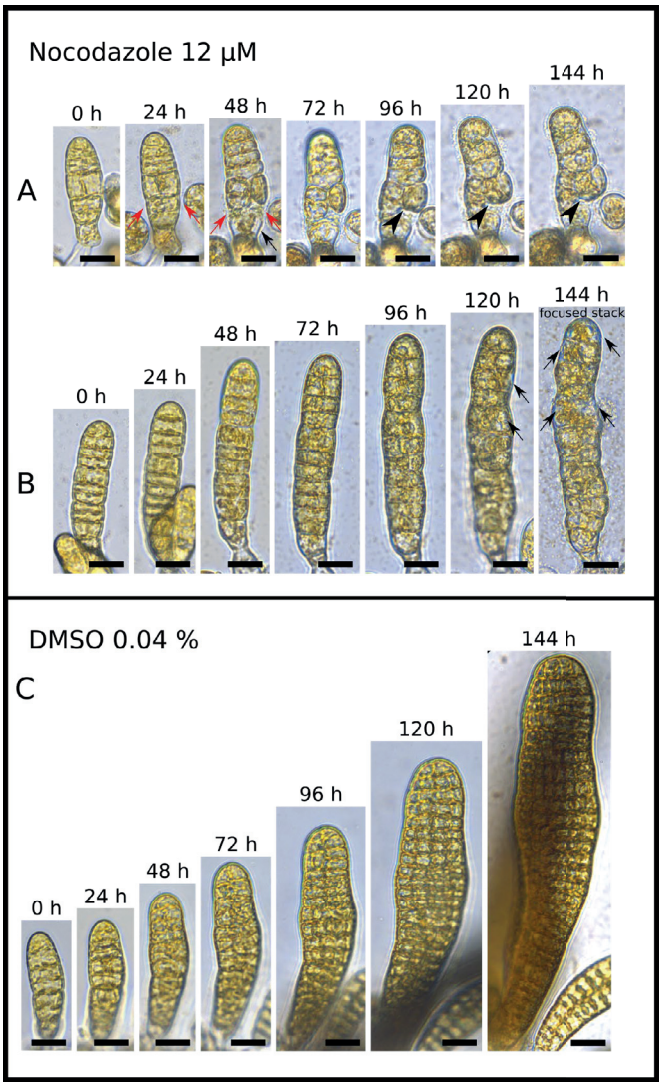

Figure 5. Image table from timelapse of Nocodazole (Noc) treatment. A – B) Noc treatment. A) Plasmolysed cell at 48 h (black arrow), crashed cell (red arrows), aberrant cell growth (black arrowhead). B) Plasmolysed cells (black arrow), aberrant cell growth (yellow arrow), there are a few longitudinal cell walls. Plasmolysed cells were observed at some timepoint in all specimen which more often was restored. Three specimen out of 7 had no restored plasmolysis. C) The 0 h is the end of Phase I for this specimen. There are the first longitudinal divisions at 24 and four columns of cells at 120h then six columns of cells at 144 h in the middle of the blade. We observe an overall normal development Both specimens demonstrate suppressed tissue growth and practically no growth. The sample size is n= 7 for Noc and n= 6 for DMSO. No differences were observed between DMSO (n=6) and NSW (n=14) (compare figs. 5 and 6, and check Table S1). Bars: 20 µm

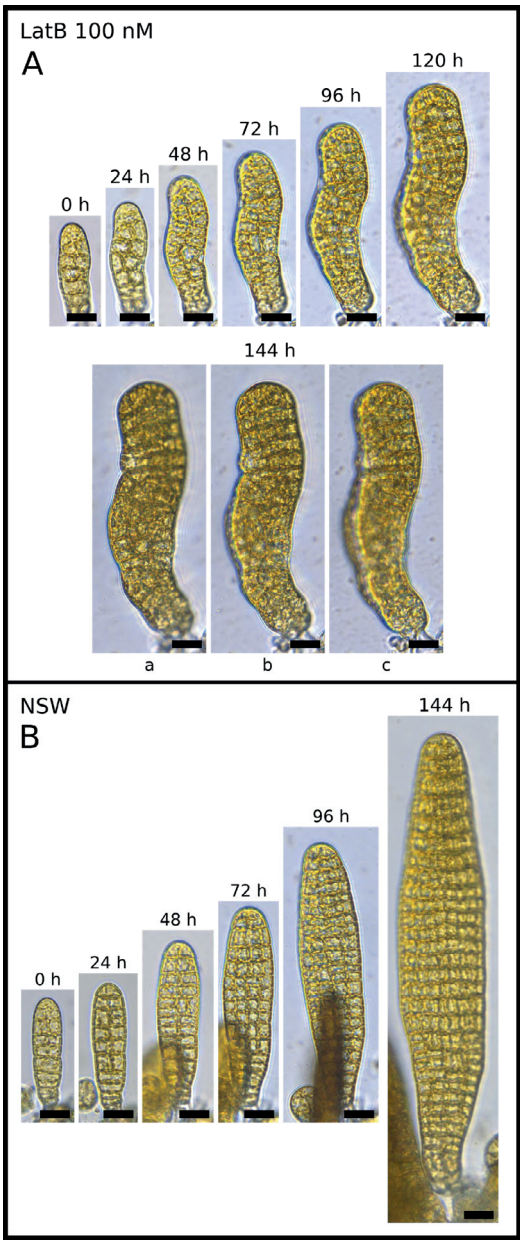

Figure 6. Image table from timelapse of Latrunculin B (LatB) treatment. A) LatB treatment. We observe a sigmoid tissue shape with oblique cells from 96 h. Rows and columns are both distinguishable until 144 h. At 144 h there are >15 cell rows (not clear) and four cell columns. At outgrowth making the tissue looking thicker is observed with the sequential sections a-c. It looks overall less developed than B. The sigmoid, rough morphology and obliqueness was observed at all the specimens (n=9). One specimen had bubble cells. No plasmolysed cells

were observed. B) NSW control. Normal development. The specimen came from a mixed population of different developmental (cell number, rows and columns) stages. No differences were observed between DMSO (n=6) and NSW (n=14) (compare figs. 5 and 6, and check Table S1). Bars: 20 µm

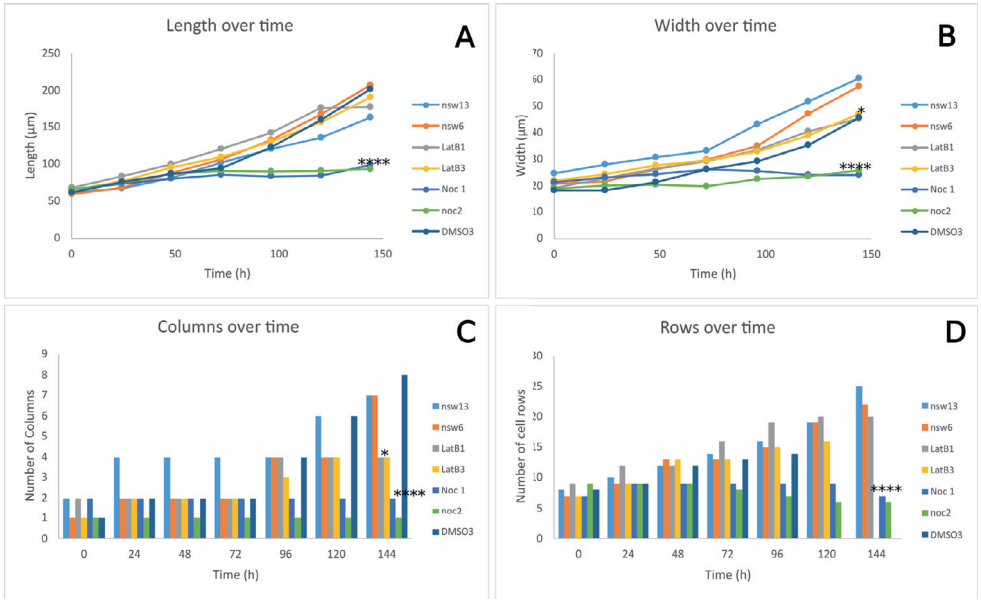

Figure 7. Plots of various morphological parameters over time from two specimen per parameter. A) Length of the embryo, B) Width of the embryo, C) Bar plot of cell columns present in the embryo, D) Bar plot of cell rows present in the embryo. Student T-tests p-values on α are indicated (Table S1)including all the specimen of the different treatments compared to the NSW. *= p-value < 0.05, **** = p-value < 0.0001.

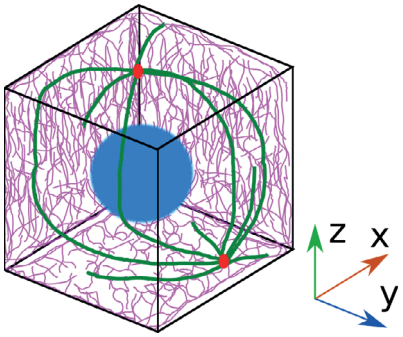

Figure 8. Schematic model of *Saccharina*'s cytoskeleton on thallus cells based on our results and those on *Dictyota dichotoma* (Katsaros and Galatis 1992). The cell wall is absent from this depiction. Magenta: Cortical sheets of actin filametns, green: microtubules, red: centriole, blue: nucleus. Details in the text.

Tables:

Table 1. Statistical analysis of Actin filaments orientation.

Cell wall position	Average AFs orientation	Standard deviation	Number of measurements
Surface	50.37 °	26.41 °	315
Lateral	77.69 °	10.43 °	54
Student T-test	Group 1	Group 2	p-value
	Lateral	Surface	$4.6\ 10^{-29}$

Supplemental material:

Link for video S1: https://we.tl/t-UYuwJd6q4c

Video S1. Z-stack from MT-immunolocalisation on cells of the thallus, projected in 3D. Radiating from the presumed centrioles, the MTs form cages around the perinuclear space.

Figure S2. Image table from timelapse of Latrunculin B (LatB) treatment. a, b, c at LatB and NSW are sequences of sections. More details in the characteristics column. Bars: LatB: 20 µm, NSW: 40 µm

Treatment	Specimen	Characteristics
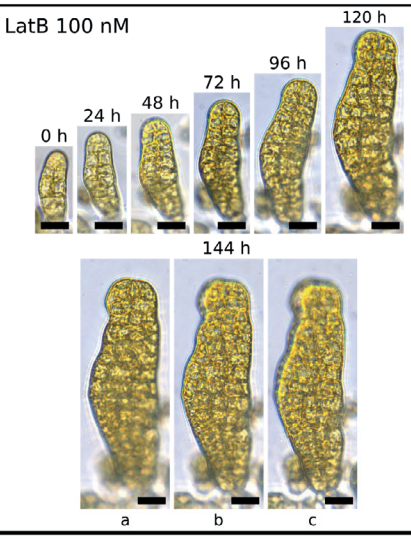	LatB_02	Aberrant shape of the thallus Oblique cells Rows and columns distinguishable At 144 h: 4 columns 17 rows Wavy shape Thick tissue Less developed
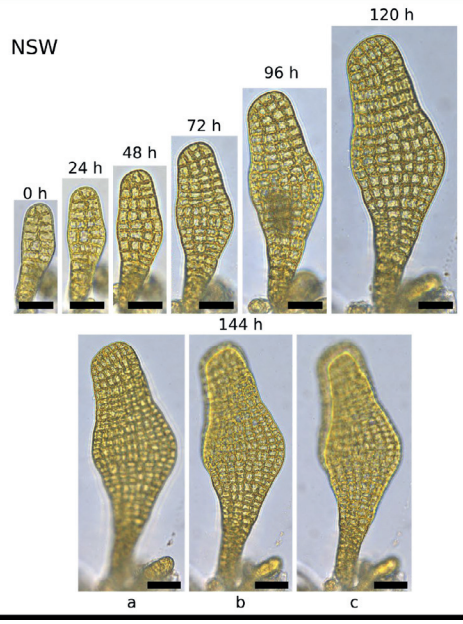	NSW_08	Normal development Wider middle region 8 columns wide Pre-stipe not observable

Table S1. Rate (α) of various morphological parameters per treatment. Average= Arithmetic mean, STD= standard deviation. New cell column or row are considered whenthey have more than two cells. The statistics are based on calculation of α per specimen (Table S2).

Treatment	NSW	NSW	DMSO	DMSO	Noc	Noc	Latb	Latb
Parameter	Average	STD	Average	STD	Average	STD	Average	STD
Length µm h^{-1}	1.28	0.64	0.85	0.41	0.22	0.087	0.87	0.33
Width µm h^{-1}	0.32	0.14	0.25	0.10	0.05	0.02	0.20	0.10
Columns columns h^{-1}	0.04	0.02	0.04	0.01	0.002	0.003	0.02	0.01
Rows rows h^{-1}	0.13	0.05	0.11	0.03	-0.01	0.01	0.10	0.06
Estimated Cell number divisions h^{-1}	1.32	1.52	0.82	0.63	0.02	0.04	0.60	0.42
Number of specimen	14		6		7		9	

Table S2. The α for each morphological parameter for every specimen per treatment.

NSW					
Specimen	Length (α_L) µm h^{-1}	Width (α_W) µm h^{-1}	Column (α_C) columns h^{-1}	Row (α_R)` rows h^{-1}	Number of cells (α_Φ) division h^{-1}
1	3.34	0.72	0.09	0.27	6.28
2	0.93	0.19	0.02	0.11	0.58
3	1.04	0.26	0.02	0.14	0.79
4	1.00	0.27	0.03	0.09	0.62
5	1.21	0.37	0.04	0.11	0.64
6	1.02	0.25	0.04	0.10	0.88
7	0.97	0.22	0.03	0.11	0.62

8	1.43	0.51	0.07	0.17	2.56
9	1.37	0.32	0.04	0.17	1.28
10	1.71	0.36			
11	0.86	0.27	0.03	0.08	0.76
12	1.58	0.27	0.02	0.17	0.82
13	0.72	0.25	0.03	0.11	0.95
14	0.77	0.25	0.03	0.06	0.37
Noc					
Specimen	Length (α_L) µm h^{-1}	Width (α_W) µm h^{-1}	Column (α_C) columns h^{-1}	Row (α_R)` rows h^{-1}	Number of cells (α_Φ) division h^{-1}
1	0.18	0.02	0.00	0.00	0.00
2	0.17	0.04	0.00	-0.03	-0.03
3	0.40	0.07	0.01	0.00	0.09
4	0.23	0.07	0.00	0.00	0.03
5	0.24	0.08	0.00	-0.01	0.05
6	0.10	0.06	0.00	-0.02	-0.02
7	0.22	0.03	0.00	-0.01	-0.01
LatB					
Specimen	Length (α_L) µm h^{-1}	Width (α_W) µm h^{-1}	Column (α_C) columns h^{-1}	Row (α_R)` rows h^{-1}	Number of cells (α_Φ) division h^{-1}
1	0.88	0.18	0.02	0.08	0.52
2	0.77	0.20	0.01	0.06	0.35
3	0.85	0.17	0.02	0.08	0.44
4	0.80	0.12	0.02	0.13	0.79
5	0.20	0.03	0.00	0.02	0.03
6	1.52	0.39	0.03	0.12	1.14

7	0.79	0.15	0.02	0.02	0.02
8	0.89	0.30	0.03	0.21	1.23
9	1.15	0.26	0.03	0.14	0.90
DMSO					
Specimen	Length (α_L) µm h^{-1}	Width (α_W) µm h^{-1}	Column (α_C) columns h^{-1}	Row (α_R)` rows h^{-1}	Number of cells (α_Φ) division h^{-1}
1	1.14	0.23	0.04	0.13	1.05
2	1.34	0.46	0.06	0.14	2.01
3	0.92	0.19	0.03	0.07	0.43
4	0.08	0.13			-0.03
5	0.61	0.24	0.05	0.07	0.62
6	1.03	0.25	0.03	0.13	0.84

Paper III: Outside in: how kelp embryos shift to 3D growth, an atlas of cell division and differentiation

State of publication: Ready for submission

Contributions: The manuscript was written by me and B. Charrier. I acquired the experimental data and interpreted them together with her.

Title: Outside in: how kelp embryos shift to 3D growth, an atlas of cell division and differentiation

Authors: Ioannis Theodorou[1,2] and Bénédicte Charrier[1]

Affiliations:

[1]Laboratory of integrative marine models, Station Biologique de Roscoff, UMR8227, CNRS, Sorbonne University, Place Georges Teissier, 29680 Roscoff, France

[2]Plant Sciences Department, Faculty of Biosciences, Norwegian University of Life Sciences, Ås, Norway

KW: 3D growth, kelp, meristoderm, cell differentiation, tissue thickening, cell division pattern, embryogenesis, asymmetrical cell division

Abstract

In most organisms, 3D growth takes place at the onset of embryogenesis. In some brown algae, 3D growth occurs later in development, when the organism consists of several hundred cells. We studied the cellular events that occur when 3D growth is established in the embryo of the brown alga *Saccharina* (a kelp species). Semi-thin sections illustrate the sequence of cellular events initiating 3D growth from a 2D monolayer cell sheet. The study of the progression through this sequence shows how 3D growth propagates through a series of asymmetric cell divisions from a peripheral monolayer of cells, the meristoderm (external epidermal meristem), in a specific region along the longest growth axis of the embryo, located between the apical lamina (blade) and the basal stipe called the transition zone. Cells in the transition zone differentiate rapidly; therefore, 3D growth in kelp is not based on the activity of a meristem where cells remain undifferentiated. Altogether, this study elucidates the cellular steps necessary for the establishment of the meristoderm and the sequence of the differentiation of its derivatives. This depiction of the cellular landscape lays the groundwork for the study of a cell fate programme controlling a novel mode of 3D growth in an organism phylogenetically distant from plants and animals.

Introduction

In most metazoans, it takes only three cell divisions to establish a mass of cells organised in 3D (Gilbert and Barresi 2016). In animal clades, which display very different cleavage patterns — including radial, spiral, bilateral and rotational patterns —this cleavage occurs as soon as the zygote is formed. Early embryonic cleavage concerns most bilaterians, except mammals, birds, reptiles and fishes where 3D growth emerges by cell migration to form a primitive streak from a pre-established 2D cell layer. Insects are a particular case in which 3D growth is established by the segmentation of an already voluminous multinucleate cell (coenocyte). The arrangement of cells during the early cleavage of animal embryos forms the embryo axes and shapes the future adult body plan (Hasley et al. 2017). Therefore, in most metazoans, the establishment of 3D growth by

cell division (as opposed to cell migration) occurs immediately after fertilisation and involves all cells, which divide almost synchronously in a different axis at each step.

Plant cells are surrounded by a cell wall, making 3D growth mechanisms necessarily more constrained mechanically than in animals. Although — in contrast to animals — plant organisms grow continuously, they initiate 3D growth as fast as most animals do. Angiosperms (*Arabidopsis*) follow exactly the same order of cell divisions as the radial cleavage pattern observed in metazoans (i.e., two perpendicular meridional divisions followed by an equatorial division) (Moukhtar et al. 2019). Somatic embryogenesis shows that although positional information most likely predominates, remote chemical information is likely involved (Smertenko and Bozhkov 2014) and indeed the initial cell division in *Arabidopsis* zygote has been shown to be under the control of maternal auxin (Robert et al. 2018). 3D growth is strikingly different in gymnosperms, in which the zygote undergoes three cycles of mitosis before cytokinesis occurs (coenocyte). It nevertheless results in two superimposed rows of four cells leading to a proper embryo and suspensor, respectively (Cairney and Pullman 2007). This pattern can be likened to segmentation of a multinucleate mother cell, as observed in insects (regardless of the presence of the cell wall/membrane and of the number of nuclei) (Gilbert and Barresi 2016).

Brown algae display the exceptional feature of developing 3D body structures long after the onset of embryogenesis. In kelps for example, the embryo grows as a monolayer cell sheet for several days before thickening by adding a new axis of growth. In brown algae, growth can be diffuse: all cells divide and expand. Alternatively, growth can be located in very precise positions within the thallus, in tissues that are reminiscent of the meristems of land plants (Charrier et al. 2012).

According to the review by Fritsch (Fritsch 1945), most parenchymatic brown algae have an external epidermal meristem, called the meristoderm (a term from the French phycologist C. Sauvageau), that ensures most of the growth in all axes (Fig. 1). In addition, several orders of brown algae have an apical meristem (Katsaros 1995) that, as in plants, is responsible for the growth of the thallus along the main longitudinal axis (usually apico-basal) (Clayton et al. 1985; Klemm and Hallam 1987; Linardić and Braybrook 2017). However, unlike plants, this apical meristem leaves the formation of thick tissues and lateral growth to the meristoderm.

For example, the brown algal order Dictyotales is characterised by a main apical meristem with one or more apical cells (Fig. 1A,B), sometimes having a lenticular shape (Fig. 1A). Interestingly, although they belong to the same order, species in genus *Dictyota* have no meristoderm, and *Dictyopteris* species rely on the meristoderm for all its widthwise growth.

Kelps have no apical meristems but instead have an intercalary zone that ensures the growth of the blade (lamina) in the upper part and the stipe in the lower part (Fig. 1c). The literature often identifies this intercalary zone as a meristem (Sykes 1908; Steinbiss and Schmitz 1974; Charrier et al. 2012; Coppin et al. 2020; Zhu et al. 2021). According to Smith (Smith 1939) and his work on several kelp species, this is not the case. As reviewed also in (Theodorou and Charrier 2021), kelps have a meristoderm, and it is more active at the base of the blade, specifically in a region called the transition zone (TZ) (Smith 1939; Fritsch 1945). Previous works summarised in Fritsch (1945) and according to a histological approach in Smith (1939) report that the cell division activity of the meristoderm is maintained throughout the growth of the mature individual up to a certain distance away from the TZ. At the TZ, two events take place: 1) anticlinal cell divisions for the formation and circumferential expansion of the meristoderm and 2) periclinal cell divisions for the radial development of internal tissues (thickening). The cells that derive from these periclinal cell

divisions eventually differentiate into cortical cells, but can also contribute to thickening of the meristoderm in mature algae (Smith 1939). Thereafter the cortical cells gradually differentiate into medullary elements, which constitute the transport tissue for photo-assimilates and nutrients in kelps (Schmitz et al. 1972; Lüning et al. 1973; Knoblauch et al. 2016). In general, there is a relatively good understanding of the growth of mature algae from a descriptive point of view based on studies carried out several decades ago (for a review, see (Theodorou and Charrier 2021)) and enhanced by the recent growing interest in kelp cultivation and breeding (Hwang et al. 2019; Li et al. 2020; Forbord et al. 2020; Monteiro et al. 2021; Liesner et al. 2022). However, little is known about when 3D growth is established in the embryonic stages of kelps because the last detailed studies date from the beginning of 20th century (Drew 1910; Yendo 1911). Although our predecessors provided detailed drawings of what tissues look like prior to and after the formation of 3D tissues, the transition from one stage to the other has not been described in detail. This gap in our knowledge precludes progress in the study of factors involved in the spatio-temporal control of cell division activity and orientation during the formation of these 3D tissues.

Therefore, in this study, we monitored the early development of the kelp *Saccharina latissima,* with a special focus on the cellular steps that are responsible for the initiation of embryo thickening (i.e. polystromatisation). We used this species because it is one of the most simple kelps at the morphological level (Starko et al. 2019), in addition to being of great economical (Theodorou et al. 2022), ecological (Christie et al. 2019) and evolutionary interest (Neiva et al. 2018).

Here, we revisited the description of the transition from 2D to 3D growth in a kelp, and more specifically the involvement of the meristoderm and of the so-called 'transition zone' defined by our predecessors 80 years ago. Our study sheds light on the cellular events prior to, during, and after the shift to 3D growth, and thereby lays the groundwork for future investigations of the molecular and mechanical control of growth.

Materials and methods

Algal cultures

Kelps are defined as conspicuous macroscopic brown algae, mainly belonging to the order Laminariales. Their life cycle is dominated by the sporophyte phase, and the male and female gametophytes are microscopic filaments (i.e. heteromorphic dioecous life cycle, Fig. 1C). *Saccharina*, like all kelps, has a heteromorphic diplobiontic cycle (Fig. 1C) (Theodorou and Charrier 2021).

Mature sporophytes were collected from the beach of Perharidy (Roscoff, Brittany, France) (48°43'33.5"N 4°00'16.7"W), and spores were isolated and treated as described in (Theodorou et al. 2021). Embryos were cultivated in Petri dishes in full Provasoli- enriched sterile filtered seawater for up to 30 days.

Semi-thin sections

Live embryos were observed for up to 14 days of development under a bright field microscope. For histogenesis observations, 20-day-old embryos were fixed with 1% glutaraldehyde (Sigma) and 1% paraformaldehyde (Sigma) in sterile, 0.2 µm-filtered seawater for 2 h at 13 °C. Then, the fixation medium was gradually changed to 0.1 M cacodylate-Na. Post-fixation consisted in

incubating the thalli in 1% OsO4 in 0.1 M cacodylate-Na at 4 °C overnight. After washing with 0.1 M cacodylate-Na, the fixed embryos were dehydrated with a gradient of ethanol:cacodylate-Na. For the infiltration step, Spurr resin gradually replaced ethanol (Spurr 1969), with fresh resin for the last step before polymerisation. Semi-thin sections of 500–750 nm were mounted on glass slides and stained with 1% w/v toluidine blue in a 1% w/v borax (sodium tetraborate) water solution or Stevenel's blue (del Cerro et al. 1980), and then observed under a light microscope (Leica DMI6000B inverted optical microscope) equipped with a motorised stage and a DFC450C colour camera, controlled by LASX version 3.0 software, or alternatively stained for 45 min with a 20 µM calcofluor white solution (fluorescent brightener 28, F-3543, Sigma-Aldrich; excitation wavelength: 380 nm, emission wavelength: 475 nm), washed three times in seawater for 15 min and observed using confocal microscopy (Leica SP5 confocal microscope, laser 405 nm, PMT emission passing band 675-745 nm).

Transmission electron microscopy protocol

For transmission electron microscopy (TEM), ultra-thin sections of 50–70 nm thickness from the embedded material were mounted on copper grids (Formvar 400 mesh; Electron Microscopy Science©) and stained with 2% uranyl acetate for 10 min (Woods and Stirling 2013) and 2% lead citrate for 3 min at room temperature (Reynolds 1963). Sections were observed with a JEM-1400 Flash TEM microscope (JEOL Ltd.)

Drawings

Illustrations of the sections were drawn using Biolographix (biolographix.blogspot.com) with Inkscape software version 1.2 (Inkscape Project) and a KAMVAS Pro 13 GT-133 pen tablet (Huion©).

Results

Saccharina *embryo develops three-dimensional tissues in three distinctive steps*

To date, the embryogenesis of *Saccharina* has not been studied formally. Therefore, we initiated our study by dividing *Saccharina* embryogenesis into three phases based on the growth axis of its tissues and on the corresponding orientation of the cell divisions (Table 1). Phase I (Fig. 2A,B) starts with the establishment of the main — apico-basal — growth axis. This occurs with the initial elongation of the zygote seemingly induced by fertilisation. It is first followed by transverse anticlinal cell division, which in most cases is unequal (fig. 2A). Transverse anticlinal cell divisions are defined here as cell division perpendicular to the growth axis of the embryo (Fig. 2C). Then, a series of transverse anticlinal cell divisions parallel to the first division reinforces this apico-basal axis and the general anisotropic shape of the embryo (Fig. 2B). The second phase Phase II is initiated by the first longitudinal (along the apico-basal axis) anticlinal cell division, after which all cells divide parallel to it (fig. 2D), thereby establishing the second — medio-lateral — growth axis (Fig. 2D-F). Longitudinal anticlinal cell divisions are defined here as cell divisions oriented along the apico-basal axis of the embryo (fig. 2G). At this stage, which ends 14 to 16 days after zygote polarisation (azp) (Table 1), the embryo develops as a monolayer cell sheet (Fig. 2D-G). This is clearly visible on orthogonal views of confocal stacks of embryos stained with calcofluor (Suppl, Fig. 1). In addition, because both the mother and the daughter cells display a cuboid shape, this first series of anticlinal (both transverse and longitudinal) cell divisions leads to a cell arrangement resembling a grid, in which the cells are spatially arranged in rows and columns in contact with

each other through four-way junctions (Suppl, Fig. 1A). Phase III starts when mature Phase II embryos (Fig. 2H) initiate the first tilting of the cell division plane on the Z-axis, thereby beginning embryo thickening (Fig. 2H-J). These cell divisions are defined as periclinal because they occur parallel to the largest surface of the embryo lamina. They are perpendicular to the anticlinal cell divisions (both transverse and longitudinal) (Fig. 2J). These three phases make up the early embryogenesis steps of *Saccharina* embryo.

The initiation of polystromatisation takes place at the base of the phase II lamina and continues in the transition zone (TZ) established in phase III

We defined the establishment of embryo thickening as polystromatisation, because it adds additional cell layers (stromata). From bright field observations of the embryo, the precise location of a specific site of growth on the Z-axis cannot be determined. Instead, it seems that the monostromatic tissue keeps growing in a diffuse way, with all cells potentially proliferating as the other tissues emerge and expand. However, the first region where polystromatisation takes place is close to the site of emergence of rhizoids, i.e. in the very basal part of the Phase II lamina (Fig. 2H). Then, this region keeps expanding by diffuse growth, both basipetally and acropetally, thereby enlarging the blade and forming the stipe, respectively, while polystromatisation continues. This region is named the transition zone (TZ) and it will be considered as a distinct tissue located between the blade and the stipe (Smith 1939; Fritsch 1945; Theodorou and Charrier 2021). Polystromatised tissues become conspicuous under the bright field microscope approximately 20 days azp, looking like dark areas that progress basipetally, acropetally and laterally into the stipe and the blade (fig. 2I). Different types of tissues emerge as the lamina thickens, as discussed in the next sections. At approximately 50 days, monostromatic tissues are no longer observed and the embryo enters the juvenile stage 60 days azp.

To accurately describe how the thickening of a monostromatic lamina takes place, we prepared and observed semi-thin longitudinal (frontal and sagittal) sections from phase III (20 days azp) embryos (Fig. 3A). The terminology of the different tissues and cell types is based on the works from Smith (1939) and Fritsch (1945).

Polystromatisation is not a uniform process. Figure 3B shows that, on a 20-day-old embryonic blade, monostromatic tissue can interrupt tissues that are already engaged in polystromatisation. The first periclinal division of one cell of the monolayer cell sheet initiates polystromatisation (Figs. 3C,D and 4A). This division is equal and symmetrical because the two daughter cells are usually of similar size and fate. Then, after cell growth, one of the daughter cells divides again periclinally into two cells of similar size (i.e. equal division: Figs. 3E and 4B). Where the first cell division was symmetrical, this second cell division is asymmetrical, because the two daughter cells have different fates. The superficial cell differentiates into a meristoderm initial and the inner cell into a cortex initial. In the third step, the meristoderm initial divides symmetrically anticlinally (both longitudinally and transversally) and produces small meristodermal cells at the surface of the lamina (Figs. 3F and 4C), and the cortex initial enlarges before dividing with no specific axis (Figs. 3F and 4D).

In parallel to this process, or subsequently, the second daughter cell of the initial cell division follows the same scheme of cell division and cell differentiation as the first one described above. It results in the establishment of a second thickening layer from the initial monolayered lamina (Figs. 3F and 4E). At this four-layer stage, the blade is composed of two cell types (Fig. 5; Table 2): 1)

small, plastid-rich outer cells that form an epidermal tissue with meristematic properties called the meristoderm, and 2) large inner cells with big vacuoles that make up the cortex (Suppl, Fig. 3). As a result, the initial cortex consists of two layers of elongated and wide transparent cells.

Tissues differentiate centripetally

The histology of mature *Saccharina* has been well described in previous works (Sykes 1908; Smith 1939; Fritsch 1945; Davies et al. 1973). However, the origin of each tissue remains obscure. Therefore, the next sections aim to identify the origin of the differentiated tissues, especially the medulla, after the meristoderm and the cortex are formed in the bistroma. We focused on the 20-day-old embryo, a stage when most of the tissues of the adult algae begin to form. Also, at this stage, the embryo is made of a blade (lamina) and a stipe (Fig. 2I) whose internal organisations differ.

The medulla differentiates rapidly in the blade

Longitudinal sagittal sections of the blade (X-axis) show that the polystromatisation initiated in the basal part of the lamina propagates towards the tip of the blade (Fig. 6A). Therefore, polystromatisation progresses acropetally. When looking along the Y-axis, polystromatisation is centrifugal, because it starts in the centre of the monostromatic blade and propagates to the 'wings' (edges) of the blade. As a result, in most of the blade, the central polystromatic region is bordered by monostromatic tissues (Fig. 6B,E,I).

In the young polystroma, at the tip of the blade, the distinction between cortex and meristoderm is apparent: the meristoderm cells are small with a dense cytoplasm and the cortical cells are large with a large white vacuole (Fig. 6B-E showing photo and schematics of sagittal and transverse sections).

Below this region, i.e. from the middle of the blade to its base, the cortical tissue is reduced and is replaced by a large intercellular space characteristic of older polystromata (Fig. 6A). Detailed observations show that, after cortical cells divide perpendicularly to the X-axis of the blade (Fig. 6A, Suppl, Fig. 4A,B), mucilage deposited along the longitudinal cell walls of the cortical cells (as per the description of stipe development in Fritsch, 1945, pp 227) fills this wide intercellular space. This mucilage deposition results in the thickening of the lateral cell walls that eventually separates the cells. These cells then differentiate into medullary cells (Sykes 1908; Fritsch 1945). Observations from the top to the bottom of the blade confirm that the cortex tissue is the origin of the medulla.

On average, medullary cells in the blade are filamentous and are thinner than cortical cells, but of similar length (along the X-axis) (Fig. 5 and Suppl, Fig. 2; Fig. 6H-I, Suppl, Fig. 4C,G,H). They seem to expand primarily along a single axis, usually parallel to the embryo apico-basal axis (fig. 6H). They generally divide anticlinally, but periclinal divisions also occur, probably as a function of branching (Suppl, Fig. 4E,F, red star,G). Several connections are visible between two medullary cells (e.g. Suppl, Fig. 4G, arrows), and also between medullary and cortical cells (schematics in Fig. 7H and Suppl, Fig. 4E,H, arrows). These connections are probably pit fields, that resist changes in cell shape during the cortex-to-medulla differentiation, looking like protrusions (Suppl, Fig. 2H, arrows). In addition, protrusions can be observed in pre-medullary cells, located at the innermost cortex (Suppl, Fig. 4C,D, arrow heads), which may potentially represent an intermediate stage

between cortical cell and medullary elements. The abundance of medullary elements in the centre of the tissue, which gradually increases from the apex to the base of the blade, points to a cortical origin of these medullary elements. Therefore, we hypothesise that transverse divisions, cell elongation and shape changes lead to the differentiation of the cortex into the medulla. The medulla is especially rich at the base of the blade, where only a few cortical cells are observed (Fig. 6F-I) and, in mature plants, the medulla resembles an intricate dense network of filaments growing in all spatial axes (not shown).

In all regions of the blade, undifferentiated cells can be observed, seemingly the result of asymmetric cell divisions of meristoderm cells (green cells schematised in Fig. 6 and seen in Fig. 6B,E,F,G,H,I), which eventually differentiate into cortical cells.

The medulla differentiates slowly in the stipe

The stipe consists of the same cell types and tissues as the blade, but lacks the undifferentiated cells of the monostroma (Fig. 7A-D). Its tissue organisation is more homogenous than in the blade and with no large intercellular spaces. Only a few medullary cells are present and mostly in central positions at the upper part of the stipe near the transition zone (fig. 7A-B). In contrast to their blade counterparts, stipe medullary cells do not branch (Fig. 7B), but in mature stipes a dense meshwork forms (not shown). In addition, we observed fewer periclinal cell divisions than in the blade confirming previous work (Smith 1939; Fritsch 1945). This reduction in the number of divisions may suggest that growth and cell differentiation in the stipe are slower than in the blade. The cortex, which is the predominant tissue, shares similarities with the cortex of a young blade. Both have large rectangular transparent cells with angular edges. However, their size differ. Their lengths along the X-axis are similar (24.93 µm ± 8.28 µm for the stipe and 23.2 ± 8.74 µm for the young polystroma, Fig. 5 and Suppl, Fig. 2), but cortical cells in the stipe are about two times narrower along the Y-axis than in the blade (11.46 µm ± 3.46 µm vs 21.79 µm ± 7.49 µm, respectively). Therefore, there are twice as many cell walls per unit of surface area in the stipe than in the blade, possibly conferring greater stiffness for the stipe compared with the blade.

At the base of the stipe, there is a slight expansion of cortex and meristoderm (Fig. 7A), that is the sign of the formation of haptera, which are intertwined digitate protrusion that help attach the embryo to the substratum (Fritsch 1945; Davies et al. 1973). Sagittal sections show that at this stage, the embryo fixes itself directly to the substrate at the bottom of the cortex where rhizoids connect (Fig. 7A,B) (Fritsch 1945; Davies et al. 1973).

The meristodermal cells in the transition zone differentiate centripetally into medullary cells in only three cell divisions

Transversal and longitudinal sections show that the TZ differentiates into the same cell types as observed in the blade and the stipe, with a specific spatial organisation (Fig. 8A,C,E) (Table 2).

Through the Y-Z plane: Interestingly, both the upper and lower TZ display a common feature: a high proportion of still undifferentiated cells that result from the asymmetrical periclinal cell division of meristoderm cells. This observation suggests that the differentiation of these cells into cortical cells and then into medullary cells (as observed in Fig. 8C,E) is slower in the TZ than in the blade and in the stipe, thereby providing the TZ with the functional traits of a meristematic tissue. Alternatively, the higher abundance of these undifferentiated cells in the TZ may be due to a

higher level of cell division in a periclinal orientation. This difference in division plane is reminiscent of Smith's observation on mature kelp, whereby the cell division rate is higher at the base of the blade and in the TZ than in any other region (Smith 1939). It is difficult to discriminate between these two hypotheses, because the observation of sections does not provide an assessment of the rate of differentiation of undifferentiated cells into cortical cells, and in turn of cortical cells into medullary cells. Nevertheless, the abundance of cortical cells in the lower TZ (Fig. 8E,F) and stipe and their rarity in the upper TZ (Fig. 8C,D) and blade suggest that the differentiation of the medulla from cortical cells is faster in the upper TZ compared with the lower TZ. Furthermore, undifferentiated cells may even directly differentiate into medullary cells without transiting through a cortical state, thereby suggesting branched signalling pathways rather than a single linear pathway.

Along the X-axis: It is also noteworthy that the upper and lower regions of the TZ display different tissue organisations. Whereas the upper TZ, which is under the base of the blade (along the X-axis), has few cortical cells, wide intercellular spaces and many medullary cells (Fig. 8A,C), the lower TZ located right above the stipe is filled with more tightly packed cortical and medullary cells (Fig. 8A-F). This difference in organisation illustrates a bipolar gradient of the TZ, with blade-like features (i.e. high abundance of medulla) in the upper part, and stipe-like features (i.e. abundant cortical cells) in the lower part. This gradient suggests that the TZ plays a role in the formation of these two distinct tissues, perhaps through different dynamics.

Figure 9 shows the overall organisation of the TZ in 3D, with its differential organisation in the upper and lower parts and their respective abundances of medullary and cortical cells. It is a stereotypical description of an organ ensuring thickening, and also most of the longitudinal and medio-lateral growth in kelp, from embryogenesis to the adult stage.

Cell types differ in size and shape along the apico-basal axis of the embryo

To better characterise the different tissues, we assessed the variability in the traits defining a given cell type. Figure 5 (and Suppl, Fig. 2) displays the 3D shape of the four cell types observed at different positions along the apico-basal axis of the embryo 20 days azp (Phase III).

First, all cells display different shapes and sizes. Meristodermal cells are the most uniform cuboids (~ cubes), and undifferentiated cells resulting from the asymmetrical cell division of the meristodermal initial are the smallest cells. Both of these two initial cells are smaller than the differentiated cortical and medullary cells, which are the largest. This difference arises mainly from the elongation of these latter cells along the apico-basal axis (Fig. 5 centre). Therefore, and interestingly, the longest cells belong to the stipe which happens to be an elongated structure (longer X-axis), and the widest cells are located at the base of blade and in the young polystroma that are much wider (Y-axis) than the those in the stipe or the TZ. This feature may be related to the mechanical stress experienced by these organs: the stipe is subject to longitudinal stress due to the forces pulling on it from the holdfast (organ attaching the alga to the substratum) and the cortical cells of the young polystroma reside between two monolayers of tightly packed meristodermal cells, which may force them to expand preferentially along the Y-axis.

Blade cells share their content through plasmodesmata

At this stage of the description of the tissue formation and organisation during the embryogenesis of *Saccharina*, an obvious question is whether the cells communicate with each other. In cell-walled organisms, the most efficient way to communicate is through plasmodesmata, which are cytoplasmic connections that span the cell walls of two neighbouring cells.

TEM observations of transverse sections on *Saccharina* Phase III embryos show the presence of plasmodesmata in both the Y- and Z-axes, concentrated in pit fields (Fig. 10A,B,C). Plasmodesmata are likely also present along the X-axis, because they have been reported in mature specimens (Schmitz and Kühn 1982). In addition, the pit field in Fig. 10A comes from a frontal section of Phase II embryo along its apico-basal axis, thereby leaving little doubt about the likeliness of plasmodesmata in all spatial dimensions of the tissue.

The widths of pit fields and plasmodesmata was measured for different tissues and regions of the blade. Accurate measurements require that the section be perpendicular to the pit field, because otherwise the angle of the section affects the measurement of the diameter of the plasmodesmata. However, it is nearly impossible to ensure that the surface of the cells in which we observed pit fields is perpendicular to the sectioning plane. With this in mind, our measurements show that, while pit fields increase in width as the blade grows from Phase II monostromata to stipe and blade polystromatic tissues (Fig. 10D; mean 0.48 ± 0.19 µm vs 0.68 ± 0.26 µm in Phase III tissues, 42% increase; Welch t-test p-value < 0.01, Suppl, Table S2), the width of the plasmodesmata decreases (Fig. 10E) (45.88 (± 10.94) nm in Phase II vs 38.67 ± 10.69 nm and 36.65 ± 7.25 nm for the base of the blade and the monostroma of Phase III embryos, respectively; Welch t-test p-value < 0.01. Suppl, Table S2). Therefore, a higher number of plasmodesmata may compensate their narrower diameter, resulting in overall wider pit fields. Regardless of the cause, wider pit fields suggest higher trafficking between cells as the embryo develops further. Whether this symplasmic trafficking is necessary for cell differentiation is unknown, but it seems that a network of cell-to-cell connections is available to share signalling or metabolic molecules throughout the embryo.

Figure 11 presents a general view of the organisation of the tissues in three spatial dimensions. It shows the main characteristics of the morphology of the *Saccharina* embryo at the stage at which it starts developing 3D tissues.

Discussion

Little is known on the development of brown algae and in kelp; most of our knowledge on tissue structure and emergence is dated. The embryo is initially monostromatic and during its development turns into a huge, complex parenchymatic thallus. Using classical histological approaches, we focused on the multiplication and differentiation of tissue layers in the late stages of embryogenesis of *Saccharina*. Polystromatisation — although not unique to brown algae — is still a distinctive process due to the late introduction of a third growth axis.

In an oversimplified and general way, cells have two fates: either they divide or they differentiate. We have not been able to measure the mitotic activity of the meristoderm cells present in the TZ, but we noticed the presence of undifferentiated cells that are the direct product of cell division of the meristoderm layer. However, we were able to monitor the cellular differentiation of these cells. We observed that meristodermal cells differentiate very quickly: within a maximum of three cell divisions, cells give rise to medullary cells that are the terminal differentiation state in vegetative kelp. At this stage, in the upper part of the TZ, we do not know whether medullary cells

originate from an ultra-fast differentiation of the meristoderm cells from a cortical cell type that is not observable in our sections, or whether the meristoderm cells can undergo two distinct differentiation programmes, one leading directly to cortical cells and the other directly to medullary cells. The latter scenario would explain why the cortical cells are absent in this tissue.

Another remarkable fact of kelp is that all thickening (in the Y-Z plane) comes from the mitotic activity of a single, peripheral cell layer, the meristoderm. This type of functioning is common to other brown algae, such as *Fucus* and *Sargassum* (Fucales) or *Dictyota* (Dictyotales) in which only one or two apical cells and their derivatives ensure all growth in the three axes (Katsaros and Galatis 1985; Bogaert et al. 2020). In contrast, in plants, shoot or root apical meristems are made up of several cell layers (Steeves and Sussex 1989). The meristoderm is a synapomorphic tissue among parenchymatic brown algae with a key role in complementing the main apical meristems in organogenesis and girth growth. In kelps, apical meristems are absent and the meristoderm located in the transition zone is responsible for the growth of all new tissue.

Thus, what distinguishes the 3D growth of *Saccharina* from the 3D growth of other brown algae (Fucales, Dictyotales), whatever the position of cells within the algal body, is the high rate of cell differentiation. Are these differences due to the fact that the implementation of 3D growth takes place well after the beginning of development, i.e. when the embryo has grown as a monolayer after several rounds of cell division, and still by and large a fully undifferentiated tissue? Whereas most plant organisms would maintain 'pockets' of undifferentiated cells while the rest of their cells commit to a given fate very early in embryogenesis, *Saccharina*, which retains its cells uncommitted for a long period of time (i.e. embryogenetic Phases I and II), appears to combine the dynamics of cell proliferation and cell differentiation in the meristoderm, seemingly making up for lost time. In plants, the cambium is a secondary meristem that generates the secondary vascular tissues (Steeves and Sussex 1989); it is a mitotically very active monolayer of cells, but its daughter cells differentiate rapidly into secondary vascular tissues. Therefore, there are tissues with similar dynamics in terms of cell proliferation and cell differentiation in the plant kingdom. However, two main differences distinguish the meristoderm from the cambium: first, the cambium functions in two directions, yielding cells of different types (secondary xylem and phloem) by alternating periclinal cell divisions in the inner and outer directions. Secondly, this tissue emerges after primary growth has developed all the organs of the adult organism, and its role is limited to the maturation of existing tissues/functions.

What triggers polystromatisation?

In *Saccharina*, the transition to 3D growth occurs approximately 14 days after the first cell division of the zygote, when the embryo contains at least 500 cells. What triggers this transition?

3D growth is considered a complex morphogenetic process. Most metazoans and land plants have developed 3D growth, and more basal organisms such as mosses or green algae "struggle" to achieve 3D growth. Basal organisms either develop 3D stem-like structures (mosses, e.g. *Physcomitrella*, (Moody 2019) or bilayer cell sheets (green algae, e.g. most charophyte green algae; (Leliaert et al. 2012) and the chlorophyte green alga *Ulva*; (Wichard et al. 2015)) and other loose 3D structures (e.g. *Volvox*; (Umen 2020)), despite the presence of most of the genetic toolkit necessary to achieve spatial control of cell division (Nishiyama et al. 2018; Szövényi et al. 2019). Furthermore, carrying out immediate 3D growth may be less complex than 2D growth or stepwise 3D. Unicellular organisms, both prokaryotic and eukaryotic can build multicellular architectures

when selected for, and 3D is always the favoured organisation (Márquez-Zacarías et al. 2021; Bozdag et al. 2021). In this context, the persistence of the 2D monolayer cellular sheet may provide evidence of strict control of cell division planes, and of the existence of a negative control of 3D growth.

Interestingly, Sauvageau (Fritsch 1945) reported on the kelp (but non-Laminariales) species *Saccorhiza bulbosa* (currently *S. polyschides*, Tilopteridales, (Bringloe et al. 2020)) in which the first periclinal cell divisions occur near the rhizoids located in the most basal cells of the embryo, an event also observed in *Saccharina* (not shown). As in Saccharina, the TZ of the ribbon-like thallus of *Chorda fillum* (Chordales, ex-Chordaceae in Laminariales) is established at the base of the monostromatic tissue next to the rhizoids, from which it gradually moves away as polystromatisation proceeds. (Kogame and Kawai 1996). Hence, rhizoid differentiation and their increased number may be the signal that triggers the initiation of polystromatisation. Once initiated, polystromatisation progresses as a wave from the rhizoid end (future holdfast, base of the embryo) to the apex end (i.e. acropetally), all the while keeping a constant distance from the apex. In Phase II, the apex is not the oldest region of the embryo, because growth is diffuse at that stage (Theodorou et al., unpublished, Paper I); active growth of the TZ occurs in Phase III. Therefore, since the establishment of the apico-basal axis at the beginning of embryogenesis, the remote position of the embryo apex with respect to rhizoid may confer certain characteristics to the apex, leading to the production of a polystromatisation-inhibiting signal. Several brown algae have been shown to produce a signal inhibiting branching and tissue regeneration through basipetal diffusion ((Tanaka et al. 2017) reviewed in (Katsaros 1995)), but all display active apical growth (apical meristem) in contrast to kelp. If this type of signal exists in kelp, then while the apical region of the mature Phase II embryo secretes a polystromatisation inhibitor and the lamina keeps growing along its apico-basal axis, the distance between the apex and the lower part of the embryo would become so great that the concentration of the inhibitory signal decreases enough to allow 3D growth. Alternatively, the polystromatisation wave is induced by a signal diffusing acropetally (from the base to the apex), as does the sporogenesis inhibitor of kelp (Buchholz and Lüning 1999; Pang and Lüning 2004), which is potentially auxin (Kai et al. 2006). In both cases, this type of wave mechanism requires a system of signal transport. We showed that, as the embryo develops, the size of the pit fields increases. This may be due to formation of *de novo* plasmodesmata being added to existing pit fields, or to new, larger pit fields being positioned as the new cell wall forms during ongoing cell divisions. Regardless of the reason, an increase in the number of plasmodesmata per pit-field area is a sign of an increase in tissue complexity (Terauchi et al. 2015). Different sizes of molecules can travel through plasmodesmata as observed in *Fucus* (Fucales) (Nagasato et al. 2015) and *Sphacelaria* (Sphacelariales) (Nagasato et al. 2017) and the transport of metabolic molecules, such as fixed carbon and phosphate organic compounds may also diffuse through plasmodesmata to reach the TZ where new growth takes place (Lüning et al. 1973). In response to signalling molecules and to the supply of metabolic compounds, undifferentiated cells of the monostroma will shift the orientation of their next cell division plane into the third spatial dimension. This shift may require the reorganisation of some cellular features, and particularly the re-orientation of actin filaments, which we have shown to be aligned as cortical sheets along the Z-axis (Theodorou & Charrier, unpublished, Paper 2) where they potentially constrain cell growth in this direction.

Conclusion

Here we describe a unique case of third-axis growth for a cell-walled organism. Polystromatisation is a distinctive phenomenon through which brown algae set up 3D growth, and the establishment of a meristoderm, which differs from primary meristem by its high rate of cell differentiation, is the necessary prerequisite step. The superficial meristoderm of *Saccharina* is not unique: it is a common tissue found in parenchymatic brown algae. However, although the meristoderm compartmentalises the function of apical meristems in other brown algal orders, in kelps it is the main tissue through which growth can occur in three spatial axes. This tissue is an evolutionary innovation, and its different functions play a key role in the plethora of brown algal body plans. Our work has shed new light in our understanding of how kelps set up 3D growth.

Acknowledgement

I.T was funded by an ARED grant from Bretagne Regional Council (Project "PUZZLE") and NMBU. We thank Sophie Le Panse at the Roscoff Marine Station for the TEM images and the Imaging center at NMBU for the semi-thin sections. We thank Nathalie Kowalczyk and Bernard Billoud for the drawings and 3D cell schemes respectively as well as detailed discussions about the 3D representation of *Saccharina* embryo. We are grateful to MITI CNRS and Hilde-Gunn Opsahl-Sorteberg for additional financial support.

References

Bogaert, K.A., Delva, S., and De Clerck, O. 2020. Concise review of the genus *Dictyota* J.V. Lamouroux. J. Appl. Phycol. **32**(3): 1521–1543. doi:10.1007/s10811-020-02121-4.

Bozdag, G.O., Zamani-Dahaj, S.A., Kahn, P.C., Day, T.C., Tong, K., Balwani, A.H., Dyer, E.L., Yunker, P.J., and Ratcliff, W.C. 2021. De novo evolution of macroscopic multicellularity. bioRxiv: 2021.08.03.454982. Cold Spring Harbor Laboratory. doi:10.1101/2021.08.03.454982.

Bringloe, T.T., Starko, S., Wade, R.M., Vieira, C., Kawai, H., De Clerck, O., Cock, J.M., Coelho, S.M., Destombe, C., Valero, M., Neiva, J., Pearson, G.A., Faugeron, S., Serrao, E.A., and Verbruggen, H. 2020. Phylogeny and Evolution of the Brown Algae. Crit. Rev. Plant Sci. **39**(4): 281–321. Taylor & Francis Inc, Philadelphia. doi:10.1080/07352689.2020.1787679.

Buchholz, C., and Lüning, K. 1999. Isolated, distal blade discs of the brown alga *Laminaria digitata* form sorus, but not discs, near to the meristematic transition zone. J. Appl. Phycol. **11**(6): 579–584. doi:10.1023/A:1008116828263.

Cairney, J., and Pullman, G.S. 2007. The cellular and molecular biology of conifer embryogenesis. New Phytol. **176**(3): 511–536. doi:10.1111/j.1469-8137.2007.02239.x.

del Cerro, M., Cogen, J., and del Cerro, C. 1980. Stevenel's Blue, an excellent stain for optical microscopical study of plastic embedded tissues. Microsc. Acta **83**(2): 117–121.

Charrier, B., Le Bail, A., and de Reviers, B. 2012. Plant Proteus: brown algal morphological plasticity and underlying developmental mechanisms. Trends Plant Sci. **17**(8): 468–477. doi:10.1016/j.tplants.2012.03.003.

Christie, H., Andersen, G.S., Bekkby, T., Fagerli, C.W., Gitmark, J.K., Gundersen, H., and Rinde, E. 2019. Shifts Between Sugar Kelp and Turf Algae in Norway: Regime Shifts or Fluctuations Between Different Opportunistic Seaweed Species? Front. Mar. Sci. **6**: 72. doi:10.3389/fmars.2019.00072.

Clayton, M.N., Hallam, N.D., Luff, S.E., and Diggins, T. 1985. Cytology of the apex, thallus development and reproductive structures of *Hormosira banksii* (Fucales, Phaeophyta). Phycologia **24**(2): 181–190. doi:10.2216/i0031-8884-24-2-181.1.

Coppin, R., Rautenbach, C., Ponton, T.J., and Smit, A.J. 2020. Investigating Waves and Temperature as Drivers of Kelp Morphology. Front. Mar. Sci. **7**. Available from https://www.frontiersin.org/articles/10.3389/fmars.2020.00567 [accessed 21 September 2022].

Davies, J.M., Ferrier, N.C., and Johnston, C.S. 1973. The Ultrastructure of the Meristoderm Cells of the Hapteron of *Laminaria*. J. Mar. Biol. Assoc. U. K. **53**(2): 237–246. doi:10.1017/S0025315400022232.

Drew, G.H. 1910. The Reproduction and early Development of *Laminaria digitata* and *Laminaria saccharina*. Ann. Bot. **24**(1): 177–189. doi:10.1093/oxfordjournals.aob.a089253.

Forbord, S., Matsson, S., Brodahl, G.E., Bluhm, B.A., Broch, O.J., Handå, A., Metaxas, A., Skjermo, J., Steinhovden, K.B., and Olsen, Y. 2020. Latitudinal, seasonal and depth-dependent variation in growth, chemical composition and biofouling of cultivated *Saccharina latissima* (Phaeophyceae) along the Norwegian coast. J. Appl. Phycol. **32**(4): 2215–2232. doi:10.1007/s10811-020-02038-y.

Fritsch, F.E. 1945. The Structure And Reproduction Of The Algae. *In* The University Press. Cambridge University Press, Cambridge.

Gilbert, S.F., and Barresi, M.J.F. 2016. Developmental Biology. *In* 11th edition. Sinauer Associates is an imprint of Oxford University Press.

Hasley, A., Chavez, S., Danilchik, M., Wühr, M., and Pelegri, F. 2017. Vertebrate Embryonic Cleavage Pattern Determination. Adv. Exp. Med. Biol. **953**: 117–171. doi:10.1007/978-3-319-46095-6_4.

Hwang, E.K., Yotsukura, N., Pang, S.J., Su, L., and Shan, T.F. 2019. Seaweed breeding programs and progress in eastern Asian countries. Phycologia **58**(5): 484–495. doi:10.1080/00318884.2019.1639436.

Kai, T., Nimura, K., Yasui, H., and Mizuta, H. 2006. Regulation of Sorus Formation by Auxin in Laminariales Sporophyte. J. Appl. Phycol. **18**(1): 95–101. doi:10.1007/s10811-005-9020-8.

Katsaros, Chr., and Galatis, B. 1985. Ultrastructural studies on thallus development in *Dictyota dichotoma* (Phaeophyta, Dictyotales). Br. Phycol. J. **20**(3): 263–276. doi:10.1080/00071618500650271.

Katsaros, Chr., and Galatis, B. 1988. Thallus development in *Dictyopteris membranacea* (Phaeophyta, Dictyotales). Br. Phycol. J. **23**(1): 71–88. doi:10.1080/00071618800650091.

Katsaros, C.I. 1995. Apical cells of brown algae with particular reference to Sphacelariales, Dictyotales and Fucales. Phycol. Res. **43**(1): 43–59. doi:10.1111/j.1440-1835.1995.tb00004.x.

Klemm, M.F., and Hallam, N.D. 1987. Branching pattern and growth in *Cystophora* (Fucales, Phaeophyta). Phycologia **26**(2): 252–261. doi:10.2216/i0031-8884-26-2-252.1.

Knoblauch, J., Drobnitch, S.T., Peters, W.S., and Knoblauch, M. 2016. In situ microscopy reveals reversible cell wall swelling in kelp sieve tubes: one mechanism for turgor generation and flow control? Plant Cell Environ. **39**(8): 1727–1736. doi:10.1111/pce.12736.

Kogame, Y., and Kawai, H. 1996. Development of the intercalary meristem in *Chorda filum* (Laminariales, Phaeophyceae) and other primitive Laminariales. Phycological Research 44(4): 247–260. doi:10.1111/j.1440-1835.1996.tb00054.x.

Leliaert, F., Smith, D.R., Moreau, H., Herron, M.D., Verbruggen, H., Delwiche, C.F., and De Clerck, O. 2012. Phylogeny and Molecular Evolution of the Green Algae. Crit. Rev. Plant Sci. **31**(1): 1–46. doi:10.1080/07352689.2011.615705.

Li, Q., Shan, T., Wang, X., Su, L., and Pang, S. 2020. Evaluation of the genetic relationship between the farmed populations on a typical kelp farm and the adjacent subtidal spontaneous population of *Undaria pinnatifida* (Phaeophyceae, Laminariales) in China. J. Appl. Phycol. **32**(1): 653–659. doi:10.1007/s10811-019-01917-3.

Liesner, D., Pearson, G.A., Bartsch, I., Rana, S., Harms, L., Heinrich, S., Bischof, K., Glöckner, G., and Valentin, K. 2022. Increased Heat Resilience of Intraspecific Outbred Compared to Inbred Lineages in the Kelp *Laminaria digitata*: Physiology and Transcriptomics. Front. Mar. Sci. **9**. Available from https://www.frontiersin.org/article/10.3389/fmars.2022.838793 [accessed 6 April 2022].

Linardić, M., and Braybrook, S.A. 2017. Towards an understanding of spiral patterning in the Sargassum muticum shoot apex. Sci. Rep. **7**(1): 13887. doi:10.1038/s41598-017-13767-5.

Lüning, K., Schmitz, K., and Willenbrink, J. 1973. CO2 fixation and translocation in benthic marine algae. III. Rates and ecological significance of translocation in *Laminaria hyperborea* and *Laminaria saccharina*. Mar. Biol. **23**(4): 275–281. doi:10.1007/BF00389334.

Márquez-Zacarías, P., Conlin, P.L., Tong, K., Pentz, J.T., and Ratcliff, W.C. 2021. Why have aggregative multicellular organisms stayed simple? Curr. Genet. doi:10.1007/s00294-021-01193-0.

Monteiro, C., Li, H., Diehl, N., Collén, J., Heinrich, S., Bischof, K., and Bartsch, I. 2021. Modulation of physiological performance by temperature and salinity in the sugar kelp *Saccharina latissima*. Phycol. Res. **69**: 48–57. doi:10.1111/pre.12443.

Moody, L.A. 2019. The 2D to 3D growth transition in the moss *Physcomitrella patens*. Curr. Opin. Plant Biol. **47**: 88–95. doi:10.1016/j.pbi.2018.10.001.

Moukhtar, J., Trubuil, A., Belcram, K., Legland, D., Khadir, Z., Urbain, A., Palauqui, J.-C., and Andrey, P. 2019. Cell geometry determines symmetric and asymmetric division plane selection in *Arabidopsis* early embryos. PLOS Comput. Biol. **15**(2): e1006771. doi:10.1371/journal.pcbi.1006771.

Nagasato, C., Tanaka, A., Ito, T., Katsaros, C., and Motomura, T. 2017. Intercellular translocation of molecules via plasmodesmata in the multiseriate filamentous brown alga, *Halopteris congesta* (Sphacelariales, Phaeophyceae). J. Phycol. **53**(2): 333–341. doi:10.1111/jpy.12498.

Nagasato, C., Terauchi, M., Tanaka, A., and Motomura, T. 2015. Development and function of plasmodesmata in zygotes of *Fucus distichus*. Bot. Mar. **58**(3): 229–238. doi:10.1515/bot-2014-0082.

Neiva, J., Paulino, C., Nielsen, M.M., Krause-Jensen, D., Saunders, G.W., Assis, J., Bárbara, I., Tamigneaux, É., Gouveia, L., Aires, T., Marbà, N., Bruhn, A., Pearson, G.A., and Serrão, E.A. 2018. Glacial vicariance drives phylogeographic diversification in the amphi-boreal kelp *Saccharina latissima*. Sci. Rep. **8**(1): 1112. doi:10.1038/s41598-018-19620-7.

Nishiyama, T., Sakayama, H., de Vries, J., Buschmann, H., Saint-Marcoux, D., Ullrich, K.K., Haas, F.B., Vanderstraeten, L., Becker, D., Lang, D., Vosolsobě, S., Rombauts, S., Wilhelmsson, P.K.I., Janitza, P., Kern, R., Heyl, A., Rümpler, F., Villalobos, L.I.A.C., Clay, J.M., Skokan, R., Toyoda, A., Suzuki, Y., Kagoshima, H., Schijlen, E., Tajeshwar, N., Catarino, B., Hetherington, A.J., Saltykova, A., Bonnot, C., Breuninger, H., Symeonidi, A., Radhakrishnan, G.V., Van Nieuwerburgh, F., Deforce, D., Chang, C., Karol, K.G., Hedrich, R., Ulvskov, P., Glöckner, G., Delwiche, C.F., Petrášek, J., Van de Peer, Y., Friml, J., Beilby, M., Dolan, L., Kohara, Y., Sugano, S., Fujiyama, A., Delaux, P.-M., Quint, M., Theißen, G., Hagemann, M., Harholt, J., Dunand, C., Zachgo, S., Langdale, J., Maumus, F., Van Der Straeten, D., Gould, S.B., and Rensing, S.A. 2018. The *Chara* Genome: Secondary Complexity and Implications for Plant Terrestrialization. Cell **174**(2): 448-464.e24. doi:10.1016/j.cell.2018.06.033.

Pang, S.J., and Lüning, K. 2004. Breaking seasonal limitation: year-round sporogenesis in the brown alga *Laminaria saccharina* by blocking the transport of putative sporulation inhibitors. Aquaculture **240**(1): 531–541. doi:10.1016/j.aquaculture.2004.06.034.

Reynolds, E.S. 1963. The use of lead citrate at high pH as an electron-opaque stain in electron microscopy. J. Cell Biol. **17**: 208–212. doi:10.1083/jcb.17.1.208.

Robert, H.S., Park, C., Gutièrrez, C.L., Wójcikowska, B., Pěnčík, A., Novák, O., Chen, J., Grunewald, W., Dresselhaus, T., Friml, J., and Laux, T. 2018. Maternal auxin supply contributes to early embryo patterning in *Arabidopsis*. Nat. Plants **4**(8): 548–553. doi:10.1038/s41477-018-0204-z.

Schindelin, J., Arganda-Carreras, I., Frise, E., Kaynig, V., Longair, M., Pietzsch, T., Preibisch, S., Rueden, C., Saalfeld, S., Schmid, B., Tinevez, J.-Y., White, D.J., Hartenstein, V., Eliceiri, K., Tomancak, P., and Cardona, A. 2012. Fiji: an open-source platform for biological-image analysis. Nat Methods 9(7): 676–682. Nature Publishing Group. doi:10.1038/nmeth.2019.

Schmitz, K., and Kühn, R. 1982. Fine structure, distribution and frequency of plasmodesmata and pits in the cortex of *Laminaria hyperborea* and *L. saccharina*. Planta **154**(5): 385–392. doi:10.1007/BF01267803.

Schmitz, K., Lüning, K., and Willenbrink, J. 1972. CO2-fixierung und stofftransport in benthischen marinen algen. II. zum ferntransport 14C-markierter assimilate bei *Laminaria hyperborea* und *Laminaria saccharina*. Z. Für Pflanzenphysiol. **67**(5): 418–429. doi:10.1016/S0044-328X(72)80042-4.

Smertenko, A., and Bozhkov, P.V. 2014. Somatic embryogenesis: life and death processes during apical-basal patterning. J. Exp. Bot. **65**(5): 1343–1360. doi:10.1093/jxb/eru005.

Smith, A.I. 1939. The Comparative Histology of Some of the Laminariales. Am. J. Bot. **26**(8): 571–585.

Spurr, A.R. 1969. A low-viscosity epoxy resin embedding medium for electron microscopy. J. Ultrastruct. Res. **26**(1): 31–43. doi:10.1016/S0022-5320(69)90033-1.

Starko, S., Soto Gomez, M., Darby, H., Demes, K.W., Kawai, H., Yotsukura, N., Lindstrom, S.C., Keeling, P.J., Graham, S.W., and Martone, P.T. 2019. A comprehensive kelp phylogeny sheds light on the evolution of an ecosystem. Mol. Phylogenet. Evol. **136**: 138–150. doi:10.1016/j.ympev.2019.04.012.

Steeves, T.A., and Sussex, I.M. 1989. Patterns in plant development. *In* 2nd ed. Cambridge [England] ; New York.

Steinbiss, H.-H., and Schmitz, K. 1974. Zur Entwicklung und funktionellen Anatomie des Phylloids von *Laminaria hyperborea*. Helgoländer Wiss. Meeresunters. **26**(2): 134–152. BioMed Central. doi:10.1007/BF01611380.

Sykes, M.G. 1908. Anatomy and Histology of *Macrocystis pyrifera* and *Laminaria saccharina*. Ann. Bot. **os-22**(2): 291–325. doi:10.1093/oxfordjournals.aob.a089171.

Szövényi, P., Waller, M., and Kirbis, A. 2019. Chapter One - Evolution of the plant body plan. *In* Current Topics in Developmental Biology. *Edited by* U. Grossniklaus. Academic Press. pp. 1–34. doi:10.1016/bs.ctdb.2018.11.005.

Tanaka, A., Hoshino, Y., Nagasato, C., and Motomura, T. 2017. Branch regeneration induced by sever damage in the brown alga *Dictyota dichotoma* (Dictyotales, phaeophyceae). Protoplasma **254**(3): 1341–1351. doi:10.1007/s00709-016-1025-4.

Terauchi, M., Nagasato, C., and Motomura, T. 2015. Plasmodesmata of brown algae. J. Plant Res. **128**(1): 7–15. doi:10.1007/s10265-014-0677-4.

Theodorou, I., and Charrier, B. 2021. Brown Algae: *Ectocarpus* and *Saccharina* as Experimental Models for Developmental Biology. *In* Handbook of Marine Model Organisms in Experimental Biology, 1st edition. CRC Press, Boca Raton. pp. 27–47.

Theodorou, I., Kovi, M.R., Liang, Z., and Opsahl-Sorteberg, H.-G. 2022. Genetic and Genomic Approaches for Improved and Sustainable Brown Algal Cultivation. *In* Sustainable Global Resources of Seaweeds Volume 2: Food, Pharmaceutical and Health Applications. *Edited by* A. Ranga Rao, G.A. Ravishankar, A. Ranga Rao, and G.A. Ravishankar. Cham. pp. 615–633. Available from https://doi.org/10.1007/978-3-030-92174-3_33 [accessed 29 March 2022].

Theodorou, I., Opsahl-Sorteberg, H.-G., and Charrier, B. 2021. Preparation of Zygotes and Embryos of the Kelp *Saccharina latissima* for Cell Biology Approaches. Bio-Protoc.: e4132–e4132.

Umen, J.G. 2020. Volvox and volvocine green algae. EvoDevo **11**: 13. doi:10.1186/s13227-020-00158-7.

Wichard, T., Charrier, B., Mineur, F., Bothwell, J.H., Clerck, O.D., and Coates, J.C. 2015. The green seaweed *Ulva*: a model system to study morphogenesis. Front. Plant Sci. **6**: 72. doi:10.3389/fpls.2015.00072.

Woods, A.E., and Stirling, J.W. 2013. 22 - Transmission electron microscopy. *In* Bancroft's Theory and Practice of Histological Techniques (Seventh Edition). *Edited by* S.K. Suvarna, C. Layton, J.D. Bancroft, S.K. Suvarna, C. Layton, and J.D. Bancroft. Oxford. pp. 493–538. Available from https://www.sciencedirect.com/science/article/pii/B9780702042263000226 [accessed 1 November 2022].

Yendo, K.R. 1911. The Development of *Costaria*, *Undaria*, and *Laminaria*. Ann. Bot. **os-25**(3): 691–716. Oxford Academic. doi:10.1093/oxfordjournals.aob.a089349.

Zhu, G., Ebbing, A., Bouma, T.J., and Timmermans, K.R. 2021. Morphological and physiological plasticity of *Saccharina latissima* (Phaeophyceae) in response to different hydrodynamic conditions and nutrient availability. J. Appl. Phycol. **33**(4): 2471–2483. doi:10.1007/s10811-021-02428-w.

Table 1: Definition of three embryonic phases. Three major phases were defined, distinguished based on the axes of cell divisions relative to the main growth axis of the embryo: Phase I is characterised by only anticlinal cell divisions in the transverse orientation relative to the elongated zygote (x-axis). It results in the reinforcement of the initial, apico-basal axis of the embryo; Phase II includes both transverse and longitudinal anticlinal cell divisions, that maintain the apico-basal axis (x-axis) and establish the medio-lateral axis (y-axis); Phase III is determined by periclinal cell divisions that result in a third growth axis (z-axis), in addition to the continuation of cell divisions observed in Phase II (fig. 2).

Phases of embryogenesis	**Axes of growth**	**Cell division mode**		**Duration (days after zygote polarisation)**
		Initiated by	**Maintained by**	
Phase I	X-axis: 1D growth, apico-basal	Anticlinal transversal		3
Phase II	X- and Y-axes: 2D growth, medio-lateral (monostromatic tissue)	Anticlinal longitudinal	Anticlinal (transversal and longitudinal)	15
Phase III	X-, Y- and Z-axes: 3D growth, in thickness (polystromatisation)	Periclinal	Anticlinal (transversal and longitudinal) and periclinal	50

Table 2. Definition of cell types. Cell type shape and position in the X-, Y- and Z-axes of the embryo as identified in Phase II and Phase III are indicated. TZ, transition zone

Developmental Phase	Tissue thickness	Cell type	Relative position in the embryo			General cell traits
			X-axis	Y-axis	Z-axis	
Phase I	Monostromatic	Undifferentiated cells	XY-growing grid		No Z-axis layers	Cuboid, rich in plastids, one large vacuole
Phase II	Bistromatic and polystromatic	Undifferentiated cells	Above the polystroma	To the left and right of the polystroma	No differentiated Z-axis layers	Cuboid, rich in plastids, one large vacuole
Phase III	Polystromatic	Meristodermatic cells	All surfaces of the polystroma			Cuboid, rich in plastids, stem cell
		Cortical cells	Stipe, TZ, old and young polystromata	Central	Between medulla and meristoderm	Angular edges, trapezoidal shape, poor or devoid of plastids, large vacuoles
		Medullary elements	Mainly TZ and older polystromata; a few in stipe	Central		Filamentous, wavy and branching, horizontal connections (pit fields) with other medullary elements or cortical cells

Figures:

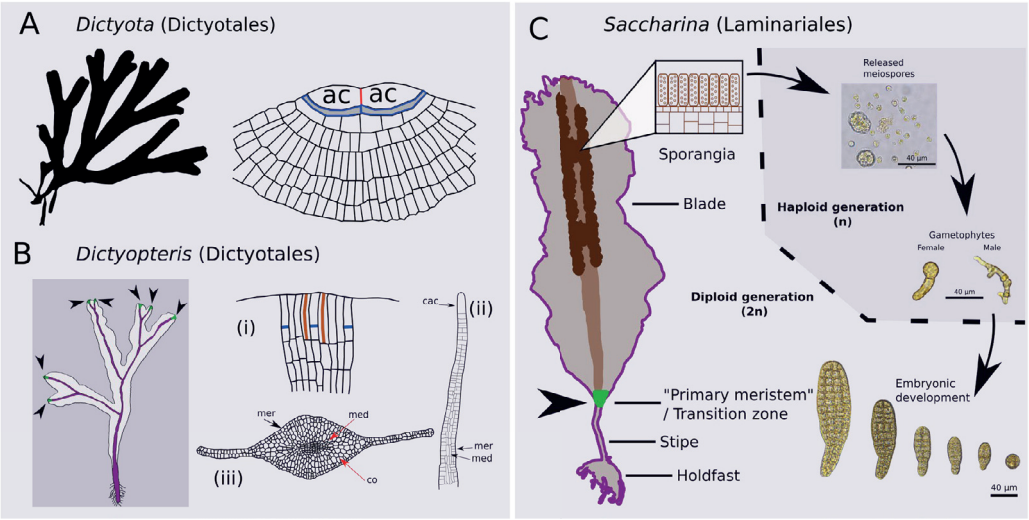

Figure 1: Main growth modes in brown algae A-C) Tissues that ensure growth in three different brown algae. A) Schematic of the thallus of *Dictyota* (Phaeophyceae, Dictyotales, Dictyotaceae) (left) and its apical meristem made of two lenticular-shaped cells (ac) from which a series of anticlinal (red) and periclinal (blue) cell divisions proceed (Katsaros and Galatis 1985; Bogaert et al. 2020)(right). The meristoderm is absent in *Dictyota.* B) Schematic of the thallus of *Dictyopteris* (Phaeophyceae, Dictyotales, Dictyotaceae) showing (left) the apical meristems (primary meristem) at the tip of each branch (black arrows and green areas) and the meristoderm in the midrib of each branch (purple area). The apical meristem is the main meristematic region as it ensures all the apico-basal growth and to some extent the medio-lateral expansion of the thallus. In mature plants, it is composed of four to eight central cells, named apical initials, that are involved in the formation of the monostromatic thallus (monolayer of cells) in the most distal region of the branches. Longitudinal anticlinal cell divisions of the central cells maintain this apical region, and transversal cell divisions contribute to the longitudinal growth. Thickening of the tissue and further medio-lateral expansion occur via the meristoderm (Katsaros and Galatis 1988) (i) Frontal view of the apical regions showing the central apical initials of the apical meristem. Anticlinal longitudinal cell walls of recent cell divisions are depicted in dark orange and the anticlinal transversal cell walls of recent divisions in blue. Longitudinal cell divisions maintain the apical region of the branches; transversal divisions contribute to the growth along the long axis of the branch. (ii) Longitudinal median (sagittal) section of a branch close to the apical region. Transverse cell divisions first take place at the most apical region and are followed by periclinal cell divisions and cell differentiation in the more basal part of the branch. (cac): central apical cell, (mer): meristoderm, (med): medulla. (iii) Transversal cross section from the main region of a branch. Different tissue types can be observed along the midrib and the blade “wings”, regions consisting of two layers of undifferentiated cells. (mer): meristoderm, (co): cortex, (med): medulla. C) Tissue in which growth occurs in *Saccharina latissima* (Phaeophyceae, Laminariales, Arthrothamnaceae) and its life cycle. The transition zone (initially called the “primary meristem”; black arrow and green region) and the meristoderm (purple line) ensure most of the longitudinal and medio-lateral growth. The meristoderm is also responsible for the thickening of the thallus. Meiospores are formed and

released from sporangia in distal areas on the surface of the mature thallus. Meiospores germinate into male or female gametophytes. Embryonic development starts with the polarisation of a spherical zygote. (A,B) Redrawn from (Katsaros and Galatis 1988) with the permission of the main author. (C) Based on schematics from (Theodorou and Charrier 2021; Theodorou et al. 2022).

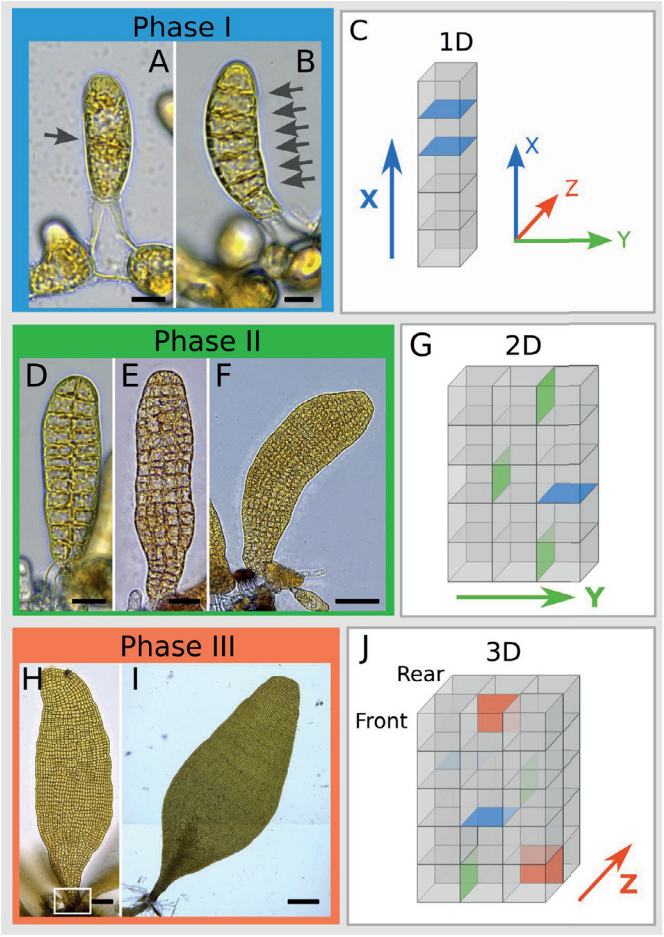

Figure 2: Developmental phases during *Saccharina*'s embryogenesis. Phase I: A) First unequal division (arrow) at the zygote stage, 24 h after zygote polarisation (azp). B) Series of transverse anticlinal cell divisions (arrows) establishing the apico-basal axis, 60 h azp. C) Simplified depiction of cell division during Phase I. Blue plane indicates a transversal anticlinal cell division plane. The blue arrow indicates the apico-basal x-axis, that is the longest body axis of the developing embryo up to the adult stage. The axis reference is indicated in the right corner. Phase II: D) Longitudinal transverse cell divisions resulting in the establishment of a secondary growth axis in the medio-lateral orientation, 132 h azp. This forms a monostromatic blade (monolayered). E) Formation of a grid of monostromatic tissue made of cells aligned in rows and columns, 240 h azp. F) Last stages of Phase II 324 hrs azp, still monostromatic. G) Simplified depiction of cell division during Phase II. Green planes indicate the longitudinal anticlinal division planes. A green arrow indicates the medio-lateral Y-axis, secondary axis of the developing embryo. Phase III: H) The embryo starts thickening. The embryo becomes polystromatic (multilayered) at the base of the embryo 16 d azp

(white box). I) Emergence of specific tissues 20 d azp. The darker area is where the blade is polystromatic. J) Simplified depiction of cell division during Phase III. Red squares indicate the periclinal cell divisions leading to the multilayer blade. A red arrow indicates the third growth axis (Z-axis) of the developing embryo. Bars: A,B: 10 µm; D,E, F: 15 µm, 25 µm, 70 µm; H, I: 90 µm, 300 µm

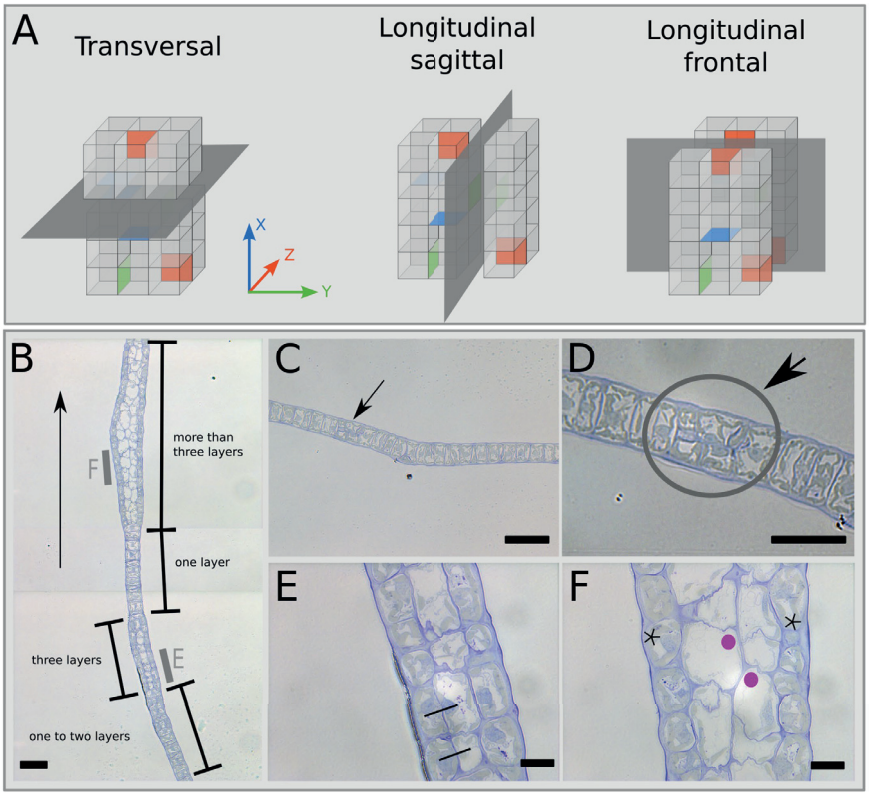

Figure 3: Semi-thin sections on polystromatisation. A) Schematics of the orientation of the semi-thin sections presented in this article based on our axis system defined in Figure 2. B) Longitudinal sagittal section from the blade of a 20-day-old embryo. This is a paracentral section in the tissue region where polystromatisation is initiated. The different states of the embryonic tissue, indicated between brackets for each region, demonstrate that polystromatisation is not a synchronous process. Arrow at the upper left corner indicates the direction of main growth axis. C and D) First symmetrical divisions in a monostromatic region viewed in longitudinal sagittal sections. The arrows and grey circle indicate the dividing cells. D) Detail of C. E and F) Formation of additional cell layers viewed in longitudinal sagittal sections. E) Detail of the three-layer region observed in B (zone E is indicated as a thick grey line in B). Black lines connect two daughter cells of the second periclinal division. F) Detail from the polystromatic region of B, where four layers are observed. The cortex is made up of large, angular transparent cells. The stars indicate the meristoderm, the purple circles the cortex layers. Bars: B, C: 50 µm; D: 30 µm; E,F: 10 µm.

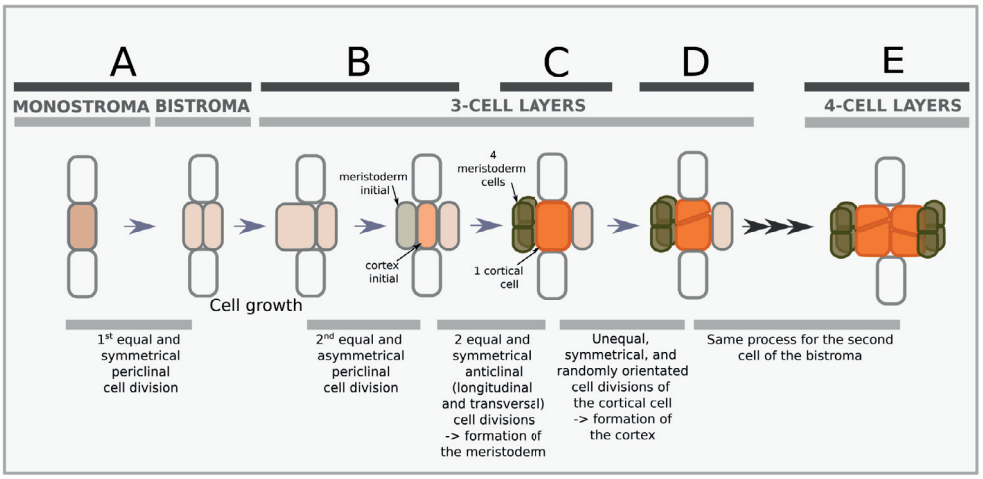

Figure 4: Schematics of the cellular events initiating polystromatisation. All the following events are described from a transversal section view (Fig. 3A) of the transition zone of a monolayered (monostromic) embryo at the end of Phase II. A) First equal and symmetrical cell division giving rise to a bilayer cell sheet (bistrom). B) Second cell division after growth of one of the daughter cells resulting from A. This time, the division is equal and asymmetrical because it results in a meristoderm cell initial and a cortex cell initial. At this stage, the blade is three cells thick. C) At the surface of the tissue, four meristodermatic cells arise from anticlinal divisions (one longitudinal and one transversal) of the meristoderm cell initial. Simultaneously, the cortex cell initial expands, forming the first cortical cell. D) Meristodermatic cells continue dividing anticlinally, while the cortical cell demonstrates a more random pattern of (un)equal, symmetrical divisions with random orientations of the cell division planes. E) The same process takes place for the second cell of the bistroma (A), after or at the same time as its sister cell. This leads to four distinct cell layers. Schematics are not drawn in scale.

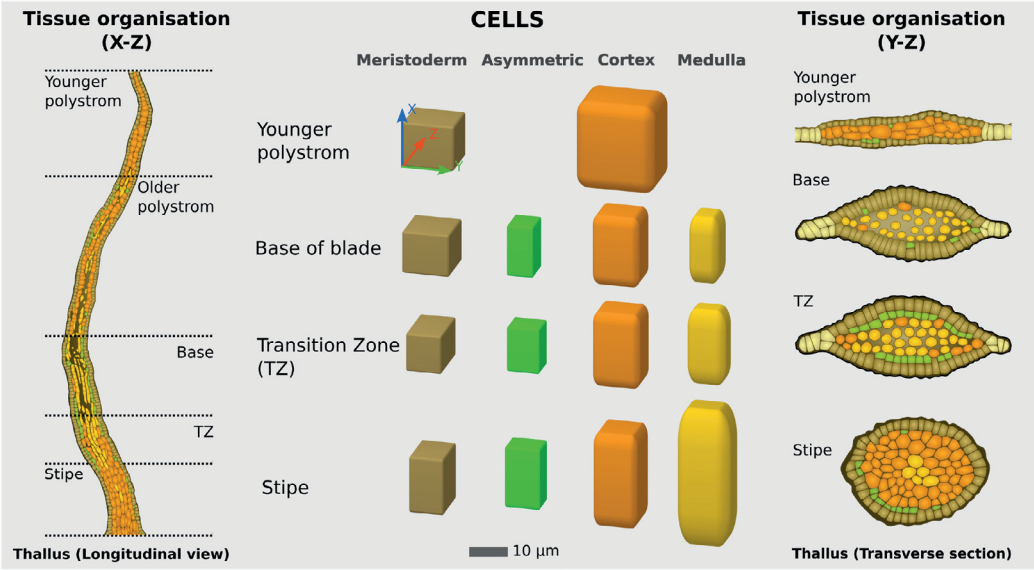

Figure 5: Cell types in *Saccharina* embryos. Cell shape and sizes are schematised (centre), depending on their position along the apico-basal axis of the embryo, which is also schematised as a sagittal section (left) or as a transversal section (right). Cell sizes were measured in the three axes X, Y and Z from semi-thin sections of embryos 20 days after zygote polarisation (azp). The same colour code applies for all the schematics. Measured dimensions are indicated in Suppl, Table 1 and analysed in Suppl, Figure 2.

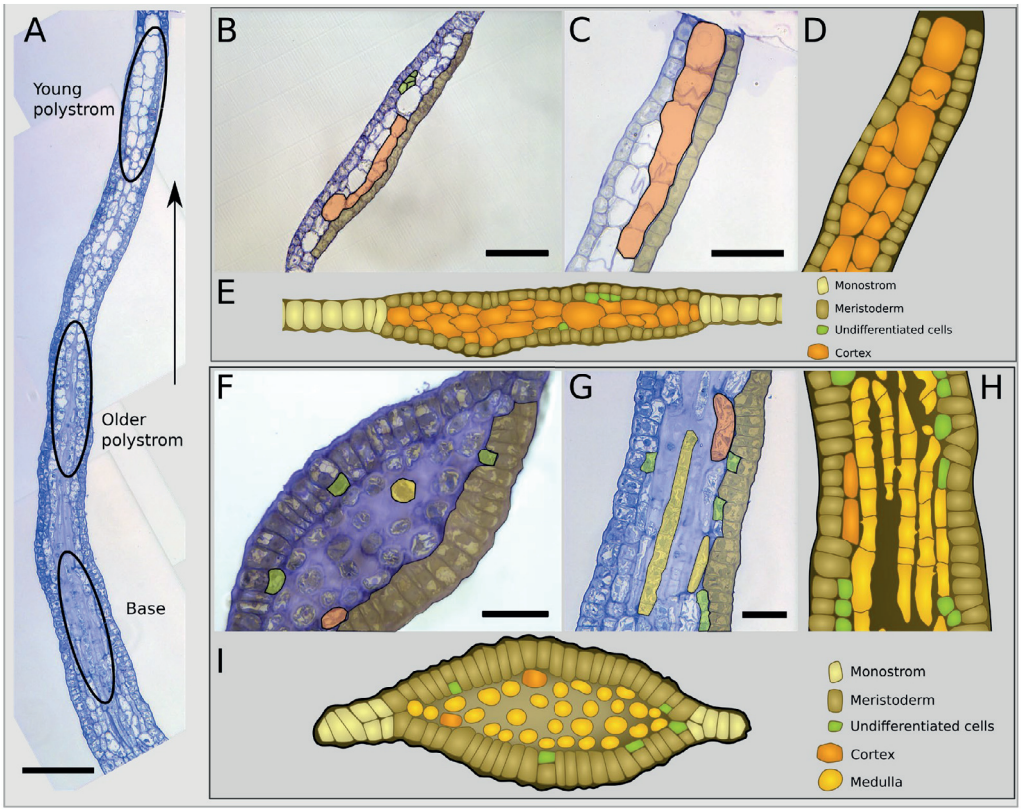

Figure 6: Longitudinal and transversal semi-thin sections of blades in Phase III. A) Median sagittal section from the base of the blade to young polystroma. Thickening (polystromatisation) progresses along the longest growth axis of the embryo. Circled areas indicate the different stages of polystromatisation, from the oldest in the lower part of the blade to the youngest in the upper part of the blade. Moving in the direction opposite to polystromatisation -- from the young polystroma to the base of the blade – the process can be described. B-E: Young polystroma. B) Transversal section of young polystromata. The different tissues are depicted following the colour scheme of D and E. The location of the section on a live specimen is shown in Figure 2I. C) Longitudinal sagittal section of young polystromata. D) General scheme of a longitudinal sagittal section in the young polystroma. E) General scheme of a transversal section in a young polystroma. F-I: Old polystroma. F) Transversal section from the base of blade of a 20-day-old embryo. The different tissues are depicted following the colour scheme in H and I. The approximate location of the section on live specimen is shown in Figure 2I. G) Longitudinal sagittal section of the base of the blade. H) Schematic of a longitudinal sagittal section at the base of the blade. I) General scheme of a transversal section at the base of a blade. Bars: A-C: 50 µm; F-G: 30 µm.

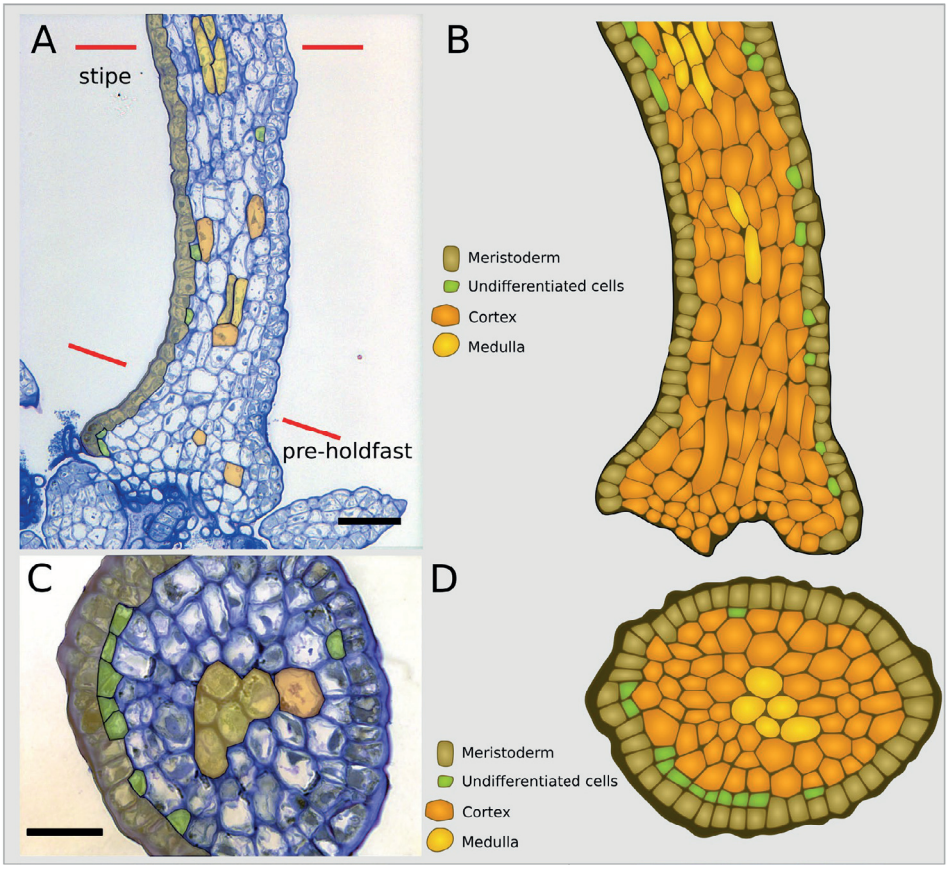

Figure 7: Longitudinal and transversal semi-thin sections on a stipe in Phase III. Compare these sections with Figure 2H,I. A-B: Photos of semi-thin sections; C-D: Scheme with the different colour-coded cell types. A) Longitudinal section. The extremities of the stipe are shown with red lines. At the bottom of the stipe is the pre-holdfast. B) Scheme of a longitudinal section from the stipe. C) Transversal section. D) Scheme of a longitudinal section from the stipe. Colour code of the different tissues follows the schemes in B and D. Bars: A: 50 µm; C: 30 µm.

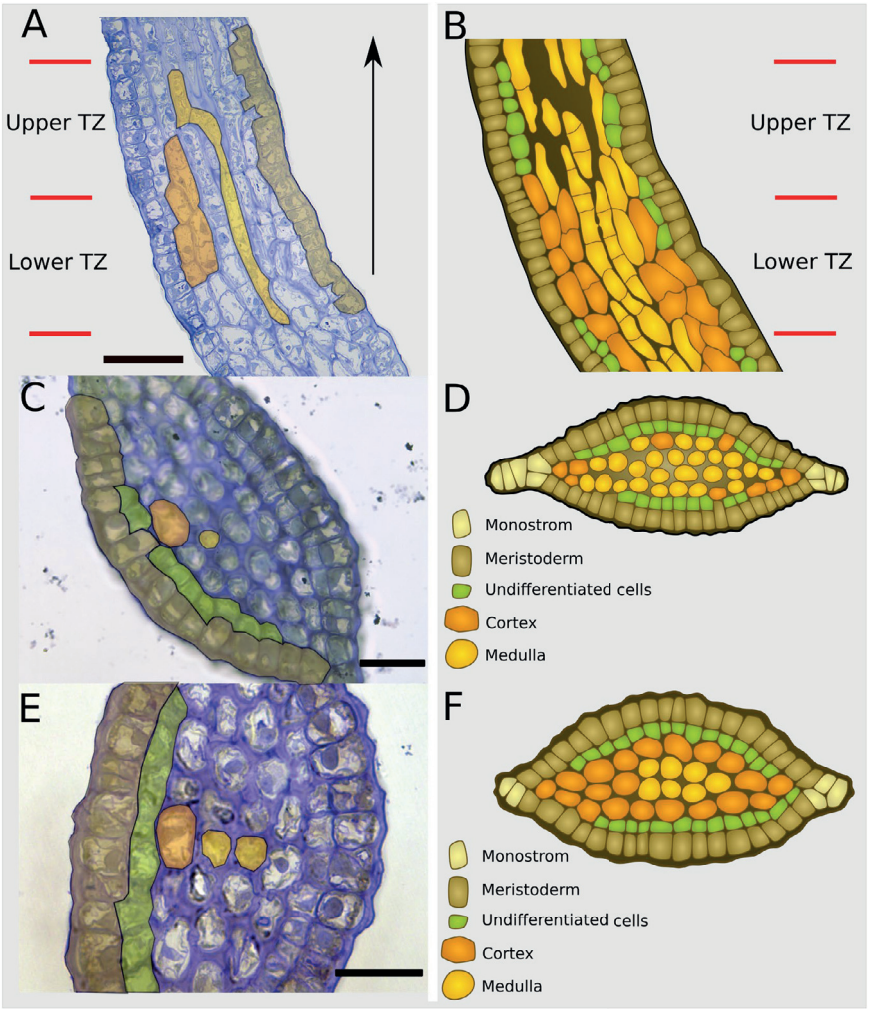

Figure 8: **Longitudinal and transversal semi-thin sections on Phase III transition zone.** A) Longitudinal section of the transition zone (TZ), divided into an upper TZ and a lower TZ. B) Schematic of a longitudinal section of the TZ. C) Transversal section of the upper TZ. D) Schematic of a transversal section of the upper TZ. E) Transversal section of the lower TZ. F) Schematic of a transversal section of the lower TZ. The different tissues are depicted according to the colour code given in D and F. Notice the asymmetric cells shown in green that are more abundant than in the transversal sections on previous figures. Bars: Bars: (A) 50, (C, E) 25 µm.

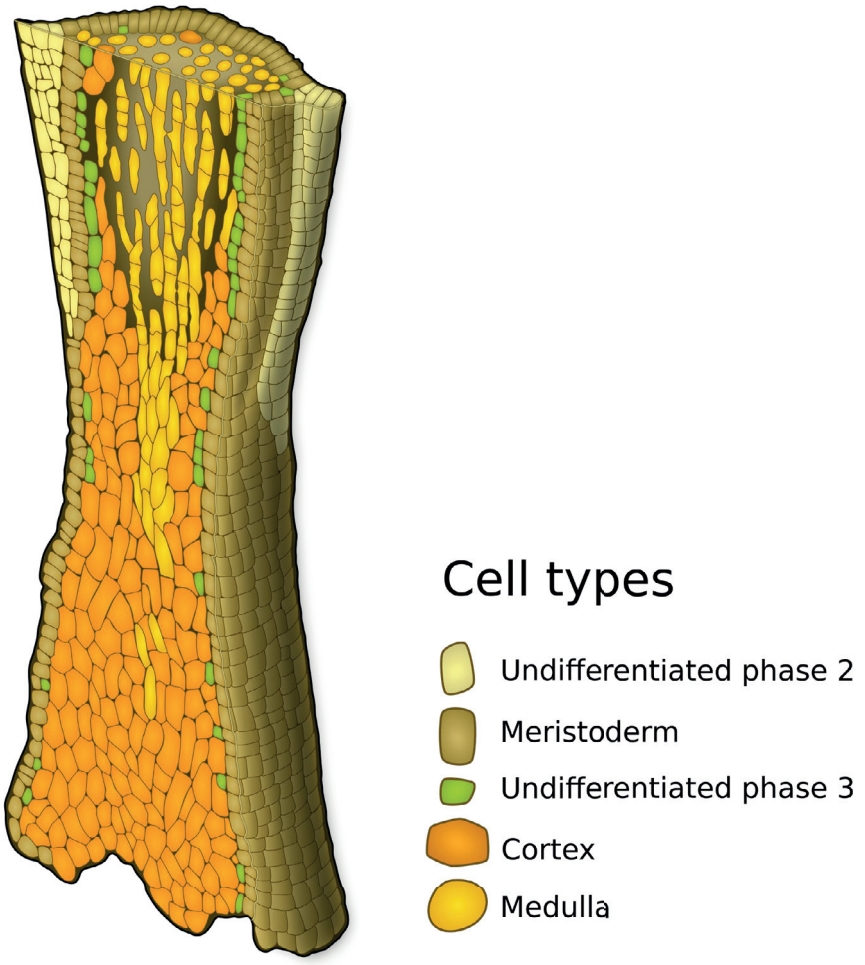

Figure 9: Partial 3D representation of the transition zone. Illustration of the rapid differentiation of the peripheral meristodermic cells into cortical cells in the lower part of the transition zone (TZ) and rich and in medullary cells in the upper part of the TZ.

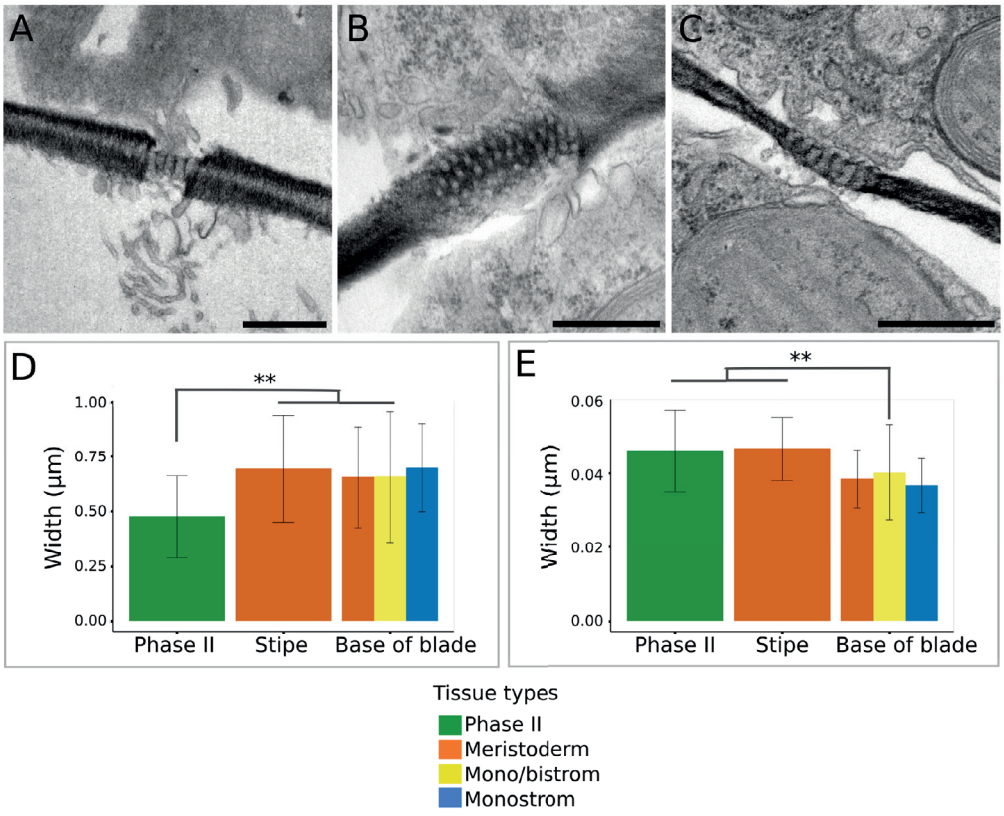

Figure 10: Plasmodesmata and pit field size analysis. (A-C) TEM acquisitions showing pit fields crossing the cell wall of two neighbouring cells. A) Pit field between cells of a Phase II embryo, B) Pit field between cells of a Phase III monostroma, C) Pit fields between meristodermatic cells of the stipe. D,E: Average width and standard deviation of pit fields and plasmodesmata. D) Size of pit fields. Pit fields in Phase II tissues are significantly narrower than pit fields in Phase III tissues (Welch t-test p-value=0.004). E) Size of plasmodesmata. Plasmodesmata are 18.64% wider in Phase II tissues than those from Phase III tissues at the base of the blade (Welch t-test p-value=0.005). Bars: 0.5 µm.

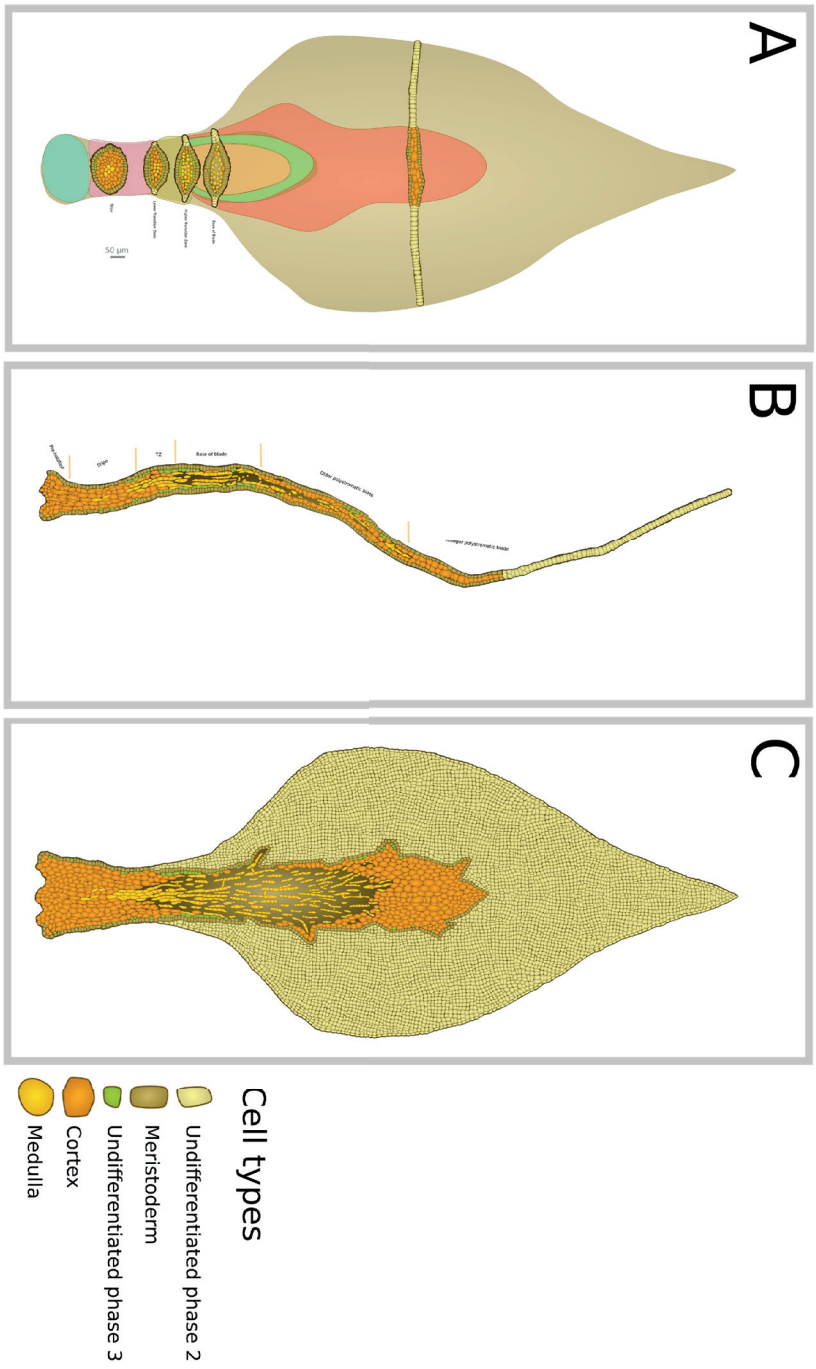

Figure 11: General view of the organisation of the tissues in a *Saccharina latissima* embryo. Drawings summarising the tissue distribution and organisation in the early embryo of *Saccharina latissima*, from A) transversal sections (positioned over a frontal shadow), B) longitudinal sagittal sections, C) longitudinal frontal sections.

Supplementary information

Supplementary Table 1: Cell type morphometrics. Dimensions of the cell in the X-, Y- and Z-axes (when available from sections) were measured using FIJI (Schindelin et al 2012). The mean and SD are indicated in Figure 5 and Supplementary Figure 2. Link: https://we.tl/t-iQyuAsLbPW

Supplementary Table 2: Widths of pit fields and plasmodesmata. The width of pitfields and plasmodesmata were measured using FIJI (Schindelin et al 2012) on TEM images of sections of different tissues and developmental stages. The mean and SD are indicated in Figure 10.
Link: https://we.tl/t-DfhB6hf2rk

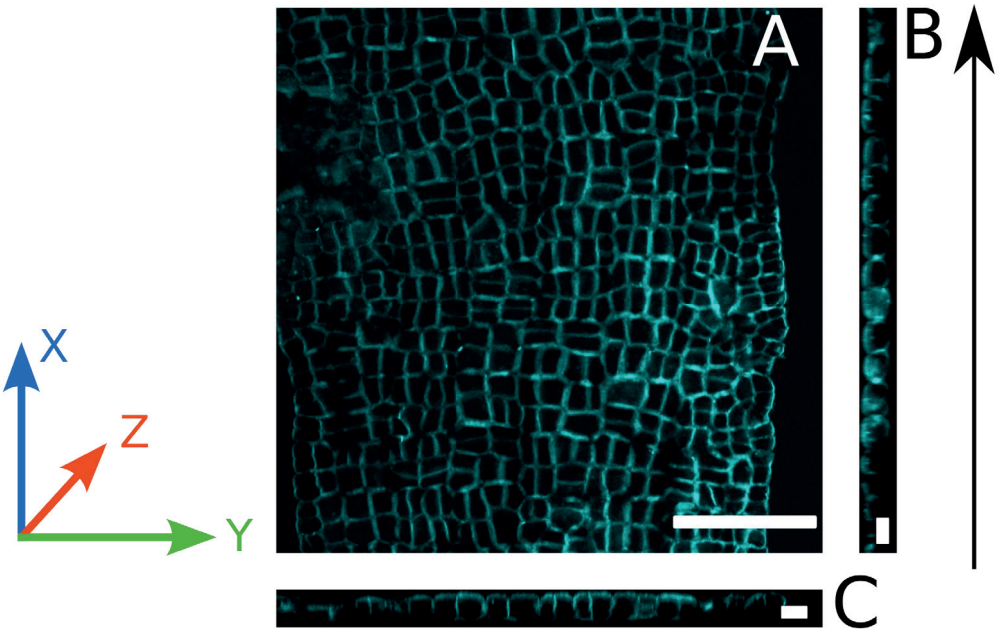

Supplementary Figure 1: Morphology of the grid of cells as observed under confocal microscopy after calcofluor staining. A) Frontal (X-Y) section of an embryo fixed in 1.5% PFA. B and C) Orthogonal views of this section. B) Longitudinal (X-Z) section, C) Transversal (Y-Z) section. The black arrow indicates the growth axis and direction. Bars: A: 90 µm; B and C: 16 µm.

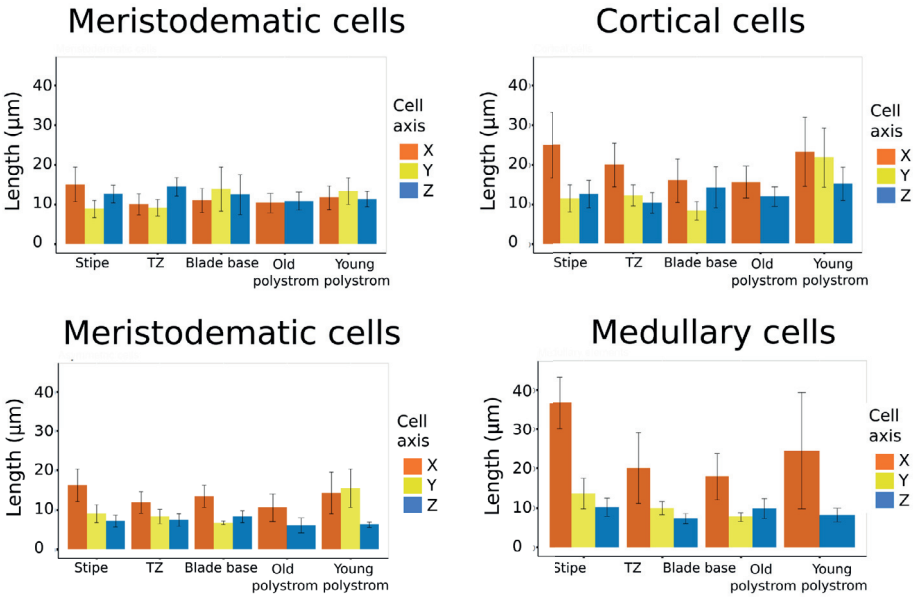

Supplementary Figure 2. Morphometrics of the different cell types in each region. Dimensions (µm) of the cells were measured in the X, Y and Z orientations from semi-thin section of an embryo 20 days azp (n Є [5;159] cells). Mean + SD are shown for each cell type in the different tissues of Phase III embryos. Measurements on the Y-axis of old polystromata are missing due to the lack of sectioned material in that region. Measured values are given in Supplemented Table 1.

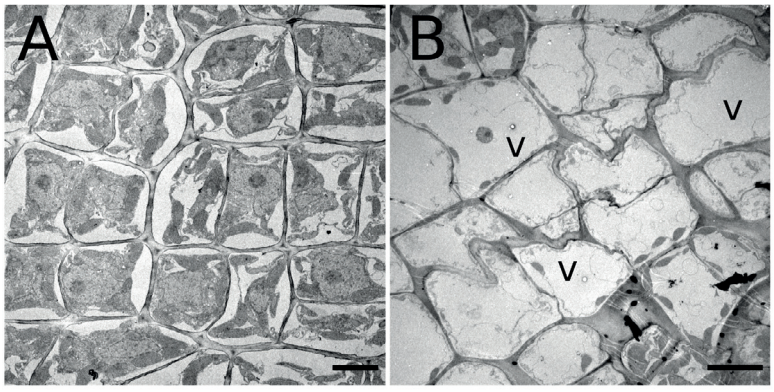

Supplementary Figure 3: Transmission electronic microscopy observations on general morphology between meristoderm and cortex tissues. A) Frontal section of meristodermatic tissue. The cells are cuboid with a dense cytoplasm rich in chloroplasts. Retraction of the protoplast is visible in some cells, due to the fixative solution. B) Frontal section of cortical cells, depicting large transparent cells. Large vacuoles are annotated with a 'V'. A few chloroplasts can

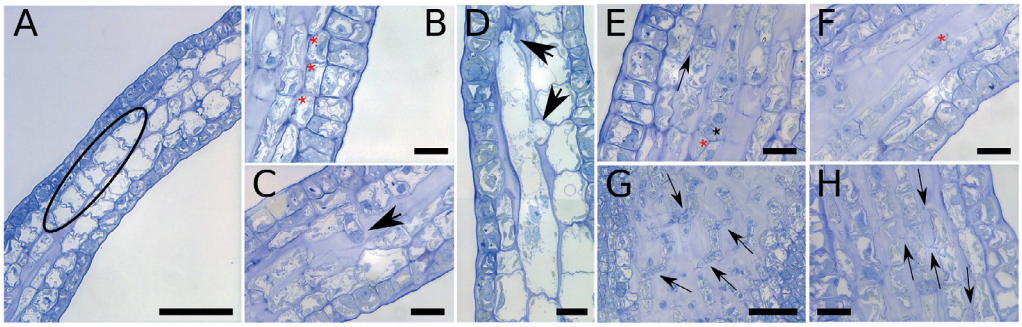

be observed at the periphery of the cells. Additional features of these two cell types are given in Table 2. Bars: A: 5 µm; B: 10 µm

Supplementary Figure 4: Longitudinal sagittal sections of the blade. A) Section from the boundary between old and young polystromata. The cortical cells in the black circle seem to have undergone a series of transverse anticlinal divisions that contribute to growth in the X-axis. B) Divisions of the meristoderm. The shape of the meristodermal cells suggests that these cells undergo many transverse anticlinal divisions. Red stars illustrate asymmetrical periclinal cell divisions. C, D) Pre-medullary cells with protrusions and characteristics of cortical cells (arrows). The cell in D appears to be multinucleate. E-H) Traits of medulla. E) Growing medullary elements. A transversal connection (pit field) between a cortical cell and a medullary element is shown with an arrow (black star: anticlinal division, red star: periclinal division). F) Initials of branching medullary cells (red star: cell division of a branch). G) Frontal section of branching medulla at the base of the blade. Different branches are shown with arrows. H) Horizontal connections (pit fields) between medullary elements. Bars: A, G: 50 µm; B,C,D,E,F,H: 14 µm.

Paper IV

The next report is part of bigger manuscript in process with title:

"The first transcriptomic analysis of *S. latissima* embryo development with possible connections between cell divisions, the cytoskeleton and eukaryotic phylogeny"

Authors:

H.G. Opsahl-Sorteberg[1], I. Theodorou[1,2], Z. Liang[3], J.C. Fletcher[4] and M.R. Kovi[1]

Affiliations:

[1]Norwegian University of Life Sciences, Biosciences, Ås, Norway

[2]Sorbonne University/Roscoff Marine Station, France

[3]Chinese Academy of Agricultural Sci (CAAS), Beijing, China

[4]UC-Berkeley/USDA, Plant Gene Expression Centre, CA, USA

Contributions: For the present report, H.G. Opsahl-Sorteberg, B. Charrier and I. Theodorou developed the experimental approach; H.G. Opsahl-Sorteberg, I. Theodorou and M. R. Kovi, analysed and interpreted the transcriptomics data; Specifically, I. Theodorou performed the growth experiments and harvesting materials at the Biological station of Roscoff then RNA extraction and sequence analysis took place at the Norwegian University of Life Sciences in Ås under the supervision and guidance of M. R. Kovi, and H.G. Opsahl-Sorteberg; Tables and Figures in this report were jointly developed by all three of them.

For the main article in process, Z. Liang is processing the phylogeny of some key transcripts and checking their importance. J.C. Fletcher is a valuable reviewer on all the efforts. Z. Liang, J. C. Fletcher , I. Theodorou, M. R. Kovi and H.G. Opsahl-Sorteberg have participated to conceptualization of the main article.

Z. Liang, J. C. Fletcher offered consultation to H.G. Opsahl-Sorteberg at the primary stages of the PhD project sharing background to support the transcriptomic approach.

Title: Report on transcriptomic analysis during early development of *Saccharina latissima*

Introduction

Saccharina's embryos begin as uniserate thalli after series of perpendicular divisions to the longest axis (Phase I), then parallel to the longest axis cell divisions introduce a second axis of growth and a planar tissue is formed growing on two axes (Phase II) ((Yendo 1911; Fritsch 1945; Theodorou and Charrier 2021). This monostromatic tissue persists for about two weeks when the introduction of a third growth axis begins with parallel cell divisions to the surface of the thallus (Paper I and Paper II). Then the different tissues emerge and the monostromatic embryo turns gradually polystromatic (Phase III) (Drew 1910; Yendo 1911; Theodorou and Charrier 2021).

The cytoskeletal organisation of *Saccharina* (Paper II) demonstrates during Phase II an anisotropy to the cortical actin filaments (AFs). The AFs below the surface of the tissue have random orientation while the AFs at the anticlinal cell walls are parallel to the perpendicular axis to the surface of the thallus (Z-axis). This alignment is reminiscent of the cortical mircrotubules (MTs) during the early leaf morphogenesis which are aligned the abaxial-adaxial axis, predicted also as the maximum tension axis (Zhao et al. 2020). In leaves, this MTs organisation follows the maximal tensile stress axis restricting cell growth on the abaxial-adaxial axis, therefore maintaining the growth of a flat organ. We hypothesise a similar phenomenon for the monostroma of *Saccharina* with the AFs restricting growth along the Z-axis. For the transition from a monostroma to polystroma tissue arrangement (Paper III), a change in cell growth direction occurs which should be followed by changes at the AFs organisation along the Z-axis. Currently, there are not works neither on the shift of AFs organisation of *Saccharina* neither on the signal that promotes this initiation of polystromatisation. In *Fucus,* during the polarization of the zygote a patch of actin is formed at the rizhoidal pole, nucleated by Arp 2/3 complexes directed by activated RAC1 (Hable 2014). This shows modulation AFs organisation is possible and expected in brown algae, following conserved pathways from animals (Marston et al. 2019) and plants (Craddock et al. 2012).

Aim of this report is the establishment of a method for transcriptomic analyses on microscopic kelp embryos as well as the exploration of potential key genes differentially expressed during the initiation of polystromatisation to build an initial hypothesis on what potentially promotes polystromatisation.

Materials and Methods

RNA sampling and preparation

We collected *Saccharina latissima* embryos from different time points between Phase II and Phase III. Whole embryos were fixed in RNAlater™(AM7021, Invitrogen™) and microdissected to remove any remnants of the maternal gametophyte. Total RNA was extracted from the embryos with the RNAqueous™ Micro total RNA isolation kit (AM1931, Invitrogen™). RNA integrity index was measured with the Agilent 2100 Bioanalyzer (Agilent Technologies. Inc.) and the Agilent RNA 6000 Pico assay (Agilent Technologies. Inc.). Samples with RNA integrity

index (RIN) ≥7 were processed further. The cDNA from polyA tail containing RNA was synthesized using the SMART-Seq® v4 Ultra® Low Input RNA Kit for Sequencing (Takara Bio USA, Inc) by Novogene Co. Ltd. Novogene was also employed for libraries generation and Illumina sequencing. They utilise the NovaSeq 6000 system based on 150 bp pair-end reads. The depth of sequencing (or read depth) was 22.1 - 32.6 million reads per sample, resulting in approximately 60 Gb of gzip compressed data.

De novo transcriptome analysis

The quality control of the raw reads, was done with FastQC v. 0.11.9 and MultiQC v. 1. (Ewels et al. 2016) for grouped comparisons. Raw reads were trimmed with Trimommatic v. 0. (Bolger et al. 2014) on paired-end mode using the following tool options: a) remove the adapters, seed mismatches = 2, palindrome clip threshold= 30, simple clip threshold = 10, b) sliding window 4 nt size, required quality 28 and c) with minimum length at 50 nt. The derived trimmed reads were checked for human, fungi and prokaryote contaminations in the sequence data using Kraken2 (Wood et al., 2019) program. The clean reads after filtering were used for generating *de novo* assembly using Trinity v. 2.13 (Grabherr et al. 2011). To evaluate the completness of transcriptome assembly, we used the BUSCO program (v. 5.3.2) on the stramenopiles lineage (Simão et al. 2015).

Estimating transcript abundance

Once the assembly quality was assessed, the *de novo* assembled transcripts, was used as a reference to map back the paired end reads from each of the sample per time point per replicate by Bowtie2 v.2.4.5, (Langmead and Salzberg 2012). Transcript abundance was estimated using RSEM version 1.1.11 (Li and Dewey 2011) to generate the read count data for the assembled transcripts. Further, we used Corset v. 1.09 (Davidson and Oshlack 2014) to generate the clusters and gene-level counts for each sample, which are tested for differential expression with edgeR.

Gene expression analysis

For the gene expression analysis we used the package edgeR v. 3.38.1 (Robinson et al. 2010; McCarthy et al. 2012) from Bioconductor in conjuction with tidyverse and other R packages. We filtered the clusters with minimum counts of 12 and normalized with a trimmed mean of M values method for every timepoint. The correlation between the samples was calculated and their biological co-variance. We estimated the the general lineal mode based tagwise, common and trended dispersions and combined with TREAT method (McCarthy and Smyth 2009; McCarthy et al. 2012) (McCarthy and Smyth 2009; McCarthy et al. 2012) for finding the differentially expressed genes (DEGs) that are over a specific fold change threshold ($\log_2$ FC> $\log_2$1.2). . The sequences with p-value adjusted (method: FDR) of less than 0.05 were deemed to be significantly differentially expressed genes (DEGs).

Functional analysis

DIAMOND v. 2.0.15 (Buchfink et al. 2021) was performed on DEGs against a database of proteins coming from three well annotated genomes: *Ectocarpus siliculosus* v2 (https://bioinformatics.psb.ugent.be/orcae/, (Cormier et al. 2016)), *Saccharina japonica* (https://bioinformatics.psb.ugent.be/orcae/, (Liu et al. 2019)) and *Undaria pinnatifida* (http://www.magic.re.kr/portal/main, (Graf et al. 2021)). DEGs without a hit on the custom database, were re-blasted with DIAMOND against a database of Phaeophyceae proteins generated from UniProt (release 2022_03). The remaining DEGs without any match went through the whole tremble Swiss-prot and NCBI databases. The best hits (lowest e-value) were used as representatives of their cluster. Interproscan v. 5.57-90.0 ((Jones et al. 2014; Blum et al. 2021)) was used to perform functiona annotation and KofamKOALA v. 2022-09-01 for KEGG IDs (Aramaki et al. 2020). Gene ontology (GO) and KEGG analysis were run through the R packages topGO v. 2.48.0 (Adrian Alexa and Jörg Rahnenführer 2022) and clusterProfiler v 4.4.4 (Wu et al. 2021).

Results & Discussion

Sampling during initiation of polystromatisation

For the purpose of this work to optimize a protocol for sampling *Saccharina* embryos, we isolated embryonic thalli from their parental gametophyte using glass pipettes and forceps. Due to the small size of the embryos we managed to successfully isolate and extract RNA from 10 and 12 days after fertilization (DAF) embryos before the first periclinal cell divisions and 14 DAF of embryos that had up to 8 cells periclinally divided cells at the base of the embryos (table 1, figure 1). The samples and their morphologicall characteristics are shown in table 1 and Z-stacks projected with the stack focuser on FIJI (Schindelin et al. 2012) in figure 1. The t0 and t1 belong to the monostromatic tissue Phase of the embryos with cell divisions perpendicular to the tissue surface, while the t3 specimen represent the initiation of polystromatization with cell divisions taking place parallel to the surface and the the apical-basal axis at the base of the embryos Paper III.

Assembly process and quality tests

Before the de-novo transcriptome assembly of polyA-containing RNA, the raw PE reads had an average phred30 score ranging from 26-36, however, some samples had a range from 11 to 36 (fig. S1) from nucleotide position 60-64 and above. Specifically, the reverse reads of most samples demonstrated that pattern. After trimming using the following software options: a) remove the adapters, seed mismatches = 2, palindrome clip threshold= 30, simple clip threshold = 10, b) sliding window 4 nt size, required quality 28 and c) with minimum length at 50 nt, the trimmed reads demonstrated average Phred30 score of approximately 36 per sample and no varying quality per nucleotide position (fig. S2). The average GC content per sequence before and after is around 50 % (fig. S3, table 1) though after trimming the curve is smoother. The high duplication level is expected for a transcriptome (fig. S3). The average reads per sample is 26.09 million sequences before trimming and 18.85 million sequences after trimming (table 2).

Trinity on default options (ref. website) for forward PE reads gave (table 3) 170 562 transcripts with 52 % GC content, N50 = 1 155 bp and the longest transcript has 24 695 bp .

The assembly was tested with Busco on the stramenopiles lineage for quality check, reaching a score of 81 % (table 3). The alignment of the reads on the assembly with bowtie2 gave on average 83.43 overall alignment rate (table 3) with a high percentage (75.52) for aligned reads more than one time, which is expectable for a transcriptome. Corset, was used to hierarchically cluster contigs resulting in 41 225 clusters and their counts.

Differentially expressed genes and their annotation

After the assembly and mapping the reads of the de-novo transcriptome, the gene expression analysis follows. First, the clusters of transcript from Corset are filtered accorting to their counts. With minimum counts 12, we proceeded with 19 590 clusters on to the next steps (>50% of the initial clusters). Next step is the normalisation of the sample's expression according to library size and TMM method. The first milestone quality tests ofn the gene expression analysis are the density plots, correlation heatmap and PCA plot for the samples. From the PCA and the correlation heatmap (fig 1), we noticed that the sample t1_3 did not group well neither with its timepoint, nor with the next. Since very distant from all samples, we removed it from the analysis as an outlier. Again, we removed all the zero counts and filter for minimum counts 12, resulting in 19 266 transcripts before the comparisons. At the supplementary material the density, library size, counts per transcript and log (count per million) plots are shown for the set of samples without the t1_3 a. After processing again, the PCA plot indicates a good grouping for the 0 h (10 DAF) and 48 h (12 DAF) timepoints, while the two samples at 96 h (14 DAF) are distant (fig. 2 B). At the correlation heatmap (fig. 2 D), we see that sample t2_2 is dissimilar with the rest of the samples while t2_1 seems closer to the t1 samples. However, since the correlation between the samples of the same timepoint can range between 0.9 and 1, this means that the samples are not very different, avoiding skewing the results towards a particular direction, neither completely random. Therefore, we estimate that this set is statistically relevant to the changes in gene expression during these studied timepoints in *Saccharina*'s development, despite some variations in expression distribution per sample and logcpm plot (fig. S4, A-D). These variations are more apparent at the biological coefficient of variation (BCV) plot (fig. S4) and the common dispersion calculation of BCV at 0.826. It is generally accepted that BCV should be within range 0.2 and 0.4 for a given condition but during development gene expression can vary between stages or their initiation and the previous Phase like in our case. In table 4, the number of DEGs per timepoint are presented while the formula for the comparison is presented at the previous column. For example, the DEGs for 48 h are inferred from the comparison of t1 with the t0 timepoints (table 4). In total the differentially expressed genes (DEGs, $\log_2$(fold-change)>$\log_2$1.2) with p-value < 0.05, adjust method: FDR, were 647 beforereduced to 600 after annotation and one last decontamination as described below (table S1). Regarding the expression patterns, from the heatmap (fig. 3) and the tables 4 and S1 we can observe a downregulation tendency being particularly obvious at 96 h. Specifically, we observe 111 DEGs at 48 h after the establishment of the grid. From these DEGs, 74 (67 %) are downregulated. At 96 h, there are in total 475 DEGs from which 339 (71 %) are downregulated. Between the two timepoints, there are 235 DEGs with 187 being down-regulated (80 %). In summary, we observe a general downregulation in gene expression taking

place after the establishment of the grid and towards the initiation of polystromatisation within a range of 67 % up to 80 % of total DEGs.

Annotation and GO analysis

For the annotation, as described in methods, we used tBLAST with the DIAMOND software against three well annotated brown algae genomes with insilico analysis of their proteome and the uniprot databases when needed. In the end out of the initially 647 DEGs, eight were one sequence clusters that still had no match when useing classic blastx on NCBI database nt-nr through the website (https://blast.ncbi.nlm.nih.gov/Blast.cgi). Then three remained without a match. After translating with EMBOSS Transeq v. (Madeira et al. 2022), the sequences had many different small open reading frames, and blastx and blastp at NCBI database gave either no alignments for those or too high expected values. They were discarded as artificial product of the assembly. These resulted in 644 DEGs. Further decontamination took place for high identity percentage and low E-value sequences aligned with human or other mammalian proteins that might not have biological relevance to a brown algal transcriptome (e.g albumin serum). Sequences aligned with uncharacterised proteins with no GO id and different taxonomy from brown algae were also removed. Finally, 600 DEGs were used for our analysis. These challenges on functional annotation are not surprising since the development of brown algae is not well studied at the molecular level, there are few annotated brown algae genomes and in general stramenopiles are mostly studied for their metabolism or cold tolerance explaining the knowledge gap. In addition, our study of early development has never been done before, naturally not matching annotated adult plants or juveniles that might rarely differentially express these proteins.

The procedure for the gene ontology (GO) terms and KEGG annotation is described in materials and methhods, from 600 DEGs, 245 have GO ID and KEGG and 118 have neither GO nor KEGG while 222 have only GO ID and 15 have only KEGG (Table S1). The GO analysis for each timepoint unravels an interesting pattern in figure 4. For the 48 h (fig. 4 A), most of the overpresented GO terms are related to cellular components (CC), where chloroplast related processes dominate. Biological processes (BP) and molecular functions (MF) are related mosty to photosynthesis and biosynthesis of secondary metabolites. So, there is a focus towards organelles functions and not developmental or other processes. This dominance of photosynthesis and secondary metabolites biosynthesis, is also confirmed/supported by the KEGG plot (fig. S5 A) at 48 h timepoint. On the contrary at 96 h (fig. 4 B), we observe several GO terms related to signaling (response to stimulus, cell surface receptor signaling pathway, cellular response to stimulus, signalling and signalling transduction) combined with three kinase activity terms of molecular functions while there is a term related to developmental processes (nervous system development), with high value and regulation of molecular function as BP. This signalling focus coincides with the divisions on Z-axis, which indicates that signalling is important to initiallise the three dimentional spacial orientation and identity, central to body development. At KEGG dotplot for 96 h (fig. S5 B), pathways related with signalling and membrane trafficking are present while GPI anchor biosynthesis is the second after fructose mannose metabolism is related with GPI anchor synthesis (Sharma et al. 2014). GPI anchor synthesis is important for proteins related to cell signalling (Robinson 1997) and generally sorting and trafficking of proteins at the cellular membranes. In addition, the

statistictically significant terms for cellular components at 96h are related with the plasma membrane, where the GPI anchored proteins may play a signalling or other regulatory role (Yadav and Khan 2018). Interestingly, the comparison of 96h with 48 h (fig. 4 C), did not present similar terms with the 96 h (fig. 4 B) neither the KEGG analysis (fig. S5). Overall, we observe a focus on cell signalling and membrane localization of proteins translational or post transaltional. This pattern is not mere coincidence and further focus is required to elucidate potential functions. On that notion we look next on the highest DEGs and classification of DEGs according to their role.

Key genes and their potential role

Based on the top 20 upregulated (table S2) and top 20 downregulated (table S3) DEGs per timepoint, we made a selection of those related to development and plotted them by time (fig. 5). The rest of the transcripts are metabolism related. In the tables the putative DEGs related to development are marked yellow (tables S2, S3, S4).

From the top 20 upregulated transcripts at 48 h (table S2), most relate to metabolism while three transcripts relate to gene and protein regulation (DN2381, DN220 and DN90012) including histone modification. Very interesting upregulated DEG at 48 h is a Mannuronan C-5-epimerase homolog (DN3894), an enzyme related to alginate modifications at the cell wall of brown algae (Fischl et al. 2016), and potentially stiffer alginates (Rabillé et al. 2019). This is an indication for a change or high maintenance of cell wall properties. It is upregulated on both timepoints but does not demostrate differential expression at the comparison of the timepoints (table S4). A transcript that matches with WD repeat-containing protein 62 from pig (DN220), is potentially related to regulation of the mitotic cycle (Yu et al. 2010). This is not surprising, and is consistent with an actively growing and developing tissue.

The most downregulated transcripts at 48h (table S3) are related to secondary metabolites (16 out of 20), but there are also, a pescadillo homologue from *Ectocarpus* (DN1040), potentially responsible for cell cycle regulation (Shen et al. 2008), there is a potential transcription factor (DN21653) and a signal transduction protein (DN12423) containing an arrestin domain. Arrestin domain containing proteins are important signal transduction regulators, implicated also in G-protein-coupled receptors trafficking (Kang et al. 2014).

Among the top 20 upregulated transcripts at 96 h (table S2) we find calmodulin (DN80478) (Love et al. 1997; Pu and Robinson 1998) and other potential signal transduction related proteins like Phospholipases (DN17765) (Deepika and Singh 2022) and an analog to dolichol kinase (DN16547) which in land plants is ER localised and higly expressed in shoot apical meristem and flowering meristems (Cho et al. 2017). These suport the GO terms and overall focus of the developing tissue on signalling. Potential targets of these could be a putative upregulated cellulose binding protein (DN2057_g3), associated probably with modifications of the cellulose at the cell walls (Linder and Teeri 1997) potentially necessary for polystromatisation.

The downregulated DEGs at 96 h (table S3) have a similar pattern with metabolites and signalling transduction (3 out of 20 DEGs for cell communication), however, among them is also an MYB TF ten-fold down regulated (DN1381). MYBs can be associated with regulation

on cell proliferation and differentiation (Zeng et al. 2022). There are two potentially MYB TFs recognized by the ELM2 Domain, present in our study (Table S1) again coinciding with the initiation of the third Phase. **The DEGs from the comparison of the two timepoints** (96 h vs 48 h, table S4), we find the same down regulated MYB TF, that we found at the 96 h. Interestingly the two MYBs are not present at 48 h. Another interesting downregulated DEG is an almost 10 fold downregulated metallocarboxypeptidase (table S4, DN4721), responsible for deglutamylation of tubulin, affecting microtubule associated proteins interactions central to the cell cycle during cell divisions. Though tubulin is not as structural as actin in brown algae, modification like this are often seen at the end of a signalling pathway (Gardiner 2019). Tubulin also has an important role to the diaphragm formation during cytokinesis in brown algae, and the cytokinesis plane determination (Katsaros et al. 2009). A potential DEG (DN62014) that expresses dynein heavy chain is downregulated in both timepoints. However, another microtubule motor protein (potential kinesin, DN734) is upregulated at 96 h. Both motors are part of microtubular dynamics during cell cycle and organelles and macromolecules carriers, in animal cells (reviewed in: (Lu and Gelfand 2017; Dwivedi and Sharma 2018). In plant cells, though kinesin and dynein are essential for MT dynamics during cell cycle, actin and myosin form the main trafficking system (Perico and Sparkes 2018), however, a role of plant specific kinesins as a crosstalk molecule on actin and microtubules organization is suggested during morphogenesis of trichome cells (Tian et al. 2015). Another mitosis related transcript (DN14310) and another associated to cell differentiation (DN5492), are both 8 fold downregulated at the comparison of the two timepoints (table S4). This is consistent with our hypothesis that a process connected with increased signal transduction takes place during the initiation of Phase III. In addition at the top 20 upregulated of the 96 h vs 48 h comparison (table S4). We observe 9 fold upregulation of a potential cAMP-dependent kinase (DN7263) and the same arrestin domain (DN12423) protein which is downregulated at 96 h which are signal transduction mediators and regulators.

From the 245 DEGs with GO ID, we chose 133 based on their role in cell signalling (50), protein regulation based on post-translation modifications (32) and gene expression (31) or structural changes (20) at the cell wall, cytoskeleton and cell cycle (table S5). These are plotted over time at the heatmaps of figure 5. What becomes easily aparrent and agrees with the previous general heatmap, is that most of the transcripts demonstrate a differential expression at 96 h. This seems general even of downregulation coincides with the initiation of polystromatisation. All categories have high ratio of negative DEGs towards positive DEGs (down/up). Specifically, we observe a ratio of 6.33 for cell signalling DEGs (fig. 5 A), and 3.14 for gene expression related DEGs. Post-translation ratio, 2.8, is closer to that of gene expression while DEGs at the category of structural changes demonstrate a 1.71 ratio. Consequently, downregulated DEGs with a role in cell signalling are approximately 6 times more than the upregulated and overall all the DEGs are mostly downregulated except in structural changes where the situation is more balanced.

Our estimation is that a switch takes place between 48 h and 96 h that depends on and promotes differential expression. This is probably of signalling nature, a conclusion coming from the gene ontology analysis and our manual classification. This switch coincides with initiation of polystromatisation, potentially indicating a strong connection to these particular

expression patterns and negative regulation of cell signalling. The downregulation to cell signalling is followed by downregulation of genes related with protein regulation at two levels of intracellular regulation on the gene expression and post-translation modifications. Even though the precise mechanism is unclear, the first stages of Phase III are highly regulated on several levels beginning from cell signalling to post-translation modifications. Changes to cytoskeleton and cell wall properties involve more downregulated DEGs than upregulated, but the difference is small. However, how the resulting proteins are modified or function on the different structures remain an obscure issue for brown algal cells.

An initial hypothesis

In Paper I and Paper II, it is postulated the presence of a mechanical feedback loop between the actin filaments, the cell wall properties and cell growth. Cell growth is restricted along a two-axes monostromatic tissue as explained earlier, while actin filaments cortical sheets and adjacent cell wall properties seem to impose and maintain this restriction. A modulation to the actin cortical sheets is necessary and probably cell wall modifications too for tilting cell division plane and growth axes. The hypothesized switch event maybe introduces a spike at Ca^{2+} concentrations which would explain the increased expression of calmodulin which can further act as secondary messenger to cytoskeletal reorganization (Izadi et al. 2018). Furthermore, Ca^{2+} interacts with Rho GTPases who can reorganize cytoskeleton, especially actin in both animals (Marston et al. 2019) and plants (Craddock et al. 2012). RAC1 is such a potential Rho GTpase (Hable 2014; Marston et al. 2019) but during tip-growth in *Ectocarpus* it seems to not interact with actin filaments organization (Nehr et al. 2021). Therefore, Ca^{2+} and calmodulins could mediate the information to post-translational modifications and differential transcriptional regulation on associate to cytoskeleton proteins that would further promote a rearrangement to actin filaments organization and cell wall properties. We base this hypothesis on a similar event taking place during the initiation of organogenesis at the apical meristem of land plants (Hamant et al. 2008; Peaucelle et al. 2011; Sampathkumar et al. 2014; Arsuffi and Braybrook 2018) where cell-walls loosen up after auxin signalling and re-arrangement of the cortical microtubules. Mannuronan C-5-epimerase, (two homologs upregulated at 96 h, table S5), could play the role of pectinases and expansins through modulation of the alginate content at cell wall of *Saccharina* like in *Ectocarpus* and *Silvetia* (Rabillé et al. 2019; Yonamine et al. 2021). Additionally, Ca^{2+} concentrations which bind to alginates play a regulatory role in cell wall integrity of *Ectocarpus* (Terauchi et al. 2016). Control over Ca^{2+} concentrations could assist on cell wall loosening during polystromatisation of *Saccharina*. A similar theory was put under test during organogenesis at *Sargassum*'s apical meristem (Linardić and Braybrook 2017). However, no connection to buds initiation was found with auxin, neither their predictions on softer cell walls based on patterns of mannuronnate and guluronic acid containing alginates followed the pattern of new buds (Linardić and Braybrook 2017). Therefore, the possible mechanism for polystromatisation can also be very different than this initial hypothesis.

Conclusions

We designed a working method for following transcriptional regulation during microscopic stages of kelps, an important ecologically and economically group of marine photosynthetis

species with particular strategy on embryogenesis and late 3D growth. The transcriptomic profile during polystromatisation indicates a series of changes on structural and cell signalling level. At this point there is no definite clue of the nature of the initiation signal. However, auxin has been shown to promote vegetative growth in isolated disc from mature kelps thallus (Kai et al. 2006) and being abundant at the growth region of *Laminaria digitata* (Buchholz and Lüning 1999). Auxin signalling could lead to a spike of Ca^{2+} concentrations (Vanneste and Friml 2013) serving as secondary message with the help of calmodulin on regulating cell wall mechanical properties together probably with the action from mannuronan C-5-epimerase leading to a more elastic cell wall. However, we did not observe down or up regulation of any auxin transport or biosynthesis related protein. Nevertheless, we speculate that the turn off switch between between 48 h and 96 h and the transcriptomic profile that we observed are related to loosen up of the anticlinal cell walls and actin reorganization which would promote perpendicular cell expansion and periclinal divisions. This would be the first step during initiation of polystromatisation (Paper III) However, these are speculations that need advances to genetic and genomic manipulations of brown algae which are in development (Badis et al. 2021) combined to a higher spatiotemporally resolution of the present experimental design, possibly through laser capture microdissection (Saint-Marcoux et al. 2015).

Acknowledgements

Sylvia Sagen Johnsen for assistance and supervisions with RNA extractions, Bénédicte Charrier for providing the embryo material and covering transferring costs and funding IT. B.C also covered the costs for the optimization of *S. latissima* embryo extraction.

References

Adrian Alexa and Jörg Rahnenführer. 2022. topGO: Enrichment Analysis for Gene Ontology. R.

Aramaki, T., Blanc-Mathieu, R., Endo, H., Ohkubo, K., Kanehisa, M., Goto, S., and Ogata, H. 2020. KofamKOALA: KEGG Ortholog assignment based on profile HMM and adaptive score threshold. Bioinformatics **36**(7): 2251–2252. doi:10.1093/bioinformatics/btz859.

Arsuffi, G., and Braybrook, S.A. 2018. Acid growth: an ongoing trip. Journal of Experimental Botany **69**(2): 137–146. doi:10.1093/jxb/erx390.

Badis, Y., Scornet, D., Harada, M., Caillard, C., Godfroy, O., Raphalen, M., Gachon, C.M.M., Coelho, S.M., Motomura, T., Nagasato, C., and Cock, J.M. 2021. Targeted CRISPR-Cas9-based gene knockouts in the model brown alga *Ectocarpus*. New Phytologist **231**(5): 2077–2091. doi:10.1111/nph.17525.

Blum, M., Chang, H.-Y., Chuguransky, S., Grego, T., Kandasaamy, S., Mitchell, A., Nuka, G., Paysan-Lafosse, T., Qureshi, M., Raj, S., Richardson, L., Salazar, G.A., Williams, L., Bork, P., Bridge, A., Gough, J., Haft, D.H., Letunic, I., Marchler-Bauer, A., Mi, H., Natale, D.A., Necci, M., Orengo, C.A., Pandurangan, A.P., Rivoire, C., Sigrist, C.J.A., Sillitoe, I., Thanki, N., Thomas, P.D., Tosatto, S.C.E., Wu, C.H., Bateman, A., and Finn, R.D. 2021. The InterPro protein families and domains database: 20 years on. Nucleic Acids Research **49**(D1): D344–D354. doi:10.1093/nar/gkaa977.

Bolger, A.M., Lohse, M., and Usadel, B. 2014. Trimmomatic: a flexible trimmer for Illumina sequence data. Bioinformatics **30**(15): 2114–2120. doi:10.1093/bioinformatics/btu170.

Buchfink, B., Reuter, K., and Drost, H.-G. 2021. Sensitive protein alignments at tree-of-life scale using DIAMOND. Nat Methods **18**(4): 366–368. Nature Publishing Group. doi:10.1038/s41592-021-01101-x.

Buchholz, C., and Lüning, K. 1999. Isolated, distal blade discs of the brown alga *Laminaria digitata* form sorus, but not discs, near to the meristematic transition zone. Journal of Applied Phycology **11**(6): 579–584. doi:10.1023/A:1008116828263.

Cho, Y., Yu, C.-Y., Nakamura, Y., and Kanehara, K. 2017. *Arabidopsis* dolichol kinase AtDOK1 is involved in flowering time control. Journal of Experimental Botany **68**(12): 3243–3252. doi:10.1093/jxb/erx095.

Cormier, A., Avia, K., Sterck, L., Derrien, T., Wucher, V., Andres, G., Monsoor, M., Godfroy, O., Lipinska, A., Perrineau, M.-M., Van De Peer, Y., Hitte, C., Corre, E., Coelho, S.M., and Cock, J.M. 2016. Re-annotation, improved large-scale assembly and establishment of a catalogue of noncoding loci for the genome of the model brown alga *Ectocarpus*. New Phytol. **214**: 219–232. doi:10.1111/nph.14321.

Craddock, C., Lavagi, I., and Yang, Z. 2012. New insights into Rho signaling from plant ROP/Rac GTPases. Trends Cell Biol. **22**(9): 492–501. doi:10.1016/j.tcb.2012.05.002.

Davidson, N.M., and Oshlack, A. 2014. Corset: enabling differential gene expression analysis for de novo assembled transcriptomes. Genome Biol. **15**(7): 410. doi:10.1186/PREACCEPT-2088857056122054.

Deepika, D., and Singh, A. 2022. Plant phospholipase D: novel structure, regulatory mechanism, and multifaceted functions with biotechnological application. Critical Reviews in Biotechnology **42**(1): 106–124. Taylor & Francis. doi:10.1080/07388551.2021.1924113.

Drew, G.H. 1910. The Reproduction and early Development of *Laminaria digitata* and *Laminaria saccharina*. Annals of Botany **24**(1): 177–189. doi:10.1093/oxfordjournals.aob.a089253.

Dwivedi, D., and Sharma, M. 2018. Multiple Roles, Multiple Adaptors: Dynein During Cell Cycle. Adv Exp Med Biol **1112**: 13–30. doi:10.1007/978-981-13-3065-0_2.

Ewels, P., Magnusson, M., Lundin, S., and Käller, M. 2016. MultiQC: summarize analysis results for multiple tools and samples in a single report. Bioinformatics **32**(19): 3047–3048. doi:10.1093/bioinformatics/btw354.

Fischl, R., Bertelsen, K., Gaillard, F., Coelho, S., Michel, G., Klinger, M., Boyen, C., Czjzek, M., and Hervé, C. 2016. The cell-wall active mannuronan C5-epimerases in the model brown alga *Ectocarpus*: From gene context to recombinant protein. Glycobiology **26**(9): 973–983. doi:10.1093/glycob/cww040.

Fritsch, F.E. 1945. The Structure And Reproduction Of The Algae. Cambridge University Press, Cambridge.

Grabherr, M.G., Haas, B.J., Yassour, M., Levin, J.Z., Thompson, D.A., Amit, I., Adiconis, X., Fan, L., Raychowdhury, R., Zeng, Q., Chen, Z., Mauceli, E., Hacohen, N., Gnirke, A., Rhind, N., di Palma, F., Birren, B.W., Nusbaum, C., Lindblad-Toh, K., Friedman, N., and Regev, A. 2011. Full-length transcriptome assembly from RNA-Seq data without a reference genome. Nat Biotechnol **29**(7): 644–652. Nature Publishing Group. doi:10.1038/nbt.1883.

Graf, L., Shin, Y., Yang, J.H., Choi, J.W., Hwang, I.K., Nelson, W., Bhattacharya, D., Viard, F., and Yoon, H.S. 2021. A genome-wide investigation of the effect of farming and human-mediated introduction on the ubiquitous seaweed *Undaria pinnatifida*. Nat Ecol Evol **5**(3): 360–368. Nature Publishing Group. doi:10.1038/s41559-020-01378-9.

Hable, W.E. 2014. Rac1 signaling in the establishment of the fucoid algal body plan. Front. Plant Sci. **5**: 690. doi:10.3389/fpls.2014.00690.

Hamant, O., Heisler, M.G., Jönsson, H., Krupinski, P., Uyttewaal, M., Bokov, P., Corson, F., Sahlin, P., Boudaoud, A., Meyerowitz, E.M., Couder, Y., and Traas, J. 2008. Developmental Patterning by Mechanical Signals in *Arabidopsis*. Science **322**(5908): 1650–1655. American Association for the Advancement of Science. doi:10.1126/science.1165594.

Izadi, M., Hou, W., Qualmann, B., and Kessels, M.M. 2018. Direct effects of Ca2+/calmodulin on actin filament formation. Biochemical and Biophysical Research Communications **506**(2): 355–360. doi:10.1016/j.bbrc.2018.07.159.

Jones, P., Binns, D., Chang, H.-Y., Fraser, M., Li, W., McAnulla, C., McWilliam, H., Maslen, J., Mitchell, A., Nuka, G., Pesseat, S., Quinn, A.F., Sangrador-Vegas, A., Scheremetjew, M., Yong, S.-Y., Lopez, R., and Hunter, S. 2014. InterProScan 5: genome-scale protein function classification. Bioinformatics **30**(9): 1236–1240. doi:10.1093/bioinformatics/btu031.

Kai, T., Nimura, K., Yasui, H., and Mizuta, H. 2006. Regulation of Sorus Formation by Auxin in Laminariales Sporophyte. J Appl Phycol **18**(1): 95–101. doi:10.1007/s10811-005-9020-8.

Kang, D.S., Tian, X., and Benovic, J.L. 2014. Role of β-arrestins and arrestin domain-containing proteins in G protein-coupled receptor trafficking. Current Opinion in Cell Biology **27**: 63–71. doi:10.1016/j.ceb.2013.11.005.

Langmead, B., and Salzberg, S.L. 2012. Fast gapped-read alignment with Bowtie 2. Nat Methods **9**(4): 357–359. Nature Publishing Group. doi:10.1038/nmeth.1923.

Li, B., and Dewey, C.N. 2011. RSEM: accurate transcript quantification from RNA-Seq data with or without a reference genome. BMC Bioinformatics **12**(1): 323. doi:10.1186/1471-2105-12-323.

Linardić, M., and Braybrook, S.A. 2017. Towards an understanding of spiral patterning in the *Sargassum muticum* shoot apex. Sci Rep **7**(1): 1–10. doi:10.1038/s41598-017-13767-5.

Linder, M., and Teeri, T.T. 1997. The roles and function of cellulose-binding domains. Journal of Biotechnology **57**(1): 15–28. doi:10.1016/S0168-1656(97)00087-4.

Liu, T., Wang, X., Wang, G., Jia, S., Liu, G., Shan, G., Chi, S., Zhang, J., Yu, Y., Xue, T., and Yu, J. 2019. Evolution of Complex Thallus Alga: Genome Sequencing of *Saccharina japonica*. Front. Genet. **10**. doi:10.3389/fgene.2019.00378.

Love, J., Brownlee, C., and Trewavas, A.J. 1997. Ca^{2+} and Calmodulin Dynamics during Photopolarization in *Fucus serratus* Zygotes. Plant Physiology **115**(1): 249–261. American Society of Plant Biologists (ASPB).

Lu, W., and Gelfand, V.I. 2017. Moonlighting motors: kinesin, dynein and cell polarity. Trends Cell Biol **27**(7): 505–514. doi:10.1016/j.tcb.2017.02.005.

Madeira, F., Pearce, M., Tivey, A.R.N., Basutkar, P., Lee, J., Edbali, O., Madhusoodanan, N., Kolesnikov, A., and Lopez, R. 2022. Search and sequence analysis tools services from EMBL-EBI in 2022. Nucleic Acids Res: gkac240. doi:10.1093/nar/gkac240.

Marston, D.J., Anderson, K.L., Swift, M.F., Rougie, M., Page, C., Hahn, K.M., Volkmann, N., and Hanein, D. 2019. High Rac1 activity is functionally translated into cytosolic structures with unique nanoscale cytoskeletal architecture. PNAS **116**(4): 1267–1272. National Academy of Sciences. doi:10.1073/pnas.1808830116.

McCarthy, D.J., Chen, Y., and Smyth, G.K. 2012. Differential expression analysis of multifactor RNA-Seq experiments with respect to biological variation. Nucleic Acids Research **40**(10): 4288–4297. doi:10.1093/nar/gks042.

McCarthy, D.J., and Smyth, G.K. 2009. Testing significance relative to a fold-change threshold is a TREAT. Bioinformatics **25**(6): 765–771. doi:10.1093/bioinformatics/btp053.

Nehr, Z., Chenivesse, S., Billoud, B., Genicot, S., Desban, N., Theodorou, I., Nasir, A., Bail, A.L., Rabillé, H., Godfroy, O., Katsaros, C., and Charrier, B. 2021, August 28. Tip growth in the brown alga *Ectocarpus* is controlled by a RHO-GAP-BAR domain protein independently from F-actin organisation. bioRxiv. doi:10.1101/2021.08.28.458042.

Peaucelle, A., Braybrook, S.A., Le Guillou, L., Bron, E., Kuhlemeier, C., and Höfte, H. 2011. Pectin-Induced Changes in Cell Wall Mechanics Underlie Organ Initiation in *Arabidopsis*. Current Biology **21**(20): 1720–1726. doi:10.1016/j.cub.2011.08.057.

Perico, C., and Sparkes, I. 2018. Plant organelle dynamics: cytoskeletal control and membrane contact sites. New Phytologist **220**(2): 381–394. doi:10.1111/nph.15365.

Pu, R., and Robinson, K.R. 1998. Cytoplasmic calcium gradients and calmodulin in the early development of the fucoid alga *Pelvetia compressa*. J Cell Sci **111 (Pt 21)**: 3197–3207. doi:10.1242/jcs.111.21.3197.

Rabillé, H., Torode, T.A., Tesson, B., Le Bail, A., Billoud, B., Rolland, E., Le Panse, S., Jam, M., and Charrier, B. 2019. Alginates along the filament of the brown alga *Ectocarpus* help cells cope with stress. Sci Rep **9**(1): 12956. doi:10.1038/s41598-019-49427-z.

Robinson, M.D., McCarthy, D.J., and Smyth, G.K. 2010. edgeR: a Bioconductor package for differential expression analysis of digital gene expression data. Bioinformatics **26**(1): 139–140. doi:10.1093/bioinformatics/btp616.

Robinson, P.J. 1997. Signal Transduction Via GPI-Anchored Membrane Proteins. *In* ADP-Ribosylation in Animal Tissues: Structure, Function, and Biology of Mono (ADP-ribosyl) Transferases and Related Enzymes. *Edited by* F. Haag and F. Koch-Nolte. Springer US, Boston, MA. pp. 365–370. doi:10.1007/978-1-4419-8632-0_48.

Saint-Marcoux, D., Billoud, B., Langdale, J.A., and Charrier, B. 2015. Laser capture microdissection in *Ectocarpus siliculosus*: the pathway to cell-specific transcriptomics in brown algae. Front Plant Sci **6**: 54. doi:10.3389/fpls.2015.00054.

Sampathkumar, A., Yan, A., Krupinski, P., and Meyerowitz, E.M. 2014. Physical Forces Regulate Plant Development and Morphogenesis. Current Biology **24**(10): R475–R483. doi:10.1016/j.cub.2014.03.014.

Schindelin, J., Arganda-Carreras, I., Frise, E., Kaynig, V., Longair, M., Pietzsch, T., Preibisch, S., Rueden, C., Saalfeld, S., Schmid, B., Tinevez, J.-Y., White, D.J., Hartenstein, V., Eliceiri, K., Tomancak, P., and Cardona, A. 2012. Fiji: an open-source platform for biological-image analysis. Nat Methods **9**(7): 676–682. Nature Publishing Group. doi:10.1038/nmeth.2019.

Sharma, V., Ichikawa, M., and Freeze, H.H. 2014. MANNOSE METABOLISM: MORE THAN MEETS THE EYE. Biochem Biophys Res Commun **453**(2): 220–228. doi:10.1016/j.bbrc.2014.06.021.

Shen, J., Cowen, L.E., Griffin, A.M., Chan, L., and Köhler, J.R. 2008. The *Candida albicans* pescadillo homolog is required for normal hypha-to-yeast morphogenesis and yeast proliferation. Proceedings of the National Academy of Sciences **105**(52): 20918–20923. Proceedings of the National Academy of Sciences. doi:10.1073/pnas.0809147105.

Simão, F.A., Waterhouse, R.M., Ioannidis, P., Kriventseva, E.V., and Zdobnov, E.M. 2015. BUSCO: assessing genome assembly and annotation completeness with single-copy orthologs. Bioinformatics **31**(19): 3210–3212. doi:10.1093/bioinformatics/btv351.

Terauchi, M., Nagasato, C., Inoue, A., Ito, T., and Motomura, T. 2016. Distribution of alginate and cellulose and regulatory role of calcium in the cell wall of the brown alga *Ectocarpus siliculosus* (Ectocarpales, Phaeophyceae). Planta **244**(2): 361–377. doi:10.1007/s00425-016-2516-4.

Theodorou, I., and Charrier, B. 2021. Brown Algae: *Ectocarpus* and *Saccharina* as Experimental Models for Developmental Biology. *In* Handbook of Marine Model Organisms in Experimental Biology. *Edited by* A. Boutet and B. Schierwater. CRC Press. pp. 27–46. Available from https://doi.org/10.1201/9781003217503.

Tian, J., Han, L., Feng, Z., Wang, G., Liu, W., Ma, Y., Yu, Y., and Kong, Z. 2015. Orchestration of microtubules and the actin cytoskeleton in trichome cell shape determination by a plant-unique kinesin. eLife **4**: e09351. eLife Sciences Publications, Ltd. doi:10.7554/eLife.09351.

Vanneste, S., and Friml, J. 2013. Calcium: The Missing Link in Auxin Action. Plants (Basel) **2**(4): 650–675. doi:10.3390/plants2040650.

Wu, T., Hu, E., Xu, S., Chen, M., Guo, P., Dai, Z., Feng, T., Zhou, L., Tang, W., Zhan, L., Fu, X., Liu, S., Bo, X., and Yu, G. 2021. clusterProfiler 4.0: A universal enrichment tool for interpreting omics data. Innovation **2**(3). Elsevier. doi:10.1016/j.xinn.2021.100141.

Yadav, U., and Khan, M.A. 2018. Targeting the GPI biosynthetic pathway. Pathog Glob Health **112**(3): 115–122. doi:10.1080/20477724.2018.1442764.

Yendo, K.R. 1911. The Development of *Costaria*, *Undaria*, and *Laminaria*. Ann Bot **os-25**(3): 691–716. Oxford Academic. doi:10.1093/oxfordjournals.aob.a089349.

Yonamine, R., Ichihara, K., Tsuyuzaki, S., Hervé, C., Motomura, T., and Nagasato, C. 2021. Changes in Cell Wall Structure During Rhizoid Formation of *Silvetia babingtonii* (Fucales, Phaeophyceae) Zygotes. Journal of Phycology **57**(4): 1356–1367. doi:10.1111/jpy.13178.

Yu, T.W., Mochida, G.H., Tischfield, D.J., Sgaier, S.K., Flores-Sarnat, L., Sergi, C.M., Topçu, M., McDonald, M.T., Barry, B.J., Felie, J.M., Sunu, C., Dobyns, W.B., Folkerth, R.D., Barkovich, A.J., and Walsh, C.A. 2010. Mutations in WDR62, encoding a centrosome-associated protein, cause microcephaly with simplified gyri and abnormal cortical architecture. Nat Genet **42**(11): 1015–1020. Nature Publishing Group. doi:10.1038/ng.683.

Zeng, Q., Liu, H., Chu, X., Niu, Y., Wang, C., Markov, G.V., and Teng, L. 2022. Independent Evolution of the MYB Family in Brown Algae. Frontiers in Genetics **12**. Available from https://www.frontiersin.org/article/10.3389/fgene.2021.811993 [accessed 1 June 2022].

Zhao, F., Du, F., Oliveri, H., Zhou, L., Ali, O., Chen, W., Feng, S., Wang, Q., Lü, S., Long, M., Schneider, R., Sampathkumar, A., Godin, C., Traas, J., and Jiao, Y. 2020. Microtubule-Mediated Wall Anisotropy Contributes to Leaf Blade Flattening. Current Biology **30**(20): 3972-3985.e6. doi:10.1016/j.cub.2020.07.076.

Tables

Table 1. Developmental characteristics of the samples from 10, 12 and 14 days after fertilisation (DAF) embryos isolated, with 2-3 biological samples. Details in the text.

Developmental stage	**Morphological traits**	**Approximate age of embryos**	**Timepoint**	**Samples**	
				N	ID
Advanced Phase II	1. Monostromatic 2. Parallel and perpendicular to the longest axis cell divisions	10 DAF	t0 = 0 h	3	t0_1 t0_2 t0_3
Late Phase II	1. Monostromatic 2. Parallel and perpendicular to the longest axis cell divisions	12 DAF	t1 = 48 h	3	t1_1 t1_2 t1_3
Initials of polystromatisation	1. Monostromatic except base 2. Anticlinal and a few periclinal divisions at the bottom of the embryos	14 DAF	t2 = 96 h	2	t2_1 t2_2

Table 2: Reads before and after trimming per sample.

Timepoint/Sample		% GC content		Reads = million sequences	
Before trimming		Forward	Reverse	Forward	Reverse
t_0= 0 h	t0_1	50	49	24.5	24.5
t_0= 0 h	t0_2	48	47	32.6	32.6
t_0= 0 h	t0_3	49	47	27.2	27.2
t_1= 48 h	t1_1	52	51	20.5	20.5
t_1= 48 h	t1_2	51	50	27.2	27.2
t_1= 48 h	t1_3	50	49	28.0	28.0
t_2= 96 h	t2_1	49	48	26.6	26.6
t_2= 96 h	t2_2	52	51	22.1	22.1
Average		50	49	26.1	

Timepoint/Sample		% GC content		Reads = million sequences	
After trimming		Forward	Reverse	Forward	Reverse
t_0= 0 h	t0_1	51	51	17.6	17.6
t_0= 0 h	t0_2	50	50	22.8	22.8
t_0= 0 h	t0_3	50	50	19.1	19.1
t_1= 48 h	t1_1	53	53	15.0	15.0
t_1= 48 h	t1_2	52	52	20.3	20.3
t_1= 48 h	t1_3	52	52	20.6	20.6
t_2= 96 h	t2_1	51	51	18.4	18.4
t_2= 96 h	t2_2	53	53	17.0	17.0
Average		52	52	18.9	

Table 3: De-novo transcriptome assembly parameters and output.

Software	Parameters	Output	Statistics
Trinity	Defaults*	Trinity genes	132180
		Transcripts	170562
		Longest transcript	24 695 bp
		N50	1 155 bp
		N50 (longest isoform per gene)	942 bp
Decontamination (kraken2)	Confidence level = 0.05		
BUSCO**	Stramenopiles lineage, 100 BUSCO groups	Complete BUSCOs	81
		Complete and single-copy BUSCOs	14
		Complete and duplicated BUSCOs	67
		Fragmented BUSCOs	4
		Missing BUSCOs	15
Bowtie2	Defaults*	Mean overall alignment rate (%)	83.43 ± 1.42
		Mean alignment >1 times (%)	75.52 ± 1.78
		Mean alignment exactly =1 times (%)	7.91 ± 0.55
		Mean aligned concordantly 0 times (%)	16.57 ± 1.42
Corset	Defaults***	Clusters	41 225

*See the wiki of the trinity software on https://github.com/trinityrnaseq/trinityrnaseq/wiki

** via the European Galaxy server on https://usegalaxy.eu

*** Github of the software https://github.com/Oshlack/Corset/wiki/InstallingRunningUsage

Table 4. Results of gene expression analysis, after annotation and last decontamination

Formula	Timepoint	Total DEGs	Downregulated		Upregulated		Unique
			number	%	number	%	
t1 – t0	48 h	111	74	66.67	37	33.33	59
t2 – t0	96 h	475	339	71.37	125	28.63	423
t2 – t1	96 h vs 48 h	235	187	79.57	48	20.43	66

Figures

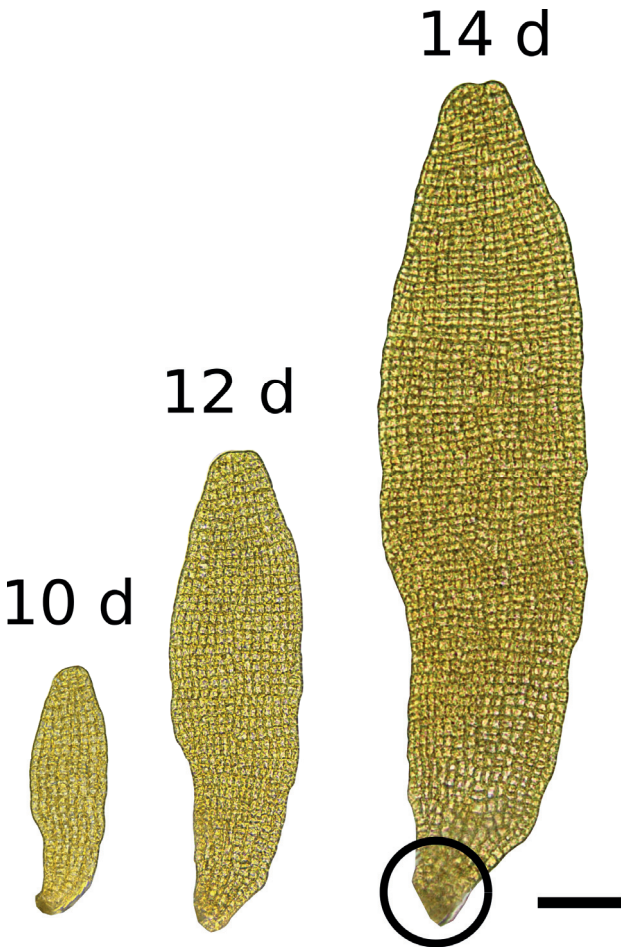

Figure 1. Specimen at the different timepoints of sampling. The embryos do not always grow parallel to bottom of the petri dish, therefore a Z-stack acquisition and projection of it are necessary. These images are projected with the stack focuser. At the bottom of 14 d (circle) a few divisions parallel to the surface of the thallus took place. Bar: 80 µm

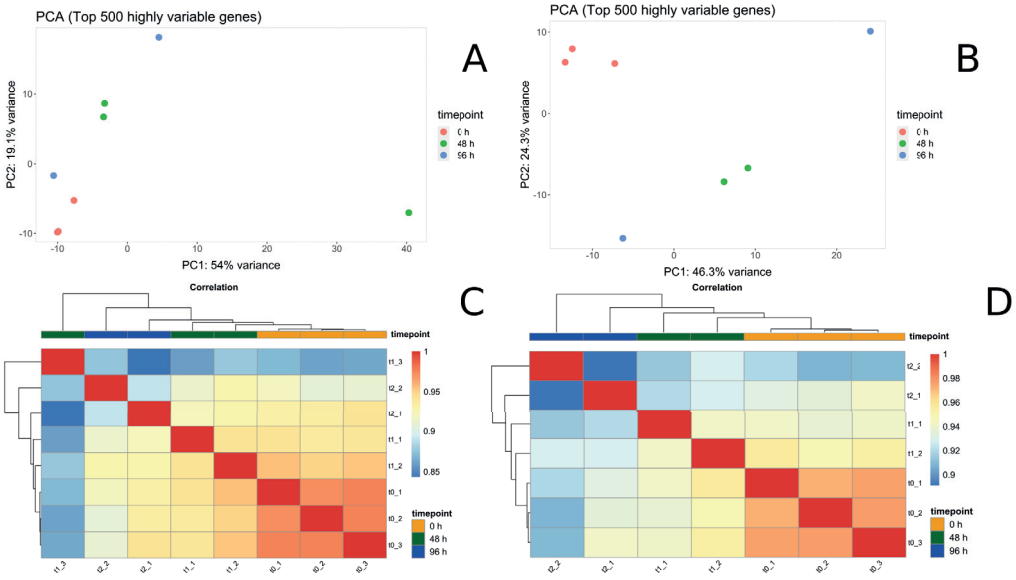

Figure 2. Correlation of the replicates in each sample. A) PCA plot before removing t1_3 (t1 = 48 h, 3d replicate), as it is clear oultlier compared to the rest of two replicates. B) PCA plot after removing t1_3, with clear clustering except for 96 h, which is a logical variation since there is variation on the entry to Phase III. C) Correlation heatmap with t1_3. Color scale on the right. D) Correlation heatmap without t1_3.

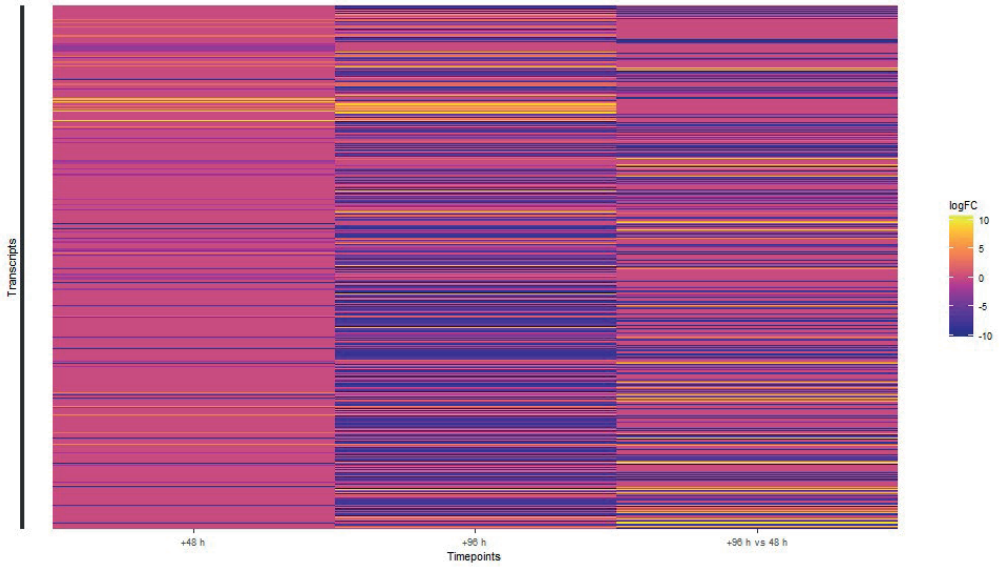

Figure 3. Heatmap with all the DEGs detected in this study. The color scale is depicted on the right side. Each line is a transcript and its profile at the different timepoints. A general downregulation can be observed for the 96 h timepoint.

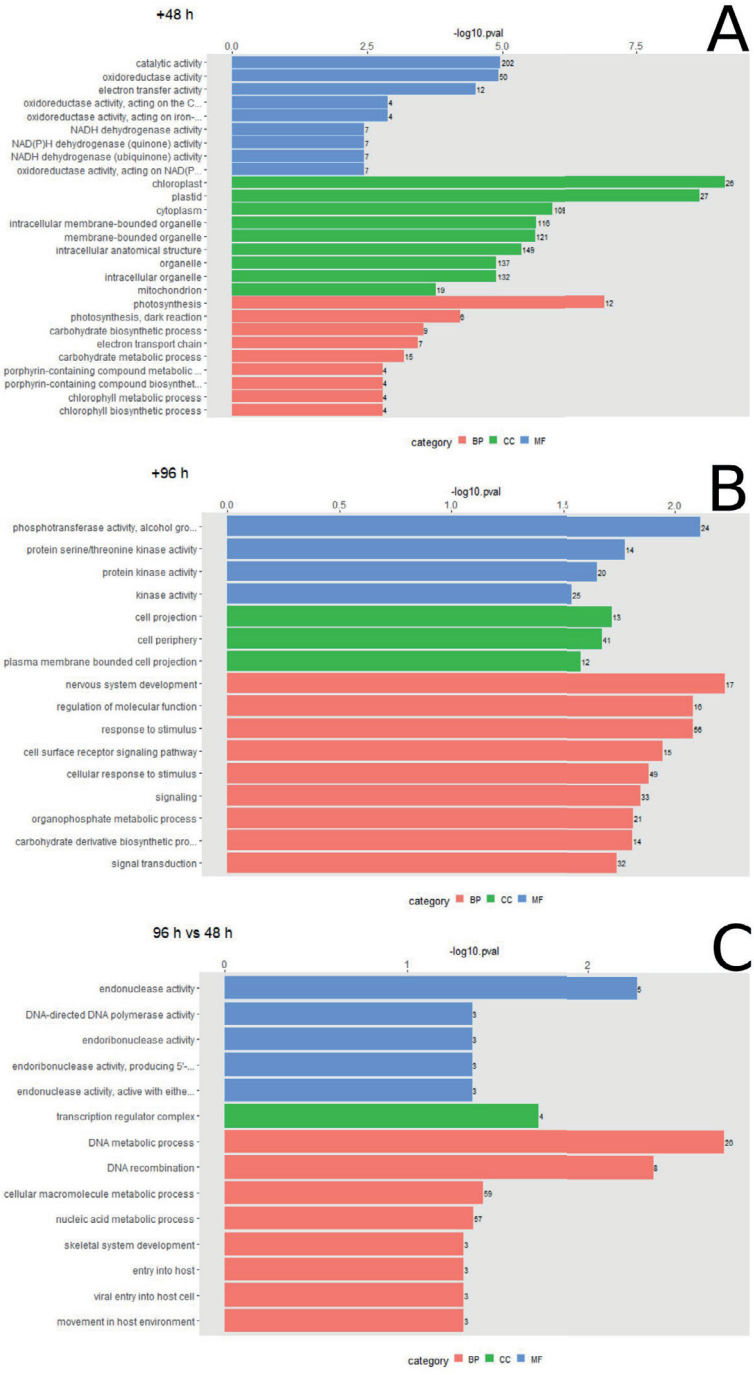

Figure 4. Gene ontology. The top 9 terms for the Biological processes (BP), Cellular Components (CC) and Molecular Function (MF) categories are presented per timepoint. A) First timepoint, 48 h after the advanced stage of Phase II, GO terms related to metabolism

and physiological process are observed. Interestingly, the CC terms are strongly enriched to organelles localization of the encoding products. However, highest p-value is shown from the chloroplast term. B) At Second timepoint, 96 h , the GO terms related to signal transduction, cell communication, protein regulations (kinases only) and development terms are observed. Overall, this increased representation of signalling terms coincides with third axis growth and initiation of polystromatisation. C) At comparison of 96h vs 48 h, there is no specific pattern with terms ranging from host cells to DNA related processes. Next to the bars the number of the DEGs with the respective GO term is presented.

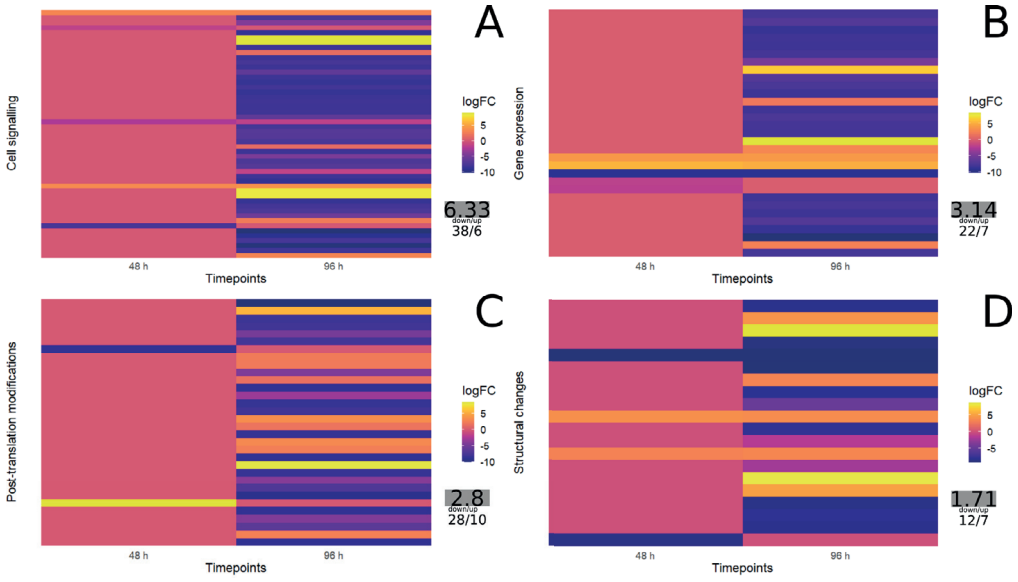

Figure 5. Gene expression changes for key DEGs. A) Heatmap of DEGs related with cell signalling, B) heatmap of DEGs with products with key role on gene expression, C) heatmap of DEGs encoding proteins related with post-translational modifications, like kinases and others, D) heatmap DEGs encoding proteins with direct interaction on cytoskeleton organization or cell wall composition and properties. Table S5 was used for the generation of the plots

Supplementary data:

All the supplementary tables can be found at the link: https://we.tl/t-MwMaTBlBVo

Table S1: The annotation table with all the DEGs, stats for their match, Trinity ID as well as the logFC for each timepoint.

Table S2: *Top20 Upregulated DEGs for the two timepoints. Details in text.*

Table S3: *Top20 Downregulated DEGs for the two timepoints. Details in text.*

Table S4: *Top20 Upregulated and Downregulated DEGs for the comparison of the two timepoints.*

Table S5: *Selection of DEGs and classified according to the role of their potential products.*

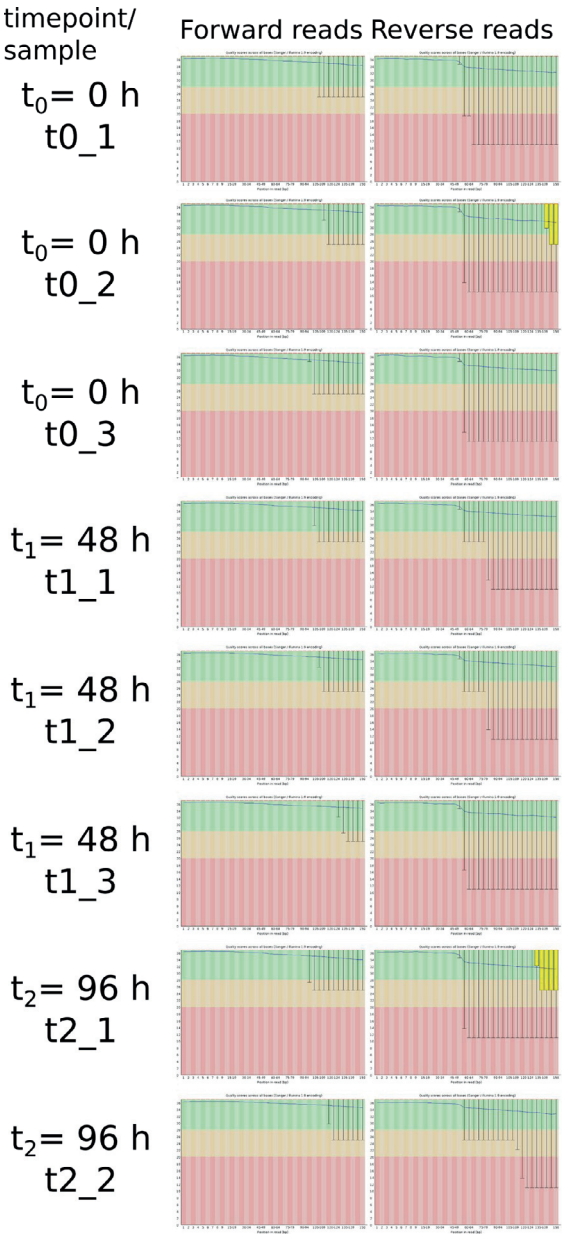

Figure S1. Phred30 score – position in read plot before trimming for each timepoint and sample.

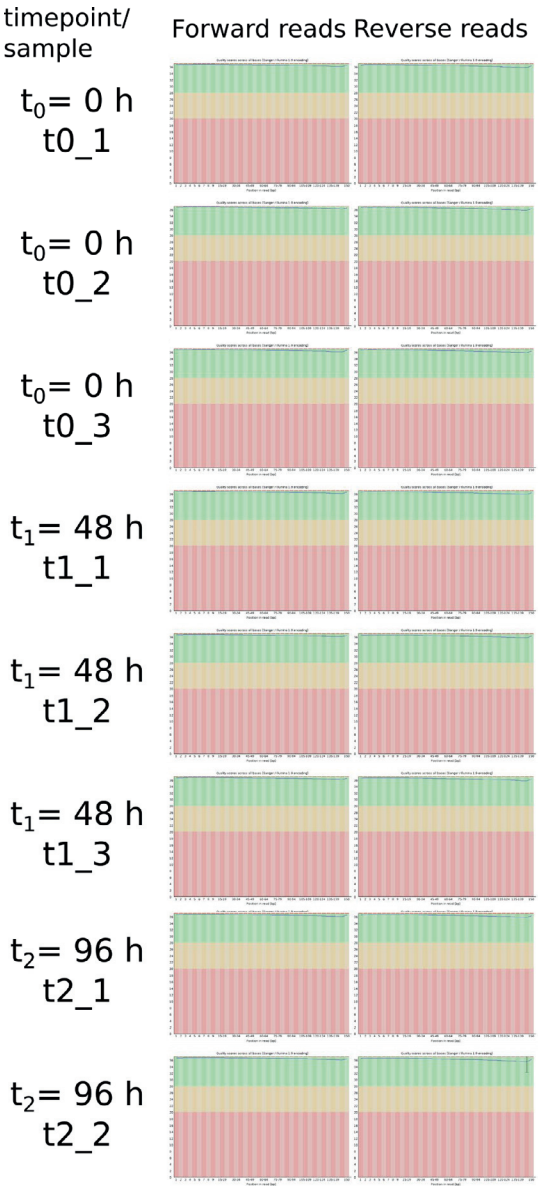

Figure S2. Phred30 score – position in read plot after trimming for each timepoint and sample.

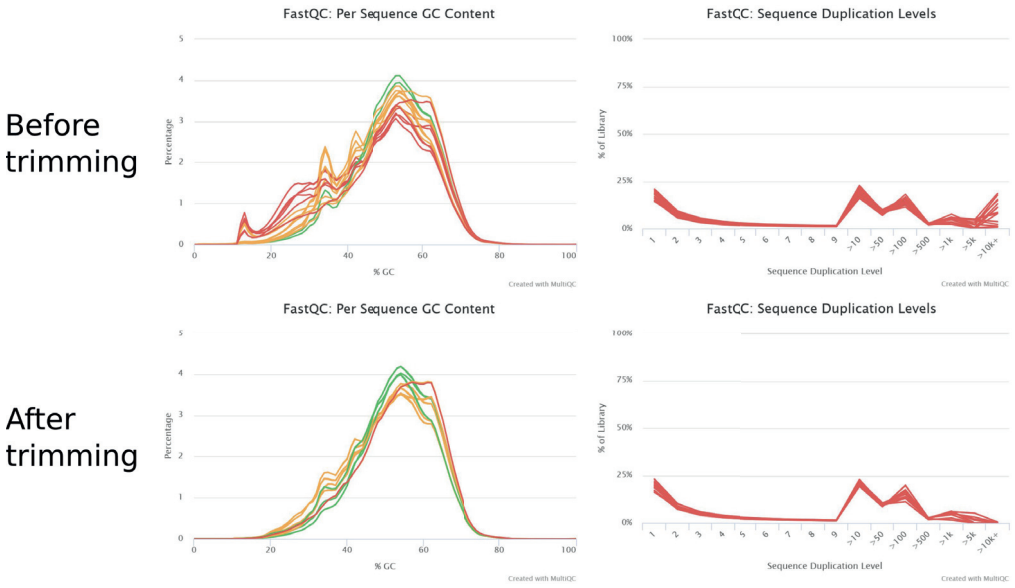

Figure S3. GC content per sample and sequence duplication level, before and after trimming.

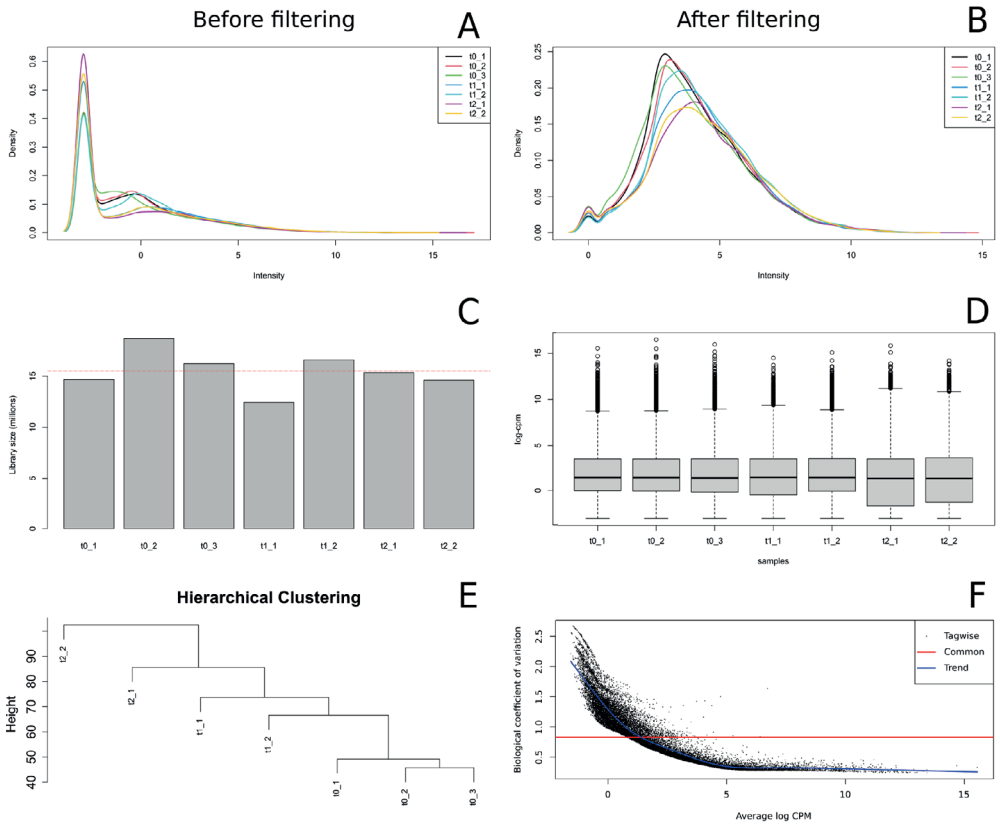

Figure S4. Plot on different parameters of gene expression analysis after the removal of sample t1_3. A) Expression distribution of the reads per sample before filtering for low counts in logarithm of counts per million, B) Expression distribution of the reads per sample after filtering for low counts. C) Library size after filtering. D) logarithm of counts per million per sample (log(CPM). E) Tree of correlation between samples. F) Biological coefficient of variation plot per average log(CPM)

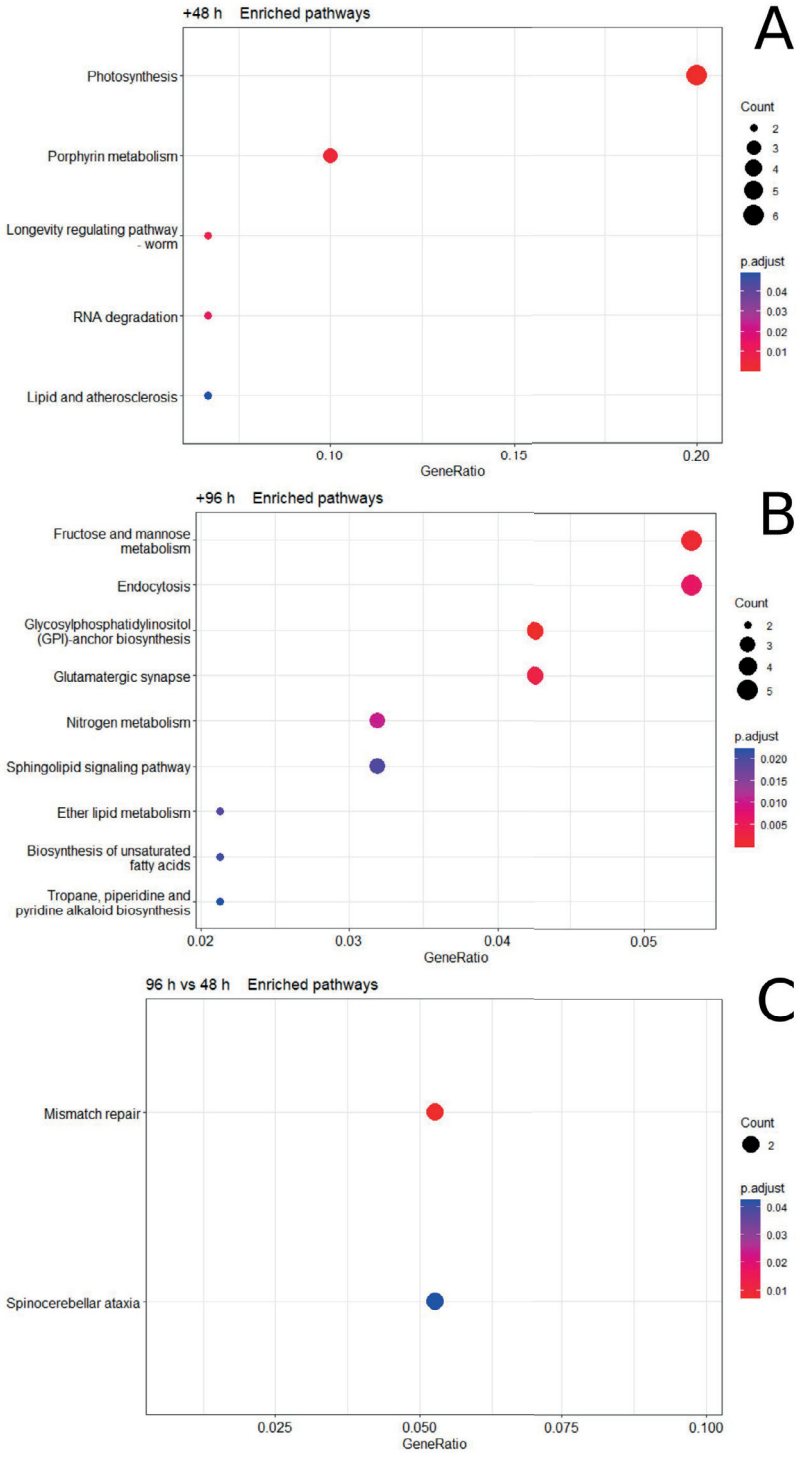
+48 h Enriched pathways
A
Photosynthesis
Porphyrin metabolism
Longevity regulating pathway - worm
RNA degradation
Lipid and atherosclerosis
0.10
0.15
0.20
GeneRatio
Count
2
3
4
5
6
p.adjust
0.04
0.03
0.02
0.01
+96 h Enriched pathways
B
Fructose and mannose metabolism
Endocytosis
Glycosylphosphatidylinositol (GPI)-anchor biosynthesis
Glutamatergic synapse
Nitrogen metabolism
Sphingolipid signaling pathway
Ether lipid metabolism
Biosynthesis of unsaturated fatty acids
Tropane, piperidine and pyridine alkaloid biosynthesis
0.02
0.03
0.04
0.05
GeneRatio
Count
2
3
4
5
p.adjust
0.020
0.015
0.010
0.005
96 h vs 48 h Enriched pathways
C
Mismatch repair
Spinocerebellar ataxia
0.025
0.050
0.075
0.100
GeneRatio
Count
2
p.adjust
0.04
0.03
0.02
0.01

Figure S5. Functional analysis: Enriched pathways. A) First timepoint, 48 h after the advanced stage of Phase II, we see increased gene ration for photosynthesis. Less prominent pathways included porphyrin metabolism and RNA degradation. B) At Second timepoint, 96 h, we observe most of the differentially expressed pathways are related with signalling and cell to cell communication (black circles), the rest of the pathways are related to metabolism. Specifically, the fructose/mannose pathway demonstrates the highest gene ratio.

Paper V: Preparation of Zygotes and Embryos of the Kelp *Saccharina latissima* for Cell Biology Approaches

State of publication: Published 2021

Please cite this article as: Theodorou, I. *et al.* (2021). Preparation of Zygotes and Embryos of the Kelp *Saccharina latissima* for Cell Biology Approaches. *Bio-101*: e4132. DOI: 10.21769/BioProtoc.4132

bio-101 www.bio-protocol.org/e4132 Bio-101: e4132. DOI:10.21769/BioProtoc.4132

Preparation of Zygotes and Embryos of the Kelp *Saccharina latissima* for Cell Biology Approaches

Ioannis Theodorou[1, 2, *], Hilde-Gunn Opsahl-Sorteberg[2] and Bénédicte Charrier[1, *]

[1]Morphogenesis of Macroalgae, Laboratory of Integrative Biology of Marine Models, UMR8227 Station Biologique, CNRS-Sorbonne University, Roscoff, France; [2]Department of Plant Sciences, Faculty of Biosciences, Norwegian University of Life Sciences, Ås, Norway

*For correspondence: benedicte.charrier@sb-roscoff.fr; ioannis.theodorou@sb-roscoff.fr

[Abstract] Embryogenesis and early development in kelps are poorly studied and understood. Cultivation protocols focus mostly either on the preparation of large volumes of vegetative gametophytes or on the production of conspicuous juvenile sporophytes as starting materials for aquaculture to grow large adult organisms for biomass. Hence, our protocol describes the optimal conditions for a) efficient gametogenesis, b) synchronization of egg release, c) control of zygote density, and d) optimal embryonic development of the kelp *Saccharina latissima*. This species is currently subject to aquaculture development in Europe, but the aim here is to provide tools for academic research aiming to identify the mechanisms underlying embryogenesis. These protocols, adaptable to different volume scales from Petri dishes to up to ten-liter containers, are the required first steps for robust downstream experiments scaled at the cytological level (immunochemistry, microdissection, laser ablation, and cell transcriptomics) and for physiological and phycopathogenesis studies at very early stages.

Graphic abstract:

Please cite this article as: Theodorou, I. *et al.* (2021). Preparation of Zygotes and Embryos of the Kelp *Saccharina latissima* for Cell Biology Approaches. *Bio-101*: e4132. DOI: 10.21769/BioProtoc.4132

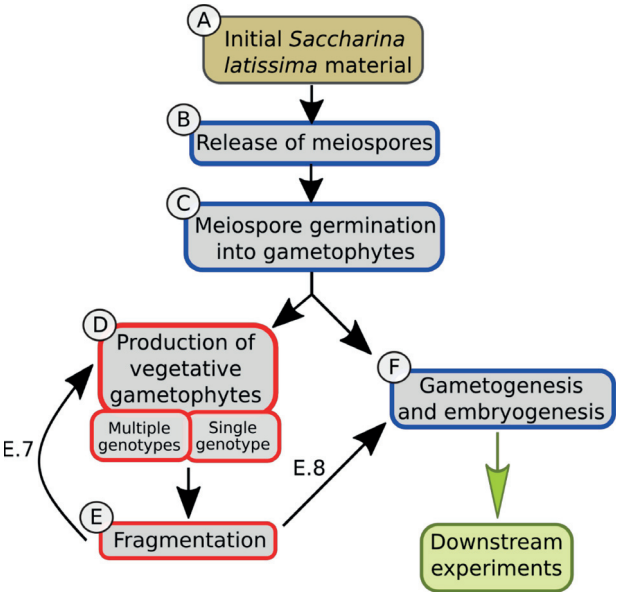

Boxes describing the different steps of the protocol. The color of the box contours (red or blue) indicates different light conditions, red light and white light, respectively.

Keywords: Brown alga, Gametogenesis, Embryogenesis, Kelp, Saccharina, Cultivation, Zygote

[Background] Brown algae are a group of mainly marine photosynthetic organisms with exclusively multicellular body plans (thallus). Their thallus ranges from small filaments like in *Ectocarpus* species to the large conspicuous parenchymatic kelps (Charrier *et al.*, 2012). Kelps in particular play a major ecological role as habitat for other organisms and are important primary producers in coastal ecosystems. Kelps also attract considerable economic interest, mainly as food sources (*e.g.*, kombu). In addition, extracts from brown algae have shown anti-tumor and anti-inflammatory effects (Cumashi *et al.*, 2007; Han *et al.*, 2019; Long *et al.*, 2019; Mohibbullah *et al.*, 2019), and their biomass is used as bioethanol (Adams *et al.*, 2009; Kraan, 2016). This altogether raises special interest in their metabolism and physiology. This is particularly the case for *Saccharina latissima,* as shown by an ~5-fold increase in publications over the past 10 years (from 40 in 2010 to more than 180 in 2020; Web of Knowledge), elevating it to currently being the most studied brown alga worldwide. However, this interest focuses mainly on its ecophysiology and less on its development, a balance that this protocol, in combination with expected publications, aims to improve.

The life cycle of *S. latissima* and kelps in general, is divided in a haploid and a morphologically distinct diploid phases (Kanda, 1936; Fritsch, 1945). During the haploid phase, the organism is prostrate and filamentous, and two sexes can be distinguished (dioicous condition). Given the appropriate conditions for gametogenesis (see next paragraph), the female gametophyte releases a spherical egg that remains fixed to the empty gametangium (also named oogonium). When the male gamete released from the

male gametophyte is chemically attracted by the egg (Maier and Müller, 1986; Kinoshita *et al.*, 2017), their fusion results in the onset of the diploid phase starting with an elongated zygote. The developing embryo will eventually grow into an impressive (>3 m) mature sporophyte after only a few months (Andersen *et al.*, 2011). Sporiangia on the surface of the mature fertile sporophyte contain the haploid meiospores. After being released, these meiospores settle and germinate into gametophytes. While the ecophysiology of both phases is well studied (an old review: Bartsch *et al.*, 2008), little is known about the embryonic development of the sporophytes, and historic studies only provide descriptive observations (reviewed in Fritsch, 1945). Given both the importance of this resource to the environment and as feed and food, as well as advances in science, this is expected to change. Therefore, to boost the developmental and cellular approaches aiming to decipher the mechanisms underlying embryogenesis in this alga, we propose a protocol focusing on the production and cultivation of zygotes and early embryos.

Gametogenesis is an important step for promoting normal embryogenesis in artificial culture conditions. Considerable work focused on environmental factors like light quality, temperature, and nutrients that can disrupt or inhibit gametogenesis. Lüning and Dring (1972) demonstrated that blue light induces the process while red light acts repressively. Normal white light acts like blue light, given low light intensity (Hsiao and Druehl, 1971; Lüning, 1980; Lee and Brinkhuis, 1988). Temperature is also crucial: temperatures above 15°C inhibit gametogenesis, while temperatures between 10 and 15°C are optimal (Lüning, 1980). A parameter often missed in these earlier works is density. For *Saccharina japonica*, high density of gametophytes inhibits gametophytic growth in *in vitro* cultures (Petri dishes; Yabu, 1965) and fertility at larger scales (20 L tanks, Zhang *et al.*, 2008). Recent work from Ebbing *et al.* (2020) further clarifies the density parameter and the effect of its combination with light quality, a correlation not considered in previous works. Specifically, gametogenesis-induction by blue light occurs only in low-density cultures combined with low light intensity. Red light has the opposite effect. In high light intensity, red light promotes higher fertility than blue light or white light. Regarding nutrients, high concentrations of chelated iron into the culture medium seem to promote gametogenesis in other kelp species (Motomura and Sakai, 1984; Lewis *et al.*, 2013). Considering the above parameters, the present protocol relies on the biological properties of different light conditions in combination with the concentration of nutrients in the medium to either arrest or promote gametogenesis.

In addition, this protocol allows the production of zygotes and embryos amenable to downstream experiments, like immunolocalization protocols, in which the steps of chemical fixation, cell wall digestion, antibody incubations, and staining can occur inside glass bottom Petri dishes. Alternatively, and depending on the size and the developmental stages of embryos, embryos can be transferred onto manufactured or homemade poly-L-Lysine (1 mg ml^{-1}) coated slides or coverslips using tweezers with thin ends. In transmission electron microscopy (TEM) protocols, while fixation and post fixation steps can occur in common plastic Petri dishes, dehydration requires incubation in acetone, which would dissolve most plastic Petri dishes. Therefore, material transfer into, *e.g.*, Falcon or Eppendorf tubes or glass Petri dishes before dehydration and infiltration will be necessary in this case.

Please cite this article as: Theodorou, I. *et al.* (2021). Preparation of Zygotes and Embryos of the Kelp *Saccharina latissima* for Cell Biology Approaches. *Bio-101*: e4132. DOI: 10.21769/BioProtoc.4132

Finally, the protocol describes how to control the density of growing embryos, which impacts the production of i) healthy embryos, ii) embryos sufficiently spread to allow subsequent monitoring of, *e.g.*, growth dynamics in time-lapse observation, and iii) embryos amenable to isolation and experimentation, *e.g.*, through microdissection and laser ablation.

Clean (close to sterile) conditions are essential through the entire protocol, especially during gametogenesis induction and embryogenesis.

Altogether, this protocol will promote further studies on the microscopic stages of kelp development.

Materials and Reagents

1. 1.5 ml sterile Eppendorf tubes
2. Sterile scalpel
3. Filter tips 1,000 µl, 100 µl, and 20 µl (Starlab, TipOne)
4. Plastic Petri dishes Ø35 mm (Sarstedt, catalog number: 82.1135.500)
5. Petri dishes with glass bottom Ø28.2 mm (NEST, catalog number: 801001)
6. Pellet pestles, blue polypropylene (autoclavable) (Sigma-Aldrich, catalog number: Z359947-100EA)
7. Cell scraper (Sarstedt, catalog number: 83.1830)
8. Cell strainer 40 µm (Falcon, catalog number: 352340)
9. Autoclaved, 0.2-5 µm filtered seawater (SW), stored at 14°C
10. Counting chamber slides (Kova glasstic slide 10 with counting grids, catalog number: 87144)
11. Pasteur pipettes, long
12. Nalgene bottles, 2 and 10 L
13. H_3BO_3
14. $FeCl_3$
15. $MnSO_4$
16. $ZnSO_4$
17. $CoSO_4$
18. EDTA
19. $(NH_4)_2Fe(SO_4)_2 \cdot 6H_2O$
20. $NaNO_3$
21. $C_3H_7Na_2O_6P$
22. Vitamin B12 (cyanocobalamin)
23. Thiamin (vitamin B1)
24. Biotin
25. Tris
26. Provasoli solution (see Recipes)

Please cite this article as: Theodorou, I. *et al.* (2021). Preparation of Zygotes and Embryos of the Kelp *Saccharina latissima* for Cell Biology Approaches. *Bio-101*: e4132. DOI: 10.21769/BioProtoc.4132

Equipment

1 Inverted Microscope Leica DMi8, light source: CTR compact, camera: RGB Leica DMC4500
2 Laminar flow hood
3 Light source: Philips, Master TL-D 18W/865, commercial sheet of red filter (LEE filters, 026 Bright Red)
4 Climate chambers with controllable temperature and light source
5 Automatic pipettes: 1,000, 100 or 50, and 10 µl
6 Lighter

Procedure

A. Collecting fertile sporophytic material from the wild

1. Depending on the geographical region, mature sporophytes are fertile from early winter until middle to late spring. They might be collected from the beach during low tide or directly underwater while diving. Fertile sporophytes have dark areas, called sori (singular: sorus), where meiosporiangia reside (Figure 1).

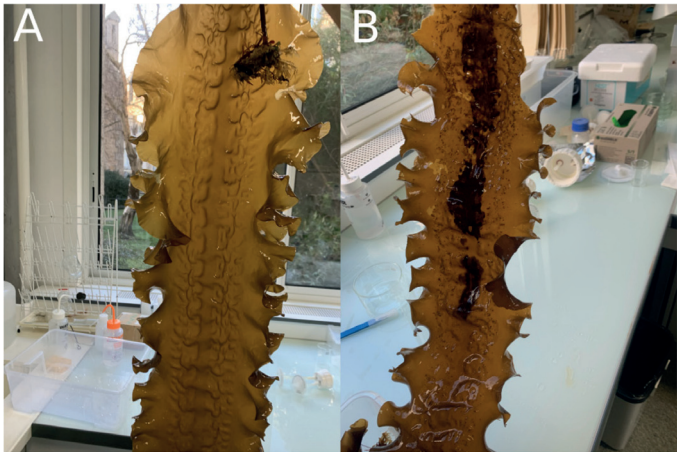

Figure 1. Comparison of fertile and non-fertile areas. A. Non-fertile area of a sporophytic blade held upside down. B. Fertile areas (sori) on the same blade a couple of meters below the non-fertile area shown in A.

Note: Look for large blades with normal morphologies: twisted stipe or other symptoms of disease (like white spots at the surface of the blade) reveal the presence of pathogens and endosymbionts. In addition, avoid collecting material covered with epiphytes. It is common for other filamentous brown algae or red algae to grow on the thallus of kelps.

2. In the Western part of France, on the Atlantic coast (Brittany), fertile months are October to April,

and our material was collected from thalli stranded on the beach of Perharidy (48°43'33.5"N 4°00'16.7"W).

3. Alternatively, large fragments (>1 m) of sporophytes can be collected, and sporogenesis can be induced. Parts of the thallus should be cut away from the intercalary meristem and the stipe. Then, they are kept in short day conditions (8 h light: 16 h dark) and 100-120 photons m^{-2} s^{-1} for at least two weeks to induce sporogenesis (Pang and Lüning, 2004; Forbord *et al.*, 2012). Depending on the geographical location where the strain has been collected and on the season, the incubation time needed to induce sporogenesis under short day conditions can vary up to 12 weeks.

B. Release of meiospores

1. Using a scalpel, remove the fertile tissue from the rest of the blade or fragments. The fertile tissue where meiosporiangia reside is darker and easily distinguishable from the rest of the blade (Figure 1). Try to dissect undamaged dark parts showing no interruption of their color and morphology.
2. Clean the surface with a paper towel dampened with distilled (osmosis) water, remove any excess water, and dry with a new paper towel.
3. Remove epiphytes by softly scratching the surface of the blade with the scalpel and wipe with a dry paper towel.
4. You can choose to release meiospores a) at this point or b) one of the next two days.
5. If a), cut the tissue in small fragments of up to 1-3 cm^2 and place them in sterile autoclaved and filtered 0.2 µm SW under ambient room light (in our case, it was 8-15 µmol photons s^{-1} m^{-2} on a cloudy day or 9-16 µmol photons s^{-1} m^{-2} in a well-lit room).
6. If b), keep large fertile fragments in a humid chamber at 4°C. This humid chamber is made of a damp (but not wet) piece of paper towel or cotton placed in a Petri dish sealed with parafilm. Under these conditions, the tissue can be preserved for up to 48 h. For the release, proceed at step 5.
7. After ~40 min, an adequate amount of meiospores swimming in the medium is visible (Figure 2A; Video 1). They color the medium amber.

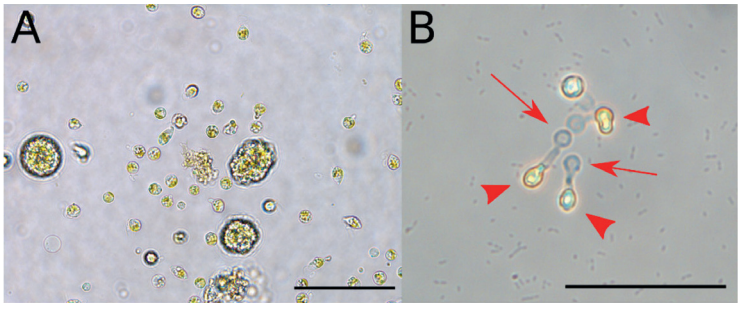

Figure 2. Meiospores. A. Freshly released meiospores. B. Meiospores germinating three days

after release; arrows: empty spore and germinating tube, arrowheads: first gametophytic cell. Scale bars = 50 µm.

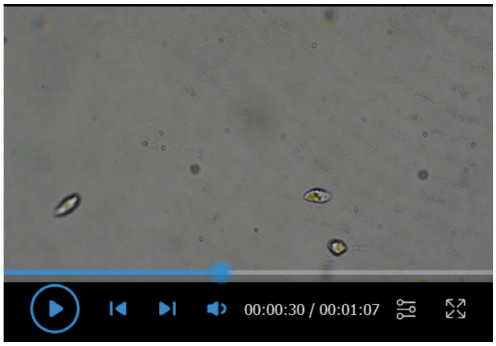

Video 1. Swimming spores with visible flagella (different magnifications: 10×, 20×, 40×, and 63×). Credit: David Wahnoun.

Note: It is essential to not let the fertile tissue into the medium for more than 1 h because, epiphytes and endophytes will be released into the medium together with the spores. This can tamper with the germination and normal vegetative development of future gametophytes.

8. Monitor the release of spores every 10 to 20 min by counting them using the counting chamber. Calculate the concentration of spores. An optimal concentration is 300,000-400,000 cells ml^{-1}.
   *Note: For counting meiospores using a counting chamber (like Neubauer), the following equation can be used. Concentration = Number of cells per volume unit (ml). Alternatively, use: Concentration (cell ml^{-1}) = Average number of cells per square × 10^4 * × dilution factor.*
   **: 0.1 µl is the volume loaded in the square. Therefore, for a final volume of 1 ml, the total number of spores = calculated number × 10^4.*
9. Transfer your material and work under the laminar flow hood for the rest of the protocol.
10. Filter 5-7 ml of meiospore-containing medium with the cell strainer.
    Note: Filtration and dilution steps additionally help to remove part of the mucus released together with the spores, which may carry contaminants or be harmful to spores.
11. Dilute adequately with fresh ½ PES SW (see Recipes) and filter once or twice more. We used 30-40 spores ml^{-1} as the final concentration. At that meiospores concentration, the gametophytes will be spread of ~300 µm, which will facilitate their isolation in the downstream steps if required (Figure 2A).

C. Meiospore germination and production of gametophytes

For the production of vegetative gametophytes as stock material, proceed to step 1.

For immediate production of zygotes, proceed to step 2.

1. Keep meiospores under red light conditions: 3 µmol photons m^{-2} s^{-1} light intensity and 14:10 light:dark photoperiod at 13°C (Figure 3A). After 12 h, the spores settle to the bottom of the Petri

Please cite this article as: Theodorou, I. *et al.* (2021). Preparation of Zygotes and Embryos of the Kelp *Saccharina latissima* for Cell Biology Approaches. *Bio-101*: e4132. DOI: 10.21769/BioProtoc.4132

dish and germinate after 2-3 days. Proceed with **D**.

2. Put the meiospores in 16 µmol photons m^{-2} s^{-1} white light intensity (low light) and 14:10 light:dark photoperiod at 13°C (Figure 3B). After approximately 10 days, polarized gametophytes are developing female gametangia on top of one to two cells (Figure 2B). Use an inverted microscope to observe them. For more details, proceed with **E**.

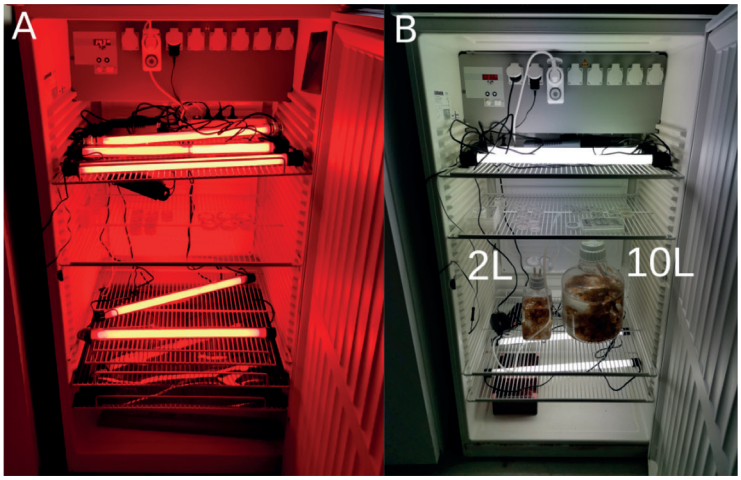

Figure 3. Culture cabinets. A. Red light conditions cabinet. B. White or normal light conditions cabinet, with 2-L and 10-L Nalgene bottles.

D. Working with stock material

1. Cultivation of mixed vegetative gametophytes

   When released from one parental sporophyte, germinating meiospores will produce a mix of gametophytes with different genotypes. At each release, the population of produced gametophytes has a different genotypic composition because the parental sporophyte is freshly collected from the wild.

   a. Avoid any exposure to white light (red light: 3 µmol photons m^{-2} s^{-1} light intensity and 14:10 light:dark photoperiod at 13°C). At the stage, the gametophytes are growing (Figure 4).

Please cite this article as: Theodorou, I. *et al.* (2021). Preparation of Zygotes and Embryos of the Kelp *Saccharina latissima* for Cell Biology Approaches. *Bio-101*: e4132. DOI: 10.21769/BioProtoc.4132

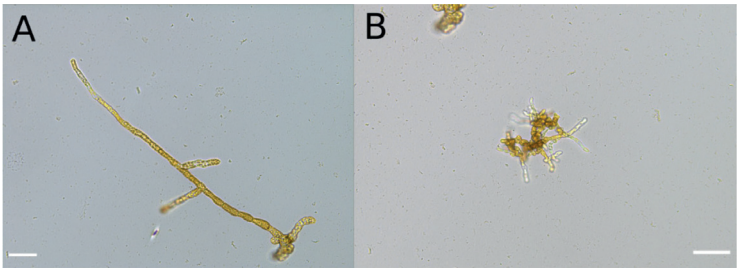

Figure 4. Two-month-old gametophytes. A. Female gametophyte. B. Male gametophyte. Scale bars: 50 µm.

b. Renew ½ PES medium once every month; decant the old medium and refill the Petri dish with freshly prepared medium.
*Note: Fragment and test gametogenesis and embryogenesis once every six months or once a year. Follow the same protocol as in **E** and **F**.*

c. Keep the gametophytic cultures dense enough to prevent gametogenesis (see Notes).

d. Fragment the cultures every 3-6 months as indicated in Procedure E and place again in same culture conditions as above.
Note: Fragment the gametophytes in the middle of the day of a 14:8 light:dark photoperiod. That way, the fragments stay under light for several hours to mitigate stresses caused by fragmentation.

e. Keep ambient to very low light conditions (maximum of 3 µmol m^{-2} s^{-1}) while handling the stock.

f. Be mindful of sterile conditions.

2. Isolating gametophytes for unialgal cultures
To control the genotype of the produced embryos at each experiment, monogenic cultures of both female and male gametophytes are prepared and maintained in stock in vegetative conditions.

a. Make a glass tool using a sterile Pasteur pipette and a lighter under the hood (Video 2).

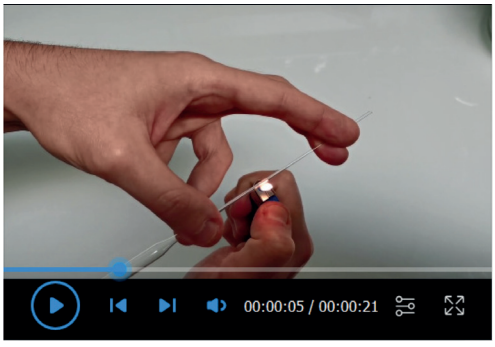

Video 2. Glass tool-making process using a glass Pasteur pipette and a lighter. Hold one side of the Pasteur pipette with your index and middle finger, specifically where the thinnest part ends. Hold the other end with your ring finger and thumb. With your other hand, place the lighter below the middle of your fingers, aiming the flame at the middle of the thinnest part of the Pasteur pipette. After 1 s, start pulling slowly without turning off the flame. When the glass becomes easy to pull, pull both ends in one go, as straight as possible.

b. Choose a gametophyte and scrape it with the glass tool. Another tool with a different diameter or a commercial tip used with an automatic or Pasteur pipette may help if the gametophyte is too small or not sticky enough (Video 3).

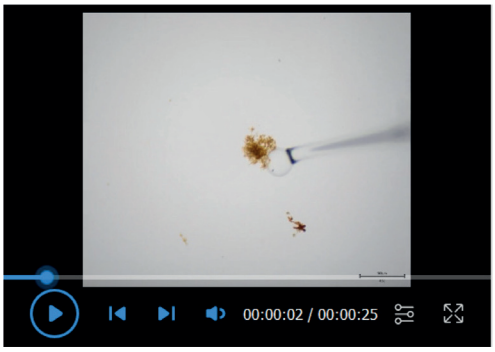

Video 3. Using a glass tool to detach and then transfer the gametophyte to another Petri dish using a sterile Pasteur pipette under the hood

c. Transfer the gametophyte carefully into new ½ PES.
d. Keep it under red light conditions until it is large enough for fragmentation. This requires about 6 months (see Notes).
e. Then, fragment the overgrown gametophyte as in E, and keep it in same culture conditions as stock.

E. Fragmentation

The aim is to induce gametogenesis and embryogenesis from 3-months-old or older material.

1. Fragment dense gametophytic cultures (3 months or older) into a 1.5-ml Eppendorf tube with 50 µl ½ PES using a sterile scraper and autoclaved pestles.
   a. Decant the culture.
   b. Scrape gametophytes from the bottom of the Petri dish and place them into the Eppendorf tube with 50 µl of ½ PES.
   c. Place the gametophytes at the bottom of the Eppendorf tube.
   d. With the pestle, press onto the gametophytes while rotating.
   e. Lift up and down to check on your progress. You can additionally press the gametophytes

on the sidewalls of the Eppendorf tube while observing the process.

f. The gametophytes can cope with high pressure on them; however, you should stop grinding when you observe that the gametophyte biomass is homogenized into the 50 µl.

g. Before committing a large number of your cultures into gametogenesis or for stock renewal, try part of them to find the right pressure and speed of rotation to be applied.
Note: Fragment gametophytes in the middle of the day of a 14:8 light:dark photoperiod. That way, the fragments stay under light for several hours to mitigate stresses caused by fragmentation.

2. Dilute fragments into 1 ml ½ PES.
3. Pipette up and down several times with a steady, slow rhythm.
4. Depending on the size of the donor Petri dish and the recipient dish, choose an adequate dilution. The aim is to have fragments distanced approximately 200 µm. A dilution series can help choose the necessary volume.
5. If female and male gametophytes were kept separated, proceed as described above.
Note: In any case (mixed gametophyte cultures), try to use an almost equal number of male and female fragments.
6. While dispensing fragmented gametophytes into new Petri dishes, avoid material clotting by pipetting up and down at least twice and stir the medium in the Eppy before inoculation of each Petri dish.
7. For stock renewal (Procedure E), part (~20%) of the vegetative fragments can be kept in Petri dishes with ½ PES.
8. For zygote production, proceed with Procedure F.

F. Production of *S. latissima* zygotes and embryos

1. Inoculate the rest of the fragmented gametophytes in full PES SW.
2. Transfer the freshly inoculated Petri dishes into low light conditions (16 µmol photons m^{-2} s^{-1} light intensity and 14:10 light:dark photoperiod, 13°C). The fragments stick slightly to the bottom (mind motion during transportation).
3. Check gametogenesis progression every day. After 5 days, several eggs should be released, and a few polarized zygotes can be potentially observed (Figure 5). The major release of eggs and male gametes should take place during the 6th and 7th days.

Please cite this article as: Theodorou, I. *et al.* (2021). Preparation of Zygotes and Embryos of the Kelp *Saccharina latissima* for Cell Biology Approaches. *Bio-101*: e4132. DOI: 10.21769/BioProtoc.4132

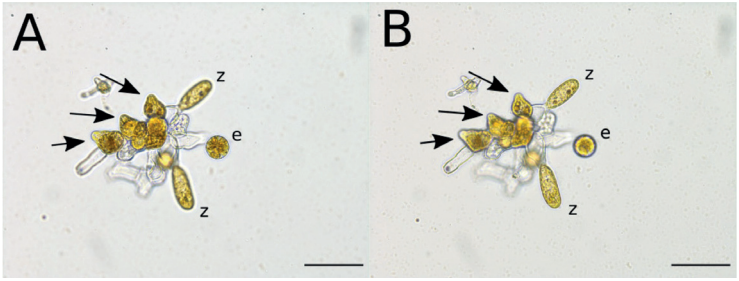

Figure 5. Gametangia, egg, and zygotes. A. Ripe gametangia (arrows), ready to release an egg (see e). B. Different focus plane showing zygotes (z) more clearly. Scale bars: 50 μm

4. To keep the release synchronized, transfer the material from low light to normal light conditions (50 μmol photons m^{-2} s^{-1}) at the beginning of the sixth day. This represses any further gametogenesis. Nevertheless, few male gametes and eggs will occasionally emerge. Most of the developing embryos will have approximately the same developmental stage (Figure 6).

Figure 6. *Saccharina* embryos. The embryos are all at similar developmental stages. Scale bar = 100 μm.

5. Check the progression of gametogenesis and embryogenesis. Fertilization and embryogenesis may be delayed by a few days and may not be efficient if the number of female and male gametophytes is unequal. Differences may exist among species or strains.
6. After one month, transfer the embryos to aerated 2-L Nalgene bottles (Figure 3B). Full PES should be changed every 4-7 days.
7. After 2-3 months, the young sporophytes should be transferred to a 10-L container (Figure 3B), depending on the needs of your experiments.
   Note: Sterile conditions are not required to maintain larger embryos and healthy sporophytes if seawater medium is changed regularly. However, gametophytes show better vegetative growth

in sterile culture medium and handling conditions (note that the algal material is not axenic as spores were originally collected from the wild and were not treated to make them axenic before germination into gametophytes).

The main conditions for the cultivation of vegetative gametophytes, gametogenesis induction, embryo formation, and production of juvenile sporophytes are summarized in Table 1.

Table 1. Summary of different culture conditions. Different light and medium conditions are necessary for induction of gametogenesis, optimization of embryo growth, and maintenance of stock cultures. Temperature is always at 13°C, and the photoperiod is 14:10 (light:dark).

Ontogenic stage	**Light quality and intensity**	**Medium composition (SW completed with)**	**Change medium**
Vegetative gametophytic growth	Red, 3 µmol photons m^{-2} s^{-1}	½ PES	Once every month
Gametogenesis	White, 16 µmol photons m^{-2} s^{-1}	Full PES	-
Embryogenesis	White, 50 µmol photons m^{-2} s^{-1}	Full PES	After 20-30 days (together with glass and plasticware)
Juveniles and Young sporophytes	White, 50 µmol photons m^{-2} s^{-1}	Full PES	Once every four to seven days

Notes

The gametophytes grow slowly and need to be maintained in red light conditions always. If gametophytes are the main interest, high culture density must be maintained as this will prevent any spontaneous embryogenesis (Ebbing *et al.*, 2020).

Recipes

1. Provasoli enriched seawater (PES) solution (Table 2)

Table 2. Provasoli solution recipe. A comprehensive recipe with chemical composition and concentration on how to prepare vitamin and trace solution for natural or artificial seawater.

Components	Final concentrations
Solution 1 (10×)	
H_3BO_3	30.0 mM
$FeCl_3$	0.3 mM
$MnSO_4$	1.6 mM
$ZnSO_4$	0.13 mM
$CoSO_4$	0.028 mM
EDTA	5.7 mM
Solution 2 (10×)	
$(NH_4)2Fe(SO_4)2{\cdot}6H_2O$	3.0 mM
EDTA	3.4 mM
Solution 3 (10×)	
$NaNO_3$	270 mM
Solution 4 (10×)	
$C_3H_7Na_2O_6P$	15.4 mM
Vitamin mix (100×)	
Vitamin B12 (cyanocobalamin)	0.0067 g L^{-1}
Thiamin (vitamin B1)	0.33 g L^{-1}
Biotin	0.0033 g L^{-1}
Tris	333 g L^{-1}

These are stock solutions in 1 L volume. Adjust the volume according to your needs and resources. The vitamin mix should be kept in the dark after filtering at 0.2 µm. Maintain all solutions at 4°C. When making Provasoli medium, mix all solutions in numbered order (*i.e.*, from solution 1 to solution 4) and dilute to 1×; then, adjust the pH to 7.8 with HCl, and then add the vitamin mix (it should be slightly diluted before adding it to the other solution). Aliquot in falcons or small bottles and autoclave. Provasoli solution is kept at 4°C and used at 20 ml L^{-1} in artificial seawater or natural seawater for full Provasoli enriched seawater (PES) medium or 10 ml L^{-1} for ½ PES. In our case, we autoclaved and filtered (at 0.2 µm) natural seawater.

Our Provasoli recipe is based on Le Bail and Charrier (2013).

Acknowledgments

I.T. is funded by the Region Bretagne, France (grant number COH18020) and the Norwegian University of Life Science (NMBU).

Competing interests

The corresponding author certifies no financial and non-financial competing interests.

References

1. Adams, J. M., Gallagher, J. A. and Donnison, I. S. (2009). Fermentation study on *Saccharina latissima* for bioethanol production considering variable pre-treatments. *J Appl Phycol* 21: 569.
2. Sogn Andersen, G., Steen, H., Christie, H., Fredriksen, S. and Moy, F. E. (2011). Seasonal patterns of sporophyte growth, fertility, fouling, and mortality of *Saccharina latissima* in Skagerrak, Norway: Implications for Forest Recovery. *J Marine Sciences* 2011: e690375.
3. Bartsch, I., Wiencke, C., Bischof, K., Buchholz, C. M., Buck, B.H., Eggert, A., Feuerpfeil, P., Hanelt, D., Jacobsen, S., Karez, R., Karsten, U., Molis, M., Roleda M. Y., Schubert, H., Schumann, R., Valentin, K., Weinberger, F., Wiese, J. (2008). The genus Laminaria sensu lato: recent insights and developments. *Eur J Phycol* 43: 1-86.
4. Charrier, B., Le Bail, A. and de Reviers, B. (2012). Plant Proteus: brown algal morphological plasticity and underlying developmental mechanisms. *Trends Plant Sci* 17(8): 468-477.
5. Cumashi, A., Ushakova, N. A., Preobrazhenskaya, M. E., D'Incecco, A., Piccoli, A., Totani, L., Tinari, N., Morozevich, G. E., Berman, A. E., Bilan, M. I., Usov, A. I., Ustyuzhanina, N. E., Grachev, A. A., Sanderson, C. J., Kelly, M., Rabinovich, G. A., Iacobelli, S., Nifantiev, N. E. and Consorzio Interuniversitario Nazionale per la Bio-Oncologia, I. (2007). A comparative study of the anti-inflammatory, anticoagulant, antiangiogenic, and antiadhesive activities of nine different fucoidans from brown seaweeds. *Glycobiology* 17(5): 541-552.
6. Ebbing, A., Pierik, R., Bouma, T., Kromkamp, J. C. and Timmermans, K. (2020). How light and biomass density influence the reproduction of delayed *Saccharina latissima* gametophytes (Phaeophyceae). *J Phycol* 56(3): 709-718.
7. Forbord, S., Skjermo, J., Arff, J., Handå, A., Reitan, K., Bjerregaard, R. and Lüning, K. (2012). Development of *Saccharina latissima* (Phaeophyceae) kelp hatcheries with year-round production of zoospores and juvenile sporophytes on culture ropes for kelp aquaculture. *J Appl Phycol* 24: 393-399.
8. Fritsch, F. E. (1945). *The Structure And Reproduction Of The Algae.* Cambridge University Press, Cambridge.
9. Han, H., Wang, L., Liu, Y., Shi, X., Zhang, X., Li, M. and Wang, T. (2019). Combination of curcuma zedoary and kelp inhibits growth and metastasis of liver cancer *in vivo* and *in vitro* via

reducing endogenous H_2S levels. *Food Funct* 10(1): 224-234.

10. Hsiao, S. I. C. and Druehl, L. D. (1971). Environmental control of gametogenesis in *Laminaria saccharina*. I. The effects of light and culture media. *Can J Botany* 49:1503-1508.
11. Pang, S. J. and Lüning, K. (2004). Breaking seasonal limitation: year-round sporogenesis in the brown alga *Laminaria saccharina* by blocking the transport of putative sporulation inhibitors. *Aquaculture* 240: 531-541.
12. Kanda, T. (1936). On the Gametophytes of Some Japanese Species of Laminariales. Scientific papers of the Institute of Algological Research, Faculty of Science, Hokkaido Imperial University 1:221-260.
13. Kinoshita, N., Nagasato, C. and Motomura, T. (2017). Chemotactic movement in sperm of the oogamous brown algae, Saccharina japonica and Fucus distichus. *Protoplasma* 254(1): 547-555.
14. Kraan, S. (2016). Seaweed and Alcohol. In: *Seaweed in Health and Disease Prevention.* Elsevier, 169-184.
15. Le Bail, A. and Charrier, B. (2013). Culture Methods and Mutant Generation in the Filamentous Brown Algae Ectocarpus siliculosus. In: *Plant Organogenesis Methods in Molecular Biology.* De Smet, I. (Ed.). Humana Press, 323-332.
16. Lee, J. A. and Brinkhuis, B. H. (1988). Seasonal Light and Temperature Interaction Effects on Development of *Laminaria saccharina* (Phaeophyta) Gametophytes and Juvenile Sporophytes. *J Phycol* 24: 181-191.
17. Lewis, R. J., Green, M. K. and Afzal, M. E. (2013). Effects of chelated iron on oogenesis and vegetative growth of kelp gametophytes (Phaeophyceae). *Phycol Res* 61: 46-51.
18. Long, M., Li, Q. M., Fang, Q., Pan, L. H., Zha, X. Q. and Luo, J. P. (2019). Renoprotective Effect of Laminaria japonica Polysaccharide in Adenine-Induced Chronic Renal Failure. *Molecules* 24(8): 1491.
19. Lüning, K. (1980). Critical Levels of Light and Temperature Regulating the Gametogenesis of Three *Laminaria* Species (Phaeophyceae). *J Phycol* 16: 1-15.
20. Lüning, K. and Dring, M. J. (1972). Reproduction induced by blue light in female gametophytes of Laminaria saccharina. *Planta* 104(3): 252-256.
21. Maier, I. and Müller, D. G. (1986). Sexual pheromones in algae. *The Biological Bulletin* 170: 145-175.
22. Mohibbullah, M., Bashir, K. M. I., Kim, S. K., Hong, Y. K., Kim, A., Ku, S. K. and Choi, J. S. (2019). Protective effects of a mixed plant extracts derived from Astragalus membranaceus and Laminaria japonica on PTU-induced hypothyroidism and liver damages. *J Food Biochem* 43(7): e12853.
23. Motomura, T. and Sakai, Y. (1984). Ultrastructural studies of gametogenesis in Laminaria angustata (Laminariales, Phaeophyta) regulated by iron concentration in the medium. *Phycologia* 23: 331-343.

24. Yabu, H. (1965). Early development of several species of Laminariales in Hokkaido. Memoirs of the Faculty of Fisheries Hokkaido University 12: 1-72.
25. Zhang, Q. S., Qu, S. C., Cong, Y. Z., Luo, S. J. and Tang, X. X. (2008). High throughput culture and gametogenesis induction of *Laminaria japonica* gametophyte clones. *J Appl Phycol* 20: 205-211.

ISBN: 978-82-575-2043-4
ISSN: 1894-6402

Norwegian University
of Life Sciences

Postboks 5003
NO-1432 Ås, Norway
+47 67 23 00 00
www.nmbu.no

11711 / ANDVORDGRAFISK.NO